The influence of wall permeability on laminar and turbulent flows

Theory and simulations

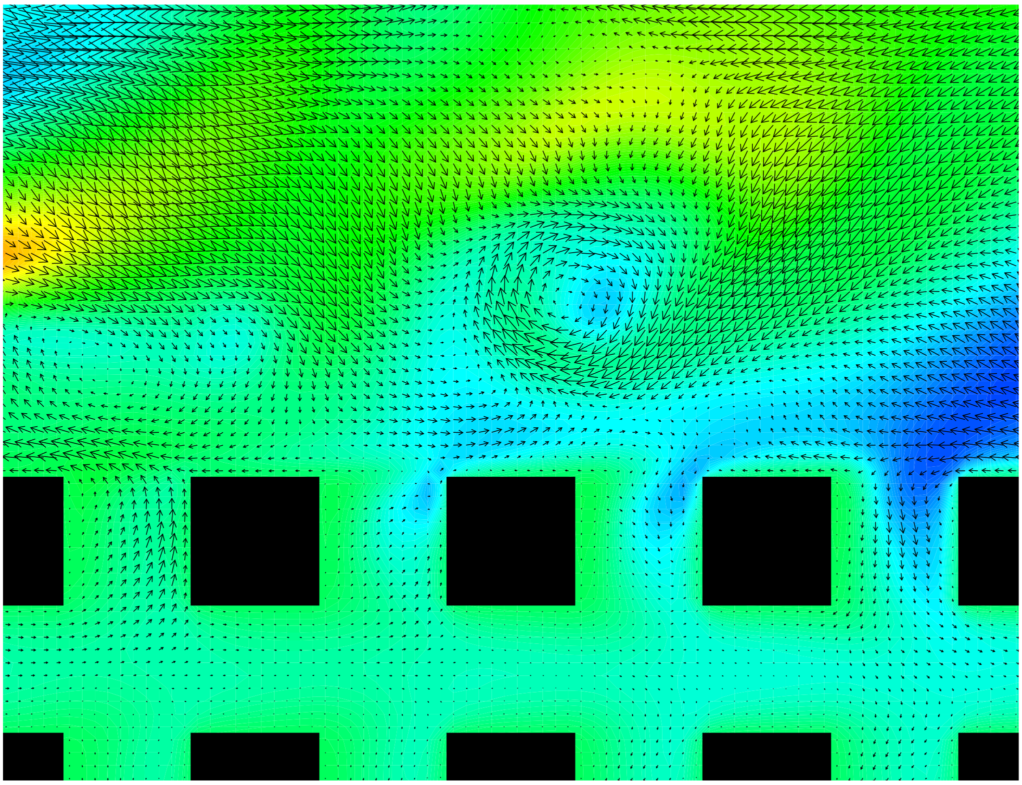

Wim-Paul Breugem

The influence of wall permeability on laminar and turbulent flows

Theory and simulations

PROEFSCHRIFT

ter verkrijging van de graad van doctor
aan de Technische Universiteit Delft,
op gezag van de Rector Magnificus prof. dr. ir. J.T. Fokkema,
voorzitter van het College voor Promoties,
in het openbaar te verdedigen op
dinsdag 11 januari 2005 om 15:30 uur

door

Wilhelmus Paulus BREUGEM
natuurkundig ingenieur
geboren te Bleiswijk.

Dit proefschrift is goedgekeurd door de promotoren:
Prof. dr. ir. F.T.M. Nieuwstadt
Dr. ir. B.J. Boersma

Samenstelling promotiecommissie:

Rector Magnificus,	voorzitter	
Prof. dr. ir. F.T.M. Nieuwstadt,	Technische Universiteit Delft,	promotor
Dr. ir. B.J. Boersma,	Technische Universiteit Delft,	toegevoegd promotor
Dr. ir. R.E. Uittenbogaard,	Waterloopkundig Laboratorium Delft	
Prof. dr. ir. G. Stelling,	Technische Universiteit Delft	
Prof. dr. ir. B.J. Geurts,	Technische Universiteit Eindhoven	
Prof. dr. ir. G.J.F. van Heijst,	Technische Universiteit Eindhoven	
Prof. dr. S.J.M.H. Hulscher,	Universiteit Twente	

Dr. ir. R.E. Uittenbogaard heeft als begeleider in belangrijke mate aan de totstandkoming van het proefschrift bijgedragen.

The work presented in this thesis was supported financially
by the Foundation for Fundamental Research on Matter (FOM).

Copyright © 2004 by W.P. Breugem
All rights reserved.
ISBN 90-9018924-6

Printed by Febodruk BV, Enschede

The picture on the cover of this thesis is an enlargement
of figure 6.8.a. The color denotes the velocity component,
which is directed normal to the plane of paper.

Contents

Summary **vii**

Samenvatting **xi**

1 Introduction **1**

1.1 Background and research objectives . . . 1
1.2 Outline . . . 6

2 The continuum approach for flows through porous media **9**

2.1 Introduction . . . 9
2.2 Derivation of the VANS equations . . . 12
2.3 On the choice of the filter . . . 17
2.4 An example of volume averaging . . . 20
2.5 Closure problem for the drag force . . . 23
2.6 Closure problem for the subfilter–scale stress . . . 25

3 The laminar boundary layer over a permeable wall **29**

3.1 Introduction . . . 30
3.2 Flow geometry and VANS equations . . . 34
3.3 The boundary–layer equations . . . 37
3.3.1 Homogeneous fluid region . . . 37
3.3.2 Homogeneous porous region . . . 38
3.3.3 Interface region . . . 39
3.3.4 Summary of equations, boundary conditions and assumptions . . . 42
3.4 Analytical solution for the flow in the ω–region . . . 44
3.5 Self–similar solution for the flow in the η–region . . . 45
3.6 Displacement and momentum thickness . . . 50
3.7 Numerical method and results . . . 52
3.7.1 Numerical method . . . 52
3.7.2 Velocity distributions . . . 52
3.7.3 Shear stress distribution . . . 55
3.8 Summary and discussion . . . 56

4 **DNS of laminar flow over a permeable wall** **59**
4.1 Introduction 60
4.2 Volume–Averaging Method and VANS equations 61
4.3 Closure problem for the drag force 63
4.4 Numerical method 67
4.5 Evaluation of the closure for the drag force 69
4.6 Results from the channel flow simulations. 71
4.7 Summary and discussion 79

5 **The influence of wall permeability on turbulent channel flow** **81**
5.1 Introduction 82
5.2 Continuum approach for flows in porous media 86
5.3 Flow geometry and drag model for the interface region 90
  5.3.1 Homogeneous porous region 91
  5.3.2 Channel region 91
  5.3.3 Interface region 92
5.4 Implications of wall permeability for scaling of turbulence 93
5.5 Numerical method 97
5.6 Turbulence statistics 99
  5.6.1 Mean velocity 99
  5.6.2 Mean kinetic energy 107
  5.6.3 Velocity and pressure fluctuations 109
  5.6.4 Vorticity fluctuations 116
  5.6.5 Reynolds and total shear stress 119
  5.6.6 Turbulent–kinetic–energy budgets 121
  5.6.7 Turbulence structure 123
5.7 Summary and discussion 128

6 **DNS of turbulent flow over a permeable wall using different approaches** **131**
6.1 Introduction 132
6.2 Cartesian grid of cubes 134
6.3 The VANS equations 136
6.4 DNS with continuum 138
  6.4.1 Homogeneous porous region 139
  6.4.2 Channel region 140
  6.4.3 Interface region 141
6.5 DNS with cubes 142
6.6 Numerical results 146
  6.6.1 Volume averaging and mean velocity profiles 148
  6.6.2 Rms profiles of velocity components and pressure 150
  6.6.3 Shear–stress profiles 154
6.7 Conclusions and discussion 156

7 Main conclusions, discussion and recommendations 159
7.1 Main conclusions 159
7.2 Discussion 162
7.3 Recommendations for future research 164

A Transport equation for the subfilter–scale kinetic energy 167

B A note on simulations of flows over and through porous media. 171
B.1 Simulations using a Reynolds–averaged form of the VANS equations. . . . 171
B.2 LES of flows over and through porous media 172

Bibliography 177

Nawoord 187

Curriculum vitae 189

Summary

The influence of wall permeability on laminar and turbulent flows: theory and simulations

– Wim-Paul Breugem –

The study of flows over permeable walls is relevant to many applications. A permeable wall is defined here as a rigid porous wall with interconnected pores through which fluid may flow. Examples are flows over and through river beds, vegetation, snow, heat exchangers of metal foam, and oil wells of porous stone. Literature on flows over permeable walls is rather scarce. Studies on laminar flows over permeable walls are restricted to spatially fully developed flows, such as channel flow and flow in a Hele–Shaw cell. A few experiments have been conducted on turbulent flows over permeable walls. These experiments indicate that wall permeability is responsible for an increase in skin friction with respect to impermeable walls with a similar surface roughness. How turbulence is exactly changed by wall permeability, is however still an open question. The main objectives of this thesis are to gain insight in the influence of wall permeability on both laminar and turbulent flows, and to develop a formalism for Direct Numerical Simulations (DNS) of turbulent flows over permeable walls.

Chapter 2 treats the theoretical background for modeling flows through porous media. The celebrated Law of Darcy predicts the pressure drop over a porous medium for a given flow rate. This equation describes the macroscopic flow behavior corresponding to Stokes flow inside the pores. A direct description of the microscopic flow field is usually unfeasible, because of the wide range of flow length scales and the complex geometrical structure of most porous media. The theoretical basis for Darcy's Law is provided by the Volume–Averaging Method. In this method the macroscopic flow is defined as a local weighted volume average of the microscopic flow. The macroscopic or volume–averaged flow is continuous throughout the porous medium, defined both in the fluid and the solid phase. Application of the volume–averaging operator to the Navier–Stokes equations yields the Volume–Averaged Navier–Stokes (VANS) equations. In order to solve the VANS equations, closures are demanded for the subfilter–scale stress and the drag force in terms of volume–averaged flow quantities. Based on an order–of–magnitude analysis, it is shown that in porous media the influence of subfilter–scale dispersion is usually negligible compared to drag.

In chapter 3, a theoretical analysis is given of the first–order effect of wall permeability on the laminar boundary layer over a wedge. The VANS equations are used to describe to the volume–averaged flow inside the permeable wall. Two different boundary layers can be distinguished: the Prandtl boundary layer above the permeable wall and the Brinkman boundary layer inside the permeable wall. The momentum–transfer model of Ochoa–Tapia & Whitaker [67] (OTW model) is used, to match the solutions for the two boundary layers at the wall interface. A generalized Falkner–Skan equation is derived for the self–similar flow in the Prandtl boundary layer. The influence of wall permeability is characterized by the perturbation parameter κ, which can be interpreted as the ratio of the Brinkman to the Prandtl boundary–layer thickness. The first–order effect of wall permeability is an apparent slip velocity at the interface. A wall–normal interface velocity is a second–order effect. Wall permeability causes furthermore a decrease in the wall–shear stress when the freestream flow accelerates in space, but an increase in the wall–shear stress when the freestream flow decelerates in space.

In chapter 4, the closure problem for the drag force in the VANS equations is investigated. Two different kinds of simulations have been conducted. The first kind of simulations concerns flow through a fully periodic Cartesian grid of cubes. A closure for the drag force is proposed, based on the models of Irmay [37] and Burke–Plummer [7], of which the coefficients are determined from these simulations. The second kind of simulations concerns Stokes flow through a plane channel with a solid top wall and a permeable bottom wall consisting of the same grid of cubes, which however now only is infinitely extended in the horizontal directions. The computed velocity field has been volume averaged using the cellular filter proposed by Quintard & Whitaker [75] for ordered porous media. The permeable wall can be divided into a homogeneous porous region with a constant porosity, and an interface region with a height–dependent porosity. Two momentum transfer models have been evaluated for the drag force in the interface region: the OTW model and a variable–permeability model. The approximate solution for the velocity profile based on the OTW model is in good agreement with the DNS results. However, the value of the tangential stress–jump parameter in this model appears to be very sensitive to the definition of the wall interface. A variable–permeability model has been proposed based on the aforementioned Irmay model, which relates the permeability in the interface region to the local value of the porosity. This model agrees not very well with the DNS data, which is possibly connected to a lower effective viscosity of the volume–averaged flow as compared to the viscosity of the unfiltered flow.

In chapter 5, a formalism is developed for a DNS of turbulent flow in a plane channel with a solid top wall and a permeable bottom wall. The permeable wall is a packed bed, which is characterized by the porosity and the mean particle diameter. The VANS equations are used to describe the flow inside the permeable wall. Distinction is made between the channel region with a porosity equal to unity, the homogeneous porous region with a constant porosity, and the interface region with a height–dependent porosity. For a sufficiently small computational mesh spacing, the VANS equations reduce to the standard Navier–Stokes equations in the channel region. To solve the VANS equations in the homogeneous porous and the interface region, closures are required for the subfilter–scale stress and the drag force. The subfilter–scale stress is neglected. The drag force is modeled

by the Ergun equation for packed beds in combination with a variable–porosity model for the interface region.

The main objective of chapter 5 is to gain insight in the influence of wall permeability on the structure and dynamics of turbulence. Results from four simulations are shown, for which only the wall porosity in the homogeneous porous region is changed. The influence of wall permeability can be characterized by the permeability Reynolds number, Re_K, which represents basically the ratio of the effective pore diameter over the typical length scale of near–wall eddies. For small Re_K, the wall behaves like a solid wall. For large Re_K, the wall is classified as a highly permeable wall near which viscous effects are of minor importance. It is observed that low– and high–speed streaks and the associated quasi–streamwise vortices are absent near a highly permeable wall. This is attributed to turbulent transport across the wall interface and the reduction in the Reynolds–averaged shear stress due to a weakening of respectively the wall–blocking and the wall–induced viscous effect. The absence of streaks is consistent with a decrease in the peak value of the streamwise rms velocity normalized by the friction velocity at the permeable wall. Despite the increase in the peak values of the spanwise and wall–normal rms velocities, the peak value of the turbulent kinetic energy is therefore smaller. Turbulence near a highly permeable wall is dominated by relatively large vortical structures, which originate possibly from a Kelvin–Helmholtz type of instability. These structures are responsible for an exchange of momentum between the channel and the permeable wall. This process contributes strongly to the Reynolds–shear stress and thus to a large increase in the skin friction. Consequently, the interception of the log–law fit is shifted downwards. Furthermore, it is found that the slope of the log–law fit is larger than the value of approximately 1/0.4 for turbulent flows over both smooth and rough walls.

Another objective of the study in chapter 5, is to check the wall similarity hypothesis. The streamwise rms velocity, the rms vorticities and the Reynolds–shear stress are self–similar in the outer region, irrespective of the porosity of the wall. On the other hand, the spanwise and wall–normal rms velocities and the rms pressure show significant departures from similarity. It is shown that the wall–normal velocity is significantly correlated over a large wall–normal distance, which is a consequence of the weakening of the wall–blocking effect. This suggests that the outer region communicates with the inner region, and this might explain the observed departures from similarity.

In chapter 6, the formalism developed in chapter 5 for DNS of turbulent flows over permeable walls, is validated. A DNS has been performed of turbulent channel flow over a permeable wall consisting of a three–dimensional Cartesian grid of 30 x 20 x 9 cubes. To enforce the no–slip and no–penetration conditions on the cubes, an Immersed Boundary Method is used. The results of the DNS are compared with a second DNS in which the VANS equations are used for the volume–averaged flow through the grid of cubes. Subfilter–scale dispersion is neglected. The drag force is modeled by means of the Irmay and the Burke–Plummer model in combination with a variable–porosity model for the interface region. The results of the DNS with the grid of cubes and the second DNS in which the VANS equations are used, agree very well. The main conclusion of this study is therefore that a DNS in combination with the continuum approach based on the VANS equations, is capable of an accurate simulation of turbulent flows over permeable walls.

Samenvatting

De invloed van wandpermeabiliteit op laminaire en turbulente stromingen: theorie en simulaties – Wim-Paul Breugem –

Het bestuderen van stromingen over permeabele wanden is relevant voor veel toepassingen. Een permeabele wand wordt hier gedefinieerd als een rigide poreuze wand met onderling verbonden poriën waardoor een fluïdum kan stromen. Voorbeelden zijn stromingen over en door een rivierbed, vegetatie, sneeuw, warmtewisselaars van schuimmetaal, en oliebronnen bestaande uit poreus gesteente. Literatuur over stromingen langs permeabele wanden is tamelijk schaars. Studies aan laminaire stromingen langs permeabele wanden zijn beperkt tot ruimtelijk volledig ontwikkelde stromingen, zoals de stroming in een kanaal of een Hele–Shaw cel. Een aantal experimenten is uitgevoerd aan turbulente stromingen langs permeabele wanden. Deze experimenten geven aan dat permeabiliteit verantwoordelijk is voor een toename in de wandfrictie ten opzichte van impermeabele wanden met een soortgelijke oppervlakteruwheid. Hoe turbulentie precies verandert door wandpermeabiliteit, is echter nog steeds een open vraag. De belangrijkste doelstellingen van dit proefschrift zijn om inzicht te verkrijgen in de invloed van wandpermeabiliteit op zowel laminaire als turbulente stromingen, en om een formalisme te ontwikkelen voor Direct Numerical Simulations (DNS) van turbulente stromingen langs permeabele wanden.

Hoofdstuk 2 behandelt de theoretische achtergrond van het modelleren van stromingen door poreuze media. De beroemde Wet van Darcy voorspelt de drukval over een poreus medium voor een gegeven debiet. Deze vergelijking beschrijft het macroscopische stromingsgedrag dat correspondeert met Stokes–stroming in de poriën. Een rechtstreekse beschrijving van het microscopische stromingsveld is meestal niet haalbaar vanwege het grote bereik van de lengteschalen van de stroming en de complexe geometrische structuur van de meeste poreuze media. De theoretische basis van de Wet van Darcy wordt gegeven door de Volume–Averaging Method. In deze methode wordt de macroscopische stroming gedefinieerd als een lokaal, gewogen volumegemiddelde van de microscopische stroming. De macroscopische of volumegemiddelde stroming is continu in het hele poreuze medium, gedefinieerd zowel in de fluïdumfase als in de vaste fase. Toepassing van de volumemiddelingsoperator op de Navier–Stokes vergelijkingen levert de Volume–Averaged Navier–Stokes (VANS) vergelijkingen op. Om deze vergelijkingen te kunnen oplossen, zijn sluitingen nodig voor de subfilterschaal–spanning en de weerstandskracht in termen

van volumegemiddelde stromingsvariabelen. Gebaseerd op een orde–van–grootte–analyse wordt aangetoond dat in poreuze media de invloed van subfilterschaal–dispersie meestal verwaarloosbaar is ten opzichte van de weerstandskracht.

In hoofdstuk 3 wordt een theoretische analyse gegeven van het eerste–orde–effect van wandpermeabiliteit op de laminaire grenslaag over een wig. De VANS vergelijkingen worden gebruikt om de volumegemiddelde stroming in de permeabele wand te beschrijven. Twee verschillende grenslagen kunnen worden onderscheiden: de Prandtl–grenslaag boven de permeabele wand en de Brinkman–grenslaag in de permeabele wand. Het impulsoverdrachtsmodel van Ochoa–Tapia & Whitaker [67] (OTW model) wordt gebruikt om de oplossingen voor de twee grenslagen op elkaar aan te sluiten op het interface. Een gegeneraliseerde Falkner–Skan vergelijking wordt afgeleid voor de gelijkvormige stroming in de Prandtl–grenslaag. De invloed van wandpermeabiliteit wordt gekarakteriseerd door de verstoringparameter κ, die kan worden geïnterpreteerd als de verhouding van de Brinkman– tot de Prandtl–grenslaagdikte. Het eerste–orde–effect van wandpermeabiliteit is een ogenschijnlijke slipsnelheid op het interface. Een wandnormale snelheid op het interface is een tweede–orde–effect. Verder veroorzaakt wandpermeabiliteit een afname in de wandschuifspanning wanneer de vrije stroming ruimtelijk versnelt, maar een toename in de wandschuifspanning wanneer de vrije stroming ruimtelijk vertraagt.

In hoofdstuk 4 wordt het sluitingsprobleem onderzocht voor de weerstandskracht in de VANS vergelijkingen. Twee verschillende soorten simulaties zijn uitgevoerd. De eerste soort betreft de stroming door een volledig periodiek Cartesisch rooster van kubussen. Een sluiting voor de weerstandskracht wordt voorgesteld, gebaseerd op het Irmay– [37] en Burke–Plummer–model [7], waarvan de coëfficiënten worden bepaald op basis van deze simulaties. De tweede soort simulaties betreft Stokes–stroming door een vlak kanaal met een permeabele onderwand bestaande uit hetzelfde rooster van kubussen, dat nu echter alleen in de horizontale richtingen oneindig uitgestrekt is. Het uitgerekende snelheidsveld is volumegemiddeld met behulp van het cellular filter die Quintard & Whitaker [75] hebben voorgesteld voor geordende poreuze media. De permeabele wand kan worden onderverdeeld in een homogeen poreus gebied met een constante porositeit, en een interfacegebied met een hoogte–afhankelijke porositeit. Twee impulsoverdrachtsmodellen worden geëvalueerd voor de weerstandskracht in het interfacegebied: het OTW model en een variabele–permeabiliteit–model. De benaderde oplossing voor het snelheidsprofiel gebaseerd op het OTW model, is in goede overeenstemming met de DNS resultaten. Echter, de waarde van de sprongparameter voor de tangentiële spanning in dit model blijkt gevoelig te zijn voor de definitie van het scheidingsvlak tussen wand en kanaal. Een variabele–permeabiliteit–model wordt voorgesteld, gebaseerd op het eerdergenoemde Irmay–model, dat de permeabiliteit in het interfacegebied relateert aan de lokale porositeit. Dit model stemt niet erg goed overeen met de DNS data, wat mogelijk samenhangt met een lagere effectieve viscositeit van de volumegemiddelde stroming vergeleken met de viscositeit van de ongefilterde stroming.

In hoofdstuk 5 wordt een formalisme ontwikkeld voor de DNS van de turbulente stroming in een vlak kanaal met een vaste bovenwand en een permeabele onderwand. De permeabele wand is een gepakt bed, dat wordt gekarakteriseerd door de porositeit en de gemiddelde korreldiameter. De VANS vergelijkingen worden gebruikt om de volumegemiddelde stroming in de permeabele wand te beschrijven. Er wordt onderscheid gemaakt tussen het kanaalgebied met een porositeit gelijk aan één, het homogene poreuze gebied met een constante porositeit, en het interfacegebied met een hoogte–afhankelijke porositeit. Wanneer de rekenroosterafstand voldoende klein is, reduceren de VANS vergelijkingen in het kanaalgebied tot de standaard Navier–Stokes vergelijkingen. Om de VANS vergelijkingen op te kunnen lossen in het homogene poreuze gebied en het interfacegebied, zijn sluitingen nodig voor de subfilterschaal–spanning en de weerstandskracht. De subfilterschaal–spanning is verwaarloosd. De weerstandskracht is gemodelleerd met de Ergun–vergelijking voor gepakte bedden in combinatie met een variabele–porositeit–model voor het interfacegebied.

De belangrijkste doelstelling van hoofdstuk 5 is om inzicht te verkrijgen in de invloed van wandpermeabiliteit op de structuur en dynamica van turbulentie. Resultaten worden getoond van vier simulaties, waar alleen de porositeit in het homogene poreuze gebied is veranderd. De invloed van wandpermeabiliteit kan worden gekarakteriseerd door het permeabiliteit–Reynoldsgetal, Re_K, dat in essentie de verhouding weergeeft van de effectieve poriediameter tot de typische lengteschaal van turbulente wervels dichtbij de wand. Wanneer Re_K klein is, gedraagt de wand zich als een vaste wand. Wanneer Re_K groot is, wordt de wand geclassificeerd als een hoog–permeabele wand in de buurt waarvan visceuze effecten verwaarloosbaar zijn. Het is waargenomen dat low– en high–speed streaks en de daarmee geassocieerde wervels, afwezig zijn in de buurt van een hoog–permeabele wand. Dit wordt toegeschreven aan turbulent transport door het wandinterface en de reductie in de Reynolds–gemiddelde schuifspanning ten gevolge van respectievelijk een verzwakking van het wall–blocking effect en van visceuze effecten geïnduceerd door de wand. De afwezigheid van streaks is consistent met een afname in de piekwaarde van de axiale–rms–snelheid genormaliseerd met de frictiesnelheid aan de permeabele wand. Ondanks de toename in de piekwaarde van de transversale– en de wandnormale–rms–snelheden, is de piekwaarde van de turbulente kinetische energie daarom kleiner. Turbulentie dichtbij een hoog–permeabele wand wordt gedomineerd door relatief grote wervelstructuren, die mogelijk hun oorsprong vinden in een instabiliteit van het type Kelvin–Helmholtz. Deze structuren zijn verantwoordelijk voor de uitwisseling van impuls tussen het kanaal en de permeabele wand. Dit proces draagt sterk bij aan de Reynoldsschuifspanning en daarom aan een grote toename in de wandfrictie. Bijgevolg verschuift de interceptie van de logaritmische fit aan het snelheidsprofiel naar beneden. Verder is gevonden dat de helling van de logaritmische fit groter is dan de waarde van ongeveer 1/0.4 voor turbulente stromingen over zowel gladde als ruwe wanden.

Een andere doelstelling van de studie in hoofdstuk 5 is om de wandgelijkvormigheidshypothese te toetsen. De axiale–rms–snelheid, de rms van de vorticiteiten en de Reynoldsschuifspanning zijn gelijkvormig in het buitengebied, ongeacht de porositeit van de wand. Aan de andere kant vertonen de transversale– en wandnormale–rms–snelheden en de rms van de druk significante afwijkingen van gelijkvormigheid. Het wordt aangetoond dat de wandnormale snelheid significant gecorreleerd is over een grote afstand in de wandnormale richting, wat een gevolg is van de verzwakking van het wall–blocking effect. Dit suggereert dat het buitengebied communiceert met het binnengebied, en dit zou de waargenomen afwijkingen in gelijkvormigheid kunnen verklaren.

In hoofdstuk 6 wordt het formalisme gevalideerd dat is ontwikkeld in hoofdstuk 5 voor de DNS van turbulente stromingen over permeabele wanden. Een DNS is uitgevoerd van de turbulente kanaalstroming over een permeabele wand bestaande uit een Cartesisch rooster van 30 x 20 x 9 kubussen. De Immersed Boundary Method is gebruikt om de no–slip– en no–penetration–condities af te dwingen op de kubussen. De resultaten van de DNS worden vergeleken met een tweede DNS waarin de VANS vergelijkingen zijn gebruikt voor de volumegemiddelde stroming door het kubusrooster. Subfilterschaal–dispersie is verwaarloosd. De weerstandskracht is gemodelleerd met behulp van het Irmay– en het Burke–Plummer–model in combinatie met een variabele–porositeit–model voor het interfacegebied. De resultaten van de DNS met het kubusrooster en de tweede DNS waarin de VANS vergelijkingen zijn gebruikt, stemmen erg goed overeen. De belangrijkste conclusie van deze studie is daarom dat een DNS in combinatie met de continuümbenadering gebaseerd op de VANS vergelijkingen, in staat is tot een nauwkeurige simulatie van turbulente stromingen over permeabele wanden.

Chapter 1

Introduction

1.1 Background and research objectives

In this thesis flows over and through permeable walls are studied. A permeable wall is defined here as a rigid porous wall with interconnected pores through which fluid may flow. In this definition, *rigid* means that the solid structure of the porous medium is not moving. We will restrict ourselves to *passive* permeable walls in the sense that no *active* suction or blowing is imposed at the interface of or inside the permeable wall. Passive permeable walls are encountered in a wide range of applications. Examples in the petrochemical industry are oil wells, where oil flows through porous stone. In hydrology one can think of flows over river beds of e.g. gravel. In the latter example, wall permeability, i.e. the fact that flow may take place in the bed pores, is expected to affect the bed friction and consequently the volume flow and the surface level of the river. Wall permeability is also expected to affect bed erosion, the exchange of oxygen between surface and subsurface flow and hence degradation of organic material [97], and the dispersion of pollutants. To some extent, densely built–up urban areas and dense vegetation can be considered as permeable wall layers as well. Related research topics are dispersion of pollutants in metropoles, the exchange of energy, oxide and carbon dioxide between forests and the atmosphere [28], and the propagation of forest fires [84]. Other examples of permeable walls are snow [27] and heat exchangers of open–cell metal foam [58],[90]. Finally, we note that permeable walls are also encountered inside the human body. Blood vessels are lined with a layer known as the endothelial glycocalyx, which has been modeled recently as a deformable porous wall layer [18],[27]. The pores of this layer have a dimension of roughly 10 nm. Current research is directed towards investigating the effect of this layer on the motion of red blood cells in the smallest capillaries with a diameter of about 10 μm, which is of the same order as the diameter of the red cells.

Before we introduce our own research objectives, we first give a short overview of the existing literature on flows over and through permeable walls.

- **Laminar flows over permeable walls**

A few experimental studies concern the influence of wall permeability on laminar flows [5],[31]. Beavers & Joseph [5] performed experiments on laminar flow in a plane channel with a lower permeable wall. It was found that wall permeability permits a non–zero velocity, i.e. an apparent slip velocity, at the interface. This causes a reduction in skin friction with respect to an impermeable wall. The degree at which wall permeability affects the flow depends on the ratio of the *effective* pore diameter $\sqrt{K}$, where K is the permeability, to the channel height. Based on their experimental investigations, Beavers & Joseph proposed a boundary condition, which incorporates the effect of wall permeability. Their work had a large impact, considering the substantial amount of subsequent investigations on the coupling between the flow inside a permeable wall and outside the wall, see e.g. the review of Alazmi & Vafai [1]. The classic paper of Brinkman [14] is probably the first one, which deals with the momentum transfer across a permeable interface. In recent years a number of numerical studies, dedicated to this problem, have been reported [52],[53],[81]. In this thesis several momentum–transfer models will be subject of investigation too.

- **Experiments on turbulent flows over permeable walls**

Literature on the influence of wall permeability on turbulent flows is scarce. A complication is that permeable walls are usually also rough, and hence it is rather difficult to isolate the effect of wall permeability from wall roughness. The opposite is not necessarily true: a rough wall could be very well impermeable in the sense that the flow becomes zero over the height of a single roughness element. For instance, a multiple–layer gravel bed is both permeable and rough, but a bed consisting of just a single layer of gravel is considered as rough and impermeable. The difference is illustrated in figure 1.1. In literature it is common practice to consider both permeable walls and impermeable walls with the same surface roughness as rough, thereby ignoring the difference in permeability and its influence on the flow. However, the experimental study of Kong & Schetz [46] revealed that the skin friction coefficient is larger for a permeable wall than for an impermeable wall with similar surface roughness. This conclusion is in agreement with the experi-

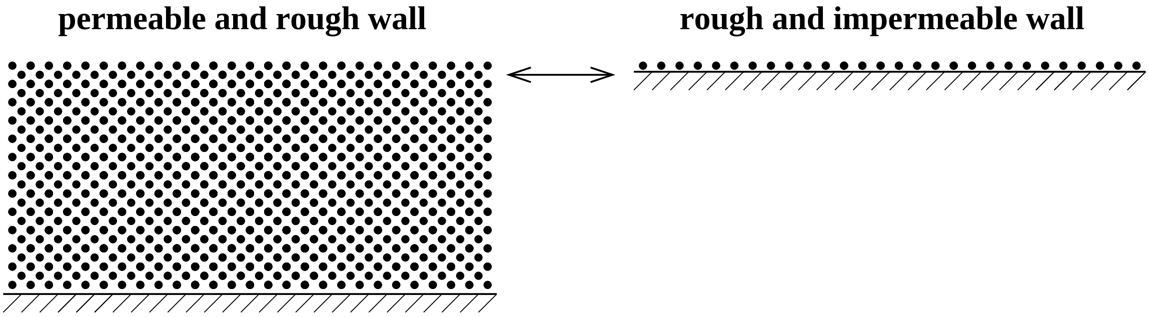

Figure 1.1: Illustration of the difference between a permeable and rough wall and an impermeable wall with the same surface roughness.

mental findings of Zagni & Smith [110] and Zippe & Graf [112]. These studies showed also that for the range of high Reynolds numbers, the skin friction coefficient increases with increasing Reynolds number for permeable walls, whereas it remains constant for impermeable walls with the same surface roughness. These observations indicate clearly that the effects of wall permeability and wall roughness on the flow are different, and they imply that wall permeability apparently alters the turbulence structure and dynamics.

Most experiments on turbulent flows over permeable walls are concerned with flow over vegetation. The review of Finnigan [28] discusses the gross features of experiments carried out in and above forests, cereal crops and model plant canopies. A problem of these experiments is that they are restricted to a limited amount of point measurements, whereas vegetation has usually a complex and inhomogeneous structure requiring observations at many locations. Despite the inherent scatter in these measurements, the experimental data have some striking features in common. Turbulence in plant canopies is dominated by large coherent structures with length scales of the order of the canopy height. It is believed that their origin lies in a Kelvin–Helmholtz type of instability of the mean velocity profile, which exhibits an inflexion point near the top of the canopy. For this reason, Raupach et al. [77] and Finnigan [28] suggested that the flow near the top of a canopy resembles more a plane mixing layer rather than a boundary layer.

- **Numerical studies on turbulent flows over permeable walls**

In recent years a number of numerical studies have been reported on turbulent flows over permeable walls, although mainly for the case of flow over vegetation. There are three different paths that can be followed for incorporating wall permeability in a simulation, which are briefly discussed below.

1. Boundary conditions

The first and computationally most simple method is to impose boundary conditions at the wall, which simulate the effect of permeability. This method was recently utilized by Hahn et al. [32] in Direct Numerical Simulations (DNS) [64] of turbulent flow in a plane channel with a lower permeable wall. The boundary conditions used are an extension of the boundary conditions of Beavers & Joseph [5]. These conditions allow for an apparent slip velocity, but impose simultaneously a zero wall–normal velocity. As pointed out by Hahn et al., the no–penetration condition is appropriate only when the effective pore diameter is sufficiently small compared to the typical size of near–wall turbulent eddies. This requirement is equivalent to a sufficiently small *permeability Reynolds number* $Re_K \equiv \sqrt{K}u_\tau/\nu$, where we recall that K is the permeability, $u_\tau \equiv \sqrt{\tau_w/\rho}$ is the friction velocity with τ_w the wall–shear stress and ρ the fluid density, and ν is the kinematic viscosity.

For large Re_K, turbulence will penetrate the permeable wall. It is not likely that for this case the complex interaction between the flow outside and the flow inside the permeable wall can be modeled by means of boundary conditions. Therefore, the other two methods for simulating flows over permeable walls, compute the flow *inside* the permeable wall as well.

2. Continuum approach

The simulation of flow through a permeable wall is not straightforward. Porous media have in general a complicated structure, which is not known in full detail. Another problem is the wide range of length scales. The smallest scales are typically of the order of the pore diameter or the dimension of the solid obstacles that form the porous medium. The largest scales may be of the order of the thickness of the permeable wall. This hampers the full simulation of flow through a permeable wall. However, the small and the large scales are usually well–separated. This motivates an approach in which only the large–scale behavior is considered. The theoretical basis for this approach is provided by the Volume–Averaged Navier–Stokes (VANS) equations [104], which can be rigorously derived from the local volume averaging of the Navier–Stokes equations. The volume–averaging technique is illustrated in figure 1.2. The well–known Law of Darcy [4] follows from the VANS equations for the case of a uniform and stationary flow through a homogeneous porous medium. The VANS equations can also be considered as a generalization of the equations used in Large–Eddy Simulations (LES) [56]. Like in LES a closure is required for the subfilter–scale stress. In addition to this, a drag force needs to be included. This force originates from the presence of solid obstacles, which exert a force on the volume–averaged (i.e. large–scale) flow field. A major benefit of using the VANS equations is that the porous medium can be considered as a continuum, because the volume–averaged flow field is continuous throughout the porous medium and no boundary conditions need to be imposed in the interior of the porous medium. For this reason, we will refer to the second method for simulating flows over and through permeable walls as the *continuum approach*. As far as we know, no DNS studies have been published on turbulent flows *over* permeable walls combined with the continuum approach for the flow *inside* the permeable

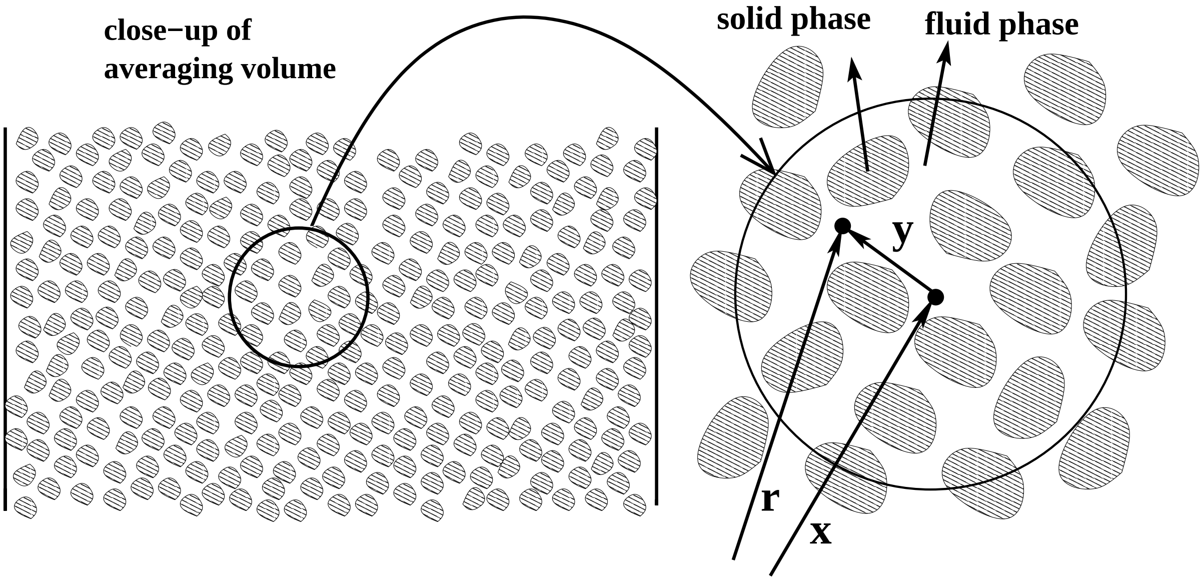

Figure 1.2: Illustration of the volume–averaging technique for flow through a porous medium.

wall. However, since the pioneering study of Shaw & Schumann [87] in 1992, the continuum approach has been utilized in a number of LES studies of flows over plant canopies [24],[100],[91],[43],[86],[70]. Other numerical studies, in which a Reynolds–averaged form of the VANS equations was used, considered not only flow over vegetation [57],[108], but also flow over a permeable wall layer with a porosity significantly lower than that of vegetation [20],[88].

3. Direct simulation

The third method for simulating flow over a permeable wall is the direct simulation of the flow over the permeable wall as well as the flow inside the pores of the permeable wall, although we are not aware of any publication on this method. Apart from the limitations for the Reynolds number, this method is restricted to porous media with a relatively simple structure. For complex porous media, one is usually forced to use the VANS equations, because a direct simulation is not possible with present–day computer facilities.

The main advantage of a direct simulation is that it solves directly the Navier–Stokes equations without the need for any closure model. This is in contrast to the continuum approach, which requires closures for the subfilter–scale stress and the drag force in order to solve the VANS equations. Another advantage of a direct simulation is that it provides the possibility of developing and evaluating these closures.

• Open questions and unsolved problems

The introduction above has given a sketch of the current state of research on flows over permeable walls. An extensive literature study revealed a number of open questions and shortcomings in literature, which are listed below:

1. Research on *laminar* flows over permeable walls is restricted to the case of spatially fully developed flows, e.g. channel flow [5] or flow in a Hele–Shaw cell [31]. As far as we know, no study has yet been made of the laminar boundary layer over a permeable wall. Besides its relevance to practical applications, this study is also important for possible future investigations on the influence of wall permeability on the stability of laminar boundary layers.

2. Crucial in the modeling of flows over permeable walls is an accurate representation of the momentum transfer across the interface. At the moment there are no satisfactory models for this transfer, so that a further development and evaluation of appropriate momentum–transfer models is important.

3. As we have discussed before, the DNS of Hahn et al. [32] of *turbulent* channel flow with permeable walls is restricted to small Re_K. For high Re_K, at which turbulent transport of momentum across the wall interface takes place, no DNS studies have been reported in literature.

4. The few experiments on *turbulent* flows over permeable walls indicate that wall permeability alters the structure and dynamics of near–wall turbulence. However, how wall permeability alters turbulence, is still an open question.

The relevance of wall permeability to many applications and the above mentioned shortcomings in the literature, motivated the present research. Because detailed experiments on flows over and especially through porous media are rather difficult, we have opted for a numerical study. The main objectives are to gain insight in the influence of wall permeability on both laminar and turbulent flows, and to develop a DNS methodology for simulating turbulent flows over permeable walls at relatively high permeability Reynolds numbers. Our study is of fundamental nature rather than restricted to a specific application. In this thesis we therefore consider idealized flow geometries, like boundary–layer flow and flow in a plane channel.

1.2 Outline

This thesis is mainly composed of papers, which have been published or submitted during research over the past four years. These papers are included in this thesis as much as possible in their original form. Consequently, the chapters can be read independently from each other and there is some overlap between the chapters.

The outline of this thesis is as follows. In chapter 2, an introduction is given to the Volume–Averaging Method [105], and the VANS equations are derived. The closure problems are discussed for the subfilter–scale stress and the drag force.

Chapter 3 and partly chapter 4 concern *laminar* flows over permeable walls, whereas chapters 5 and 6 deal with *turbulent* flow over a permeable wall.

In chapter 3, an analysis is presented of the laminar boundary layer over a permeable wedge. The objective is to find a self–similar solution for the velocity profile. It is shown that, on condition that a few assumptions are satisfied, the boundary–layer flow can be described by a generalization of the Falkner–Skan equation with the effect of wall permeability incorporated in the boundary conditions. Solutions of this equation are presented for various wedge angles.

The objective of chapter 4 is to investigate the closure problem for the drag force in the VANS equations. Two different kinds of simulations are presented. The first kind of simulations concerns flow through a *fully periodic* 3D Cartesian grid of cubes. A closure for the drag force is proposed and validated numerically. The second kind of simulations concerns Stokes flow in a plane channel with a lower permeable wall consisting of the same grid of cubes, which now is only infinitely extended in the horizontal directions. Special attention is paid to the modeling of the drag force in the interface region, which is characterized by a spatially varying porosity. Two momentum–transfer models are evaluated for the momentum transfer across this region.

In chapter 5, results will be shown from DNS of turbulent flow in a plane channel with a lower permeable wall. The DNS is combined with the continuum approach for the flow inside the permeable wall, using the VANS equations. The main objective is a systematic investigation of the influence of wall permeability on the structure and dynamics of turbulence. To this purpose simulations have been performed for which only the wall porosity is varied.

In chapter 6, results are presented from DNS of turbulent flow in a plane channel with a lower permeable wall consisting of a 3D Cartesian grid of cubes. A direct simulation, which completely resolves the flow field inside the pores, is compared with a DNS in which the continuum approach is used. In the latter simulation, the VANS equations are solved in order to simulate the flow inside the permeable wall.

Finally, in chapter 7 the main conclusions are summarized together with a brief discussion and recommendations for future work.

Chapter 2

The continuum approach for flows through porous media

Abstract *In this chapter the continuum approach is discussed for flows in porous media, starting with the celebrated Law of Darcy. The theoretical basis for the continuum approach is provided by the Volume–Averaging Method. According to this method the macroscopic or volume–averaged flow field is defined as a local weighted volume average of the flow field in the pores. Provided that the averaging volume is sufficiently large, the volume–averaged flow field and its governing equations are continuous in space. Formal application of the volume–averaging filter to the Navier–Stokes equations yields the Volume–Averaged Navier–Stokes (VANS) equations. A discussion is given of the filter and the constraints for the filter length. To illustrate the volume–averaging technique, the porosity profile is computed corresponding to a permeable wall consisting of a 2D Cartesian grid of cubes. In order to solve the VANS equations, closures are required for the drag force and the subfilter–scale stress in terms of volume–averaged flow quantities. For the drag force many semi–empirical relations exist in literature. An analysis is made of the subfilter–scale stress. Distinction is made between mechanical and turbulent subfilter–scale dispersion, for which separate closures are proposed. Based on an order–of–magnitude analysis, it is shown that in porous media the effect of drag is usually much more important than the effect of subfilter–scale dispersion and consequently the latter may be neglected.*

2.1 Introduction

One of the first studies on flow through porous media was made by Darcy [19]. He performed experiments on the filtration of water through a packed column of sand, as illustrated in figure 2.1. Based on these experiments, Darcy proposed the following relation for the flow rate Q:

$$Q = kA\left(\frac{p_2 - p_1}{\rho g L}\right) \tag{2.1}$$

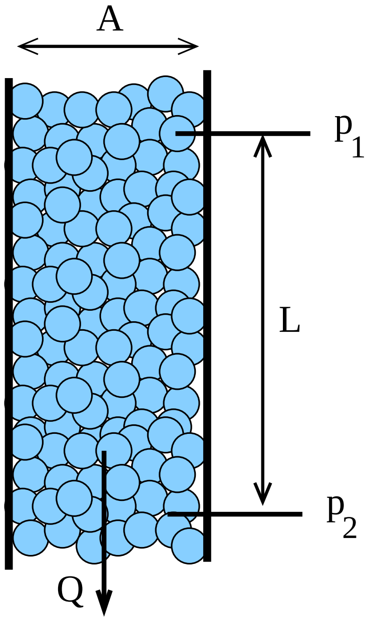

Figure 2.1: Illustration of flow through a packed column.

where A is the cross–sectional area of the column, ρ is the mass density, g is the gravitational acceleration, p_1 and p_2 are the measured pressures, L is the thickness of the sand layer over which the pressure difference is measured, and k is the hydraulic conductivity in ms^{-1}. After the pioneering work of Darcy, it was found by others that the hydraulic conductivity depends on the kinematic viscosity ν according to [4]:

$$k = \frac{gK}{\nu} \tag{2.2}$$

where K is the permeability. The permeability depends only on the material structure of the packed bed, and not on the properties of the fluid. Typical values for the permeability of various bed materials are presented in table 2.1 and can be found in many textbooks on flows through porous media.

Substituting equation (2.2) into equation (2.1), and rewriting the result in a more general form, leads to the following form of Darcy's Law for Stokes flow through a packed bed [4]:

$$0 = -\nabla p - \mu \mathbf{K}^{-1} \cdot \mathbf{U}_d \tag{2.3}$$

where the permeability is now represented by the tensor $\mathbf{K}$, $\mu = \rho\nu$ is the dynamic viscosity and $\mathbf{U}_d$ is the Darcy velocity equal to the flow rate per unit cross–sectional area. An interesting review on the historical background of Darcy's Law is given by Lage [50]. We remark that Darcy's Law is a *macroscopic* equation, which does not hold for the *microscopic* flow at the level of the pores. For low Reynolds numbers for which Darcy's

Material	Permeability (m^2)
Clean gravel	$10^{-7}..10^{-9}$
Clean sand or sand and gravel	$10^{-9}..10^{-12}$
Very fine sand, silt, loam	$10^{-12}..10^{-16}$
Peat	$10^{-11}..10^{-13}$
Stratified clay	$10^{-13}..10^{-15}$
Unweathered clay	$10^{-16}..10^{-20}$
Oil rocks	$10^{-11}..10^{-14}$
Sandstone	$10^{-14}..10^{-16}$
Good limestone, dolomite	$10^{-16}..10^{-18}$
Breccia, granite	$10^{-18}..10^{-20}$

Table 2.1: Some typical permeability values for different materials. Taken from Bear [4] (p. 136).

Law holds, $|\mathbf{U}_d|\sqrt{K}/\nu \ll 1$, the microscopic flow is described by the Stokes equations:

$$0 = -\nabla p + \mu \nabla^2 \mathbf{u} \tag{2.4a}$$

$$\nabla \cdot \mathbf{u} = 0 \tag{2.4b}$$

Most porous media have a very complicated structure, which is not known in full detail. Furthermore, the flow inside a porous medium exhibits a wide range of length scales. The smallest scales are typically of the order of the pore diameter or the dimension of the solid obstacles that form the porous medium. The largest scales might be of the order of the dimensions of the porous medium, like the pipe diameter in figure 2.1. These aspects of flow through porous media strongly hamper a direct approach in which the microscopic equations are solved. Consequently, for analyzing flows through porous media, one is usually forced to consider the flow at a macroscopic level.

From a historical point of view, Darcy's Law is born out of empiricism. However, quite recently theoretical support for the validity of Darcy's Law has been given by Whitaker [103] by means of the Method of Volume Averaging. In this method the microscopic flow field is averaged over a small spatial volume to obtain the macroscopic or *volume–averaged* flow field. Whitaker showed that Darcy's Law (2.3) can be derived from applying the volume–averaging technique to the Stokes equations (2.4a) and (2.4b) for the microscopic flow. In a later study, Whitaker [104] applied the volume–averaging technique to the full Navier–Stokes equations as well, which yields the Volume–Averaged Navier–Stokes (VANS) equations. These equations can be considered as a generalization of Darcy's Law. The VANS equations will be derived in the next section, followed by a discussion on the volume–averaging filter in section 2.3. The volume–averaging technique is illustrated by means of a theoretical example in section 2.4. In order to solve the VANS equations, closures are demanded for the drag force and the subfilter–scale stress in terms of volume–averaged quantities, which we will discuss in sections 2.5 and 2.6 respectively.

2.2 Derivation of the VANS equations

The first step in the derivation of the VANS equations for the macroscopic flow through a porous medium, is the introduction of the *superficial volume average* of an arbitrary quantity ψ. The latter is denoted by $\langle\psi\rangle^s$ and is defined according to [74]:

$$\langle\psi\rangle^s_{\mathbf{x}} \equiv \int_V m(\mathbf{y})\, \gamma(\mathbf{r})\, \psi(\mathbf{r})\, dV \tag{2.5}$$

where the subscript $\mathbf{x}$ means that $\langle\psi\rangle^s$ is evaluated at the centroid $\mathbf{x}$ of the averaging volume V, $\mathbf{y} = \mathbf{r} - \mathbf{x}$ is the relative position vector, γ is the phase–indicator function that equals unity when $\mathbf{r}$ points in the fluid phase and zero when $\mathbf{r}$ points in the solid phase, and m is a weighting function. The volume–averaging technique is illustrated in figure 2.2. Notice that the volume–averaging operator acts as a filter, which passes only information on the large–scale structure of the flow field. Furthermore, we note that the filtered or volume–averaged flow field is continuous in the sense that it is defined both in the fluid and the solid phase. This is the basis for the continuum approach for flows in porous media. Finally, we remark that the volume–averaging operator can be regarded as a generalization of the filter operator used in LES [56], where in LES γ is always equal to one due to the absence of a solid phase.

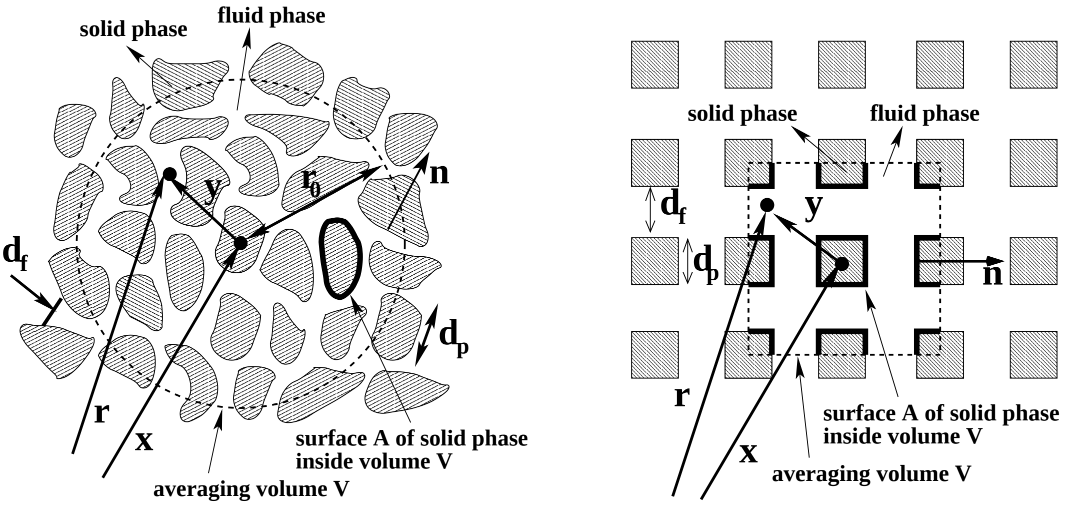

Figure 2.2: Illustration of the volume–averaging technique for a disordered (left) and for an ordered porous medium (right).

In literature equation (2.5) is sometimes rewritten into a convolution product according to [74]:

$$\langle\psi\rangle^s_{\mathbf{x}} = \int_{\mathbb{R}^3} \overline{m}(\mathbf{x} - \mathbf{r})\gamma(\mathbf{r})\, \psi(\mathbf{r})\, dV = \overline{m} * [\gamma\psi] \tag{2.6}$$

where the integration is over the entire $\mathbb{R}^3$ space and where for convenience $\overline{m}$ is defined as $\overline{m}(\mathbf{y}) \equiv m(-\mathbf{y})$. A nice property of a convolution product is that its Fourier Transform, denoted by $\mathcal{F}\{..\}$, can be calculated from:

$$\mathcal{F}\{\langle\psi\rangle^s_{\mathbf{x}}\} = \mathcal{F}\{\overline{m}\}\mathcal{F}\{\gamma\psi\} \tag{2.7}$$

An appropriate weighting function modulates the spectrum of the unfiltered flow field only in the range of large wave numbers, thus leaving the large–scale spatial structure of the flow field unchanged. We remark that in some cases it could be advantageous to compute a volume average from equation (2.7) followed by an Inverse Fourier Transform rather than from equation (2.5).

For a meaningful definition of a volume average, the weighting function must satisfy the following normalization condition:

$$\int_V m(\mathbf{y})dV = 1 \tag{2.8}$$

In principle the weighting function can be chosen freely, although it is desirable that the volume–averaged flow field contains negligible variations on scales smaller than the filter length, which can be defined as $l_f \equiv [\int_{\mathbb{R}^3} m(\mathbf{y})/m(\mathbf{0})\, dV]^{1/3}$. A more detailed discussion on the filter will be given in the next section.

According to equation (2.5), the porosity or void fraction can be defined as:

$$\epsilon(\mathbf{x}) \equiv \int_V \gamma(\mathbf{r})m(\mathbf{y})dV \tag{2.9}$$

An arbitrary quantity ψ can be decomposed into its volume average and a contribution from the *subfilter–scale* field $\tilde{\psi}$ according to [30]:

$$\psi = \langle\psi\rangle + \tilde{\psi} \tag{2.10}$$

where $\langle\psi\rangle \equiv \langle\psi\rangle^s/\epsilon$ is the *intrinsic volume average*. When ψ is a constant, then $\langle\psi\rangle = \psi$ and consequently $\tilde{\psi} = 0$. This nice property of the above decomposition has been the motivation to base the decomposition on $\langle\psi\rangle$ instead of $\langle\psi\rangle^s$.

In order to derive the volume–averaged form of the Navier–Stokes equations, it is necessary to relate the volume average of a derivative to the derivative of the volume average. Such relations have been derived quite recently both for time and spatial derivatives. The relation for time derivatives is known as the *general transport theorem* [89] (p. 19),[74]:

$$\langle\frac{\partial\psi}{\partial t}\rangle^s_{\mathbf{x}} = \frac{\partial\langle\psi\rangle^s_{\mathbf{x}}}{\partial t} - \int_A m(\mathbf{y})\,\mathbf{n}\cdot\mathbf{w}\,\psi(\mathbf{r})\,dA \tag{2.11}$$

where A is the interface area between the fluid and the solid phase inside the averaging volume V, $\mathbf{n}$ is the unit normal at A that points from the fluid into the solid phase (see figure 2.2), and $\mathbf{n}\cdot\mathbf{w}$ is the local speed of displacement of the surface A. Because we restrict ourselves to rigid porous media, it holds that $\mathbf{w} = \mathbf{u} = \mathbf{0}$ at A. Consequently, for rigid porous media, the volume average of a time derivative is equal to the time derivative of the volume average. The single constraint for the validity of the general transport theorem is that the weighting function m does not depend on time. The relation for the volume average of a spatial derivative is known as the *spatial averaging theorem* [102],[74]:

$$\langle \nabla \psi \rangle^s_{\mathbf{x}} = \nabla \langle \psi \rangle^s_{\mathbf{x}} + \int_A m(\mathbf{y})\, \mathbf{n}\, \psi(\mathbf{r})\, dA \tag{2.12}$$

with the single constraint that the weighting function m does not depend on $\mathbf{x}$. Cushman [17] has derived generalizations of equations (2.11) and (2.12), in which m is allowed to depend on $\mathbf{x}$ as well as on t. These generalizations are of importance when considering for example the interface region between a homogeneous porous and a homogeneous fluid region, or multiphase flows with strong temporal fluctuations in the volume fractions.
From the substitution of $\psi = 1$ in equation (2.12), the following interesting relation can be found for the porosity:

$$\nabla \epsilon = - \int_A m\, \mathbf{n}\, dA \tag{2.13a}$$

A generalization of this equation has been derived by Quintard & Whitaker [75]:

$$\nabla \langle \mathbf{Y} \rangle^s_{\mathbf{x}} = - \int_A m\, \mathbf{n}\, \mathbf{Y} dA \tag{2.13b}$$

where $\mathbf{Y} \equiv \mathbf{yy}...\mathbf{y}$ is a tensor of nth–order rank with $\mathbf{y}$ the position vector relative to $\mathbf{x}$. The case of n=0 is equivalent to (2.13a). We will use these equations later on.
We will now apply the volume–averaging operator $\langle .. \rangle^s$ to the Navier–Stokes equations for incompressible, Newtonian flow:

$$\begin{aligned} \langle \frac{\partial \mathbf{u}}{\partial t} \rangle^s + \langle \nabla \cdot \mathbf{uu} \rangle^s &= \langle -\frac{1}{\rho} \nabla p \rangle^s + \langle \nu \nabla^2 \mathbf{u} \rangle^s && (2.14a) \\ \langle \nabla \cdot \mathbf{u} \rangle^s &= 0 && (2.14b) \end{aligned}$$

The first term on the left–hand side of (2.14a) can be rewritten with help of the general transport theorem and the fact that for rigid porous media $\mathbf{w} = \mathbf{u} = \mathbf{0}$ at the solid–fluid interface:

$$\langle \frac{\partial \mathbf{u}}{\partial t} \rangle^s = \frac{\partial \langle \mathbf{u} \rangle^s}{\partial t}$$

Application of the spatial averaging theorem to the advective term in (2.14a) yields:

$$\langle \nabla \cdot \mathbf{uu} \rangle^s = \nabla \cdot \langle \mathbf{uu} \rangle^s + \int_A m \mathbf{n} \cdot \mathbf{uu}\, dA = \nabla \cdot \langle \mathbf{uu} \rangle^s$$

where the last equality holds, because $\mathbf{u} = \mathbf{0}$ at the interface area A. Similarly, the terms on the right–hand side of (2.14a) can be written as:

$$\begin{aligned}
\langle -\frac{1}{\rho}\nabla p\rangle^s &= -\frac{1}{\rho}\nabla\langle p\rangle^s - \int_A m\mathbf{n}\frac{p}{\rho}\,dA \\
\langle \nu\nabla^2\mathbf{u}\rangle^s &= \nu\nabla\cdot\langle\nabla\mathbf{u}\rangle^s + \int_A m\mathbf{n}\cdot\nu\nabla\mathbf{u}\,dA \\
&= \nu\nabla^2\langle\mathbf{u}\rangle^s + \int_A m\mathbf{n}\cdot\nu\nabla\mathbf{u}\,dA
\end{aligned}$$

Finally, applying the spatial averaging theorem to the continuity equation (2.14b) gives:

$$\langle\nabla\cdot\mathbf{u}\rangle^s = \nabla\cdot\langle\mathbf{u}\rangle^s$$

Substitution of the above equations into equations (2.14a) and (2.14b) yields the Volume–Averaged Navier–Stokes (VANS) equations [89] (pp. 196–199),[104]:

$$\begin{aligned}
\frac{\partial\langle\mathbf{u}\rangle^s}{\partial t} + \nabla\cdot\left[\frac{\langle\mathbf{u}\rangle^s\langle\mathbf{u}\rangle^s}{\epsilon}\right] + \nabla\cdot[\epsilon\boldsymbol{\tau}] &= -\frac{1}{\rho}\nabla\langle p\rangle^s + \nu\nabla^2\langle\mathbf{u}\rangle^s + \epsilon\mathbf{f} && \text{(2.15a)} \\
\nabla\cdot\langle\mathbf{u}\rangle^s &= 0 && \text{(2.15b)}
\end{aligned}$$

where $\boldsymbol{\tau}$ is the subfilter–scale stress, which in the LES literature is known as the subgrid–scale stress, and $\mathbf{f}$ is the drag force that the solid phase exerts on the fluid phase. The expressions for $\boldsymbol{\tau}$ and $\mathbf{f}$ read:

$$\begin{aligned}
\boldsymbol{\tau} &\equiv \frac{1}{\epsilon}\left[\langle\mathbf{u}\mathbf{u}\rangle^s - \frac{\langle\mathbf{u}\rangle^s\langle\mathbf{u}\rangle^s}{\epsilon}\right] = \\
&\quad \langle\langle\mathbf{u}\rangle\langle\mathbf{u}\rangle\rangle - \langle\mathbf{u}\rangle\langle\mathbf{u}\rangle + \langle\langle\mathbf{u}\rangle\tilde{\mathbf{u}}\rangle + \langle\tilde{\mathbf{u}}\langle\mathbf{u}\rangle\rangle + \langle\tilde{\mathbf{u}}\tilde{\mathbf{u}}\rangle && \text{(2.16a)} \\
\mathbf{f} &\equiv \frac{1}{\epsilon}\int_A m\mathbf{n}\cdot\left[-\frac{p}{\rho}\mathbf{I} + \nu\nabla\mathbf{u}\right]dA = -\frac{1}{\epsilon}\int_A m\,\mathbf{n}\,\frac{\langle p\rangle}{\rho}dA \\
&\quad +\frac{\nu}{\epsilon}\int_A m\,\mathbf{n}\cdot\nabla\langle\mathbf{u}\rangle\,dA + \frac{1}{\epsilon}\int_A m\mathbf{n}\cdot\left[-\frac{\tilde{p}}{\rho}\mathbf{I} + \nu\nabla\tilde{\mathbf{u}}\right]dA && \text{(2.16b)}
\end{aligned}$$

where we applied the spatial decomposition (2.10) to the velocity and the pressure.
The VANS equations given above are formulated in the superficial form. Sometimes it is more convenient to make use of the intrinsic form, which is readily obtained from a division of equations (2.15a) and (2.15b) by the porosity:

$$\begin{aligned}
\frac{\partial\langle\mathbf{u}\rangle}{\partial t} + \frac{1}{\epsilon}\nabla\cdot[\epsilon\langle\mathbf{u}\rangle\langle\mathbf{u}\rangle] + \frac{1}{\epsilon}\nabla\cdot[\epsilon\boldsymbol{\tau}] &= -\frac{1}{\epsilon\rho}\nabla[\epsilon\langle p\rangle] + \frac{\nu}{\epsilon}\nabla^2[\epsilon\langle\mathbf{u}\rangle] + \mathbf{f} && \text{(2.17a)} \\
\nabla\cdot[\epsilon\langle\mathbf{u}\rangle] &= 0 && \text{(2.17b)}
\end{aligned}$$

The continuity equations (2.15b) and (2.17b) underline the importance to distinguish between superficial and intrinsic volume averages, because in case of a spatially varying porosity only the superficial velocity is divergence free.

- **Darcy's Law and the LES equations**

Darcy's Law (2.3) follows from equation (2.17a) for uniform, stationary flow through a homogeneous porous medium (i.e. with a constant porosity):

$$0 = -\nabla\langle p\rangle - \mu\mathbf{K}^{-1}\langle\mathbf{u}\rangle^s$$

where the drag force has been replaced by $\mathbf{f} = -\mu\mathbf{K}^{-1}\langle\mathbf{u}\rangle^s$ [103]. The closure problem for the drag force will be discussed in more detail in sections 2.5 and 2.6. Notice the use of the *intrinsic* pressure and the *superficial* velocity in Darcy's Law. This originates from the ability to measure these quantities relatively easy, whereas this is rather difficult for respectively the superficial and the intrinsic counterpart.

The VANS equations can be considered as a generalization of the LES equations as well. The latter follow from the VANS equations for $\epsilon = 1$, i.e. the absence of a solid phase, and consequently a zero drag force:

$$\begin{aligned} \frac{\partial\langle\mathbf{u}\rangle}{\partial t} + \nabla\cdot\langle\mathbf{u}\rangle\langle\mathbf{u}\rangle + \nabla\cdot\boldsymbol{\tau} &= -\frac{1}{\rho}\nabla\langle p\rangle + \nu\nabla^2\langle\mathbf{u}\rangle \\ \nabla\cdot\langle\mathbf{u}\rangle &= 0 \end{aligned}$$

- **Local form of VANS equations**

The VANS equations (2.15a) and (2.17a) are sometimes termed as *non–local* transport equations [75], because in the expressions for the subfilter–scale stress and the drag force volume–averaged quantities appear *inside* volume and surface integrals. This is a strong complication for the modeling of the drag force as well as the subfilter–scale stress, because it means that they depend on the structure of the volume–averaged flow field over a distance equal to the filter length. An important simplification can be made when the volume–averaged flow field is well–behaved [30], which means that it contains negligible variations on a distance smaller than the dimensions of the averaging volume: $\langle\langle\mathbf{u}\rangle\rangle \approx \langle\mathbf{u}\rangle$ and $\langle\tilde{\mathbf{u}}\rangle \approx \mathbf{0}$. This then justifies to take volume–averaged quantities out of the volume and surface integrals. Equations (2.16a) and (2.16b) can then be approximated by:

$$\boldsymbol{\tau} \approx \langle\tilde{\mathbf{u}}\tilde{\mathbf{u}}\rangle \tag{2.18a}$$

$$\mathbf{f} \approx -\frac{1}{\epsilon}\nabla\epsilon\cdot\left[-\frac{\langle p\rangle}{\rho}\mathbf{I} + \nu\nabla\langle\mathbf{u}\rangle\right] + \frac{1}{\epsilon}\int_A m\mathbf{n}\left[-\frac{\tilde{p}}{\rho}\mathbf{I} + \nu\nabla\tilde{\mathbf{u}}\right]dA \tag{2.18b}$$

where we made use of equation (2.13a). Substitution of the above two equations into equation (2.17a) yields the *local* form of the intrinsic VANS equations:

$$\begin{aligned} \frac{\partial\langle\mathbf{u}\rangle}{\partial t} + \frac{1}{\epsilon}\nabla\cdot[\epsilon\langle\mathbf{u}\rangle\langle\mathbf{u}\rangle] + \nabla\cdot\langle\tilde{\mathbf{u}}\tilde{\mathbf{u}}\rangle &= -\frac{1}{\rho}\nabla\langle p\rangle + \frac{\nu}{\epsilon}\nabla^2[\epsilon\langle\mathbf{u}\rangle] - \frac{\nu}{\epsilon}\nabla\epsilon\cdot\nabla\langle\mathbf{u}\rangle + \\ & \quad \frac{1}{\epsilon}\int_A m\mathbf{n}\left[-\frac{\tilde{p}}{\rho}\mathbf{I} + \nu\nabla\tilde{\mathbf{u}}\right]dA \end{aligned} \tag{2.19}$$

In order to solve equation (2.19), closures must be found for the subfilter–scale stress and the drag force in terms of volume–averaged quantities. This will be discussed in more detail in sections 2.5 and 2.6.

2.3 On the choice of the filter

As we have mentioned in the previous section, in principle the filter for the volume averaging can be chosen freely, provided that the weighting function m satisfies the normalization condition (2.8). There are however a few considerations that has to be kept in mind when choosing a filter:

1. The averaging volume should match the topology of the porous medium. This becomes clear from figure 2.2. A spherical averaging volume seems to be appropriate for disordered porous media, whereas a rectangular averaging volume is more suitable for ordered porous media.

2. To guarantee that the volume–averaged flow field and VANS equations are continuous, the filter length should be sufficiently large such that no boundary conditions need to be applied to the interior of the porous medium. On the other hand, the filter length should be sufficiently small to preserve as much information of the unfiltered flow field as possible in the volume–averaged flow field.

3. The *local* form of the VANS equations demands that the volume–averaged flow field contains negligible variations on scales smaller than the filter length: $\langle\langle \mathbf{u} \rangle\rangle \approx \langle \mathbf{u} \rangle$. By virtue of the spatial decomposition (2.10), this is equivalent to the requirement that the subfilter–scale flow field does not exhibit length scales larger than the filter length: $\langle \tilde{\mathbf{u}} \rangle \approx \mathbf{0}$. With respect to these requirements, it can be expected that some filters perform better than other filters.

With these considerations in mind, Quintard & Whitaker [75] presented appropriate filters for different types of porous media and derived constraints for the respective filter lengths. They make distinction between *ordered* and *disordered* porous media, as illustrated in figure 2.2.

- **Disordered porous media**

A porous medium is defined as disordered with respect to an averaging volume V when the following condition holds:

$$\left| \nabla_{\mathbf{x}} \left[\frac{1}{V_f} \int_V \gamma \mathbf{y} dV \right] \right| \ll 1 \tag{2.20}$$

with V_f the volume of the fluid phase inside the averaging volume V. For disordered porous media, Quintard & Whitaker propose a spherical averaging volume with radius r_0

and a *top–hat* distribution for the weighting function:

$$m(\mathbf{y}) = \begin{cases} 3/(4\pi r_0^3) & ,|\mathbf{y}| \leq r_0 \\ 0 & ,|\mathbf{y}| > r_0 \end{cases} \tag{2.21}$$

To obtain the constraints for the filter length, Quintard & Whitaker expand the volume–averaged quantities inside the volume and surface integrals in equations (2.16a) and (2.16b) in the position vector $\mathbf{y}$ relative to the centroid $\mathbf{x}$ of the averaging volume. The next step is an order–of–magnitude analysis of the expansion terms that are neglected in the local form of the intrinsic VANS equation (2.19). We will illustrate this below with an example.

The Taylor expansion of $\langle p \rangle$ in the first term on the right–hand side of equation (2.16b) reads:

$$\begin{aligned} -\frac{1}{\rho\epsilon}\int_A m\mathbf{n}\langle p\rangle_{\mathbf{x}+\mathbf{y}} dA &= -\frac{1}{\rho\epsilon}\int_A m\mathbf{n}\left[\langle p\rangle_{\mathbf{x}} + \mathbf{y}\nabla\langle p\rangle_{\mathbf{x}} + \frac{1}{2}\mathbf{y}\mathbf{y}\nabla\nabla\langle p\rangle_{\mathbf{x}} + ...\right] dA \\ &= -\frac{1}{\rho\epsilon}\left[\int_A m\,\mathbf{n}\,dA\right]\langle p\rangle_{\mathbf{x}} - \frac{1}{\rho\epsilon}\left[\int_A m\,\mathbf{n}\,\mathbf{y}\,dA\right]\nabla\langle p\rangle_{\mathbf{x}} \\ &\quad -\frac{1}{\rho\epsilon}\left[\int_A m\,\mathbf{n}\,\frac{1}{2}\mathbf{y}\mathbf{y}\,dA\right]\nabla\nabla\langle p\rangle_{\mathbf{x}} - ... \end{aligned} \tag{2.22}$$

With help of equation (2.13b), this equation can be rewritten according to:

$$-\frac{1}{\rho\epsilon}\int_A m\mathbf{n}\langle p\rangle_{\mathbf{x}+\mathbf{y}} dA = \frac{1}{\rho\epsilon}[\nabla\epsilon]\langle p\rangle_{\mathbf{x}} + \frac{1}{\rho\epsilon}[\nabla\langle\mathbf{y}\rangle^s]\nabla\langle p\rangle_{\mathbf{x}} + \frac{1}{2\rho\epsilon}[\nabla\langle\mathbf{y}\mathbf{y}\rangle^s]\nabla\nabla\langle p\rangle_{\mathbf{x}} + ... \tag{2.23}$$

In the derivation of the local VANS equations (2.19), it has been assumed that the second and subsequent terms on the right–hand side can be neglected with respect to $-(1/\rho)\nabla\langle p\rangle$. By definition, for disordered porous media $|\nabla\langle\mathbf{y}\rangle| \ll 1$ holds, and consequently the second term on the right–hand side can be neglected. Based on computer simulations, Quintard & Whitaker [76] showed that the condition $|\nabla\langle\mathbf{y}\rangle| \ll 1$ is satisfied when $d_f \ll r_0$ holds, where d_f is the typical pore diameter. The third term on the right–hand side of (2.23) may be approximated by [75] (p. 189):

$$\frac{1}{2\rho\epsilon}[\nabla\langle\mathbf{y}\mathbf{y}\rangle^s]\nabla\nabla\langle p\rangle_{\mathbf{x}} = O\left(\frac{r_0^2}{L_\epsilon L_p}\right)\cdot\left[-\frac{1}{\rho}\nabla\langle p\rangle_{\mathbf{x}}\right]$$

where L_ϵ and L_p are typical length scales for spatial variations in the porosity ϵ and in $\nabla\langle p\rangle$, respectively. Thus, this term can be neglected with respect to $-(1/\rho)\nabla\langle p\rangle$, when $r_0^2 \ll L_\epsilon L_p$ holds. Based on a similar analysis of the other terms in equations (2.16a) and (2.16b), we arrive at the following constraints for the filter length $l_f = (4\pi/3)^{1/3} r_0$ of the top–hat filter:

$$\begin{aligned} d_f \ll \; l_f &\ll L_u \\ l_f^2 &\ll L_\epsilon L_u \\ l_f^2 &\ll L_\epsilon L_p \end{aligned} \tag{2.24}$$

where L_u is a characteristic length scale for spatial variations of the volume–averaged flow field. We remark that the constraint $l_f \ll L_u$ originates from the approximation of the subfilter–scale stress. This constraint is new with respect to the work of Quintard & Whitaker, because their analysis is restricted to Stokes flow.

- **Ordered porous media**

Ordered porous media do not satisfy condition (2.20), but are characterized by a unit cell that can be extended periodically in space. The centers of the solid objects are located at:

$$\mathbf{x} = n_1\mathbf{l}_1 + n_2\mathbf{l}_2 + n_3\mathbf{l}_3 \tag{2.25}$$

where $\mathbf{l}_1$, $\mathbf{l}_2$ and $\mathbf{l}_3$ are the basic vectors of the unit cell, and n_1, n_2 and n_3 are integer numbers. An appropriate weighting function for ordered porous media is the *cellular* filter, which has a triangular shape:

$$m(\mathbf{y}) = \begin{cases} \prod_{i=1}^{3} \left(l_i - |y_i|\right)/l_i^2 & , |y_i| \leq l_i \\ 0 & , |y_i| > l_i \end{cases} \tag{2.26}$$

The reader may notice that the weighting function has a discontinuous first derivative at $x = 0$. As pointed out by Quintard & Whitaker, this problem can be easily solved by smoothing the weighting function slightly, just enough to remove the discontinuities, without affecting other properties of the filter. This ensures that volume–averaged quantities are infinitely differentiable.

The choice for the above filter is motivated by the fact that, when applying this filter to ordered porous media, the following interesting relation holds:

$$\langle \mathbf{Y} \rangle^s = \begin{cases} \text{constant} & , \text{n is even} \\ \mathbf{0} & , \text{n is odd} \end{cases} \tag{2.27}$$

where we recall that $\mathbf{Y} \equiv \mathbf{yy}...\mathbf{y}$ is a n^{th}–order tensor. As a consequence of this property of the cellular filter, the right–hand side of equation (2.23) equals zero and equation (2.18b) for the drag force is *exact*. The single constraint for the filter length of the cellular filter, $l_f = (\Pi_{i=1}^{3} l_i)^{1/3}$, originates from the approximation for the subfilter–scale stress (2.16a) by equation (2.18a):

$$l_f \ll L_u \tag{2.28}$$

Note that the filter length of the cellular filter is of the order of the pore size d_f and the particle diameter d_p (see figure 2.2). This is different from disordered porous media for which the filter length must be much larger than d_f.

We note that for *hybrid* porous media, which are neither fully ordered nor fully disordered, a hybrid form of the cellular and the top–hat filters may be used [75].

The top–hat and cellular weighting functions are illustrated in figure 2.3.a, together with the respective Fourier Transforms in figure 2.3.b. The expressions for these Fourier transforms read:

$$\mathcal{F}\{m\} \equiv \frac{1}{2\pi}\int_{-\infty}^{\infty} e^{-iky} m(y)dy = \begin{cases} \frac{\sin(kl_f/2)}{\pi k l_f} & \text{, top–hat filter} \\ \frac{1-\cos(kl_f)}{\pi (kl_f)^2} & \text{, cellular filter} \end{cases} \tag{2.29}$$

The Fourier Transform of the cellular filter decays more rapidly towards zero and has much smaller oscillations for high wavenumbers than the Fourier Transform of the top–hat filter.

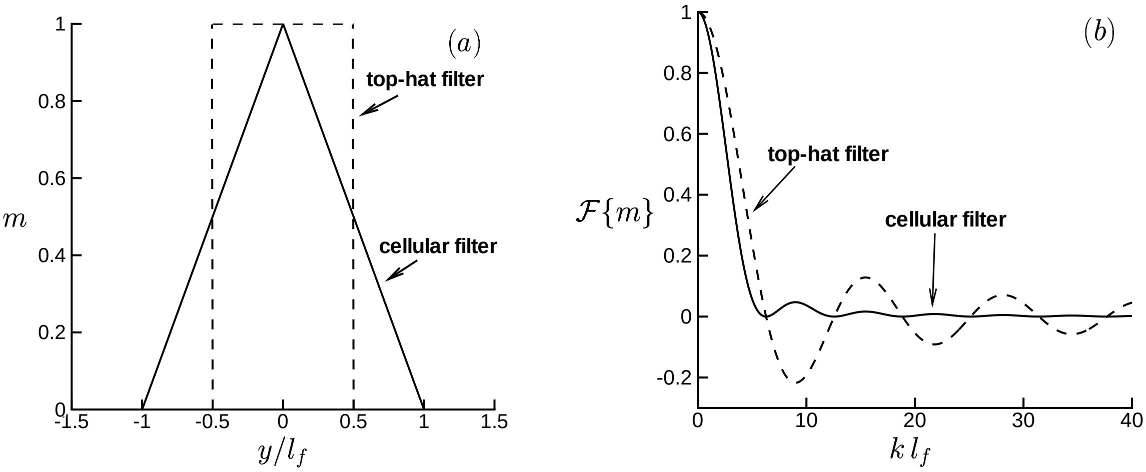

Figure 2.3: The weighting function m of the top–hat and the cellular filter. (a) Real space; (b) Fourier Transform.

2.4 An example of volume averaging

In this section we illustrate the volume–averaging technique by means of an example. We calculate the porosity profile corresponding to a permeable wall consisting of a 2D Cartesian grid of cubes as sketched in figure 2.4. In this example, the rib d_p of the cubes is taken equal to the distance d_f between the cubes. The interface with the permeable wall is defined as the height $z = 0$ at which the porosity starts to deviate from one. The porosity is computed analytically from equation (2.9) using the cellular filter given by (2.26):

$$\epsilon(z) \;=\; \frac{1}{l^2}\frac{1}{l^2}\int_{-l}^{+l}\int_{-l}^{+l} \gamma\, m\, da\, db = 1 - \frac{1}{l^2}\frac{1}{l^2}\int_{-l}^{+l}\int_{-l}^{+l} (1-\gamma)\, m\, da\, db$$

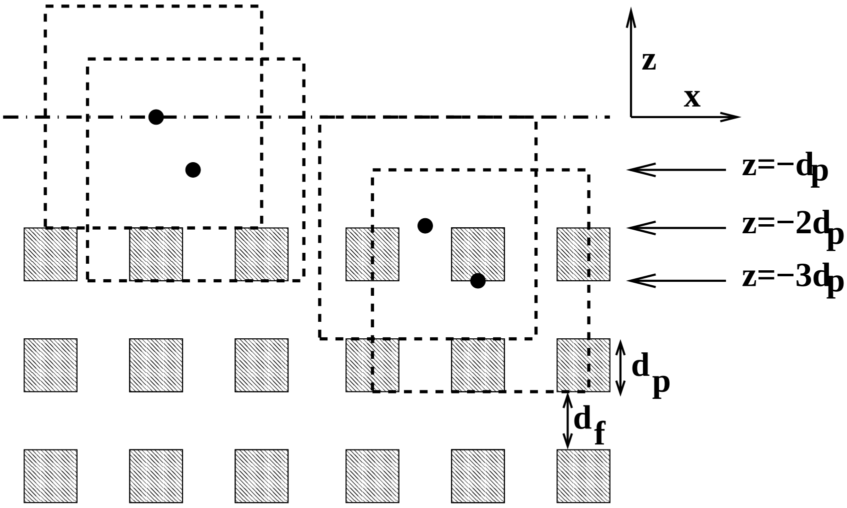

Figure 2.4: A permeable wall consisting of a 2D Cartesian grid of cubes. The rib d_p of the cubes is equal to the distance d_f between the cubes. The dashed rectangles and the dots are averaging volumes (corresponding to the cellular filter) and their centroids respectively.

where $l = d_f + d_p = 2d_p$ is the dimension of a unit cell. For convenience we first introduce a quantity Q defined by:

$$Q \equiv \frac{2}{l^2} \int_0^{d_p/2} (l - a)\, da + \frac{2}{l^2} \int_{3d_p/2}^{2d_p} (l - a)\, da$$

It is easy to show that $Q = 1/2$. We now compute the porosity as follows:

$$\begin{aligned}
z \geq 0 \;:\; \epsilon(z) &= 1 \\
-d_p \leq z \leq 0 \;:\; \epsilon(z) &= 1 - \frac{1}{l^2} \int_{-2d_p}^{-2d_p - z} Q\,(l + b)\, db = 1 - \frac{1}{16} \left(\frac{z}{d_p} \right)^2 \\
-2d_p \leq z \leq -d_p \;:\; \epsilon(z) &= 1 - \frac{1}{l^2} \int_{-3d_p - z}^{-2d_p - z} Q\,(l + b)\, db = 1 + \frac{1}{8} \left(\frac{z}{d_p} + \frac{1}{2} \right) \\
-3d_p \leq z \leq -2d_p \;:\; \epsilon(z) &= 1 - \frac{1}{l^2} \int_{-2d_p}^{-4d_p - z} Q\,(l + b)\, db - \frac{1}{l^2} \int_{-3d_p - z}^{0} Q\,(l + b)\, db \\
&\quad - \frac{1}{l^2} \int_0^{-2d_p - z} Q\,(l + b)\, db \\
&= 1 + \frac{1}{16} \left(\left[\frac{z}{d_p} \right]^2 + 6 \left[\frac{z}{d_p} \right] + 5 \right) \\
z \leq -3d_p \;:\; \epsilon(z) &= 0.75
\end{aligned}$$

The above porosity profile is depicted in figure 2.5. Following Ochoa–Tapia & Whitaker [67], we use this porosity profile to divide the flow domain into three regions:

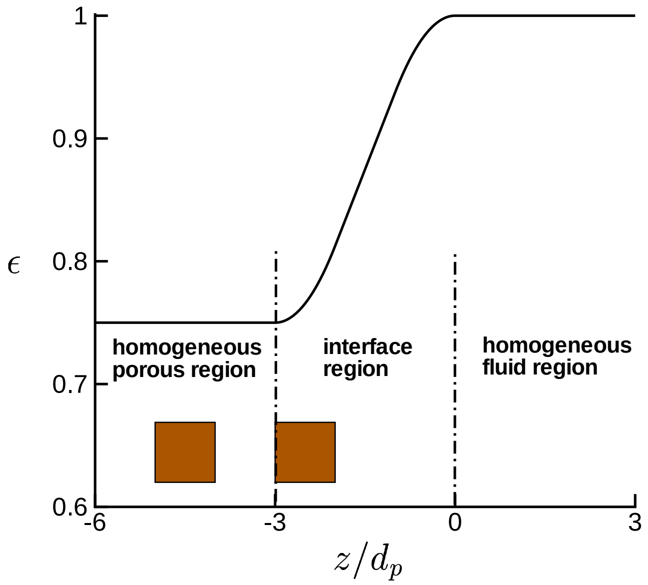

Figure 2.5: Porosity profile corresponding to a 2D Cartesian grid of cubes as sketched in figure 2.4. The squares mark the location of the cubes. The porosity has been calculated from equation (2.9) using the cellular weighting function given by (2.26).

1. The homogeneous fluid region for $z \geq 0$ in which the porosity is equal to unity.
2. The interface region between $-3d_p \leq z \leq 0$, which is characterized by a spatially varying porosity.
3. The homogeneous porous region for $z \leq -3d_p$, with a constant porosity.

We note that the thickness δ_i of the interface region, which in our example equals $3d_p$, depends on the choice of the filter and consequently on the geometrical structure of the permeable wall. For disordered porous media, for which the top–hat filter may be used, it can be expected that $\delta_i \gg d_p$.

The above distinction between three different regions is very important when considering flow over a permeable wall. It is clear from figure 2.4 that with respect to the averaging volume, the geometrical structure of the interface region is heterogeneous and more complex than the structure of the homogeneous porous region. Furthermore, the flow field in the interface region is more complex as well. These aspects hamper the closure problems for the subfilter–scale stress and the drag force in the VANS equations. We will discuss these closure problems in the next two sections, where we restrict ourselves to flow through *homogeneous* porous media. The modeling of subfilter–scale dispersion and the drag force in the *interface region* will be discussed in more detail in forthcoming chapters.

2.5 Closure problem for the drag force

For a stationary and uniform volume–averaged flow in a porous medium with a constant porosity, the VANS equations (2.19) reduce to:

$$0 = -\frac{1}{\rho}\nabla\langle p\rangle + \frac{1}{\epsilon}\int_A m\mathbf{n}\left[-\frac{\tilde{p}}{\rho}\mathbf{I} + \nu\nabla\tilde{\mathbf{u}}\right]dA \tag{2.30}$$

This momentum balance expresses that the pressure drop is caused by the sum of the pressure drag and the viscous drag resulting from the no–slip and no–penetration conditions at the solid–fluid interface.

Whitaker [104] gave theoretical support to the following convenient parameterization for the drag force:

$$\frac{1}{\epsilon}\int_A m\mathbf{n}\left[-\frac{\tilde{p}}{\rho}\mathbf{I} + \nu\nabla\tilde{\mathbf{u}}\right]dA = -\nu\mathbf{K}^{-1}\epsilon\langle\mathbf{u}\rangle - \nu\mathbf{K}^{-1}\mathbf{F}\epsilon\langle\mathbf{u}\rangle \tag{2.31}$$

where **K** and **F** are respectively the permeability and the Forchheimer tensor. In general the Forchheimer tensor depends on the Reynolds number $|\langle\mathbf{u}\rangle|\, d_f/\nu$, on the geometrical parameters of the porous medium and also on the orientation of the solid obstacles relative to the direction of the volume–averaged flow. For small Reynolds number the Forchheimer tensor can be neglected and in this limit, equation (2.31) reduces to Darcy's Law. Darcy's Law represents the drag in the limit of Stokes flow in the pores, and the inclusion of the Forchheimer tensor in (2.31) is a correction for inertial effects at higher Reynolds numbers. In general the permeability tensor depends only on the geometry of the porous medium. Bear [4] and, in a different manner, Whitaker [104] proved that for all porous media the permeability tensor is a symmetric second–order tensor. We note that the first term on the right–hand side of equation (2.31) is usually neglected in studies on flow through vegetation [1] , because the Reynolds number is relatively large.

Generally valid expressions for the permeability and the Forchheimer tensor do not exist, as they are strongly related to the geometry of the porous medium and the Reynolds number. Experiments or numerical calculations of flow through a representative region of the porous medium are required to determine them. Numerical calculations of the

---

[1] In studies on flow through vegetation, it is actually more convenient to parameterize the drag force according to [28]:

$$\frac{1}{\epsilon}\int_A m\mathbf{n}\left[-\frac{\tilde{p}}{\rho}\mathbf{I} + \nu\nabla\tilde{\mathbf{u}}\right]dA = -C_d a\,|\langle\mathbf{u}\rangle|\,\langle\mathbf{u}\rangle$$

where a is the frontal foliage area per unit volume and C_d the drag coefficient. The drag coefficient is usually assumed to be isotropic, i.e. independent of the flow direction. In the literature several values for C_d are reported. In the LES of Dwyer et al. [24], Shaw & Schumann [87] and Su et al. [91] the value of C_d is fixed at 0.15 based on experiments on flow through a deciduous forest [85]. In the simulations of Kanda & Hino [43] the value of C_d is 0.5. López & García [57] take in their simulations of flow over aquatic vegetation a value of $C_d = 0.57$, which is based on flume experiments on flow over cylindrical dowels.

permeability and the Forchheimer tensor for several geometries are presented by Zick & Homsy [111], Larson & Higdon [52],[53], Sahraoui & Kaviany [81], Ma & Ruth [60], Lee & Yang [55] and Breugem et al. [13]. A few references to experiments are MacDonald et al. [61], Fand et al. [26], Kececioglu & Jiang [44] and Lage et al. [51].
For flows through packed beds, a widely used relation for the drag force is the modified Ergun equation [7], which is given by (2.31) with the following relations for the permeability and the Forchheimer tensor:

$$\mathbf{K} = \frac{{d_p}^2\epsilon^3}{180(1-\epsilon)^2}\mathbf{I} \tag{2.32a}$$

$$\mathbf{F} = \tilde{F}\,|\langle\mathbf{u}\rangle|\,\mathbf{I} \quad , \quad \tilde{F} \equiv \frac{\epsilon}{100(1-\epsilon)}\frac{d_p}{\nu} \tag{2.32b}$$

where $d_p \equiv 6V_p/A_p$ is the mean particle diameter with V_p the volume and A_p the surface area of the solid obstacles. In case of a sphere d_p equals the diameter of the sphere. The coefficients in the above expressions for the permeability and the Forchheimer tensor are determined from many experiments with different materials (such as glass beads, cylindrical fibers, granular material and cylindrical packings), and in which the particle sizes, the porosity and the Reynolds number were varied [61].

• Energy cascade for flows in porous media
The drag in a porous medium transfers kinetic energy from the volume–averaged flow field to the subfilter–scale flow field. This becomes clear from the equation for the subfilter–scale kinetic energy, which is defined as $e \equiv \langle u_i u_i\rangle/2 - \langle u_i\rangle\langle u_i\rangle/2$. Assuming that $\langle\langle u_i\rangle\rangle \approx \langle u_i\rangle$, the subfilter–scale kinetic energy is approximately equal to $e \approx \langle\tilde{u}_i\tilde{u}_i\rangle/2$. If we furthermore assume that the porosity is constant, then the transport equation for e reads:

$$\begin{aligned}\frac{\partial e}{\partial t} + \langle u_j\rangle\frac{\partial e}{\partial x_j} &= -\langle\tilde{u}_i\tilde{u}_j\rangle\frac{\partial\langle u_i\rangle}{\partial x_j} + \frac{\partial}{\partial x_j}\left[-\frac{1}{\rho}\langle\tilde{p}\tilde{u}_i\rangle\delta_{ij} - \langle\frac{1}{2}\tilde{u}_i\tilde{u}_i\tilde{u}_j\rangle + \nu\frac{\partial e}{\partial x_j}\right] \\ &\quad -\langle\nu\left(\frac{\partial\tilde{u}_i}{\partial x_j}\right)^2\rangle - f_i\langle u_i\rangle \end{aligned}\tag{2.33}$$

where δ_{ij} is the Kronecker delta. A derivation of equation (2.33) is given in appendix A. The last term on the right–hand side is the production of subfilter–scale kinetic energy due to the work done by the drag force f_i. This terms appears with an opposite sign in the transport equation for the kinetic energy $\langle u_i\rangle\langle u_i\rangle/2$ of the volume–averaged flow. There are two interesting cases to consider. The first case is turbulence in a homogeneous fluid region, i.e. in the absence of solid obstacles. If it is assumed that local energy equilibrium exists, then the energy equation reduces to a balance between the shear–production term and the viscous dissipation term: $-\langle\tilde{u}_i\tilde{u}_j\rangle\partial\langle u_i\rangle/\partial x_j \approx \langle\nu\,(\partial\tilde{u}_i/\partial x_j)^2\rangle$. The second case is a uniform volume–averaged flow in a porous medium. When again local energy equilibrium is assumed, then the energy equation reduces to: $-f_i\langle u_i\rangle \approx \langle\nu\,(\partial\tilde{u}_i/\partial x_j)^2\rangle$. Finnigan [28] refers to this phenomenon as a spectral short–cut, because it bypasses the standard

energy cascade [93] of turbulence in a homogeneous fluid region.
The subfilter–scale kinetic energy can be quite high. At the surface A_p of the solid obstacles the velocity equals zero, $\mathbf{u} = \mathbf{0}$. From equation (2.10) it then follows that at A_p the subfilter–scale velocity is equal to $\tilde{\mathbf{u}} = -\langle \mathbf{u} \rangle$. This implies that when the typical length scale d_f of the pores is small relative to the mean particle diameter d_p of the solid obstacles, then the subfilter–scale kinetic energy is of the same order as the kinetic energy of the volume–averaged flow field:

$$e = O\left(\frac{1}{2}\langle u_i \rangle^2\right) \quad , \quad d_f/d_p \ll 1 \tag{2.34}$$

2.6 Closure problem for the subfilter–scale stress

The nature of the subfilter–scale stress in a porous medium is more complex than the subgrid–scale stress in LES. In a homogeneous fluid region, subgrid–scale turbulent motions contribute to the diffusion of resolved–scale momentum when a resolved–scale strain field is present. We refer to this as *turbulent dispersion*. In a porous medium the fluid is forced to move around the solid obstacles, and this causes an additional contribution to diffusion of volume–averaged momentum. We call this *mechanical dispersion*. Both types of dispersion are illustrated in figure 2.6. The distinction between mechanical and

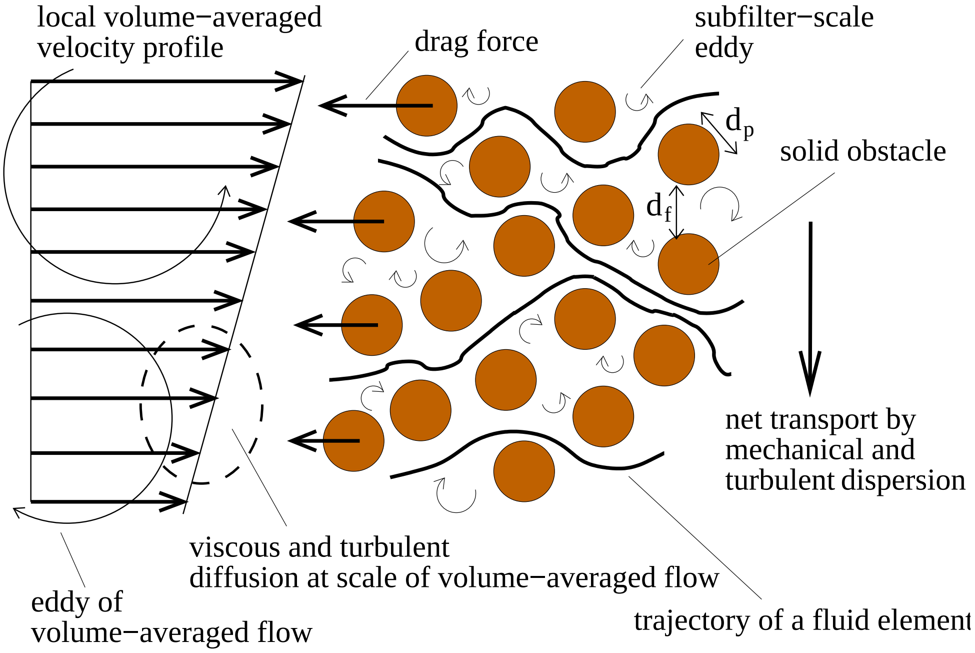
local volume−averaged
velocity profile
drag force
subfilter−scale
eddy
d_p
solid obstacle
d_f
net transport by
mechanical and
turbulent dispersion
viscous and turbulent
diffusion at scale of volume−averaged flow
eddy of
volume−averaged flow
trajectory of a fluid element

Figure 2.6: Illustration of turbulent and mechanical dispersion in a porous medium. The figure also shows the presence of large–scale eddies, which are responsible for turbulent diffusion at the scale of the volume–averaged flow, and the drag force that the solid obstacles exert on the volume–averaged flow.

turbulent dispersion was made also by Nepf [65] in order to model diffusion of a scalar in emergent aquatic vegetation, where mechanical dispersion originates from the obstruction of the flow by the plants. Masuoka & Takatsu [63] introduced the concept of void vortices and pseudo vortices. Void vortices are turbulent eddies in the pores, and pseudo vortices are motions of fluid elements along the solid obstacles. From our point of view, these vortices are related to turbulent and mechanical dispersion respectively. Masuoka & Takatsu used the concept of dispersion by void vortices to explain the Forchheimer correction to Darcy's Law for high Reynolds numbers, but this explanation is disputable [66], [21]. In this section we argue that in general both the mechanical and the turbulent subfilter–scale stress have a negligible influence on the volume–averaged flow field.

From figure 2.6 it can be inferred that mechanical and turbulent dispersion take place only when a volume–averaged strain field is present. This motivates a parameterization for the subfilter–scale stress according to:

$$\tau_{ij} = -\left(K_p + K_t\right)\left(\frac{\partial\langle u_i\rangle}{\partial x_j} + \frac{\partial\langle u_j\rangle}{\partial x_i}\right) \tag{2.35}$$

where K_p and K_t are respectively the mechanical and the turbulent viscosity. The summation of the two viscosities in equation (2.35) is allowed, provided that they do not mutually correlate. To be more specific, we assume that the induced motion of a fluid element by the presence of a solid obstacle does not correlate with the induced motion of the fluid element by the presence of eddies in the pores.

When a fluid element with a velocity $\tilde{\mathbf{u}}$ approaches a solid obstacle of diameter d_p, it has to move around it. From this consideration we estimate the mechanical viscosity by:

$$K_p = c_p d_p \sqrt{e} \tag{2.36a}$$

where c_p is a coefficient that depends on the geometry of the porous medium. It is expected that for porous media for which solid obstacles are aligned relative to each other, c_p will be very small, whereas this coefficient will be larger for porous media where the solid obstacles are staggered or randomly distributed. The turbulent viscosity is estimated by a similar consideration. It is assumed that the typical length scale of the eddies is proportional to the typical pore diameter d_f. This yields:

$$K_t = c_t d_f \sqrt{e} \tag{2.36b}$$

where c_t is a coefficient that depends on the characteristic Reynolds number for the flow in the pores. For low Reynolds numbers the flow in the pores is laminar and consequently the coefficient c_t is very small, but for large Reynolds numbers the flow in the pores is turbulent and c_t is of order unity. This was recognized before by Uittenbogaard [94] (p. 5), who developed a k-ϵ turbulence model for flow over aquatic vegetation, where a parameterization similar to equation (2.36b) was employed for the turbulent subfilter–scale stress inside the vegetation layer.

Let us now consider two limiting cases, namely the case that turbulent dispersion dominates over mechanical dispersion, and the opposite case where mechanical dispersion is dominant.

- **Mechanical dispersion dominant over turbulent dispersion**

Mechanical dispersion dominates strongly over turbulent dispersion for $d_f/d_p \ll 1$ and/or a low Reynolds number for the flow in the pores, $|\langle \mathbf{u} \rangle|\, d_f/\nu$. These conditions are often encountered in packed beds. In this case mechanical dispersion turns out to be of minor importance as compared to the influence of the drag on the volume–averaged flow. As discussed in the previous section, for $d_f/d_p \ll 1$ the subfilter–scale kinetic energy will be of the order of the kinetic energy of the volume–averaged flow. The dispersion term in the VANS equation (2.19) can therefore be estimated by:

$$\frac{1}{\epsilon}\frac{\partial \epsilon \tau_{ij}}{\partial x_j} = O\left(\frac{c_p d_p \left|\langle \mathbf{u} \rangle\right| \langle u_i \rangle}{L_u^2}\right)$$

where L_u is a typical length scale of the volume–averaged flow. An estimate for the drag term is found from equation (2.31). Neglecting the Forchheimer term and modeling the permeability tensor according to equation (2.32a), the drag term in equation (2.19) reads:

$$f_i = -\nu \frac{180\,(1-\epsilon)^2}{d_p^2 \epsilon^2} \langle u_i \rangle$$

The ratio of the dispersion to the drag term in equation (2.19) can thus be estimated by:

$$\left|\frac{1}{f_i}\frac{1}{\epsilon}\frac{\partial \epsilon \tau_{ij}}{\partial x_j}\right| = O\left(\frac{c_p}{180}\frac{\epsilon\left[1-\epsilon^{1/3}\right]^3}{\left[1-\epsilon\right]^2}\left[\frac{\left|\langle \mathbf{u} \rangle\right| d_f}{\nu}\right]\left[\frac{d_f}{L_u}\right]^2\right) \ll 1$$

in which we used the estimate that $(d_p/d_f)^3 = O(\left[1-\epsilon^{1/3}\right]^3/\epsilon)$. This result shows that if mechanical dispersion dominates over turbulent dispersion, then the influence of drag on the volume–averaged flow is much more important than mechanical dispersion.

- **Turbulent dispersion dominant over mechanical dispersion**

Turbulent dispersion dominates over mechanical dispersion when both the Reynolds number $|\langle \mathbf{u} \rangle|\, d_f/\nu$ and the ratio d_f/d_p are large. The last condition is equivalent to a very high porosity, close to unity, which can be encountered in a forest. In this case the turbulent subfilter–scale stress can be neglected when the turbulent viscosity K_t is much smaller than the eddy viscosity K_T of the turbulent volume–averaged flow. The difference between the eddies of the subfilter–scale flow and of the volume–averaged flow is illustrated in figure 2.6. The value of K_T can be estimated by $K_T = \mathcal{L}\mathcal{U}$, where $\mathcal{L}$ is the mixing length and $\mathcal{U} = [\frac{1}{2}\overline{\langle u_i \rangle' \langle u_i \rangle'}]^{1/2}$ is a characteristic velocity scale of the large–scale eddies. The ratio of K_t to K_T is given by:

$$\frac{K_t}{K_T} = c_t \frac{d_f}{\mathcal{L}} \frac{\sqrt{e}}{\mathcal{U}}$$

If $d_f/\mathcal{L} \ll 1$ holds, then also $\sqrt{e}/\mathcal{U} \ll 1$ holds, while the large eddies are much more energetic than the small eddies. Thus, when $d_f/\mathcal{L} \ll 1$ holds, the turbulent subfilter–scale stress can be neglected. This is typically the case in a forest in which the turbulence is dominated by scales of the order of the height of the forest [28]. Turbulent dispersion can be neglected because the height of the forest (estimate for $\mathcal{L}$) is much larger than the typical length scale of the individual forest elements (estimate for d_f).

The above analysis suggests that also when mechanical and turbulent dispersion are *equally* important, the effect of subfilter–scale dispersion on the volume–averaged flow can still be neglected.

Finally we note that it is clear from this section that the nature of subfilter–scale dispersion is fundamentally different from turbulent diffusion by the volume–averaged flow. We have shown that the former can usually be neglected, but that the latter may be important. This has implications for simulations of flows over plant canopies and porous media in general, in which a Reynolds–averaged form or a LES approach of the VANS equations is used. This is discussed in more detail in appendix B.

Chapter 3

The laminar boundary layer over a permeable wall [1]

Abstract *An analysis is given of the laminar boundary layer over a permeable wall. The permeable wall is passive in the sense that no suction or blowing velocity is imposed. To describe the flow inside and above the permeable wall a continuum approach is employed based on the Volume–Averaging Method [105]. With help of an order–of–magnitude analysis the boundary–layer equations are derived. The analysis is constrained by: a) a low wall permeability; b) a low Reynolds number for the flow inside the permeable wall; c) a sufficiently high Reynolds number for the flow above the permeable wall. Two boundary layers lying on top of each other can be distinguished: the Prandtl boundary layer above the permeable wall, and the Brinkman boundary layer inside the permeable wall. Based on the analytical solution for the Brinkman boundary layer in combination with the momentum transfer model of Ochoa-Tapia & Whitaker [67] for the interface region, a closed set of equations is derived for the Prandtl boundary layer. For the stream function a power series expansion in the perturbation parameter κ is adopted, where κ is proportional to the ratio of the Brinkman to the Prandtl boundary–layer thickness. A generalization of the Falkner–Skan equation for boundary–layer flow past a wedge is derived, which incorporates the effect of wall permeability. Numerical solutions of the Falkner–Skan equation for various wedge angles are presented. Up to first order in κ, wall permeability causes a positive streamwise velocity at the permeable wall, whereas a non–zero wall–normal interface velocity is a second–order effect. Furthermore, wall permeability causes a decrease in the wall shear stress when the freestream flow accelerates, but an increase in the wall shear stress when the freestream flow decelerates. From the latter it follows that separation, as indicated by zero wall shear stress, is delayed to a larger positive pressure gradient.*

---

[1] A slightly different version of this chapter has been accepted for publication in *Transport in Porous Media* [12].

3.1 Introduction

The study of flows over permeable walls has quite different applications. Examples in the field of hydrology are flows in rivers with a porous bed, and underground water flow which may develop a boundary layer over finer porous material in a large void. Another application is the lubrication of red blood cells in small capillaries which are coated with the endothelial–cell glycocalyx. Damiano et al. [18] modeled the glycocalyx as a deformable porous wall layer. As a last example we mention boundary–layer suction through a permeable surface. Already in 1904 Prandtl reported about experiments where suction was successfully applied at the rear of a cylinder to prevent boundary–layer separation [83]. From the 1930's on, boundary–layer suction has been applied to aircraft wings. By means of suction the retarded fluid in the boundary layer is removed so that separation is delayed or even avoided. Consequently, the pressure drag is reduced and the maximum lift coefficient increases, because boundary–layer suction at the upper side of the airfoil enables higher incidence angles of the flow at the leading edge. Furthermore, suction appears to have a stabilizing influence on the flow, i.e. transition to turbulence is delayed, and this contributes also to a reduction in drag.

In the theoretical analysis of boundary–layer suction, distinction is made between an uniform and a non–uniform streamwise distribution of the suction velocity. For the case of boundary–layer flow over a flat plate with an uniform suction velocity, an exact solution is known of the Prandtl boundary–layer equations [83]. Berman [6] published a perturbation solution for self–similar channel flow in which an uniform suction velocity is imposed at both walls. A theoretical analysis of non–uniform boundary–layer suction through a permeable wedge is given by Schlichting and Bussmann [83]. In this case, for some special non–uniform streamwise distributions of the suction velocity, the boundary–layer flow is self–similar and can be described by the Falkner–Skan equation.

Characteristic for the previously mentioned analyses of boundary–layer suction through a permeable wall, is the assumption that the tangential velocity at the wall is zero. In general, this assumption is not true, although for thick boundary layers the effect of a non–zero tangential velocity at the wall will be small. One may wonder what happens when no suction is applied and the effect of a non–zero tangential velocity at the wall can not be neglected. To the knowledge of the authors no studies have been made yet of a boundary–layer development over a passive permeable wall, although there is quite some literature that is concerned with *fully developed* laminar flow over a passive permeable wall. This deficiency in literature motivated the present research.

Analytical solutions for fully developed laminar flow in a plane channel with a permeable bottom wall are given by Beavers & Joseph [5], Ochoa-Tapia & Whitaker [68] and Kuznetsov [49], to name a few. Poulikakos & Kazmierczak [73] give also an analytical solution for forced convection in a cylindrical pipe covered with a permeable wall layer. These studies have in common that a continuum approach is employed for the permeable wall. The theoretical basis for this approach is provided by the Volume–Averaging Method [105] in which the flow field is averaged over a small spatial volume. Different in the above mentioned studies is the way in which the volume–averaged flow in the permeable wall is modeled and how the coupling is accomplished between the flow outside and inside the permeable wall. This is discussed in more detail below.

Beavers & Joseph [5] (BJ for short) performed experiments on flow in a plane channel with a solid top wall and a lower permeable wall. They assumed that the volume-averaged flow in the core of the permeable wall is governed by Darcy's Law [4]:

$$0 = -\frac{d\langle p\rangle}{dx} - \frac{\mu}{K}\langle u\rangle^s \tag{3.1}$$

Here $\langle p\rangle$ is the *intrinsic* volume–averaged pressure, $\langle u\rangle^s = \epsilon\langle u\rangle$ denotes the *superficial* volume–averaged velocity with ϵ the porosity or void fraction, μ is the dynamic viscosity, and K is the permeability. The difference between intrinsic and superficial volume averages is that the former is weighted over only the volume of the fluid phase inside the averaging volume, whereas the latter is weighted over the total averaging volume. The flow in the channel is governed by the Stokes equations:

$$0 = -\frac{dp}{dx} + \mu\frac{d^2u}{dz^2} \tag{3.2}$$

where z denotes the coordinate for the wall–normal direction. The solution of this equation is a parabolic function for the velocity in z with a still unknown velocity U_i at the interface. In order to determine U_i, BJ proposed the following boundary condition at the interface with the permeable wall:

$$\frac{du}{dz} = \frac{\alpha}{\sqrt{K}}(U_i - U_d) \tag{3.3}$$

where α is a dimensionless coefficient and U_d is the creep velocity given by (3.1). When the ratio of $\sqrt{K}$ to the channel height H is very small, the wall behaves as a solid wall and U_i is approximately zero. Based on the experimental data BJ could determine the value of α, which ranged from 0.1 till 4 dependent of the porous material (foametal or aloxite) that was used and the permeability.

The BJ interface condition has been the subject of many later publications. Theoretical support to it is given by Saffman [80]. Saffman showed that the value of α is sensitive to the definition of the location of the interface. This conclusion was confirmed by the numerical simulations of Larson & Higdon [52],[53] of respectively axial and transverse flow over a lattice of cylinders. Based on similar numerical simulations, Sahraoui & Kaviany [81] showed that α depends not only on the interfacial position, but also on the Reynolds number, the flow direction, the channel height, the porosity and the surface topology. Other studies that support the BJ interface condition were made by Taylor [92] and Richardson [78], who used a grooved plate as an idealized model for a permeable wall.

Recently Ochoa-Tapia & Whitaker [67] (OTW for short) developed a modification of the BJ interface condition. In their analysis they made distinction between a homogeneous porous region (ω–region for short) with a constant porosity and permeability, a homogeneous fluid region (η–region for short) above the permeable wall, and an interface region in between these two regions with a thickness of order $\sqrt{K}$. Different from previous approaches, they utilized the Brinkman equation [14] to model the volume–averaged flow in the ω–region. This equation is an extension to Darcy's Law by the inclusion of a diffusion term. The flow in the η–region is governed by the Stokes equations. Based on the non–local form of the volume–averaged Stokes equations for the interface region, they showed that this leads to a continuous superficial volume–averaged velocity in combination with a jump condition for the intrinsic volume–averaged stress at the interface. For one–dimensional flow parallel to the interface the OTW interface conditions read:

$$\langle u\rangle_\omega^s = u_\eta \quad = \quad U_i \tag{3.4a}$$

$$\mu\frac{d\langle u\rangle_\omega}{dz} - \mu\frac{du_\eta}{dz} \quad = \quad \mu\frac{\beta_t}{\sqrt{K}}U_i \tag{3.4b}$$

where the subscripts ω and η refer to respectively the ω– and the η–region. The jump condition for the tangential stress contains a dimensionless coefficient β_t, which can be either positive or negative and which is estimated to be of order unity. In a subsequent paper [68] OTW used these interface conditions to obtain an analytical expression for the laminar flow in a plane channel with a lower permeable wall, and they compared the results with the experimental data of BJ. The value of β_t calculated from these experiments ranged from -1 till 1.5. Thus β_t appears to be less sensitive to the permeability of the wall as compared to the coefficient α in the BJ interface condition, which varied over a factor fourty for the same experiments. This improvement is attributed to the incorporation of the diffusion term in the Brinkman equation relative to Darcy's Law. In a later publication OTW [69] extended their analysis by the incorporation of inertial effects. This yields an additional term on the right–hand side of the jump condition for the tangential stress.

For the special case that $\beta_t = 0$, the OTW interface conditions are the same as the interface conditions originally proposed by Brinkman [14] (p. 29), which were used by Vafai & Kim [96] and Poulikakos & Kazmierczak [73], among others. The Brinkman model (i.e. the Brinkman equation in combination with the OTW interface conditions with $\beta_t = 0$) was evaluated in the study of James & Davis [40] of Stokes flow over a very sparse array of circular cylinders. By means of a singularity method they obtained an approximate analytical solution for the flow field. The agreement between the Brinkman model and the analytical solution was rather poor. Similar conclusions about the performance of the Brinkman model were drawn in the numerical studies of Larson & Higdon [52],[53] and Sahraoui & Kaviany [81], and in the experimental study of Gupte & Advani [31], who used LDA to measure flow in a Hele–Shaw cell that was partially filled with a random fiber mat. Although not mentioned in these papers the poor performance of the Brinkman model might be very well explained by the actual non–zero value for β_t in the simulations and experiments.

The OTW interface conditions with a non–zero value for β_t were used in an analytical study of Kuznetsov [49], who also added a non–linear (Forchheimer) drag term to the Brinkman equation to account for a high Reynolds number effect. Support to the OTW interface conditions is given by Breugem et al. [13], who performed numerical simulations of Stokes flow in a plane channel with a lower permeable wall that consisted of a 3D Cartesian grid of cubes. To compare the simulations with the analytical solution of OTW, the velocity field obtained from the simulations was averaged locally in space by means of the cellular filter proposed by Quintard & Whitaker [75] for ordered porous media. A good agreement was found between the volume–averaged velocity field and the OTW solution. The value of β_t calculated from the numerical simulations ranged from 0.45 till 0.91 dependent of the location of the interface. These results gives us confidence to employ the OTW interface conditions in the present analysis.

Besides the BJ and OTW interface conditions, slightly different conditions have been developed by Hassanizadeh & Gray [34] and Jäger et al. [39], to name two other references. A comparison of several different interface conditions is made by Alazmi & Vafai [1]. A further discussion of these conditions is beyond the scope of this study and the interested reader is referred to the above references.

Instead of the specification of interface conditions, the literature provides also other approaches to model the momentum transfer at the interface between a permeable wall and a homogeneous fluid domain. We mention here models which make use of either a variable effective viscosity and/or a variable permeability in the interface region, see for instance Ochoa-Tapia & Whitaker [68] and Sangani & Behl [82]. A discussion and evaluation of these models is given by Sahraoui & Kaviany [81] and Breugem et al. [13], among others. In the present analysis however we prefer the use of interface conditions, because they are more appealing for a simple analytical treatment of boundary–layer flow over a permeable wall.

The objective of the present study is to find an analytical solution for the boundary–layer flow over a passive permeable wall. The structure of this chapter is as follows. In section 3.2 the flow geometry is presented and the VANS equations are introduced. In the next section the boundary–layer equations for flow over a passive permeable wall are derived, where we make use of the OTW interface conditions. As will be seen, two boundary layers can be distinguished: the Prandtl boundary layer above the permeable wall, and the Brinkman boundary layer inside the permeable wall. In section 3.4 an analytical solution is given for the Brinkman boundary layer. This solution enables the formulation of a closed system of equations for the flow in the Prandtl boundary layer. In section 3.5 we show that the flow in the Prandtl boundary layer is self–similar and governed by a generalization of the Falkner–Skan equation in which the effect of wall permeability is incorporated. In section 3.6 the definitions of the displacement and the momentum thickness of a boundary layer are adjusted to include the effect of wall permeability. In the next section numerical solutions are presented of the Falkner–Skan equation. Section 3.8 gives a summary and a discussion.

3.2 Flow geometry and VANS equations

Figure 3.1 shows the flow geometry that we consider. Following Ochoa-Tapia and Whitaker [67], we make distinction between three regions, as indicated in figure 3.1:

1. The homogeneous fluid region or η–region for short, with a porosity equal to unity;
2. The homogeneous porous region or ω–region for short, with a constant porosity;
3. The interface region characterized by a spatially varying porosity.

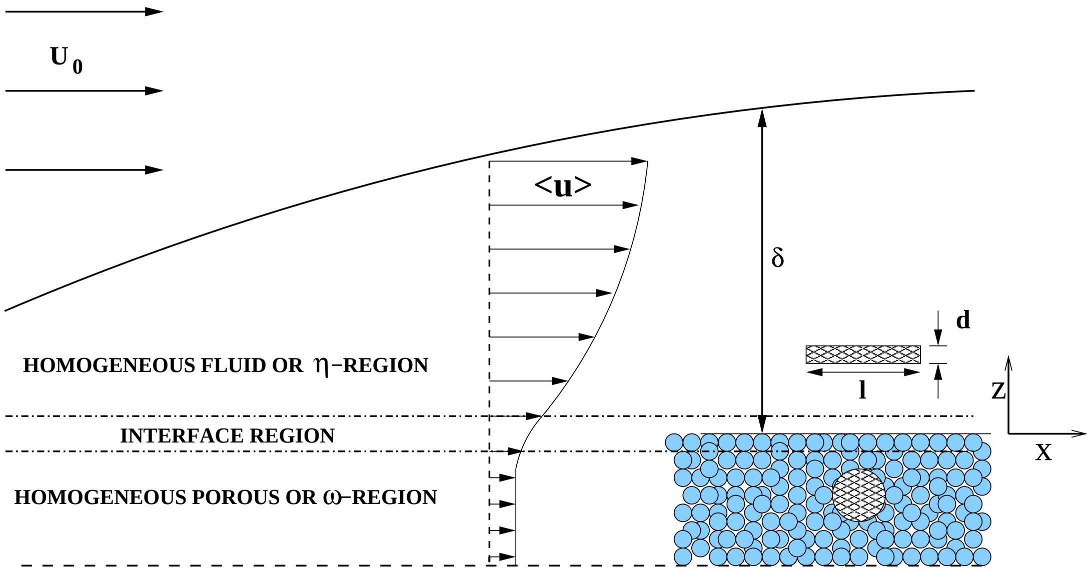

Figure 3.1: Sketch of the boundary–layer flow over a flat permeable wall at $z = 0$. The shaded rectangle and circle refer to the averaging volume in respectively the η– and the ω–region.

To describe the flow in the ω–region, it is convenient to employ a continuum approach based on the Volume-Averaging Method [105]. In this method the flow variables are averaged over a small spatial volume, as illustrated by figure 3.2. To avoid confusion we will refer to the unfiltered velocity as the *point* velocity, to distinguish it from the *volume–averaged* velocity. Before the governing equations for the volume–averaged flow are given, we first need to introduce some definitions.
The *intrinsic* volume average is denoted by $\langle ... \rangle$ and is defined according to:

$$\langle \mathbf{u} \rangle \equiv \frac{1}{V_\beta} \int_{V_\beta} \mathbf{u}(\mathbf{r}) dV \tag{3.5}$$

where V_β is the volume of the fluid phase inside the averaging volume V. The vector $\mathbf{r}$ is equal to $\mathbf{x} + \mathbf{y}$, where $\mathbf{x}$ is the centroid of V and $\mathbf{y}$ is the position vector relative to $\mathbf{x}$,

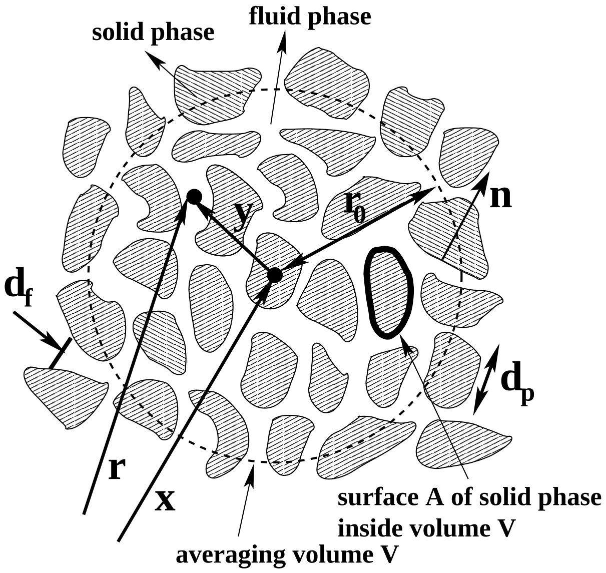

Figure 3.2: Illustration of the volume–averaging process for a disordered porous medium.

and points only in the fluid phase (see figure 3.2). The intrinsic volume average is related to the *superficial* volume average, denoted by $\langle ... \rangle^s$, by:

$$\langle \mathbf{u} \rangle^s \equiv \frac{1}{V} \int_{V_\beta} \mathbf{u}(\mathbf{r}) dV = \epsilon \langle \mathbf{u} \rangle \tag{3.6}$$

The porosity ϵ is the void fraction:

$$\epsilon \equiv \langle 1 \rangle^s = V_\beta / V \tag{3.7}$$

The *deviation* of the point velocity or the point pressure from the corresponding volume–averaged quantity is denoted by a tilde:

$$\tilde{\mathbf{u}} = \mathbf{u} - \langle \mathbf{u} \rangle \tag{3.8a}$$

$$\tilde{p} = p - \langle p \rangle \tag{3.8b}$$

Application of the volume–averaging filter $\langle ... \rangle$ to the incompressible Navier–Stokes equations for the point flow yields the Volume–Averaged Navier–Stokes (VANS) equations [104]:

$$\frac{\partial \langle \mathbf{u} \rangle}{\partial t} + \frac{1}{\epsilon} \nabla \left[\epsilon \langle \mathbf{u} \rangle \langle \mathbf{u} \rangle \right] + \frac{1}{\epsilon} \nabla \left[\epsilon \langle \tilde{\mathbf{u}} \tilde{\mathbf{u}} \rangle \right] = -\frac{1}{\rho \epsilon} \nabla [\epsilon \langle p \rangle] + \frac{\nu}{\epsilon} \nabla^2 [\epsilon \langle \mathbf{u} \rangle] + \mathbf{f} \tag{3.9a}$$

$$\nabla \cdot [\epsilon \langle \mathbf{u} \rangle] = 0 \tag{3.9b}$$

where ρ is the fluid density, ν is the kinematic viscosity and $\mathbf{f}$ is the drag force per unit mass of the fluid phase that the solid phase exerts on the fluid phase. The drag force is given by:

$$\mathbf{f} = \frac{1}{V_\beta} \int_A \mathbf{n} \left[-\frac{\tilde{p}}{\rho} \mathbf{I} + \nu \nabla \tilde{\mathbf{u}} \right] dA + \frac{1}{\epsilon} \nabla \epsilon \frac{\langle p \rangle}{\rho} - \frac{\nu}{\epsilon} \nabla \epsilon \cdot \nabla \langle \mathbf{u} \rangle \tag{3.10}$$

where A is the contact area between the fluid and the solid phase inside the averaging volume V, $\mathbf{n}$ is the unit normal at A that points from the fluid into the solid phase (see figure 3.2), and $\mathbf{I}$ is the unit tensor. The length scale constraints associated with the *local* form of the VANS equations as given above, are [75]:

$$d_f \ll r_0 \ll L_u \tag{3.11}$$

where d_f is the typical dimension of the pores and L_u a characteristic length scale of the volume–averaged flow.

As pointed out by Ochoa–Tapia and Whitaker [67] there is a mismatch in length scales at the interface (at $z = 0$) between the volume–averaged flow in the ω–region and the point flow in the η–region. They solved this problem by using the volume–averaging approach also for the η–region. An appropriate averaging volume for the nearly one–dimensional flow in the η–region is a thin disk oriented parallel to the interface, as illustrated in figure 3.1. The volume–averaged flow variables are approximately equal to the corresponding point variables ($\langle \mathbf{u} \rangle \approx \mathbf{u}$) on condition that:

$$d \ll \delta \quad \text{and} \quad l \gg d_f \tag{3.12}$$

where d and l are respectively the thickness and the length of the disk, and δ is the boundary–layer thickness. These requirements can be easily satisfied.

In order to use the momentum equation (3.9a), closures must be found for the subfilter–scale stress $\langle \tilde{\mathbf{u}}\tilde{\mathbf{u}} \rangle$ and the drag force $\mathbf{f}$ in terms of the volume–averaged velocity $\langle \mathbf{u} \rangle$. In our analysis we restrict ourselves to Stokes flow in the ω–region, which implies that the left–hand side of (3.9a) and hence the subfilter–scale stress can be neglected. Whitaker [104] gave theoretical support to the following convenient parameterization for the drag force:

$$\frac{1}{V_\beta} \int_A \mathbf{n} \left[-\frac{\tilde{p}}{\rho}\mathbf{I} + \nu \nabla \tilde{\mathbf{u}} \right] dA = -\nu \mathbf{K}^{-1} \langle \mathbf{u} \rangle^s - \nu \mathbf{K}^{-1} \mathbf{F} \langle \mathbf{u} \rangle^s \tag{3.13}$$

where $\mathbf{K}$ and $\mathbf{F}$ are referred to as respectively the permeability and the Forchheimer tensor. In literature many semi–empirical relations are available for $\mathbf{K}$ and $\mathbf{F}$ for homogeneous porous media. A popular and widely used relation is the modified Ergun equation for randomly packed beds [61]:

$$\mathbf{F} = \frac{1}{100(1-\epsilon)} \frac{d_p |\langle \mathbf{u} \rangle^s|}{\nu} \mathbf{I} \tag{3.14a}$$

$$\mathbf{K} = \frac{{d_p}^2 \epsilon^3}{180(1-\epsilon)^2} \mathbf{I} \tag{3.14b}$$

where $d_p \equiv 6V_p/A_p$ is the *mean particle diameter*, which is defined as six times the ratio of the total volume V_p to the total surface area A_p of the solid phase. The coefficients in equations (3.14a) and (3.14b) are determined from many experiments in which different materials were used (such as glass beads, cylindrical fibers, granular material and cylindrical packings), and in which the particle sizes, the porosity and the Reynolds number were varied.

3.3 The boundary–layer equations

3.3.1 Homogeneous fluid region

In the η–region we distinguish a region with potential flow and close to the permeable wall a laminar boundary layer with a thickness δ. The boundary layer is characterized by the importance of viscous diffusion, whereas this is not important outside the boundary layer. The flow in the boundary layer is governed by the well–known Prandtl boundary–layer equations:

$$\langle u\rangle_\eta \frac{\partial\langle u\rangle_\eta}{\partial x} + \langle w\rangle_\eta \frac{\partial\langle u\rangle_\eta}{\partial z} = U_0 \frac{\partial U_0}{\partial x} + \nu \frac{\partial^2\langle u\rangle_\eta}{\partial z^2} \tag{3.15a}$$

$$0 = -\frac{1}{\rho}\frac{\partial\langle p\rangle_\eta}{\partial z} \tag{3.15b}$$

$$\frac{\partial\langle u\rangle_\eta}{\partial x} + \frac{\partial\langle w\rangle_\eta}{\partial z} = 0 \tag{3.15c}$$

where the subscript η refers to the η–region, U_0 is the freestream velocity outside the boundary layer, z is the wall–normal position relative to the interface with the permeable wall, and x is the streamwise distance to the leading edge of the boundary layer. The first term on the right–hand side of (3.15a) enters the equation by virtue of equation (3.15b) and Bernoulli's Law for the potential flow outside the boundary layer:

$$-\frac{1}{\rho}\frac{\partial\langle p\rangle_\eta}{\partial x} = U_0 \frac{\partial U_0}{\partial x} \tag{3.16}$$

Schlichting [83] gives a derivation of these equations, which can be found also in many other textbooks on boundary–layer theory. It is based on an order–of–magnitude analysis of the Navier–Stokes equations in which it is assumed that $\delta/x \ll 1$. Because it can be shown that [83] (p. 136):

$$\frac{\delta}{x} \propto \left(\frac{U_0 x}{\nu}\right)^{-1/2} \tag{3.17}$$

this implies that the following condition must be satisfied:

$$\left(\frac{U_0\, x}{\nu}\right)^{1/2} \gg 1 \tag{3.18}$$

For a large value of the Reynolds number $U_0\, x/\nu$, the boundary layer becomes turbulent. Because we restrict ourselves to a laminar boundary layer, it is therefore also required that $U_0\, x/\nu$ is sufficiently small such that the flow is in the laminar regime.

3.3.2 Homogeneous porous region

The ω–region is characterized by a constant porosity denoted by ϵ_c. We assume that the permeability is isotropic, $\mathbf{K} = K\mathbf{I}$. Furthermore, as mentioned before in section 3.2, we assume that the point flow is governed by the Stokes equations. As will be shown below, this implies that the volume–averaged flow is governed by the Brinkman equation [14]. Although in literature this equation is frequently used to describe flow in porous media, in this section we will still give a derivation. This derivation is based on an order–of–magnitude analysis of the VANS equations and it serves to obtain the conditions on which the Brinkman equation is valid.

The condition for Stokes flow in the pores is that the characteristic Reynolds number for the flow in the pores is much smaller than unity [3] (p. 223). A typical velocity scale for $\mathbf{u}$ is the streamwise interface velocity U_i. A typical length scale is the pore diameter d_f, which is of the same order as $\sqrt{K}$. Thus the condition for Stokes flow in the pores is that:

$$\frac{\sqrt{K}U_i}{\nu} \ll 1 \tag{3.19}$$

If this condition holds, then the left–hand side of equation (3.9a) can be neglected. For the drag force on the right–hand side of (3.9a) we adopt the parameterization given by equation (3.13). By virtue of (3.19) the Forchheimer tensor can be neglected, because $|\mathbf{F}| \propto \sqrt{K}U_i/\nu$ (see Whitaker [104], p. 47). Therefore the VANS equations (3.9a) and (3.9b) can be simplified to:

$$0 = -\frac{1}{\rho}\nabla\langle p\rangle_\omega + \nu\nabla^2\langle\mathbf{u}\rangle_\omega - \frac{\nu\epsilon_c}{K}\langle\mathbf{u}\rangle_\omega \tag{3.20a}$$

$$\nabla\cdot\langle\mathbf{u}\rangle_\omega = 0 \tag{3.20b}$$

where the subscript ω refers to the ω–region.

For an order–of–magnitude analysis of the above equations, we need to specify characteristic length and velocity scales of the volume–averaged flow. Characteristic length scales are $\sqrt{K}$ and x for respectively variations in the wall–normal and streamwise direction. The typical velocity scale for the streamwise velocity is estimated by the streamwise interface velocity U_i. Based on the continuity equation (3.20b), a typical velocity scale for the wall–normal velocity is then given by $U_i\sqrt{K}/\nu$. The porosity ϵ_c is of order unity. To summarize the characteristic scales are:

$$\begin{cases} \frac{\partial}{\partial x} \propto \frac{1}{x} \ ; \ \frac{\partial}{\partial z} \propto \frac{1}{\sqrt{K}} \\ \langle u\rangle_\omega \ \propto \ U_i \ ; \ \langle w\rangle_\omega \ \propto \ U_i\sqrt{K}/\nu \\ \epsilon_c \ \propto \ 1 \end{cases} \tag{3.21}$$

Let us consider the streamwise component of equation (3.20a). Based on the scales given in (3.21) we estimate the following ratios by:

$$\nu\frac{\partial^2\langle u\rangle_\omega}{\partial x^2} \Big/ \nu\frac{\partial^2\langle u\rangle_\omega}{\partial z^2} \ \propto \ \frac{K}{x^2} \tag{3.22a}$$

$$\nu\frac{\epsilon_c}{K}\langle u\rangle_\omega \Big/ \nu\frac{\partial^2\langle u\rangle_\omega}{\partial z^2} \ \propto \ 1 \tag{3.22b}$$

Thus if, in addition to (3.19), it holds that:

$$K/x^2 \ll 1 \tag{3.23}$$

then the streamwise component of (3.20a) reduces to the Brinkman equation:

$$0 \;=\; -\frac{1}{\rho}\frac{\partial \langle p \rangle_\omega}{\partial x} + \nu \frac{\partial^2 \langle u \rangle_\omega}{\partial z^2} - \nu \frac{\epsilon_c}{K} \langle u \rangle_\omega \tag{3.24}$$

This equation describes the Brinkman boundary layer that is set by the balance between diffusion of streamwise momentum from the Prandtl boundary layer above the permeable wall on the one hand and the drag force inside the permeable wall on the other hand. This is a fundamentally different type of boundary layer than the Prandtl boundary layer, which is characterized by a balance between inertial and viscous forces.

Based on a similar analysis and the same conditions (3.19) and (3.23), the wall–normal component of equation (3.20a) can be simplified to:

$$0 \;=\; -\frac{1}{\rho}\frac{\partial \langle p \rangle_\omega}{\partial z} \tag{3.25}$$

This equation expresses that pressure variations in the wall–normal direction are negligible.

3.3.3 Interface region

The interface region is the thin layer in between the ω– and the η–region. It has a thickness of order $\sqrt{K}$ [67]. The structure of the porous medium and the flow inside this layer are highly complicated. Furthermore, the simple parameterization of the drag integral as given by equation (3.13), does not hold in this layer [104]. In the introduction we discussed several models for the momentum transfer in this layer and arguments were given for the use of the OTW interface conditions in our analysis. In the derivation of these conditions, OTW [67] expand the ω– and η–region to the core of the interface region. The Brinkman equation is adopted for the ω–region and the Stokes equation is used for the η–region. Formally these equations are not correct inside the interface region, because in this region the permeability is not constant like in the ω–region, and it is also not infinite like in the η–region. These errors inherent to this approximation are compensated by means of an artificial jump condition for the intrinsic stress in combination with a continuous superficial velocity across the interface. This is illustrated in figure 3.3. The OTW interface conditions read:

$$\langle \mathbf{u} \rangle^s_\omega = \langle \mathbf{u} \rangle^s_\eta = \mathbf{U}_i \tag{3.26a}$$

$$\mathbf{n}_{\omega\eta} \cdot \left[\langle \boldsymbol{\tau} \rangle_\omega - \langle \boldsymbol{\tau} \rangle_\eta \right] = \frac{\boldsymbol{\beta} \cdot \mathbf{U}_i}{\sqrt{K}} \tag{3.26b}$$

where $\mathbf{n}_{\omega\eta}$ is the unit normal at the interface, pointing from the ω– into the η–region, $\langle \boldsymbol{\tau} \rangle = -p\mathbf{I} + \mu \left[\nabla \langle \mathbf{u} \rangle + \nabla \langle \mathbf{u} \rangle^T \right]$ is the intrinsic stress tensor and $\boldsymbol{\beta}$ is the dimensionless

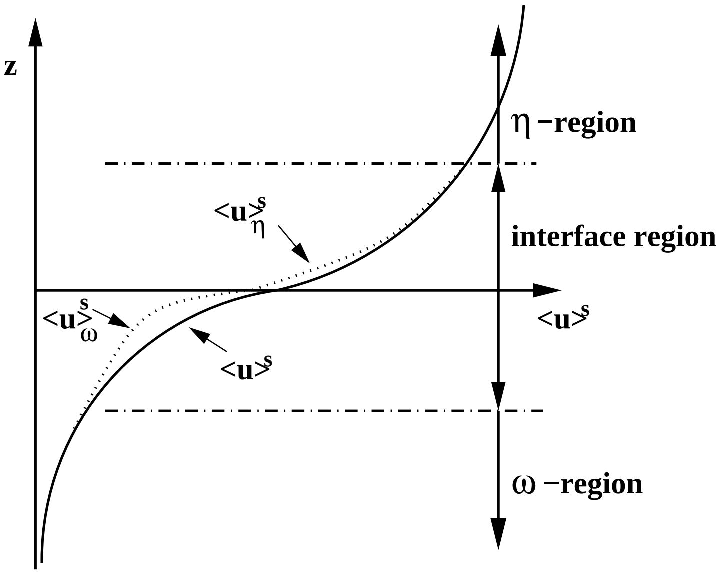

Figure 3.3: Illustration of the OTW interface conditions with an artificial jump in the intrinsic stress. $\langle u\rangle^s$ is the 'true' velocity profile, which within the interface region is estimated by $\langle u\rangle^s_\omega$ and $\langle u\rangle^s_\eta$.

stress–jump tensor with coefficients of order unity. We remark here that OTW assumed Stokes flow in the η–region, whereas in our analysis we have the additional effect of advection. However, close to the permeable wall the flow is strongly dominated by viscous effects and therefore we can still use the OTW interface conditions.

Based on a similar order–of–magnitude analysis as used in the derivation of the Brinkman equation, we can simplify the OTW interface conditions. Let us first consider the conditions for the streamwise velocity and the tangential stress:

$$\langle u\rangle^s_\omega = \langle u\rangle^s_\eta = U_i \tag{3.27a}$$

$$\mu\left[\frac{\partial\langle u\rangle_\omega}{\partial z} - \frac{\partial\langle w\rangle_\omega}{\partial x}\right] - \mu\left[\frac{\partial\langle u\rangle_\eta}{\partial z} - \frac{\partial\langle w\rangle_\eta}{\partial x}\right] = \mu\frac{\beta_t}{\sqrt{K}}U_i \tag{3.27b}$$

where β_t is the tangential stress–jump parameter. The characteristic length scales for the η–region are δ and x for variations in respectively the wall–normal and streamwise direction, and characteristic velocity scales are the freestream velocity U_0 and $U_0\delta/x$ for respectively the streamwise and the wall–normal velocity. The characteristic scales for the ω–region are summarized in (3.21). Based on these scales we can estimate the following ratios by:

$$\frac{\partial\langle w\rangle_\omega}{\partial x}/\frac{\partial\langle u\rangle_\omega}{\partial z} \propto \frac{K}{x^2} \tag{3.28a}$$

$$\frac{\partial\langle w\rangle_\eta}{\partial x}/\frac{\partial\langle u\rangle_\eta}{\partial z} \propto \frac{\delta^2}{x^2} \propto \left(\frac{U_0 x}{\nu}\right)^{-1} \tag{3.28b}$$

By virtue of (3.18) and (3.23), equation (3.27b) can therefore be simplified to:

$$\frac{\partial\langle u\rangle_\omega}{\partial z}-\frac{\partial\langle u\rangle_\eta}{\partial z}=\frac{\beta_t}{\sqrt{K}}U_i \tag{3.29}$$

Based on this equation we can derive a scaling relation for the ratio $\langle u\rangle_\omega/\langle u\rangle_\eta$:

$$\frac{\langle u\rangle_\omega}{\langle u\rangle_\eta}\propto\frac{U_i}{U_0}\propto\frac{\sqrt{K}}{\delta} \tag{3.30}$$

The ratio of the characteristic wall–normal velocities in the ω– and η–region can be estimated by:

$$\frac{\langle w\rangle_\omega}{\langle w\rangle_\eta}\propto\left[\frac{U_i\sqrt{K}}{x}\right]\Big/\left[\frac{U_0\delta}{x}\right]=\frac{U_i}{U_0}\frac{\sqrt{K}}{\delta}\propto\left[\frac{\sqrt{K}}{\delta}\right]^2 \tag{3.31}$$

From the comparison between equations (3.30) and (3.31), it follows that the wall–normal velocity in the permeable wall is of second order in the parameter $\sqrt{K}/\delta$, whereas the streamwise velocity is of first order in the same parameter. Thus it can be expected that for small values of $\sqrt{K}/\delta$, the wall–normal velocity is negligible compared to the streamwise velocity.

We now consider the interface conditions for the wall–normal velocity and stress:

$$\langle w\rangle_\omega^s=\langle w\rangle_\eta^s = W_i \tag{3.32a}$$

$$\left[-\langle p\rangle_\omega+2\mu\frac{\partial\langle w\rangle_\omega}{\partial z}\right]-\left[-\langle p\rangle_\eta+2\mu\frac{\partial\langle w\rangle_\eta}{\partial z}\right] = \frac{\beta_n}{\sqrt{K}}W_i \tag{3.32b}$$

where W_i is the wall–normal component of the interface velocity and β_n is the normal stress–jump parameter. Based on the length and velocity scales for the ω– and η–region we estimate the following ratios by:

$$\mu\frac{\partial\langle w\rangle_\omega}{\partial z}/\langle p\rangle_\omega \propto \frac{K}{x^2} \tag{3.33a}$$

$$\mu\frac{\partial\langle w\rangle_\eta}{\partial z}/\langle p\rangle_\eta \propto \left(\frac{U_0x}{\nu}\right)^{-1} \tag{3.33b}$$

$$\frac{\beta_nW_i}{\sqrt{K}}/\langle p\rangle_\omega \propto \frac{K}{x^2} \tag{3.33c}$$

By virtue of (3.18) and (3.23), equation (3.32b) for the normal stress can therefore be simplified to:

$$\langle p\rangle_\omega=\langle p\rangle_\eta \tag{3.34}$$

From this equation and equations (3.15b) and (3.25), we conclude that the intrinsic pressure is not varying in the wall–normal direction in both the ω– and η–region. This implies also that the streamwise pressure gradient in the ω–region is the same as in the η–region. Therefore we can write for the pressure gradient in the Brinkman equation (3.24):

$$-\frac{1}{\rho}\frac{\partial\langle p\rangle_\omega}{\partial x} = U_0\frac{\partial U_0}{\partial x} \tag{3.35}$$

We have already concluded that for small values of $\sqrt{K}/\delta$, in the ω–region the wall-normal velocity is negligible with respect to the streamwise velocity. Consistent with our order–of–magnitude analysis would therefore be to put $W_i = 0$. As a consequence then also $\langle w\rangle_\omega = 0$, which implies that the continuity equation for the ω–region is not satisfied exactly. When we would like to satisfy the continuity equation exactly we have to allow for $W_i \neq 0$. However, in this case we need an extra interface condition. This condition can be obtained by subtracting equation (3.34) from equation (3.32b). The result is:

$$2\mu\left[\frac{\partial\langle w\rangle_\omega}{\partial z} - \frac{\partial\langle w\rangle_\eta}{\partial z}\right] = \mu\frac{\beta_n}{\sqrt{K}}W_i \tag{3.36}$$

This equation provides enough freedom in the choice of either satisfying the continuity equation or to put $W_i = 0$. The case of $W_i = 0$ can be accomplished by putting the value of β_n to a very large negative or positive value. Based on the continuity equations for the ω– and the η–region, the first term on the left–hand side of equation (3.36) can be rewritten into:

$$\frac{\partial\langle w\rangle_\omega}{\partial z} = \frac{1}{\epsilon_c}\frac{\partial\langle w\rangle_\eta}{\partial z} = -\frac{1}{\epsilon_c}\frac{\partial U_i}{\partial x} \quad \text{at z=0} \tag{3.37}$$

Substitution of this equation into equation (3.36) yields the following relation between the wall–normal and the streamwise component of the interface velocity:

$$W_i = \frac{2\sqrt{K}}{\beta_n}\left(1 - \frac{1}{\epsilon_c}\right)\frac{\partial U_i}{\partial x} \tag{3.38}$$

3.3.4 Summary of equations, boundary conditions and assumptions

For convenience we summarize the boundary–layer equations, the boundary conditions and the assumptions.
The equations for the η–region are:

$$\langle u\rangle_\eta\frac{\partial\langle u\rangle_\eta}{\partial x} + \langle w\rangle_\eta\frac{\partial\langle u\rangle_\eta}{\partial z} = U_0\frac{\partial U_0}{\partial x} + \nu\frac{\partial^2\langle u\rangle_\eta}{\partial z^2} \tag{3.39a}$$

$$0 = -\frac{1}{\rho}\frac{\partial\langle p\rangle_\eta}{\partial z} \tag{3.39b}$$

$$\frac{\partial\langle u\rangle_\eta}{\partial x} + \frac{\partial\langle w\rangle_\eta}{\partial z} = 0 \tag{3.39c}$$

with boundary conditions:

$$\begin{aligned} z = 0 \quad &: \quad \langle u \rangle_\eta = U_i \\ & \quad\;\; \langle w \rangle_\eta = W_i \\ z \to \infty \quad &: \quad \langle u \rangle_\eta \to U_0 \end{aligned} \tag{3.40}$$

The equations for the ω–region are:

$$0 = U_0 \frac{\partial U_0}{\partial x} + \nu \frac{\partial^2 \langle u \rangle_\omega}{\partial z^2} - \nu \frac{\epsilon_c}{K} \langle u \rangle_\omega \tag{3.41a}$$

$$0 = -\frac{1}{\rho} \frac{\partial \langle p \rangle_\omega}{\partial z} \tag{3.41b}$$

$$\frac{\partial \langle u \rangle_\omega}{\partial x} + \frac{\partial \langle w \rangle_\omega}{\partial z} = 0 \tag{3.41c}$$

The boundary conditions for the ω–region are:

$$\begin{aligned} z = 0 \quad &: \quad \epsilon_c \langle u \rangle_\omega = U_i \\ & \quad\;\; \epsilon_c \langle w \rangle_\omega = W_i \\ z \to -\infty \quad &: \quad \langle u \rangle_\omega \text{ bounded} \end{aligned} \tag{3.42}$$

The interface condition for the intrinsic pressure is given by: $\langle p \rangle_\omega = \langle p \rangle_\eta$. The streamwise and wall-normal components of the interface velocity can be calculated from:

$$U_i = \frac{\sqrt{K}}{\beta_t} \left[\frac{\partial \langle u \rangle_\omega}{\partial z} - \frac{\partial \langle u \rangle_\eta}{\partial z} \right] \tag{3.43a}$$

$$W_i = \frac{2\sqrt{K}}{\beta_n} \left(1 - \frac{1}{\epsilon_c} \right) \frac{\partial U_i}{\partial x} \tag{3.43b}$$

The assumptions in the derivation of the above equations are that $\sqrt{K}/\delta$ is small but not negligible and that:

$$\left(\frac{U_0 x}{\nu} \right)^{1/2} \gg 1 \tag{3.44a}$$

$$\frac{K}{x^2} \ll 1 \tag{3.44b}$$

$$\frac{U_i \sqrt{K}}{\nu} \ll 1 \tag{3.44c}$$

The last assumption can be combined with equations (3.17), (3.30) and assumption (3.44a) to obtain an equivalent assumption:

$$\frac{K}{\delta^2} \ll \left(\frac{U_0 x}{\nu} \right)^{-1/2} \ll 1 \tag{3.45}$$

Thus our analysis is essentially valid for only the first–order effect of permeability in $\sqrt{K}/\delta$ and second– and higher–order effects, like a non–zero wall–normal velocity in the ω–region (3.31), are actually assumed to be negligible.

3.4 Analytical solution for the flow in the ω–region

The boundary–layer equations (3.41a)–(3.41c) for the flow in the ω–region can be solved analytically. The solutions for the streamwise and wall–normal velocity read:

$$z < 0 \; : \; \langle u \rangle_\omega = \left[\frac{U_i - U_d}{\epsilon_c}\right] \cdot \exp\left(\sqrt{\frac{\epsilon_c}{K}} \cdot z\right) + \frac{U_d}{\epsilon_c} \tag{3.46a}$$

$$\begin{aligned} \langle w \rangle_\omega &= \sqrt{\frac{K}{\epsilon_c}} \cdot \frac{\partial}{\partial x}\left[\frac{U_i - U_d}{\epsilon_c}\right] \cdot \left[1 - \exp\left(\sqrt{\frac{\epsilon_c}{K}} \cdot z\right)\right] \\ &\quad - \frac{1}{\epsilon_c}\frac{\partial U_d}{\partial x} \cdot z + \frac{W_i}{\epsilon_c} \end{aligned} \tag{3.46b}$$

Here U_d represents the uniform creep velocity for $z \ll -\sqrt{K/\epsilon_c}$:

$$U_d = U_0 \frac{\partial U_0}{\partial x} \frac{K}{\nu} \tag{3.47}$$

We define the thickness δ_B of the Brinkman boundary layer as the height with respect to the interface where the difference of the velocity with the creep velocity U_d is reduced to 1 % of the corresponding value at the interface, i.e.

$$\frac{\langle u(z = -\delta_B) \rangle_\omega^s - U_d}{U_i - U_d} \equiv 0.01 \tag{3.48}$$

An expression for δ_B can be obtained from the streamwise velocity distribution (3.46a):

$$\delta_B \approx 4.6 \sqrt{\frac{K}{\epsilon_c}} \tag{3.49}$$

Thus δ_B scales with $\sqrt{K/\epsilon_c}$, where $\sqrt{K}$ is also known as the Brinkman screening distance, and it is not a function of x.

The solutions (3.46a) and (3.46b) for respectively the streamwise and wall–normal velocity are in fact not valid for $z \to -\infty$. When the freestream flow (U_0) in the η–region accelerates or decelerates, the solutions predict that the creep flow in the core of the permeable wall (U_d) also accelerates or decelerates and by virtue of mass conservation this is accompanied by an infinite wall–normal velocity at $z = -\infty$. Of course it is physically not realistic that the wall–normal velocity becomes infinite. It is also not realistic that the flow far down in the permeable wall communicates with the freestream flow in the η–region. The infinite wall–normal velocity contradicts the simplification of the wall–normal momentum equation as given by equation (3.25), which was obtained from our order–of–magnitude analysis. The origin of this singularity lies in our choice of $\sqrt{K}$ as the characteristic scale for the variation of the flow in the wall–normal direction. This assumption is true inside the Brinkman boundary layer with $z \in [-\delta_B, 0]$, but it is not valid for $z \ll -\delta_B$, where the characteristic length scale for wall–normal variations in the flow is much larger. For $z \ll -\delta_B$ the wall–normal momentum equation (3.41b) should actually be replaced by Darcy's Law:

$$0 = -\frac{1}{\rho}\frac{\partial \langle p \rangle_\omega}{\partial z} - \nu \frac{\epsilon_c}{K}\langle w \rangle_\omega \tag{3.50}$$

For $z \ll -\delta_B$ the Brinkman equation for the streamwise velocity reduces also to Darcy's Law:

$$0 = -\frac{1}{\rho}\frac{\partial \langle p \rangle_\omega}{\partial x} - \nu \frac{\epsilon_c}{K}\langle u \rangle_\omega \tag{3.51}$$

Combining the above equations with the continuity equation yields a Laplace equation for the pressure:

$$\frac{\partial^2 \langle p \rangle_\omega}{\partial x^2} + \frac{\partial^2 \langle p \rangle_\omega}{\partial z^2} = 0 \tag{3.52}$$

The general solutions of this equation are functions in x and z, which either decrease or increase exponentially in z. The physically realistic solution is the one which decreases exponentially when $z \to -\infty$. The substitution of this solution into equations (3.50) and (3.51) shows that both $\langle u \rangle_\omega$ and $\langle w \rangle_\omega$ will go to zero for $z \to -\infty$, as expected. Because our basic interest concerns only the Brinkman boundary layer, we abandon a more elaborate analysis of the flow for $z \ll -\delta_B$. We simply keep in mind that the velocity distributions (3.46a) and (3.46b) are only valid approximations inside the Brinkman boundary layer.

The analytical expressions for the velocity distributions in the ω–region can be used to obtain the following expressions for the streamwise and the wall–normal component of the interface velocity:

$$U_i = \frac{\sqrt{K}}{\gamma}\frac{\partial \langle u \rangle_\eta}{\partial z} + \frac{U_d}{\gamma\sqrt{\epsilon_c}} \tag{3.53a}$$

$$W_i = \frac{2\sqrt{K}}{\gamma\beta_n}\left(1 - \frac{1}{\epsilon_c}\right)\left[\sqrt{K}\frac{\partial^2 \langle u \rangle_\eta}{\partial x \partial z} + \frac{1}{\epsilon_c}\frac{\partial U_d}{\partial x}\right] \tag{3.53b}$$

where for convenience γ is defined according to:

$$\gamma \equiv \frac{1}{\sqrt{\epsilon_c}} - \beta_t \tag{3.54}$$

3.5 Self–similar solution for the flow in the η–region

In this section we seek a similarity solution for the flow in the boundary layer above the interface. Characteristic for a self–similar solution is that the velocity distribution, if properly scaled, does not depend on the streamwise coordinate x. For the case of a fully impermeable wall (i.e. $K = 0$) such a solution exists and a derivation can be found for instance in Schlichting [83]. In that case a similarity solution is found, if one adopts the following form for the stream function ψ:

$$\psi = U_0 \delta f(\eta) \tag{3.55}$$

where f is a dimensionless function of η alone, defined by:

$$\eta \equiv \frac{z}{\delta(x)} \tag{3.56}$$

In the case of a permeable wall, equation (3.55) is expected to give only a self–similar solution for the limit of $\sqrt{K}/\delta \to 0$. In this limit the interface velocity, which according to (3.30) is linear in $\sqrt{K}/\delta$, goes to zero. This suggests that an important parameter for the boundary–layer development over a permeable wall is given by the ratio $\sqrt{K}/\delta$. Therefore let us define a perturbation parameter κ given by:

$$\kappa \equiv \frac{\sqrt{K}}{\gamma \delta} \tag{3.57}$$

The parameter γ is given before by equation (3.54) and is included in the perturbation parameter to simplify our analysis later on. From a physical point of view, κ is proportional to the ratio of the thickness δ_B of Brinkman boundary layer to the thickness δ of the Prandtl boundary layer.

We now propose a similarity solution in which the stream function is expanded in κ according to:

$$\psi = U_0 \delta f_0(\eta) + U_0 \delta \sum_{r=1}^{\infty} \kappa^r f_r(\eta) \tag{3.58}$$

where r denotes the r^{th}–order perturbation. Substitution of equation (3.58) into the streamwise momentum equation (3.39a) yields the following equation:

$$\begin{aligned} &\sum_{r=0}^{\infty} \kappa^r f_r''' + \alpha_f \cdot \sum_{r,s=0}^{\infty} \kappa^{r+s} f_r f_s'' + \beta_f \cdot \left[1 - \sum_{r,s=0}^{\infty} \kappa^{r+s} f_r' f_s' \right] \\ &\quad - (\alpha_f - \beta_f) \cdot \left[\left(\sum_{r,s=0}^{\infty} r \kappa^{r+s} f_r f_s'' \right) - \left(\sum_{r,s=0}^{\infty} s \kappa^{r+s} f_r' f_s' \right) \right] = 0 \end{aligned} \tag{3.59}$$

where the coefficients α_f and β_f are given by:

$$\alpha_f = \frac{\delta}{\nu} \frac{\partial (U_0 \delta)}{\partial x} \tag{3.60a}$$

$$\beta_f = \frac{\delta^2}{\nu} \frac{\partial U_0}{\partial x} \tag{3.60b}$$

Substitution of equations (3.58), (3.53a) and (3.53b) into the boundary conditions (3.40) gives:

$$\eta = 0 \ : \ \sum_{r=0}^{\infty} \kappa^r f_r' = \sum_{r=0}^{\infty} \kappa^{r+1} f_r'' + \beta_f \cdot \left(\frac{\gamma}{\sqrt{\epsilon_c}} \right) \cdot \kappa^2 \tag{3.61a}$$

$$\sum_{r=0}^{\infty} \kappa^r f_r = \frac{2\gamma}{\beta_n} \left(\frac{1}{\epsilon_c} - 1 \right) \sum_{r=0}^{\infty} \kappa^{r+1} f_r' \tag{3.61b}$$

$$\eta \to \infty \ : \ \sum_{r=0}^{\infty} \kappa^r f_r' \to 1 \tag{3.61c}$$

The second term on the right–hand side of equation (3.61a) represents the influence of the acceleration or deceleration of the creep flow (U_d) in the core of the ω–region on the boundary layer in the η–region. As this term is quadratic in the perturbation parameter κ, this is a second–order effect. Notice furthermore from the boundary conditions that, besides the dependence on the coefficients α_f and β_f, the first–order perturbation function does only depend on β_t and ϵ_c, whereas the second– and higher–order perturbation functions do also depend on β_n.

Equation (3.59) is a generalization of the Falkner–Skan equation [83] in which the effect of wall permeability is incorporated. This equation, and hence our choice of the stream function (3.58), describes a self–similar flow when the parameters α_f and β_f are independent of the streamwise coordinate x. From this requirement the freestream velocity $U_0(x)$ and the boundary layer thickness $\delta(x)$ can be calculated. Because of the nature of the perturbation solution, U_0 and δ are exactly the same as for the case of an impermeable wall [83]. From the definitions of α_f and β_f it can be seen that for $\alpha_f \neq 0$ we may put $\alpha_f = 1$ without loss of generality. There are 3 cases to consider:

1. $\alpha_f = 1$ and $\beta_f \neq 2$

   For this case it is convenient to introduce a new coefficient m which is related to β_f by:

   $$m \equiv \frac{\beta_f}{2 - \beta_f} \tag{3.62}$$

   The expressions for U_0 and δ are given by respectively:

   $$U_0(x) = C \cdot x^m \tag{3.63a}$$

   $$\delta(x) = \left[\frac{\nu}{C} \frac{2}{1+m} \right]^{1/2} \cdot x^{(1-m)/2} \tag{3.63b}$$

   with C a constant, which dimension depends on m.

   The velocity distribution (3.63a) is a power law in x. This is similar to the potential flow distribution past a wedge with an angle $\pi\beta/2$ as illustrated in figure 3.4. Some examples of the wedge flow family are the flow over a flat plate ($\beta_f = 0$), the three–dimensional axisymmetric stagnation flow on a flat plate ($\beta_f = 1/2$), the

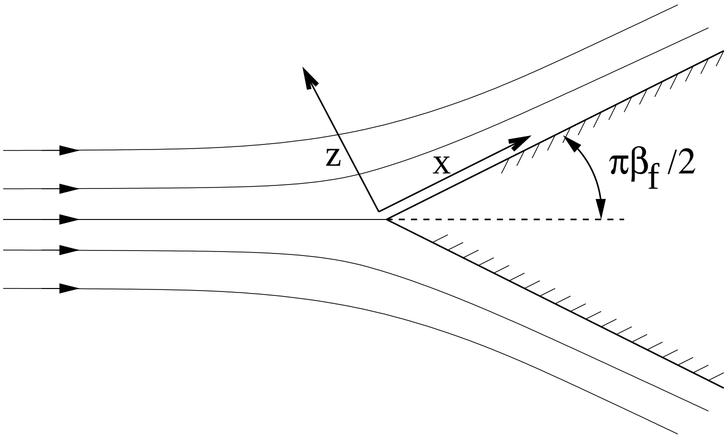

Figure 3.4: Illustration of the flow past a wedge.

gravity driven liquid film along a vertical wall ($m = 2/3$) and the two–dimensional stagnation flow on a flat plate ($\beta_f = 1$) [83]. According to (3.63b) the boundary layer thickness and hence κ does not depend on x when $\beta_f = 1$. Therefore it might be expected that in this case also the stream function does not directly depend on κ. Indeed it can be shown that for $\beta_f = 1$, equation (3.55) leads also to a similarity solution. From the numerical solution of the Falkner–Skan equation we have found that both similarity solutions are identical.

2. $\alpha_f = 0$ and $\beta_f \neq 0$
   The expressions for $U_0(x)$ and $\delta(x)$ are given by respectively:

$$U_0(x) = \left[-\frac{1+m}{2m}\frac{C^2}{\nu}\right] \cdot \frac{1}{x} \tag{3.64a}$$

$$\delta(x) = \left[\frac{2m}{m+1}\frac{\nu}{C}\right] \cdot x \tag{3.64b}$$

   with C a constant in $m^2 s^{-1}$.
   The velocity distribution is proportional to the inverse of x. This kind of potential flow is associated with flow in a two–dimensional convergent channel towards a sink.

3. $\alpha_f = 1$ and $\beta_f = 2$
   The expressions for $U_0(x)$ and $\delta(x)$ read:

$$U_0(x) = C \cdot e^{sx} \tag{3.65a}$$

$$\delta(x) = \left[\frac{2\nu}{sC}\right]^{1/2} e^{-\frac{1}{2}sx} \tag{3.65b}$$

   with C and s constants in respectively ms^{-1} and m. We abandon a more detailed discussion of this case.

We will now have a closer look at the zeroth– and the first–order problem. The zeroth–order problem is obtained from equations (3.59) and (3.61a)–(3.61c) by collecting all terms with zero powers in κ. The result is the classic Falkner–Skan equation for flow over an impermeable wall:

$$f_0''' + \alpha_f \cdot f_0 f_0'' + \beta_f \cdot \left[1 - (f_0')^2\right] = 0 \tag{3.66}$$

The corresponding boundary conditions are given by:

$$\eta = 0 \quad : \quad f_0' = 0 \tag{3.67a}$$
$$f_0 = 0 \tag{3.67b}$$
$$\eta \to \infty \quad : \quad f_0' \to 1 \tag{3.67c}$$

The first–order problem is found in a similar way by collecting all terms which are of first order in κ. The result reads:

$$f_1''' + \alpha f_1'' f_0 + \beta_f f_0'' f_1 + (\alpha_f - 3\beta_f) f_0' f_1' = 0 \tag{3.68}$$

For the boundary conditions we get:

$$\eta = 0 \quad : \quad f_1' = f_0'' \tag{3.69a}$$
$$f_1 = 0 \tag{3.69b}$$
$$\eta \to \infty \quad : \quad f_1' \to 0 \tag{3.69c}$$

From the boundary conditions we find that up to first order in κ, permeability causes a non–zero streamwise velocity at the interface, whereas the wall–normal interface velocity is still zero. We already expected this behavior, based on our scaling relations (3.30) and (3.31). A non–zero wall–normal interface velocity appears for the first time in the second–order problem and it can be shown that it is a correction for the existence of a streamwise interface velocity in the first–order problem in order to satisfy mass conservation.
It is interesting to note that the first–order problem appears to be related to the zeroth–order problem according to:

$$f_1 = f_0' \tag{3.70}$$

To prove this, we substitute this relation into equation (3.68) and subsequently we integrate this equation to obtain:

$$f_0''' + \alpha_f \cdot f_0 f_0'' - \beta_f [f_0']^2 = C \tag{3.71}$$

where C is a constant that is found by taking the limit $\eta \to 0$. With help of equations (3.66)–(3.67b) we find that $C = -\beta_f$ and hence equation (3.71) is identical to equation (3.66) for the zeroth–order problem. For the second– and higher–order problems no analytical relations to lower–order problems have been found, but we do not exclude that other recurrence relations exist.

3.6 Displacement and momentum thickness

The *displacement thickness* δ_1 of a boundary layer is defined as the distance by which the streamlines in the potential flow region outside the boundary layer are displaced by the presence of the boundary layer. The *momentum thickness* δ_2 of a boundary layer is related to the viscous shear stress that the flow encounters at the wall. The common expressions for the displacement and momentum thickness for the boundary layer over an impermeable wall (see for instance [83],[106]) are not directly applicable to the case where the wall is permeable. In this section we therefore modify the expressions for the displacement and the momentum thickness in order to account for wall permeability. The derivation below is similar to the one given by White [106] for an impermeable wall.
We consider the mass and momentum balance for the control volume sketched in figure 3.5. At $x = 0$, which corresponds to the leading edge of the boundary layer at which $\delta = 0$, uniform flow enters the control volume. For the upper side of the control volume a streamline is chosen and thus no mass and momentum is transported in the direction perpendicular to this line. The mass balance for the control volume reads:

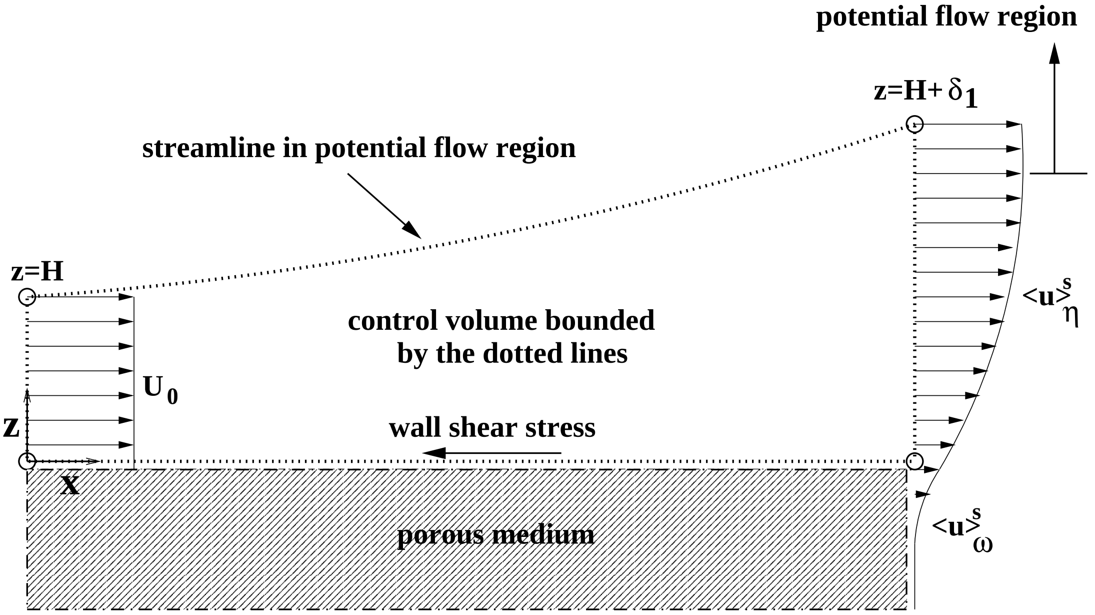

Figure 3.5: A sketch of the control volume used to derive modified expressions for the displacement and the momentum thicknesses of a boundary layer over a flat permeable wall. The control volume, which is bounded by the dotted lines, encloses the boundary layer and part of the potential flow region.

$$U_0 H = \int_0^{H+\delta_1} \langle u \rangle_\eta dz - \int_0^x W_i dx \tag{3.72}$$

The last term on the right–hand side of equation (3.72) is easily integrated with help of equation (3.43b) for the wall–normal component W_i of the interface velocity. Furthermore, equation (3.72) can be rewritten into an expression for δ_1. By taking the limit of $H \to \infty$ the following equation is obtained:

$$\frac{\delta_1}{\delta} = \int_0^\infty \left(1 - \frac{\langle u \rangle_\eta}{U_0}\right) d\eta + \kappa \frac{2\gamma}{\beta_n}\left(\frac{1}{\epsilon_c} - 1\right)\left(1 - \frac{U_i}{U_0}\right) \tag{3.73}$$

The second term on the right–hand side of this equation is new with respect to the common definition for the case of an impermeable wall. It represents the influence of a mass flux across the wall interface on the displacement thickness. Notice that this term is first order in κ, although the wall–normal velocity at the interface is of second order. Up to first order in κ, the expression for δ_1 can be approximated by:

$$\frac{\delta_1}{\delta} = [\eta_\infty - f_0(\eta_\infty)] - \kappa\left[1 - \frac{2\gamma}{\beta_n}\left(\frac{1}{\epsilon_c} - 1\right)\right] + O(\kappa^2) \tag{3.74}$$

where η_∞ is a point far outside the boundary layer. The second term on the right–hand side is the first–order correction on δ_1 for wall permeability. For very large values of $|\beta_n|$, for which the wall–normal interface velocity is negligible, the first–order correction is a reduction of δ_1/δ with κ. When the wall–normal interface velocity is not negligible, the correction in the displacement thickness might be either positive or negative dependent of the values of β_t, β_n and ϵ_c.

The momentum balance for the control volume yields for the loss in momentum flux D per unit volume of the fluid and per unit width of the wall:

$$D \;=\; \rho U_0^2 H - \int_0^{H+\delta_1} \rho \langle u \rangle_\eta^2 dz + \int_0^x \rho W_i U_i dx \tag{3.75}$$

This equation is actually only valid for a flat plate ($\beta_f = 0$), because the presence of a streamwise pressure gradient is ignored. Equation (3.72) can be rewritten into an expression for H. Substituting this into the above equation, and taking again the limit of $H \to \infty$, yields for the total momentum thickness δ_2:

$$\frac{\delta_2}{\delta} \equiv \frac{D}{\rho U_0^2 \delta} = \int_0^\infty \frac{\langle u \rangle_\eta}{U_0}\left(1 - \frac{\langle u \rangle_\eta}{U_0}\right) d\eta - \frac{1}{\delta}\int_0^x \frac{W_i}{U_0}\left(1 - \frac{U_i}{U_0}\right) dx \tag{3.76}$$

The second term on the right–hand side is new with respect to the definition for the case of an impermeable wall.

Up to first order in κ the momentum thickness can be approximated by:

$$\frac{\delta_2}{\delta} = \left[f_0(\eta_\infty) - \int_0^\infty (f_0')^2 d\eta\right] - \kappa\gamma\left[\frac{1}{\beta_n}\left(\frac{1}{\epsilon_c} - 1\right)\right] + O(\kappa^2) \tag{3.77}$$

The second term on the right–hand side is the first–order correction for permeability. Whether δ_2 increases or decreases depends only on β_n. For $\beta_n > 0$, δ_2 decreases, whereas for $\beta_n < 0$, it increases. For very large values of β_n, the first–order correction appears to be negligible.

3.7 Numerical method and results

In this section we briefly discuss the numerical method to solve the Falkner–Skan equation and subsequently some numerical results are shown. Because our order–of–magnitude analysis is essentially valid for only small values of κ, recall the discussion of equation (3.45), we focus on only the first–order effect of permeability.

3.7.1 Numerical method

The Falkner–Skan equation has been solved by means of a standard numerical technique as described by for instance Chow [16] and Cebeci & Bradshaw [15]. The third–order differential equation is rewritten into a set of three first–order differential equations. For the integration in space we use the fourth–order Runge–Kutta scheme. A shooting method is utilized in which the computation is started with an arbitrary guess of f_r''' at $\eta = 0$. This is followed by the numerical integration of the set of first–order differential equations till a point outside the boundary layer. If at this point the velocity does not satisfy the boundary condition given by equation (3.61c), then the guess of f_r''' at $\eta = 0$ is adjusted and the numerical integration starts from the beginning again until finally equation (3.61c) is satisfied. The Newton–Raphson iteration method is employed to obtain a quadratic convergence.

3.7.2 Velocity distributions

Up to first order in κ the dimensionless streamwise velocity is given by:

$$\frac{\langle u\rangle_\eta^s}{U_0} = f_0' + \kappa f_1' + O(\kappa^2) \tag{3.78a}$$

$$\frac{\langle u\rangle_\omega^s}{U_0} = \kappa f_1'(0)\exp\left(\frac{\sqrt{\epsilon_c}}{\gamma}\frac{\eta}{\kappa}\right) + O(\kappa^2) \tag{3.78b}$$

The first term on the right–hand side of (3.78a) is the zeroth–order term (in κ) and represents the streamwise velocity in case of a fully impermeable wall. The second term at the right–hand side of (3.78a) represents the first–order correction for wall permeability. We remark that the term on the right–hand side of (3.78b) is actually only first order in κ when $|\eta|/\kappa \ll 1$, which holds very close to the interface. The streamwise velocity distribution is shown in figure 3.6.a–d for various values of the wedge angle $\pi\beta_f/2$. Positive values of β_f correspond to an accelerating freestream flow, whereas negative values of β_f correspond to a decelerating freestream flow. The case of $\beta_f = -0.1985$ corresponds to a boundary layer which is on the verge of separation with a wall shear stress of almost zero. For clarity the zeroth– and the first–order term are shown separately in 3.6.a and 3.6.b, and summed up in 3.6.c and 3.6.d. The value of κ in the first–order term is put to 0.1, which is in the range for which our order–of–magnitude analysis is expected to be valid. This will be verified later on. In order to plot the velocity profile in the permeable wall,

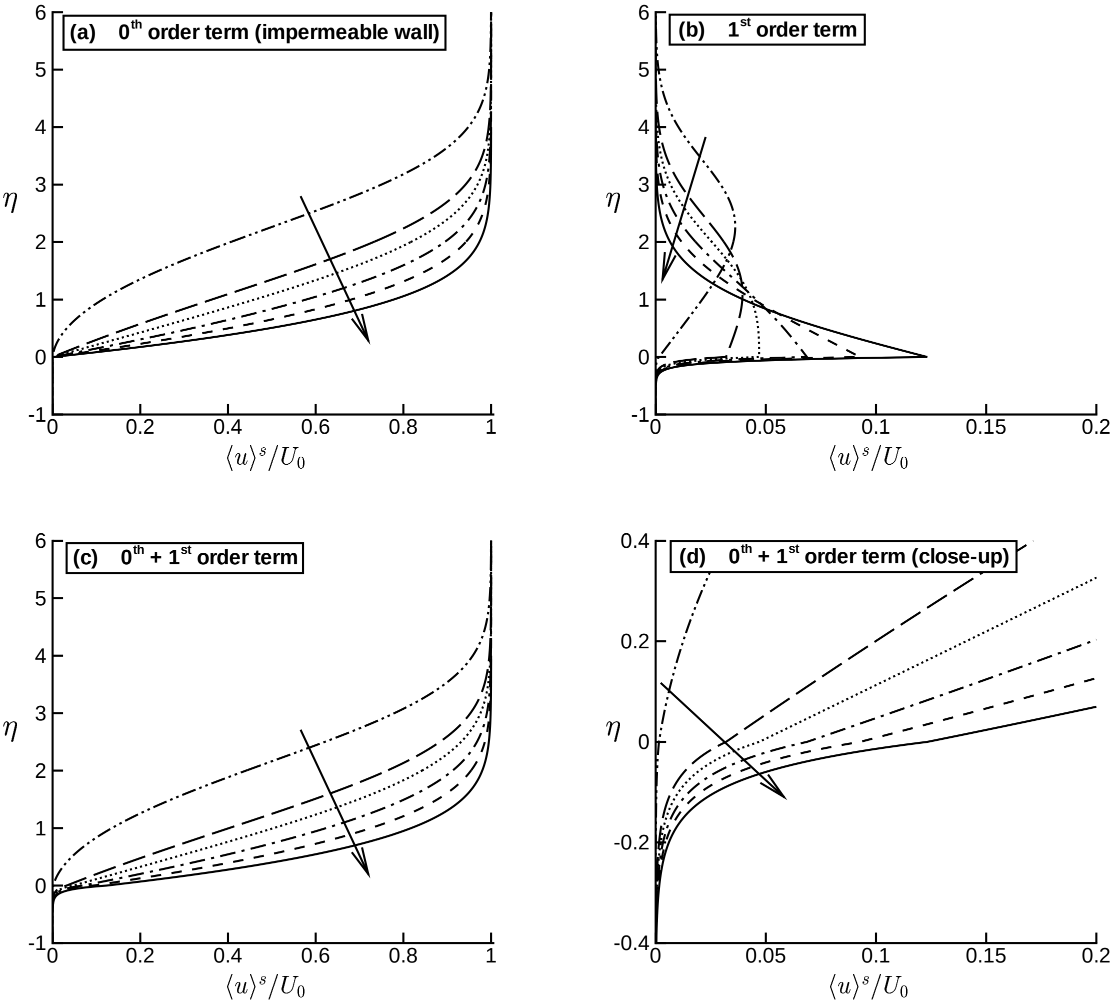

Figure 3.6: Streamwise velocity distribution for various wedge angles. The arrow points in the direction of increasing β_f with values: -0.1985, -0.1, 0, 0.2, 0.5, 1. Value perturbation parameter: $\kappa = 0.1$. Parameters permeable wall: $\epsilon_c = 0.875$ and $\beta_t = 0.45$. (a) 0^{th}–order term (impermeable wall); (b) 1^{st}–order term; (c) sum 0^{th}– and 1^{st}–order term; (d) Close–up sum 0^{th}– and 1^{st}–order term.

we have taken $\epsilon_c = 0.875$ and $\beta_t = 0.45$. The value of β_t was calculated by Breugem et al. [13] from a simulation of Stokes flow in a plane channel with a lower permeable wall that consisted of a 3D Cartesian grid of cubes for which $\epsilon_c = 0.875$ and $K = 0.132\, d_p^2$.
In figure 3.6.b–d it is observed that for all values of β_f shown, the first–order correction for permeability causes a positive streamwise velocity at the wall interface up to about $0.12 \cdot U_0$ for $\beta_f = 1$. This originates from the wall shear stress, which drags the fluid in the permeable wall. The balance between the wall shear stress and the drag force determines the equilibrium value of the interface velocity. Because for larger values of β_f the wall shear stress is larger, the interface velocity increases with β_f. From figure 3.6.b we observe furthermore that if $\beta_f > 0$, then the highest increase in the streamwise

velocity takes place at the interface. If $\beta_f < 0$, then the highest increase in the streamwise velocity takes place further away from the interface. This effect is most pronounced for $\beta_f = -0.1985$, which is somewhat surprising, because in this case the wall shear stress is almost zero and hence one would not expect any influence of wall permeability. This behavior of the perturbation solution is not well understood. Figure 3.6.d shows that the flow inside the permeable wall rapidly decreases till zero. The value of the Brinkman boundary–layer thickness, defined according to equation (3.49), is small: $\delta_B \approx 0.3\delta$.

Of the assumptions in our analysis given by equations (3.44a)–(3.44c), the most restrictive one is the assumption (3.44c) of Stokes flow in the permeable wall. With help of equations (3.62)–(3.63b) and (3.78a), this assumption in combination with assumption (3.44a) leads to the following requirement for the Reynolds number based on U_0 and x:

$$1 \ll \left(\frac{U_0 x}{\nu}\right)^{1/2} \ll \frac{1}{\gamma\kappa^2 f_1'(0)\sqrt{2-\beta_f}} \tag{3.79}$$

For the values of κ, β_t and ϵ_c given before, the right–hand side of this equation is equal to ≈ 1030 when $\beta_f = -0.1985$ and ≈ 130 when $\beta_f = 1$. These values for the upper bound of (3.79) are sufficiently large such that a range of Reynolds numbers does exist for which (3.79) is satisfied.

We now focus on the wall–normal velocity. Up to first order in κ the wall–normal velocity is given by:

$$\frac{\langle w\rangle_\eta^s \delta}{\nu} = \left[-f_0 + (1-\beta_f)\eta f_0'\right] + \kappa\left[-f_1 + (1-\beta_f)\left(f_1 + \eta f_1'\right)\right] + O\left(\kappa^2\right) \tag{3.80a}$$

$$\frac{\langle w\rangle_\omega^s \delta}{\nu} = 0 + O\left(\kappa^2\right) \tag{3.80b}$$

The wall–normal velocity in the permeable wall is of second order in κ and therefore negligible. The wall–normal velocity distribution is shown in figure 3.7 for various values of β_f. For clarity distinction is made between the zeroth–order term and the first–order correction for permeability with $\kappa = 0.1$. The first–order correction for wall permeability is small compared to the zeroth–order term, and therefore we do not show the sum of the two terms, because differences with figure 3.7.a would be hardly discernible. Notice that the wall–normal velocity is made dimensionless with ν/δ instead of U_0 like for the streamwise velocity. Therefore it seems that the wall–normal velocity is quite large, but for large values of $\sqrt{U_0 x/\nu}$ the wall–normal velocity is actually much smaller than the streamwise velocity.

Figure 3.7.a shows an interesting behavior for large values of η. In the limit of $\eta \to \infty$ the wall–normal velocity becomes infinite, except for the case that $\beta_f = 0$. Of course an infinite wall–normal velocity is physically not realistic. Besides, the linearly increasing or decreasing wall–normal velocity for larger z (respectively for $\beta_f < 0$ and $\beta_f > 0$) is accompanied by extremely large values for $\langle w\rangle_\eta \partial\langle w\rangle_\eta/\partial z$. This contradicts equation (3.39b) in which this term was neglected. This singularity originates from the choice of the length scale δ for wall–normal variations in the flow. While this is true inside the Prandtl

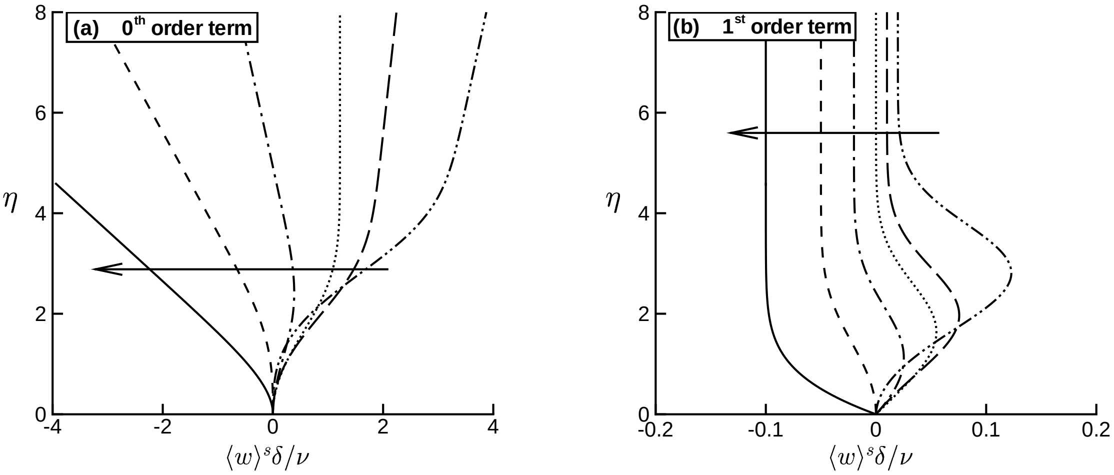

Figure 3.7: Wall-normal velocity distribution for various wedge angles. The arrow points in the direction of increasing β_f with values: -0.1985, -0.1, 0, 0.2, 0.5, 1. (a) 0^{th}–order term (impermeable wall); (b) 1^{st}–order term with $\kappa = 0.1$.

boundary layer, this is not true far outside the boundary layer where the characteristic length scale is much larger. Thus the wall–normal velocity distribution is actually only valid inside the boundary layer. In figure 3.7.b we observe that in the top region of the boundary layer the first–order correction is a constant negative wall–normal velocity for $\beta_f > 0$ and a constant positive wall–normal velocity for $\beta_f < 0$. This can be explained by the fact that when $\beta_f > 0$ the streamwise flow accelerates and hence this must be accompanied by a negative wall–normal velocity to satisfy mass conservation. When $\beta_f < 0$ the streamwise flow decelerates and the wall–normal velocity must therefore be positive.

3.7.3 Shear stress distribution

Up to first order in κ the intrinsic shear stress is given by:

$$\frac{\partial \langle u \rangle_\eta}{\partial z} \frac{\delta}{U_0} = f_0'' + \kappa f_1'' + O(\kappa^2) \tag{3.81a}$$

$$\frac{\partial \langle u \rangle_\omega}{\partial z} \frac{\delta}{U_0} = \frac{f_1'(0)}{\gamma \sqrt{\epsilon_c}} \exp\left(\frac{\sqrt{\epsilon_c}\eta}{\gamma\kappa}\right) + \kappa \left[\frac{f_1''(0)}{\gamma \epsilon_c} + \frac{\beta_f \beta_t}{\sqrt{\epsilon_c}}\right] \exp\left(\frac{\sqrt{\epsilon_c}\eta}{\gamma\kappa}\right) + O(\kappa^2) \tag{3.81b}$$

where the shear stress is made dimensionless by $\mu U_0/\delta$. Notice that the first term on the right–hand side of (3.81b) is a zeroth–order term in the limit of $\eta/\kappa \to 0$. However, this term goes to zero when the wall is impermeable, because in the limit of $\kappa \to 0$, $\eta/\kappa \to -\infty$. The intrinsic shear stress distribution is shown in figure 3.8 for various wedge angles. For clarity the zeroth– and the first–order term are shown separately. As before for the velocity distributions we have taken $\kappa = 0.1$, $\epsilon_c = 0.875$ and $\beta_t = 0.45$. The

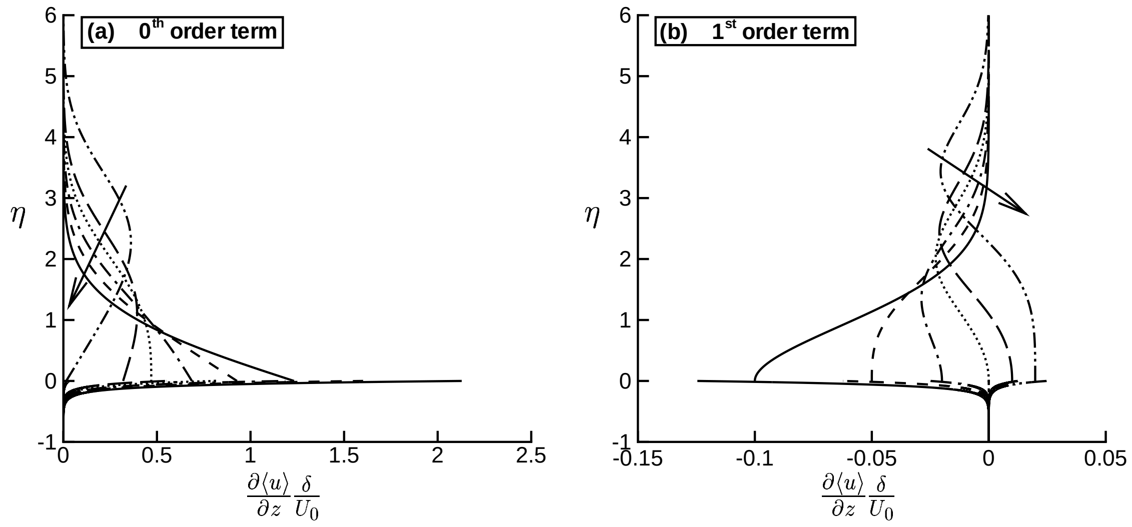

Figure 3.8: Shear stress distribution for various wedge angles. The arrow points in the direction of increasing β_f with values: -0.1985, -0.1, 0, 0.2, 0.5, 1. Parameters permeable wall: $\epsilon_c = 0.875$ and $\beta_t = 0.45$. (a) 0^{th}–order term; (b) 1^{st}–order term with $\kappa = 0.1$.

jump in the intrinsic shear stress at the wall interface is clearly visible in figure 3.8. In figure 3.8.b we observe that for $\eta \gtrsim 2$, the first–order correction is negative for all values of β_f. This implies that viscous effects become more confined to the wall when the wall is permeable. Furthermore, figure 3.8.b shows that the first–order correction for the wall shear stress is negative for $\beta_f > 0$ and positive for $\beta_f < 0$. Thus for $\beta_f > 0$ the flow over a permeable wall experiences less skin friction compared to an impermeable wall. The decrease amounts approximately 8 % for $\beta_f = 1$. Furthermore, because wall permeability increases the wall shear stress for $\beta_f < 0$, boundary–layer separation is delayed towards lower values of β_f. Apparently, a boundary layer over a permeable wall is able to sustain a larger positive pressure gradient compared to the boundary layer over an impermeable wall.

3.8 Summary and discussion

In our analysis we have distinguished two boundary layers lying on top of each other: the Prandtl boundary layer above the permeable wall, and the Brinkman boundary layer inside the permeable wall. The former is described by the balance between inertial and viscous forces. The latter is described by the balance between diffusion of momentum from the Prandtl boundary layer into the permeable wall on the one hand and the drag force inside the permeable wall on the other hand. Based on an order–of–magnitude analysis of the VANS equations the constraints for the validity of the boundary–layer equations are found to be: a) a low wall permeability; b) a low Reynolds number for the flow inside the permeable wall; c) a sufficiently high Reynolds number for the flow outside the permeable wall.

The analytical solution for the Brinkman boundary layer in combination with the OTW interface conditions is used to derive a closed system of equations for the Prandtl boundary layer. For the stream function of the flow in the Prandtl boundary layer a power series expansion in the perturbation parameter κ is adopted, where κ can be interpreted as the ratio of the Brinkman to the Prandtl boundary–layer thickness. A generalization of the Falkner–Skan equation is found, which describes a self–similar boundary layer past a permeable wedge. The κ parameter is comparable to the inverse of the σ parameter in the channel flow studies of Beavers & Joseph [5] and Ochoa-Tapia & Whitaker [68]. In these studies σ is defined as the ratio of the channel height H to the Brinkman screening distance $\sqrt{K}$. Wall permeability has only significant influence on the flow field when κ is sufficiently large or σ is sufficiently small.

The definitions of the displacement and the momentum thickness have been modified to include the effect of wall permeability. For large values of the normal stress–jump parameter β_n and thus a negligible wall–normal interface velocity, the first–order effect of permeability is a decrease in the displacement height. When the wall–normal interface velocity is not neglected, the first–order correction in the displacement thickness is either an increase or a decrease dependent of the values of the porosity ϵ_c and the stress–jump parameters β_t and β_n. For the case of a flat plate, the first–order correction of permeability on the momentum thickness depends only on the value of β_n. For $\beta_n < 0$ it increases, whereas for $\beta_t > 0$ it decreases. For large values of $|\beta_n|$ and hence when the wall–normal interface velocity is negligible, the momentum thickness is unchanged up to first order in κ.

The numerical results showed that the first–order effect of permeability causes a positive streamwise velocity at the interface of and inside the permeable wall. The appearance of a wall–normal interface velocity is a second–order effect. Furthermore, wall permeability causes that viscous effects get more confined to the wall. It is also observed that wall permeability causes a decrease in the wall shear stress when the freestream flow accelerates ($\beta_f > 0$), but an increase in the wall shear stress when the freestream flow decelerates ($\beta_f < 0$). In general, both effects are favorable for boundary layers, as in the former case the skin friction decreases and in the latter case separation is delayed to a larger positive pressure gradient as compared to a fully impermeable wall.

Our analysis is essentially valid for only small values of κ and therefore we examined only the first–order correction for permeability. Furthermore we considered only positive values of κ. In the OTW interface model the value of β_t might in principle be larger than $1/\sqrt{\epsilon_c}$ and this would then lead to a negative value of κ. However, this would then not produce physically realistic results, because a negative value of κ would predict a negative streamwise interface velocity. For qualitatively meaningful results the value of β_t should therefore be smaller than $1/\sqrt{\epsilon_c}$. For an accurate quantitative prediction it is furthermore required that the value of β_t is such that the prediction velocity resembles as closely as possible the 'true' velocity profile like sketched in figure 3.3.

Chapter 4

Direct Numerical Simulations of laminar flow over and through a permeable wall consisting of a 3D Cartesian grid of cubes [1]

Abstract *In this chapter, we investigate the closure problem for the drag force in the Volume–Averaged Navier–Stokes equations for flow through a porous medium. Two different kinds of simulations have been performed. The first kind of simulations concerns flow through a fully periodic 3D Cartesian grid of cubes. An Immersed Boundary Method has been successfully applied to enforce the no–slip and no–penetration conditions on the cubes. A closure for the drag force is proposed based on the Irmay [37] and the Burke–Plummer model [7] for the low and high Reynolds–number range respectively, of which the coefficients are determined from these simulations. The second kind of simulations concerns Stokes flow in a plane channel with a permeable bottom wall consisting of the same grid of cubes, which is however now only fully periodic in the horizontal directions. The computed velocity field has been volume averaged using the cellular filter proposed by Quintard & Whitaker [75] for ordered porous media. The permeable wall can be divided into a homogeneous porous region with a constant porosity and a small interface region with a height–dependent porosity. Two momentum–transfer models have been evaluated for the drag force in the interface region: the model of Ochoa–Tapia & Whitaker [68] (OTW model), which has been used in the previous chapter, and a variable–permeability model. The approximate solution for the velocity profile based on the OTW model is in good agreement with the simulation results. However, the value of the tangential stress–jump parameter in this model appears to be very sensitive to the definition of the wall interface. A variable–permeability model has been proposed based on the aforementioned Irmay model, which relates the permeability in the interface region to the local value of*

---

[1] This chapter is an extended version of a paper presented at the *International Conference on Applications of Porous Media 2004* [13].

the porosity. This model agrees not very well with the simulation data, which is possibly connected to a lower effective viscosity of the volume–averaged flow field as compared to the viscosity of the unfiltered flow field.

4.1 Introduction

A permeable wall can be defined as a rigid porous wall with interconnected pores through which fluid may flow, interacting with the flow outside the wall. Examples are flows over plant canopies and flows in rivers with a bed of stones or pebbles. The understanding of the influence of wall permeability on the flow dynamics and structure is crucial for the development of accurate models for e.g. the exchange of oxide and carbon dioxide between a forest and the atmosphere or the erosion of a river bed.

A permeable wall can be modeled numerically in several ways. Hahn et al. [32] performed Direct Numerical Simulations (DNS) of *turbulent* flow in a plane channel with a lower permeable wall. The effect of wall permeability was incorporated in boundary conditions proposed originally by Beavers and Joseph [5] for *laminar* flow over a permeable wall. These boundary conditions allow for a slip velocity parallel to the wall, with a slip coefficient that has to be specified, whereas the wall–normal velocity is put to zero. Another approach was followed by Breugem and Boersma [9], who performed a DNS of the same flow, but they simulated the flow inside the permeable wall as well. For describing the flow inside the permeable wall, a continuum approach was adopted based on the Volume–Averaged Navier–Stokes (VANS) equations [104]. A major advantage of this approach is that no boundary conditions need to be specified at the interface with the permeable wall. The main difficulty that is encountered in this approach, is that closures are required for the subfilter–scale stress and the drag force in order to solve the VANS equations. This problem motivated the present study, in which we investigate numerically the closure problem for the drag force experienced by flow through a 3D Cartesian grid of cubes. Two different kinds of DNS are performed. The first kind of simulations concerns flow through a fully periodic Cartesian grid of cubes. The second kind of simulations concerns Stokes flow in a plane channel with a permeable bottom wall consisting of the same grid of cubes, which is now however only fully periodic in the horizontal directions. The permeable wall can be divided into a homogeneous porous region with a constant porosity and a small interface region with a spatially varying porosity. The topology of the interface region is heterogeneous and thus different from the homogeneous porous region. Special attention is paid to the modeling of the drag force in the interface region.

This paper is organized as follows. First a brief introduction is given to the Volume–Averaging Method and the VANS equations. The next section presents a theoretical investigation of the closure problem for the drag force experienced by flow through a fully periodic 3D Cartesian grid of cubes. Thereafter a description is given of the numerical method that is used in the DNS. Separate simulations of uniform flow through the aforementioned grid of cubes have been performed to evaluate the closure for the drag force. Results are then shown for Stokes flow in a plane channel with a lower permeable wall consisting of the same grid of cubes. The last section gives a summary and a discussion.

4.2 Volume–Averaging Method and VANS equations

The Volume–Averaging Method provides the theoretical basis for a continuum approach for flows in porous media. In this method the flow is averaged over a small spatial volume such that the volume–averaged flow field is continuous in space, i.e. it is defined in the fluid as well as in the solid phase. The volume–averaged velocity can be defined mathematically as:

$$\langle \mathbf{u} \rangle^s_{\mathbf{x}} \equiv \int_V \gamma(\mathbf{r})\, m(\mathbf{r}-\mathbf{x})\, \mathbf{u}(\mathbf{r})\, dV \tag{4.1}$$

where the brackets $\langle ... \rangle^s$ with the superscript s denote the *superficial* volume average, the subscript $\mathbf{x}$ means that the volume average is evaluated at the centroid $\mathbf{x}$ of the averaging volume V, γ is the phase–indicator function that equals unity when the vector $\mathbf{r}$ points in the fluid phase and equals zero when $\mathbf{r}$ points in the solid phase, and m is a weighting function. The weighting function must satisfy the normalization condition:

$$\int_V m(\mathbf{y}) dV = 1 \tag{4.2}$$

In principle the weighting function can be chosen freely, but it is desirable that the filtered flow field has negligible variations inside the averaging volume. For an ordered porous

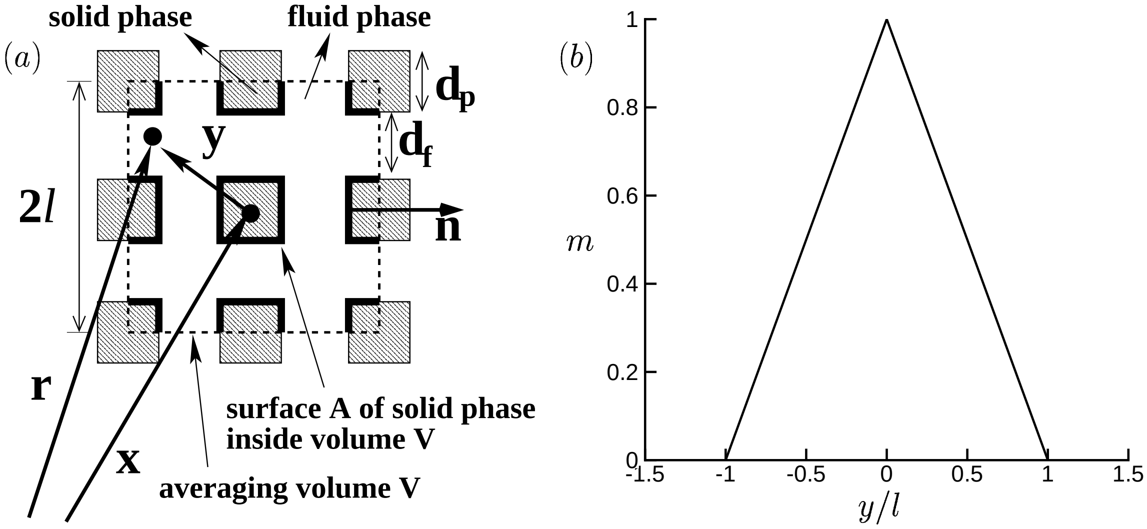

Figure 4.1: The averaging volume (a) and the weighting function (b) of the cellular filter for flows through ordered porous media.

medium, which is characterized by a unit cell that can be extended periodically, Quintard & Whitaker [75] proposed the following weighting function:

$$m(\mathbf{y}) = \begin{cases} \prod_{i=1}^{3}\left(l_i - |y_i|\right)/l_i^2 & , |y_i| \leq l_i \\ 0 & , |y_i| > l_i \end{cases} \tag{4.3}$$

where l_i represents the length of the unit cell in direction i. Figure 4.1 illustrates the above averaging volume and weighting function, which is referred to as the *cellular* filter. The velocity at an arbitrary point in a porous medium can be decomposed in a contribution from the volume–averaged velocity at this point and a subfilter–scale velocity according to:

$$\mathbf{u} = \langle\mathbf{u}\rangle + \tilde{\mathbf{u}} \tag{4.4}$$

where $\langle\mathbf{u}\rangle \equiv \langle\mathbf{u}\rangle^s/\epsilon$ is the *intrinsic* volume–averaged velocity, with ϵ the porosity or void fraction. According to equation (4.1) the porosity is defined as:

$$\epsilon \equiv \int_V \gamma(\mathbf{r})\, m(\mathbf{r}-\mathbf{x})\, dV \tag{4.5}$$

Application of the volume–averaging operator $\langle ... \rangle^s$ to the Navier–Stokes equations yields the VANS equations [104]:

$$\frac{\partial\langle\mathbf{u}\rangle^s}{\partial t} + \nabla\cdot\left[\frac{\langle\mathbf{u}\rangle^s\langle\mathbf{u}\rangle^s}{\epsilon}\right] + \nabla\cdot\left[\epsilon\boldsymbol{\tau}\right] = -\frac{1}{\rho}\nabla\langle p\rangle^s + \nu\nabla^2\langle\mathbf{u}\rangle^s + \epsilon\,\mathbf{f} \tag{4.6a}$$

$$\nabla\cdot\langle\mathbf{u}\rangle^s = 0 \tag{4.6b}$$

where $\boldsymbol{\tau}$ is the subfilter–scale stress and $\mathbf{f}$ is the drag force. They are defined according to:

$$\boldsymbol{\tau} \equiv \langle\mathbf{u}\mathbf{u}\rangle - \langle\mathbf{u}\rangle\langle\mathbf{u}\rangle \tag{4.7a}$$

$$\mathbf{f} \equiv \frac{1}{\epsilon}\int_A m\mathbf{n}\left[-\mathbf{I}\frac{p}{\rho} + \nu\nabla\mathbf{u}\right] dA \tag{4.7b}$$

where $\mathbf{I}$ is the unit tensor, A is the contact area between the solid and the fluid phase inside the averaging volume V, and $\mathbf{n}$ is the unit normal at A that points from the fluid into the solid phase. Irrespective the filter used, the VANS equations as given above are exact for Newtonian and incompressible flows through rigid porous media.

The VANS equations can be simplified when the volume–averaged flow is well–behaved [30], which means that it contains negligible variations on a distance smaller than the dimensions of the averaging volume: $\langle\langle\mathbf{u}\rangle\rangle \approx \langle\mathbf{u}\rangle$ and $\langle\tilde{\mathbf{u}}\rangle \approx \mathbf{0}$. This then justifies to take volume–averaged quantities out of volume and surface integrals. Equations (4.7a) and (4.7b) can then be approximated by [104]:

$$\boldsymbol{\tau} \approx \langle\tilde{\mathbf{u}}\tilde{\mathbf{u}}\rangle \tag{4.8a}$$

$$\mathbf{f} \approx -\frac{1}{\epsilon}\nabla\epsilon\cdot\left[-\frac{\langle p\rangle}{\rho}\mathbf{I} + \nu\nabla\langle\mathbf{u}\rangle\right] + \frac{1}{\epsilon}\int_A m\mathbf{n}\left[-\frac{\tilde{p}}{\rho}\mathbf{I} + \nu\nabla\tilde{\mathbf{u}}\right] dA \tag{4.8b}$$

In order to solve the VANS equations, closures are needed for the subfilter–scale stress as well as for the drag force in terms of the volume–averaged velocity. The next section presents a theoretical investigation of the closure problem for the drag force.

4.3 Closure problem for the drag force

In this section a discussion is given of the closure problem for the drag encountered by flow through a *fully periodic* 3D Cartesian grid of cubes as illustrated in figure 4.2. For a stationary and uniform volume–averaged flow through a *homogeneous* porous medium, the VANS equations reduce to:

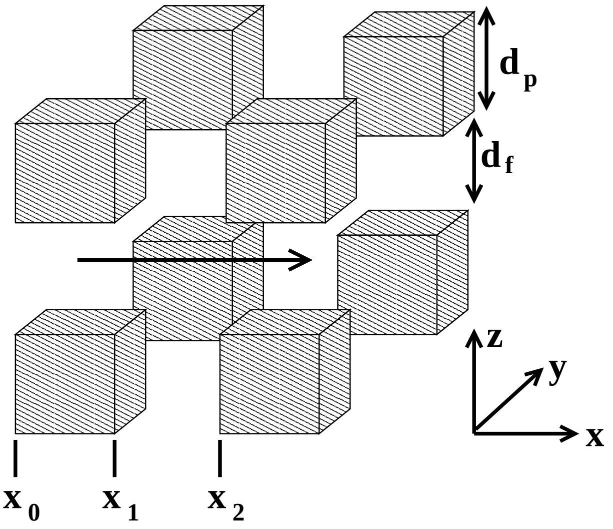

Figure 4.2: Flow through a fully periodic 3D Cartesian grid of cubes. The direction of the volume–averaged flow is parallel to the x–axis.

$$0 = -\frac{1}{\rho}\nabla\langle p\rangle + \frac{1}{\epsilon}\int_A m\mathbf{n}\left[-\frac{\tilde{p}}{\rho}\mathbf{I} + \nu\nabla\tilde{\mathbf{u}}\right] dA \tag{4.9}$$

Whitaker [104] gave theoretical support to the following parameterization of the surface integral in the above equation:

$$\frac{1}{\epsilon}\int_A m\mathbf{n}\left[-\frac{\tilde{p}}{\rho}\mathbf{I} + \nu\nabla\tilde{\mathbf{u}}\right] dA = -\nu\mathbf{K}^{-1}\langle\mathbf{u}\rangle^s - \nu\mathbf{K}^{-1}\mathbf{F}\langle\mathbf{u}\rangle^s \tag{4.10}$$

where **K** and **F** are respectively the permeability and the Forchheimer tensor. In general, the Forchheimer tensor depends on the Reynolds number, on the geometrical parameters of the porous medium and on the direction of the volume–averaged flow. For sufficiently high Reynolds numbers, the first term on the right–hand side of (4.10) may be neglected. For sufficiently small Reynolds numbers, the Forchheimer term can be neglected and equation (4.9) then reduces to the well–known Law of Darcy [4] for Stokes flow through a porous medium:

$$0 = -\frac{1}{\rho}\nabla\langle p\rangle - \nu\mathbf{K}^{-1}\langle\mathbf{u}\rangle^s \tag{4.11}$$

For all porous media, the permeability tensor is a symmetric second–order tensor [4],[104]. The 3D Cartesian grid of cubes falls in the class of spherically isotropic porous media [33] for which the permeability tensor is isotropic: $\mathbf{K} = K\mathbf{I}$. (The proof of isotropy is based on the linearity of the Stokes equations and the symmetry properties of the grid of cubes.) Let us now derive expressions for the permeability and the Forchheimer tensor for the grid of cubes sketched in figure 4.2. The porosity of the grid of cubes is equal to:

$$\epsilon = 1 - \frac{1}{(1 + d_f/d_p)^3} \tag{4.12}$$

Below we consider the case of a very small, a very high and an intermediate value for the porosity, respectively.

- **Very small porosity**

In the limit of an almost zero porosity, the ratio d_f/d_p is very small. The flow in between positions x_0 and x_1 in figure 4.2 can then be approximated by plane channel flow.
To derive an expression for the permeability, we assume that the Reynolds number $U_b d_f/\nu$, with U_b the bulk velocity, is small. In this case the pressure drop between x_0 and x_1 is easily calculated from the Stokes equations:

$$0 = -\frac{1}{\rho}\left[\frac{p_1 - p_0}{d_p}\right] - \nu\frac{12}{d_f^2}U_b \tag{4.13}$$

The bulk velocity can be related to the superficial volume–averaged velocity $\langle u\rangle^s$ according to:

$$U_b \approx \langle u\rangle^s \left[\frac{(d_p + d_f)^2}{(d_p + d_f)^2 - d_p^2}\right] \tag{4.14}$$

Because $d_f/d_p \ll 1$, the pressure drop between x_1 and x_2 may be neglected. Consequently, the pressure drop between x_0 and x_1 is approximately equal to:

$$\frac{p_1 - p_0}{d_p} \approx \left[\frac{p_2 - p_0}{d_p + d_f}\right]\left[\frac{d_p + d_f}{d_p}\right] = \frac{\partial\langle p\rangle}{\partial x}\left[\frac{d_p + d_f}{d_p}\right] \tag{4.15}$$

Substituting the above two equations into equation (4.13) yields:

$$0 = -\frac{1}{\rho}\frac{\partial\langle p\rangle}{\partial x} - \nu\left(\frac{12}{d_f^2}\left[\frac{d_p}{d_p + d_f}\right]\left[\frac{(d_p + d_f)^2}{(d_p + d_f)^2 - d_p^2}\right]\right)\langle u\rangle^s \tag{4.16}$$

From the comparison of this equation with Darcy's Law (4.11), we find for the permeability:

$$\begin{aligned} K &= \frac{d_f^2}{12}\left[\frac{(d_p + d_f)^2 - d_p^2}{(d_p + d_f)^2}\right]\left[\frac{d_p + d_f}{d_p}\right] \\ &= \frac{\left[1 - (1 - \epsilon)^{1/3}\right]^3\left[1 + (1 - \epsilon)^{1/3}\right]}{12(1 - \epsilon)}d_p^2 \ , \quad \epsilon \ll 1 \end{aligned} \tag{4.17}$$

We now derive an expression for the diagonal components of $\mathbf{F}$. Because of the symmetry properties of the grid of cubes, the non–diagonal components of the Forchheimer tensor $\mathbf{F}$ are zero.
The pressure drop between x_0 and x_1 can be written as:

$$\left[\frac{p_1 - p_0}{d_p}\right] = -\frac{\rho U_b^2}{d_f} f_c \tag{4.18}$$

where f_c is the friction factor or skin friction coefficient. The friction factor depends on the Reynolds number $U_b d_f/\nu$ and the relative surface roughness height k/d_f. We assume that the Reynolds number $U_b d_f/\nu$ is large, such that the flow is fully turbulent.
If the cubes are dynamically smooth, i.e. k/d_f sufficiently small, then the friction factor is equal to [22]:

$$f_c \;=\; 0.073\left(\frac{U_b d_f}{\nu}\right)^{-1/4} \tag{4.19}$$

Substituting equations (4.14), (4.15) and (4.19) into equation (4.18) and rewriting the result, yields:

$$0 \;=\; -\frac{1}{\rho}\frac{\partial\langle p\rangle}{\partial x} - \frac{\nu\langle u\rangle^s}{K}\left(0.073\left[\frac{\langle u\rangle^s d_f}{\nu}\right]^{3/4}\left[\frac{d_p}{d_p+d_f}\right]\left[\frac{(d_p+d_f)^2}{(d_p+d_f)^2-d_p^2}\right]^{7/4}\frac{K}{d_f^2}\right) \tag{4.20}$$

Using equation (4.17) for the permeability, we obtain the following estimate for F_{xx} in the dynamically smooth regime:

$$\begin{aligned} F_{\mathrm{xx}} &= \frac{0.073}{12}\left[\frac{\langle u\rangle^s d_p}{\nu}\right]^{3/4}\left[\left(\frac{d_p}{d_p+d_f}\right)\left(1+\frac{d_p}{d_p+d_f}\right)\right]^{-3/4} \\ &= \frac{0.073}{12}\left[\frac{\langle u\rangle^s d_p}{\nu}\right]^{3/4}\left[(1-\epsilon)^{1/3}\left(1+(1-\epsilon)^{1/3}\right)\right]^{-3/4}\;,\ \epsilon\ll 1\,,\ \frac{k}{d_f}\ \text{small} \end{aligned} \tag{4.21}$$

The expressions for F_{yy} and F_{zz} are similar to F_{xx}, with $\langle u\rangle^s$ replaced by respectively $\langle v\rangle^s$ and $\langle w\rangle^s$.
If the cubes are dynamically rough, i.e. k/d_f sufficiently large, then the friction factor is equal to:

$$f_c \;=\; C \tag{4.22}$$

with C a constant depending on the ratio k/d_f. Similarly, we find the following estimate for F_{xx} in the dynamically rough regime:

$$F_{\mathrm{xx}} \;=\; \frac{C}{12}\left[\frac{\langle u\rangle^s d_p}{\nu}\right]\left[(1-\epsilon)^{1/3}\left(1+(1-\epsilon)^{1/3}\right)\right]\;,\ \epsilon\ll 1\,,\ \frac{k}{d_f}\ \text{large} \tag{4.23}$$

- **Very high porosity**

In the limit of the porosity close to unity, the flow near a cube is not influenced by the presence of other cubes and a closure for the drag force can be estimated from the drag force for flow around a single cube:

$$\int_A \mathbf{n}\cdot[-p\mathbf{I}+\mu\nabla\mathbf{u}]\,dA = -f_c\,d_p^2\frac{1}{2}\rho|\mathbf{U}_\infty|\mathbf{U}_\infty \tag{4.24}$$

where f_c is the friction factor for a single cube, which is a function of the Reynolds number $|\mathbf{U}_\infty|d_p/\nu$ and the direction of the far–field velocity $\mathbf{U}_\infty$.

For flow through a grid of cubes with a very high porosity, the far–field velocity may be estimated by $\langle\mathbf{u}\rangle^s$. For $d_p/d_f \ll 1$, we may approximate equation (4.9) by:

$$0 \;=\; -\frac{1}{\rho}\nabla\langle p\rangle + \frac{1}{\epsilon l^3\rho}\int_A \mathbf{n}\cdot[-p\mathbf{I}+\mu\nabla\mathbf{u}]\,dA \tag{4.25}$$

with l the dimension of the unit cell and where the integral is now carried out over the surface area of a single cube. Substituting equation (4.24) into equation (4.25) and rewriting the result, yields:

$$0 \;=\; -\frac{1}{\rho}\nabla\langle p\rangle - \left[\left(\frac{1-\epsilon}{\epsilon}\right)\left(\frac{f_c}{2d_p^2}\right)\left(\frac{|\langle\mathbf{u}\rangle^s|d_p}{\nu}\right)\right]\nu\langle\mathbf{u}\rangle^s \tag{4.26}$$

To derive an expression for the permeability, we assume that the Reynolds number $|\langle\mathbf{u}\rangle^s|d_p/\nu$ is sufficiently small such that the flow is in the Stokes regime. Because a cube is spherically isotropic [33] (p. 187), the friction factor is independent of the flow direction in the Stokes regime. Furthermore, Batchelor [3] (p. 239) shows that in the Stokes regime the friction factor is inversely proportional to the Reynolds number:

$$f_c = C\left(\frac{\nu}{d_p|\mathbf{U}_\infty|}\right) \quad , \quad Re \ll 1 \tag{4.27}$$

with C a constant. Substituting this equation into (4.26) yields for the permeability:

$$K \;=\; \frac{2d_p^2}{C}\left[\frac{\epsilon}{1-\epsilon}\right] \quad , \quad 1-\epsilon \ll 1 \tag{4.28}$$

We now derive an expression for the Forchheimer tensor $\mathbf{F}$. As mentioned before, the non–diagonal components of $\mathbf{F}$ are zero. An equation for the tensor component F_{xx} is found from equation (4.26):

$$\begin{aligned} F_{\mathrm{xx}} \;&=\; \left(\frac{1-\epsilon}{\epsilon}\right)\left(\frac{f_c}{2}\right)\left(\frac{|\langle\mathbf{u}\rangle^s|d_p}{\nu}\right)\left(\frac{K}{d_p^2}\right) \\ &=\; \left[\frac{|\langle\mathbf{u}\rangle^s|d_p}{\nu}\right]\frac{f_c}{C} \quad , \quad 1-\epsilon \ll 1 \end{aligned} \tag{4.29}$$

where we made use of equation (4.28) for K and f_c is the friction factor dependent of $\langle \mathbf{u} \rangle^s / |\langle \mathbf{u} \rangle^s|$ and $|\langle \mathbf{u} \rangle^s| d_p/\nu$. For flow around a single sphere, the friction factor is almost constant over a wide range of Reynolds numbers [7]. This behavior is expected for a cube as well, which then implies that F_{xx} is proportional to $|\langle \mathbf{u} \rangle^s| d_p/\nu$.

- **Intermediate range of porosities**

The above derived closures for the permeability and the Forchheimer tensor are less accurate in the range of intermediate porosities, say $0.1 \lesssim \epsilon \lesssim 0.9$. We expect intuitively that in this range of porosities, the flow through the grid of cubes has more resemblance to channel flow than to flow around a single cube.

For sufficiently small Reynolds numbers, such that the flow is in the Stokes regime, the pressure loss between x_1 and x_2 in figure 4.2 may still be small compared to the pressure loss between x_0 and x_1. For this reason, we adopt equation (4.17) as a model for the permeability in the intermediate range of the porosities as well:

$$K = \frac{\left[1-(1-\epsilon)^{1/3}\right]^3 \left[1+(1-\epsilon)^{1/3}\right]}{C_K(1-\epsilon)} d_p^2 \tag{4.30}$$

where C_K is a (probably weak) function of the porosity, with $C_K = 12$ for $\epsilon \to 0$.

For large Reynolds numbers, i.e. when the flow is turbulent, the pressure loss between x_1 and x_2 may be substantial compared to the pressure loss between x_0 and x_1 as a consequence of turbulent diffusion. Therefore equation (4.21) for the Forchheimer tensor is probably not accurate for the intermediate range of porosities.

For packed beds the Burke–Plummer equation appears to be successful. A derivation of this equation, which is equivalent to the non–linear part of the Ergun equation, is given by Bird et al. [7]. Although a Cartesian grid of cubes is quite different from a packed bed, we will adopt this equation as a model for the Forchheimer tensor in the intermediate range of porosities. According to this model the Forchheimer tensor is isotropic, $\mathbf{F} = F\mathbf{I}$, with F equal to:

$$F = C_F \left(\frac{1-\epsilon}{\epsilon^3}\right) \left(\frac{|\langle \mathbf{u} \rangle^s| d_p}{\nu}\right) \left(\frac{K}{d_p^2}\right) \tag{4.31}$$

where K is given by equation (4.30), and C_F is a constant equal to approximately 1.8 for many different kinds of packed beds [61].

For an accurate determination of the values of C_K and C_F, detailed numerical computations have been performed at a porosity of $\epsilon = 0.875$. This will be discussed in section 4.5.

4.4 Numerical method

This section deals with the numerical method that is used in the simulations. The full Navier–Stokes equations are solved on a fully staggered and uniform Cartesian mesh.

For the spatial discretization of the equations the finite–volume method is used with the second–order central–differencing scheme. The following second–order pressure–correction scheme is used:

$$\frac{\hat{u}_i - u_i^n}{\Delta t} = \frac{5}{4} g_i^n - \frac{1}{4} g_i^{n-2} - \frac{1}{\rho}\frac{dP}{dx}\delta_{i1} \tag{4.32a}$$

$$\frac{1}{\rho}\frac{\partial^2 \hat{p}}{\partial x_i^2} = \frac{1}{\Delta t}\frac{\partial \hat{u}_i}{\partial x_i} \tag{4.32b}$$

$$u_i^{n+1} = \hat{u}_i - \frac{\Delta t}{\rho}\frac{\partial \hat{p}}{\partial x_i} \tag{4.32c}$$

$$p^{n+1} = p^n + \hat{p} \tag{4.32d}$$

where $\hat{u}_i$ is the prediction velocity, dP/dx the constant pressure gradient that drives the flow, and $\hat{p}$ the correction pressure. The function g_i in equation (4.32a) is given by:

$$g_i = -\frac{1}{\rho}\frac{\partial p}{\partial x_i} - \frac{\partial u_i u_j}{\partial x_j} + \nu \frac{\partial^2 u_i}{\partial x_j^2} + f_i \tag{4.33}$$

For the implementation of the cubes an Immersed Boundary Method (IBM) ([25] and references therein) is used. In this method forces are added to the flow field, i.e. to the right–hand side of equation (4.33), to accomplish a zero velocity on the cubes. This is illustrated in figure 4.3.

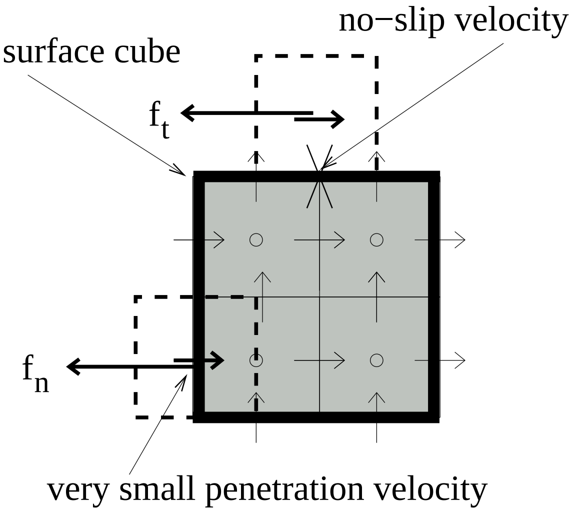

Figure 4.3: Illustration of the IBM in which forces (indicated by f_t and f_n) are applied at mesh points close or on the surface of the cube to enforce the no–slip and no–penetration conditions. The horizontal and vertical arrows mark the mesh points of the streamwise and wall–normal velocity respectively, whereas the circles indicate the mesh points of the pressure.

The main benefits of the IBM are that no boundary conditions have to be imposed on the cubes and the ability of using fast FFT–based solvers for equation (4.32b). The particular IBM that is used here, is similar to the one developed by Fadlun et al. [25]. An advantage in applying the IBM in the present study over the problems discussed by Fadlun et al., which concern rather complicated geometries, is that the cubes can be aligned along the mesh such that their surfaces coincide with mesh points for the normal (with respect to the surface) velocity. This enables an exact implementation of the no–slip boundary condition on the cubes:

$$\mathbf{u} \times \mathbf{n} = \mathbf{0} \tag{4.34a}$$

Thus we are able to compute the force f_t in figure 4.3 such that the flow experiences a no–slip condition at the position of the cross.

In our IBM the no–penetration condition for the normal velocity on the cube is enforced by putting the prediction velocity to zero. According to equation (4.32c) this yields however a small penetration velocity equal to:

$$\mathbf{u} \cdot \mathbf{n} = -\frac{\Delta t}{\rho} \nabla \hat{p} \cdot \mathbf{n} \approx 0 \tag{4.34b}$$

By updating the pressure every time step, see equation (4.32d), the correction pressure remains very small. Because the computational time step is small as well, the right–hand side of (4.34b) is thus very small. For the special case of stationary flow, the correction pressure is zero and consequently the no–penetration velocity is enforced exactly.

The use of the IBM has consequences for the stability of the numerical scheme. The forces that are added to the flow field represent the drag force that the flow encounters by the presence of cubes. From equation (4.10) it can be deduced that this may cause a large negative shift in the real part of the eigenvalues of g_i. This motivated the choice of our time integration scheme with coefficients 5/4 at time step n and -1/4 at time step n-2 rather than the popular Adams–Bashforth scheme [101]. The latter would impose stronger restrictions on the computational time step.

In the DNS the ratio d_p/d_f is taken equal to unity, which according to equation (4.30) corresponds to a rather high value of the permeability. Furthermore, the choice for $d_p = d_f$ seems intuitively good from a computational point of view as well, because both the boundary layers along the side walls of the cubes as well as the wakes in between the cubes must be resolved.

4.5 Evaluation of the closure for the drag force

To determine the values of C_K and C_F in equations (4.30) and (4.31), separate simulations have been performed of a uniform flow (in a volume–averaged sense) through a fully periodic Cartesian grid of cubes with $d_f = d_p$ and thus $\epsilon = 0.875$. The numerical method has been described in the previous section. In the DNS a finite computational domain is used and periodic boundary conditions are applied to all directions. Multiple simulations

have been performed in which the Reynolds number $Re_p \equiv \langle u \rangle^s d_p/\nu$ was varied. The number of cubes in the computational domain and the number of mesh points were adjusted dependent of the Reynolds number.
Figure 4.4 shows a cross–section of the calculated flow field at $Re_p = 215$, which is resolved on 192x96x96 mesh points. At this Reynolds number the flow is laminar. Furthermore, this simulation reveals that the assumptions of the Irmay model (4.30) for the permeability are fairly correct even at a high porosity of 0.875. In between $z/d_p = 0$ and $z/d_p = 0.5$, the velocity profile is approximately parabolic, and in between $x/d_p = 1.5$ and $x/d_p = 2.5$, the viscous shear stress at $z/d_p = 0.5$ is small.

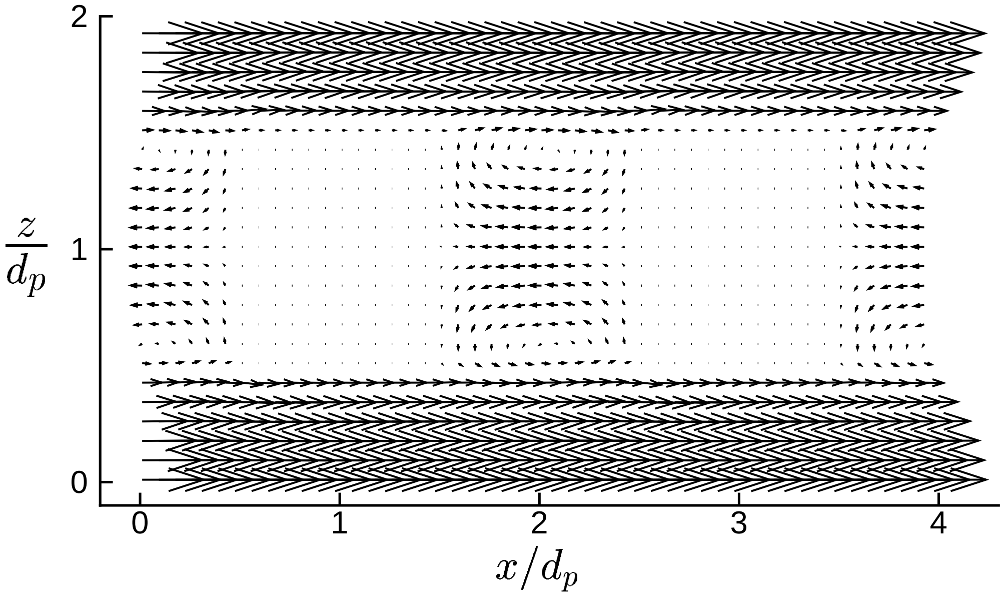

Figure 4.4: Two–dimensional snapshot of the flow field at $Re_p = 215$. The number of vectors is reduced by a factor four in each direction.

Figure 4.5 shows a cross–section of the flow field at $Re_p \approx 430$. At this Reynolds number the flow is turbulent. Between $x/d_p = 1.5$ and $x/d_p = 2.5$ large vortical structures are present in the wake regions of the cubes. These vortices are responsible for exchange of momentum between the wake and the channel zones. Different from the case of laminar flow, the pressure loss between $x/d_p = 1.5$ and $x/d_p = 2.5$ can therefore not be neglected.
We have inspected the accuracy of the IBM for the above simulation at $Re_p \approx 430$. The *largest* penetration velocities, given by equation (4.34b), were found near the front corners of the cubes at $z/d_p = 0.5$ and $z/d_p = 1.5$. These velocities were of the order of $10^{-4}\langle u \rangle^s$, which is considered as sufficiently small.
Figure 4.6 presents the drag force experienced by the flow through the grid of cubes as function of the Reynolds number. Each dot corresponds to a separate simulation. The dimensionless drag force has a local minimum at approximately $Re_p \approx 325$. This

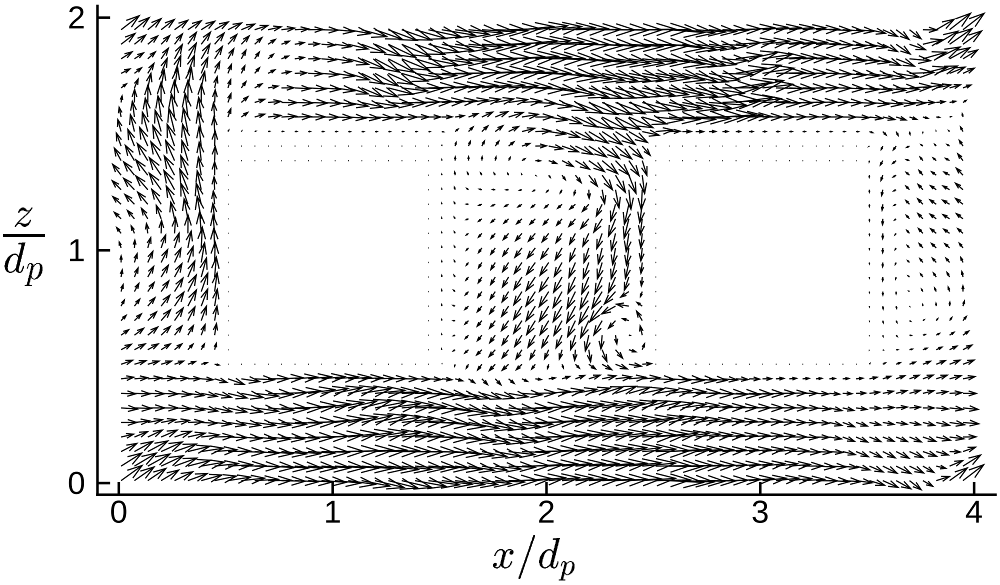

Figure 4.5: Two–dimensional snapshot of the flow field at $Re_p \approx 430$. The number of vectors is reduced by a factor three in each direction.

minimum corresponds to the transition from a laminar to a turbulent flow at higher Reynolds numbers. The dashed line in figure 4.6 is a fit of the model for the drag force given by equations (4.10), (4.30) and (4.31). The fit overestimates the drag force in the transitional regime where both linear and non–linear drag are important, but gives a good fit in the low and to a less extent in the high Reynolds number regime. Based on this fit, the following values has been found for C_K and C_F:

$$\begin{aligned} C_K &= 11.4 \\ C_F &\approx 0.4 \end{aligned} \qquad (4.35)$$

Notice that the value of C_K is close to 12, which is an indication that the Irmay model (4.30) is valid for a wide range of porosities. Based on this value for C_K, we find that the permeability of the grid of cubes with $\epsilon = 0.875$ is equal to $K = 0.132\, d_p^2$. The value of C_F appears to be much smaller than the value of 1.8 for packed beds. This may explained by the fact that a grid of cubes falls in the class of ordered porous media, whereas packed beds are disordered.

4.6 Results from the channel flow simulations.

In this section, results are shown from the channel flow simulations. A sketch of the flow geometry is given in figure 4.7. As mentioned in the introduction, the permeable wall

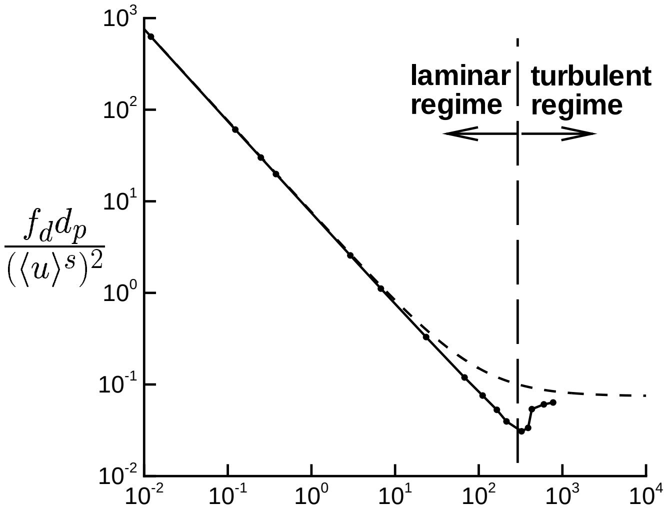

Figure 4.6: Drag force $f_d = (1/\epsilon)\int_A m\mathbf{n}\cdot[-\mathbf{I}\tilde{p}/\rho + \nu\nabla\tilde{\mathbf{u}}]\cdot\mathbf{n}_x dA$ as function of the Reynolds number, where $\mathbf{n}_x$ is the unit vector in the streamwise direction. Each dot corresponds to a separate simulation of flow through a fully periodic 3D Cartesian grid of cubes with a porosity of 0.875. The simulation results are compared with a fit based on equations (4.10), (4.30) and (4.31) with $C_K = 11.4$ and $C_F = 0.4$. —, linear interpolation of simulation results; - - -, model.

in these simulations can be divided into a homogeneous porous region with a constant porosity and an interface region with a spatially varying porosity. In this section special attention is paid to the modeling of the drag force in the interface region.

The Reynolds number based on the bulk velocity in the channel and the channel height is fixed at $Re_b \equiv U_bH/\nu = 1$. We note that the channel height H is defined as the distance between the top wall and the location where the porosity starts to deviate from unity, which corresponds to the position of the centroid of averaging volume 2 in figure 4.7. Because the flow is laminar, it suffices to simulate only a single column of cubes on top of each other and to apply periodic boundary conditions to the horizontal directions. In the z–direction seven cubes have been used to ensure that in the core region of the porous medium the volume–averaged flow is uniform. Consequently, the flow in the channel is not influenced by the presence of a solid wall underneath the cubes at $z = -h$. The ratio d_p/H was fixed at 0.0625 and the ratio $d_p/d_f = 1$. The flow is resolved on 28x28x448 mesh points.

- **Porosity profile**

Figure 4.8 presents the porosity profile, which has been computed from a second–order discretization of equation (4.5) with the cellular weighting function given by equation (4.3). Note that the calculation of the porosity, or a volume–averaged quantity in gen-

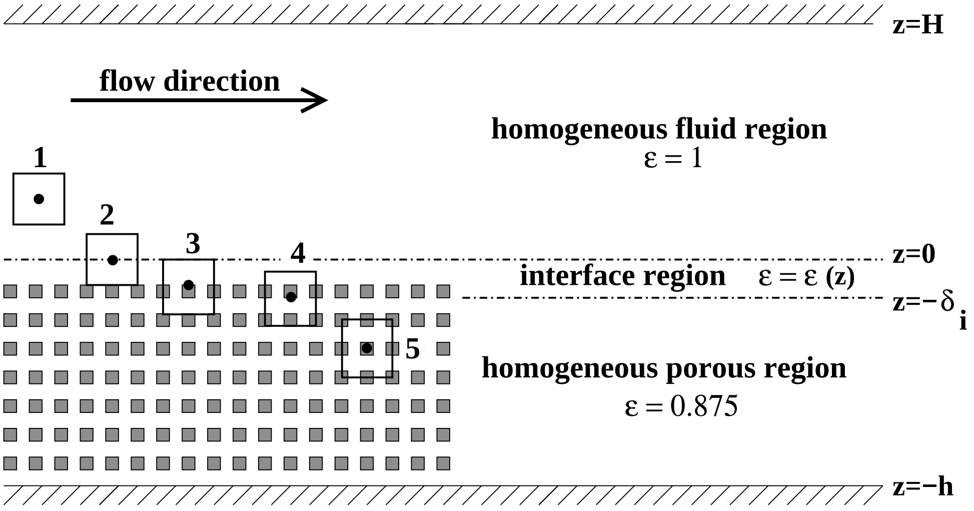

Figure 4.7: Flow in a plane channel with a solid top wall and a lower permeable wall consisting of a 3D Cartesian grid of cubes. The rectangles represent averaging volumes at different locations indicated by the black dots.

eral, requires the evaluation of a volume integral over $56^3 = 175616$ neighboring mesh points for the mesh resolution used and thus is fairly time–consuming.

Dependent of the behavior of the porosity, the flow domain has been divided into different regions. The homogeneous fluid or channel region between $z = 0$ and $z = H$ is the region where the porosity equals unity. In the interface region with a thickness of $\delta_i = 3d_p$, the porosity is varying as function of the height. In the homogeneous porous region with $z \in [-h + 2d_p : -\delta_i]$, the porosity is a constant denoted by ϵ_c. In our case $\epsilon_c = 0.875$ holds. In the region with $z \in [-h : -h + 2d_p]$, the porosity is varying again. This is a consequence of the reduction of the wall–normal extent of the averaging volume close to the wall, which would otherwise overlap with the wall.

- **Volume–averaged velocity profile**

Figure 4.9 presents the profile of the volume–averaged velocity. The solid line has been computed from equation (4.1) using the DNS data, whereas the two other lines are approximate solutions based on a model of Ochoa–Tapia & Whitaker [68]. We will refer to their model as the OTW model. The DNS profile is parabolic in the homogeneous fluid region, decreases rapidly in the interface region, and is constant in the core of the homogeneous porous region. From this figure it is clear that wall permeability causes a reduction in skin friction, at least for laminar flow, due to a reduction in the viscous shear stress at the interface with the permeable wall. Furthermore, because the skin friction at the permeable wall is smaller than at the top wall, the location of the maximum velocity is below the centerline of the channel region.

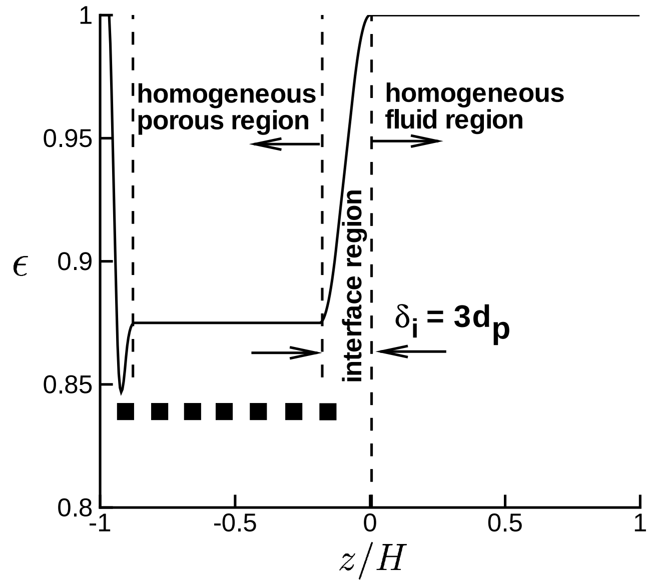

Figure 4.8: Porosity profile corresponding to flow over a 3D Cartesian grid of cubes with $d_f = d_p$. The black squares mark the positions of the cubes.

- **The OTW model**

The OTW model is a modification of the model of Beavers & Joseph [5] mentioned in the introduction. This model extends the solutions for the homogeneous fluid and porous regions to the interior of the interface region. Thus, this approach circumvents the difficulty of modeling the drag force in the interface region. The error made in this approach is that the porosity and the permeability in the interface region are not constant, like in the homogeneous fluid and porous regions, but are varying as function of the height. This error is however compensated by means of a jump in the volume–averaged viscous shear stress at $z = z_i$, where z_i is located somewhere inside the interface region, in combination with a continuous volume–averaged velocity according to:

$$\frac{\mu}{\epsilon_c}\frac{\partial\langle u\rangle^s}{\partial z}\bigg|_{z\uparrow z_i} - \mu\frac{\partial\langle u\rangle^s}{\partial z}\bigg|_{z\downarrow z_i} = \beta_t \frac{\mu U_i}{\sqrt{K_c}} \tag{4.36a}$$

$$\langle u\rangle^s\big|_{z\uparrow z_i} = \langle u\rangle^s\big|_{z\downarrow z_i} = U_i \tag{4.36b}$$

where β_t is the tangential stress–jump parameter of order unity, U_i is the interface velocity and K_c is the permeability in the homogeneous porous region. The choice of z_i is a bit arbitrary, but Ochoa–Tapia & Whitaker [68] (p. 2652) suggested to locate z_i at the center of the interface region when the filter length is thought to be constant across this region. The approximate velocity profile based on the OTW model is easily found from solving the Stokes equations for the homogeneous fluid region and the so–called Brinkman equation

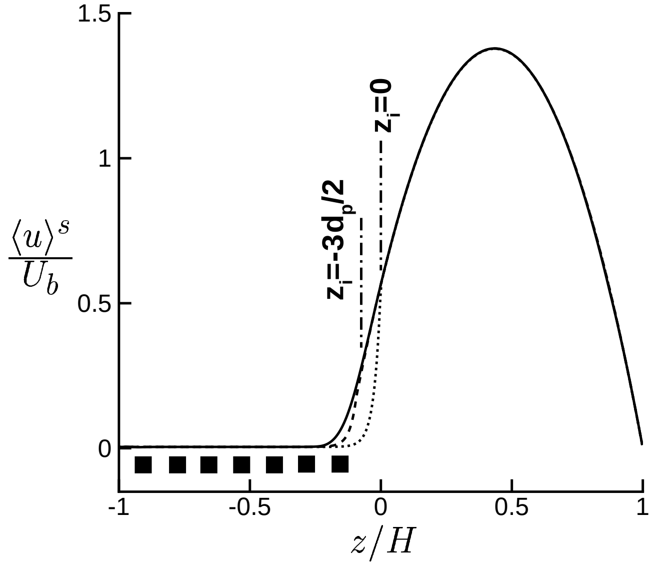

Figure 4.9: Volume–averaged velocity profiles. —, DNS; · · ·, OTW model with the wall interface chosen at $z_i = 0$; − − −, OTW model with $z_i = -3d_p/2$. The black squares mark the position of the cubes.

[14] for the homogeneous porous region:

$$z \in [0:H] \quad : \quad 0 = -\frac{1}{\rho}\frac{\partial\langle p\rangle}{\partial x} + \nu\frac{\partial^2\langle u\rangle^s}{\partial z^2} \tag{4.37a}$$

$$z \leq 0 \quad : \quad 0 = -\frac{1}{\rho}\frac{\partial\langle p\rangle}{\partial x} + \frac{\nu}{\epsilon_c}\frac{\partial^2\langle u\rangle^s}{\partial z^2} - \frac{\nu\langle u\rangle^s}{K_c} \tag{4.37b}$$

where for simplicity the porous medium is thought to be semi–infinite, and where the origin of the coordinate system is redefined such that $z = 0$ corresponds to $z = z_i$ in the old coordinate system. The boundary conditions are the no–slip and the free–slip boundary condition at $z = H$ and $z \to -\infty$ respectively. The solution for the volume–averaged velocity profile reads:

$$z \in [0:H] \quad : \quad \frac{\langle u\rangle^s}{U_b} = \left(6 - 3\frac{U_i}{U_b}\right)\frac{z}{H}\left(1 - \frac{z}{H}\right) + \frac{U_i}{U_b}\left(1 - \frac{z}{H}\right) \tag{4.38a}$$

$$z \leq 0 \quad : \quad \frac{\langle u\rangle^s}{U_b} = \frac{U_d}{U_b} + \left[\frac{U_i - U_d}{U_b}\right]\exp\left[\frac{z}{H}\sqrt{\frac{\epsilon_c}{Da}}\right] \tag{4.38b}$$

where $Da \equiv K_c/H^2$ is the Darcy number, and U_i and U_d are the interface and the constant creep velocity given by respectively:

$$\frac{U_i}{U_b} = \frac{1 + 2\sqrt{Da/\epsilon_c}}{\frac{1}{6\sqrt{Da}}\left(\frac{1}{\sqrt{\epsilon_c}} - \beta_t\right) + \frac{2}{3} + \sqrt{\frac{Da}{\epsilon_c}}} \qquad (4.39a)$$

$$\frac{U_d}{U_b} = 6Da\left(2 - \frac{U_i}{U_b}\right) \qquad (4.39b)$$

The analytical solution requires the specification of the tangential stress–jump parameter β_t. This parameter can be determined from the DNS data by means of equation (4.39b), which is rewritten into the following expression for β_t:

$$\beta_t = \frac{1}{\sqrt{\epsilon_c}} + \sqrt{Da} - \frac{3\sqrt{Da}\left(1 + 2\sqrt{Da/\epsilon_c}\right)}{12Da(U_b/U_d) - 1} \qquad (4.40)$$

Notice that β_t depends not only on ϵ_c, Da and the ratio U_d/U_b, but on z_i as well. It is found that $\beta_t = 0.45$ for $z_i = -3d_p/2$ and $\beta_t = 0.91$ for $z_i = 0$. These values are in agreement with the estimate made by Ochoa–Tapia & Whitaker that $\beta_t = O(1)$. However, because these values differ from each other by a factor two, β_t appears to be quite sensitive to the choice of z_i.

The velocity profiles corresponding to the above values of β_t are presented in figure 4.9. The approximate solutions based on the OTW model and the exact DNS solution overlap almost entirely, except in the interface region. Especially the solution corresponding to $z_i = -3d_p/2$ underestimates the velocity in this region.

- **Volume–averaged momentum balance**

For stationary, horizontally homogeneous and laminar volume–averaged flow with a small Reynolds number, equation (4.6a) reduces to:

$$0 = \underbrace{-\frac{1}{\rho}\frac{\partial\langle p\rangle}{\partial x}}_{\text{I}} + \underbrace{\frac{\nu}{\epsilon}\frac{\partial^2\langle u\rangle^s}{\partial z^2}}_{\text{II}} \underbrace{-\frac{1}{\epsilon}\int_A m\,\mathbf{n}\cdot\mathbf{n}_x\frac{p}{\rho}\,dA}_{\text{III}} + \underbrace{\frac{1}{\epsilon}\int_A m\,\nu\,\mathbf{n}\cdot\nabla\mathbf{u}\cdot\mathbf{n}_x\,dA}_{\text{IV}} \qquad (4.41)$$

where $\mathbf{n}_x$ is the unit vector pointing in the streamwise direction. Notice that this equation is similar to the Brinkman equation (4.37b). The terms on the right–hand side represent respectively the pressure gradient that drives the flow, viscous diffusion, form or pressure drag, and viscous drag. Based on the DNS data, the different terms in the momentum balance have been computed and the result is shown in figure 4.10. The profiles are only shown for $z/H \in [-0.875 : 0.875]$, because close to the solid walls at $z/H = -1$ and $z/H = 1$ the filter length had to be reduced and the above momentum equation is exact only when the filter length is kept constant.

In the channel region ($z \geq 0$) the pressure–gradient term is in balance with the diffusion term. In the interface region the diffusion term becomes positive, which represents

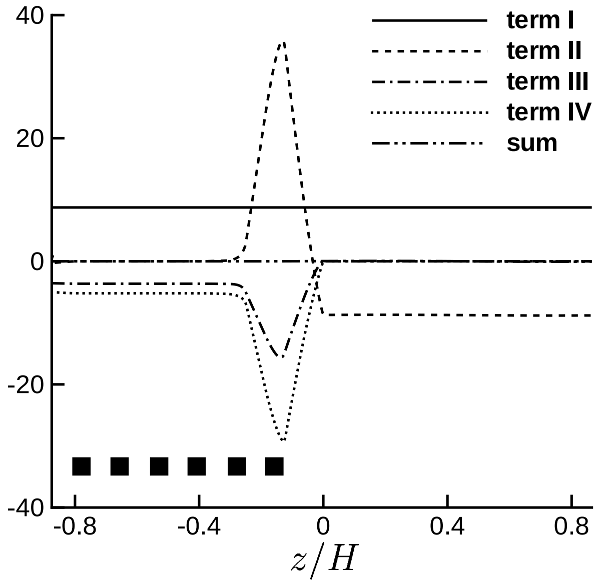

Figure 4.10: Profiles of the different terms on the right–hand side of equation (4.41) for the volume–averaged streamwise momentum, normalized by U_b^2/H. The black squares mark the position of the cubes.

transport of momentum from the channel region into the permeable wall. Furthermore, all terms in the momentum balance are important in this region. Further down inside the permeable wall, for $z \lesssim -4d_p$, the flow is uniform and consequently the diffusion term is zero. In this region the pressure–gradient term is balanced by the sum of viscous and form drag. Viscous drag dominates over form drag throughout the permeable wall.

- **Variable–permeability model**

The Irmay model (4.30) for the permeability has been derived assuming a constant porosity and an uniform volume–averaged flow. These assumptions are not satisfied in the interface region. However, let us adopt the Irmay model not only for the homogeneous porous region, but for the interface region as well, using the local value of the porosity. In literature this approach is known as a variable–porosity [68] or variable–permeability model [81]. The main benefit of this model is that it guarantees that the permeability approaches at least the expected values in the homogeneous porous and in the homogeneous fluid region: $K = K_c$ for $z \leq -\delta_i$ and $K \to \infty$ for $z \geq 0$. On the other hand, the functional dependence of the permeability is probably not modeled correctly, because the topology of the interface region is different from the topology of the homogeneous porous region. This is clear from the mutual comparison of averaging volumes 3 and 5 in figure 4.7.

Based on the DNS data, we are able to evaluate this variable–permeability model. The permeability can been calculated from equation (4.10), where the Forchheimer term can be neglected as the Reynolds number is small. Thus:

$$\frac{d_p^2}{K} = -\frac{d_p^2}{\nu\epsilon\langle u\rangle^s}\int_A m\mathbf{n}\left[-\frac{\tilde{p}}{\rho}\mathbf{I} + \nu\nabla\tilde{\mathbf{u}}\right]\cdot\mathbf{n}_x dA \tag{4.42}$$

In figure 4.11 the profiles of d_p^2/K are shown, obtained from respectively the DNS and the variable–permeability model based on the Irmay model (4.30) with $C_K = 11.4$. The DNS and the variable–permeability model agree not very well in the interface region, but almost overlap near the solid wall at $z = -H$. It is striking that the permeability computed from the DNS, is not only varying in the interface region, but also in the top layer of the homogeneous porous region. In this thin layer with $-4d_p \lesssim z \lesssim -3d_p$, the permeability is even smaller than K_c. Notice from the non–zero diffusion term in figure 4.10 that in the same layer the volume–averaged velocity is non–uniform, whereas it is approximately constant for $z \lesssim -4d_p$. The observation that the permeability computed from (4.42) varies in a layer with a constant porosity, but a non–uniform velocity, suggests that:

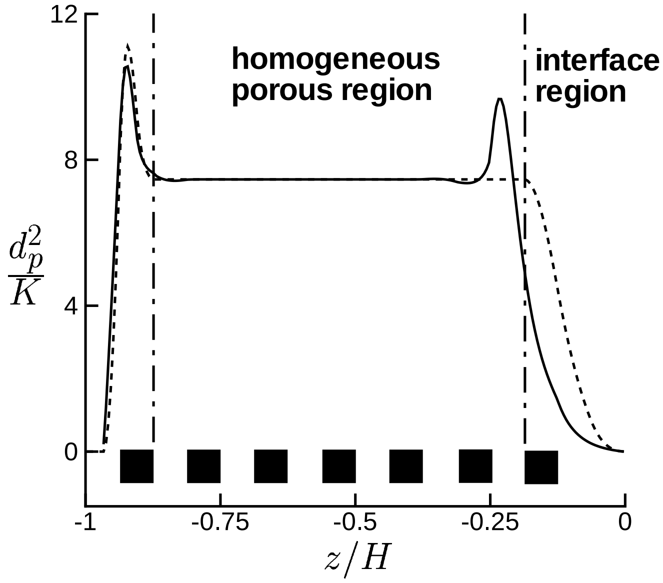

Figure 4.11: Profile of the inverse of the dimensionless permeability, d_p^2/K. —, computed from the DNS by means of equation (4.42); – – –, variable–permeability model based on the Irmay model (4.30) with $C_K = 11.4$. The black squares mark the position of the cubes.

1. either the permeability computed from (4.42) depends not only on the porosity, but also on the non–uniformity of the volume–averaged velocity,

2. or the parameterization (4.10) of the drag integral is not correct when the flow is non–uniform.

It is interesting to note that the second suggestion was made also by Lundgren [59] in a study of Stokes flow through a random bed of fixed spheres with a constant porosity. Lundgren suggested that for this particular bed the drag force should be parameterized according to:

$$\frac{1}{\epsilon}\int_A m\mathbf{n}\left[-\mathbf{I}\frac{\tilde{p}}{\rho}+\nu\nabla\tilde{\mathbf{u}}\right]dA = -\frac{\nu}{K}\langle\mathbf{u}\rangle^s + \frac{\nu_c}{\epsilon}\nabla^2\langle\mathbf{u}\rangle^s \tag{4.43}$$

where ν_c is a function of the solidity $1-\epsilon$. Lundgren found that ν_c is positive for small values of the solidity, in agreement with the well–known result of Einstein for the effective viscosity of dilute *suspensions* [3], but ν_c is negative for relatively large values of the solidity. In principle ν_c could be calculated from the DNS data assuming that $K = K_c$ in the homogeneous porous region. This would then yield $\nu_c < 0$, although no attempt is made here to compute this quantitatively. Thus this suggests that the *effective* viscosity $(\nu + \nu_c)$ experienced by the volume–averaged flow through the grid of cubes is smaller than the viscosity (ν) experienced by the unfiltered flow field.

4.7 Summary and discussion

In this study the closure problem for the drag force has been investigated for flow over and through a permeable wall consisting of a 3D Cartesian grid of cubes. The permeable wall can be divided into a homogeneous porous region with a constant porosity, and an interface region characterized by a spatially varying porosity. It is important to make this distinction when investigating the closure problem for the drag force, because the topology of the two regions is different. For this reason two different kinds of simulations have been performed. In these simulations an Immersed Boundary Method has been successfully applied to enforce a zero velocity on the cubes.

The first kind of simulations concerned flow through a homogeneous porous medium consisting of a *fully periodic* grid of cubes with a porosity of 0.875. These simulations served to determine the coefficients in a closure for the drag force based on the Irmay [37] and the Burke–Plummer model [7] for the low and high Reynolds–number range respectively. The coefficient found for the Irmay model is close to the value of 12 for very small porosities. This indicates that the Irmay model is valid for a wide range of porosities. The coefficient found for the Burke–Plummer model is much smaller than the value of approximately 1.8 found experimentally for many packed beds. This may originate from the fact that the Cartesian grid of cubes is ordered, whereas packed beds are usually strongly disordered.

The second kind of simulations concerned Stokes flow in a plane channel with a lower permeable wall consisting of the same grid of cubes as before, which is now however only fully periodic in the horizontal directions. Two momentum–transfer models for the interface region were investigated: the OTW model and a variable–permeability model. To

this purpose the DNS data has been volume averaged by means of the cellular filter.
The model of Ochoa–Tapia & Whitaker [68] extends the homogeneous fluid and porous regions to the core of the interface region, and thus circumvents the difficulty of modeling the drag force in the interface region. The error in this approach is corrected by means of an artificial jump condition for the viscous shear stress at the wall interface. The analytical solution for the velocity profile based on the OTW model agrees well with the DNS data. A disadvantage is however that this model contains a stress–jump parameter which has to be specified. It is shown that the value of this parameter is very sensitive to the choice of the location of the wall interface.
A variable–permeability has been proposed for the interface region, in which the permeability given by the Irmay model is related to the local value of the porosity. The parameterization according to Whitaker [104] of the drag force has been used to compute the permeability profile from the DNS data. The agreement between the variable–permeability model and the DNS data is rather poor. However, Whitaker's parameterization of the drag force yields a permeability that is varying even in the homogeneous porous region. Following Lundgren [59], we suggest that Whitaker's parameterization of the drag force should actually include a diffusion–like term to account for the non–uniformity of the volume–averaged flow field. Assuming that the permeability is constant in the homogeneous porous region, we found that the effective viscosity experienced by the volume–averaged flow field is smaller than the viscosity experienced by the unfiltered flow field.

Chapter 5

The influence of wall permeability on turbulent channel flow [1]

Abstract *Direct Numerical Simulations (DNS) have been performed of turbulent flow in a plane channel with a solid top wall and a permeable bottom wall. The permeable wall is a packed bed, which is characterized by the mean particle diameter and the porosity. The main objective is to study the influence of wall permeability on the structure and dynamics of turbulence. The flow inside the permeable wall is described by means of a continuum approach based on the Volume–Averaged Navier–Stokes equations. Results from four simulations are shown, for which only the wall porosity is changed. The influence of wall permeability can be characterized by the permeability Reynolds number,* Re_K*, which represents basically the ratio of the effective pore diameter over the typical length scale of near–wall eddies. For small* Re_K*, the wall behaves like a solid wall. For large* Re_K*, the wall is classified as a highly permeable wall near which viscous effects are of minor importance. It is observed that low– and high–speed streaks and the associated quasi–streamwise vortices are absent near a highly permeable wall. This is attributed to turbulent transport across the wall interface and the reduction in mean shear due to a weakening of respectively the wall–blocking and the wall–induced viscous effect. The absence of streaks is consistent with a decrease in the peak value of the streamwise rms velocity normalized by the friction velocity at the permeable wall. Despite the increase in the peak values of the spanwise and wall–normal rms velocities, the peak value of the turbulent kinetic energy is therefore smaller. Turbulence near a highly permeable wall is dominated by relatively large vortical structures, which originate possibly from a Kelvin–Helmholtz type of instability. These structures are responsible for an exchange of momentum between the channel and the permeable wall. This process contributes strongly to the Reynolds–shear stress and thus to a large increase in the skin friction. Consequently, the interception of the log–law fit is shifted downwards. Furthermore, it is found that the slope of the log–law fit is larger than the value of approximately 1/0.4 for turbulent flows over both smooth*

---

[1] A shortened version of this chapter has been submitted for publication to *Journal of Fluid Mechanics* [11].

and rough walls. Another objective of this study is to check the wall similarity hypothesis. The streamwise rms velocity, the rms vorticities and the Reynolds–shear stress are self–similar in the outer region, irrespective of the porosity of the wall. On the other hand, the spanwise and wall–normal rms velocities and the rms pressure show significant departures from similarity.

5.1 Introduction

Turbulent flows over permeable walls, i.e. rigid porous walls with interconnected pores through which fluid may flow, are encountered in a wide range of problems. Examples are: flows in oil wells, catalytic reactors, heat exchangers of open–cell metal foam [58],[90], and river beds of e.g. gravel. In the latter example, wall permeability is expected to affect the bed friction and consequently the volume flow and surface level of the river. Wall permeability is expected to affect also bed erosion, the exchange of oxygen between surface and subsurface flow and hence the degradation of organic material [97], and the dispersion of pollutants. Also densely built–up urban areas and plant canopies can be considered as permeable wall layers. Related research topics are dispersion of pollutants in metropoles, the exchange of energy and oxide and carbon dioxide between forests and the atmosphere [28], and the propagation of forest fires [84].

Despite its relevance to the aforementioned applications, the effect of wall permeability has received relatively little attention in literature. A complication is that permeable walls are also rough, and hence it is rather difficult to isolate the effect of wall permeability from wall roughness. The opposite is not necessarily true: rough walls could be very well impermeable in the sense that over the height of a single roughness element the flow is forced to zero. For instance a multiple–layer gravel bed is both permeable and rough, but a bed consisting of just a single layer of gravel is considered as rough and impermeable. The difference between these two walls is illustrated in figure 5.1. In literature it is common practice to consider both permeable and impermeable walls with the same surface roughness as rough, thereby ignoring the effect of wall permeability. Exceptions hereupon are a few experimental studies, which we will discuss below.

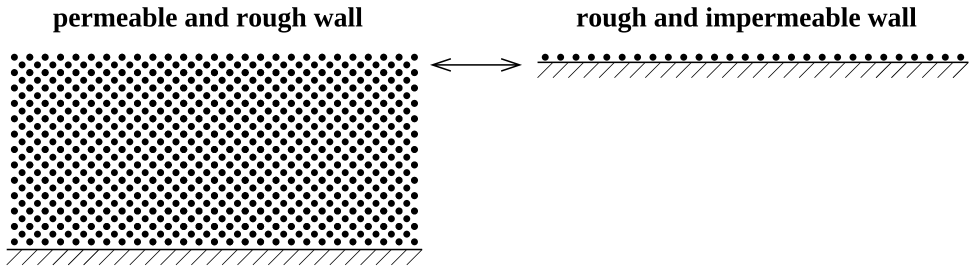

Figure 5.1: Illustration of the difference between a permeable and rough wall and an impermeable wall with similar surface roughness.

Zagni & Smith [110] conducted experiments on open channel flow over permeable beds of graded spheres. Twenty multiple–layer bed configurations were studied, for which the size and gradings of the spheres were varied. Velocities above the bed were measured by means of a Pitot tube. For the high Reynolds number range investigated, it was found that the friction factor was higher and increasing with the Reynolds number compared to the constant friction factor for flow over impermeable walls with the same surface roughness. Zagni & Smith related the increase in the friction factor to turbulent transport across the bed interface.

Zippe & Graf [112] performed experiments in a wind tunnel on boundary–layer flow over a permeable bed composed of nearly ellipsoidal grains. The thickness of the bed layer was varied, where the bed configuration with just a single layer of grains was considered as rough and impermeable. Velocities were measured by means of hot film anemometry. It was found that the friction factor for the multiple–layer (i.e. permeable) bed configurations was higher than the friction factor for the single–layer bed configuration. Furthermore, for the high Reynolds number range investigated, the friction factor was increasing with the Reynolds number, which substantiates the findings of Zagni & Smith.

In a series of wind–tunnel experiments, Kong & Schetz [46] studied boundary–layer flow over various surfaces: a solid wall, a perforated plate, a plate of sintered metal, a bonded screen and sandpaper. These surfaces were classified as rough or smooth and permeable or impermeable, and combinations of that. For instance sandpaper was considered as rough and impermeable, and the plate of sintered metal as rough and permeable. Their objective was to investigate the influence of wall permeability and small surface roughness independently and their combined effect. Mean velocities were measured by means of a Pitot rake. The measurements revealed that both surface roughness and wall permeability cause an increase in the skin friction coefficient compared to a solid (i.e. smooth and impermeable) wall. Wall permeability alone could be responsible for an increase by about 30-40 %. The combined effect of roughness and permeability was roughly the sum of their individual effects.

The experiments of Zagni & Smith, Zippe & Graf and Kong & Schetz indicate clearly that the effects of wall permeability and wall roughness are different from each other, and they imply that wall permeability apparently alters the turbulence structure and dynamics. The way on which permeability alters turbulence is however still an open question.

Ruff & Gelhar [79] performed experiments on turbulent flow in a pipe covered with a layer of polyurethane foam with a porosity of 97 %. One of the objectives was to determine the penetration depth of turbulence in the foam layer. Velocities inside the foam layer were measured by means of miniature hot wire probes in combination with a helium tracer technique. The measurements showed evidence of a non–zero velocity at the wall interface and of turbulent transport of momentum across the interface, which was also observed in the experiments of Zagni & Smith [110]. The turbulence penetration depth amounted roughly one–fourth of the total foam layer thickness.

Most experiments on turbulent flows over permeable walls are concerned with flow over vegetation. The review of Finnigan [28] discusses the gross features of experimental data from forests, cereal crops and model plant canopies. Despite the scatter in these mea-

surements, the experimental data have some striking features in common. Turbulence in plant canopies is dominated by large coherent structures of the order of the canopy height. It is believed that their origin lies in a Kelvin–Helmholtz type of instability of the mean velocity profile, which exhibits an inflexion point near the top of the canopy. For this reason, Raupach et al. [77] and Finnigan [28] suggested that the flow near the top of a canopy has more resemblance with a plane mixing layer rather than a boundary layer.
In recent years a number of numerical studies have been reported on turbulent flows over permeable walls, although mainly for the case of flow over vegetation. In literature two different methods can be found for simulating flow over and through a permeable wall. The first and computationally most simple method is the specification of boundary conditions, which incorporate the effect of wall permeability. This approach was followed by Hahn et al. [32] in DNS of turbulent flow in a plane channel with permeable walls. The boundary conditions used were similar to the ones proposed by Beavers & Joseph [5]:

$$\nabla \mathbf{u} \cdot \mathbf{n} = \frac{\alpha}{\sqrt{K}} (\mathbf{u} - \mathbf{U}_d) \tag{5.1a}$$

$$\mathbf{u} \times \mathbf{n} = \mathbf{0} \tag{5.1b}$$

where $\mathbf{n}$ is the unit normal at the wall interface, α is an empirical coefficient of order unity and K the permeability of the wall. The velocity $\mathbf{U}_d$ is given by the well–known Law of Darcy [4]:

$$\mathbf{U}_d = -\frac{K}{\mu} \nabla p \tag{5.2}$$

where μ is the dynamic viscosity and ∇p the imposed pressure gradient. Saffman [80] showed that the boundary conditions of Beavers & Joseph can be derived by the assumption of Stokes flow. These boundary conditions can therefore be applied to turbulent channel flow only when close to the permeable walls a viscous sublayer exists, in which the flow is governed by the Stokes equations. As pointed out by Hahn et al. [32], this requirement is satisfied only when $\sqrt{K}$ is small compared to ν/u_τ, where $\nu \equiv \mu/\rho$ is the kinematic viscosity and ρ the mass density, $u_\tau \equiv \sqrt{\tau/\rho}$ is the friction velocity and τ is the wall–shear stress. The ratio of these two length scales yields the permeability Reynolds number $Re_K \equiv \sqrt{K} u_\tau/\nu$, which expresses basically the ratio of the effective pore diameter ($\sqrt{K}$) to the characteristic length scale of near–wall turbulent eddies (ν/u_τ). For small values of Re_K, the eddies in the channel are blocked by the permeable wall and consequently a viscous sublayer is present. For large values of Re_K, the eddies may penetrate the permeable wall and this prohibits the formation of a viscous sublayer. It is not likely that the penetration of turbulence in this case can be modeled in a simple manner by means of boundary conditions. Therefore, for an accurate description of the flow field for large Re_K, we have to describe the flow also *inside* the permeable wall. This is the second method for simulating flow over a permeable wall.
The problem of the second method is however, that a direct simulation, which completely resolves the flow inside the pores, is often unfeasible. Most porous media found in practical applications have a very complex geometry of which the details are not fully known.

Furthermore, flows in porous media often exhibit a wide range of length scales. The smallest scales are typically of the order of the pore size or the typical size of the solid obstacles forming the porous medium. The largest scales will be limited by the dimensions of the porous medium, like its depth, or they are imposed by an external flow field and/or forcing. An advantage is however, that in general the small and large scales are well–separated. This motivates an approach in which only the large–scale behavior is described. The theoretical basis for this approach is provided by the Volume–Averaging Method [105]. In this method the flow is averaged over a small spatial volume with dimensions sufficiently large to smooth inhomogeneities at pore scales, but on the other hand sufficiently small to retain the flow dynamics of interest. An important advantage of this method is that the porous medium can be considered as a continuum, because the large–scale or volume–averaged flow field is defined both in the fluid and in the solid phase. We will therefore refer to the second method as the *continuum approach.*

As shown by Whitaker [104], the volume–averaged flow field is governed by the Volume–Averaged Navier–Stokes (VANS) equations. Darcy's Law (5.2) follows from the VANS equations for an uniform and stationary flow through a homogeneous porous medium. The VANS equations are similar to the equations used in Large–Eddy Simulations (LES) [56]. Like in LES a closure is demanded for the subfilter–scale stress. In addition to this, a drag force needs to be modeled. The latter originates from the presence of solid obstacles, which exert a force on the volume–averaged flow field.

The continuum approach has been used in a number of recent LES studies of flows over forests, e.g. Shaw & Schumann [87], Dwyer et al. [24] and Watanabe [100]. Other studies, in which a Reynolds–averaged form of the VANS equations was used, considered not only flow over vegetation [57],[108], but also flow over a permeable wall layer with a porosity significantly lower than that of vegetation [20],[88]. The VANS equations were used also in a previous preliminary DNS study [9] and the present study is an extension of this work. It deals with the DNS of turbulent flow in a plane channel with one permeable wall and one solid wall. This flow geometry allows for the comparison between the influence of a permeable wall and of a solid wall on the turbulent flow. In the DNS the permeable wall is a packed bed, which is characterized by the porosity and the mean particle diameter. The choice for a packed bed is motivated by the fact that packed beds are encountered in many applications. The main research objective is to investigate *exclusively* the effect of wall permeability on the turbulence structure and dynamics. In order to isolate the effect of wall permeability from wall roughness, we therefore consider a permeable wall with a high porosity and consisting of solid obstacles with a small dimension.

To some extent, the effect of wall permeability on turbulence has been investigated before by Perot & Moin [72]. They conducted DNS with artificial boundary conditions with the objective to study the influence of a solid wall on turbulence in the absence of mean shear. Two effects were considered: a viscous and a kinematic effect. The viscous effect originates from the fact that the flow must satisfy the no–slip condition at a solid wall. The kinematic effect is the wall–blocking effect, which means that the flow can not penetrate a solid wall. Wall permeability is expected to weaken both these viscous and kinematic effects. It allows for an apparent slip velocity and for turbulent transport of momentum across the wall interface, which causes respectively a decrease and an increase in the skin friction. The reduction in mean shear is expected to weaken also the shear–sheltering effect analyzed by Hunt & Durbin [36]. They showed that the presence of a layer with strong mean shear prevents the interaction between turbulence in the adjacent regions.

Another objective of this study is to check the wall similarity hypothesis [77], which states that for large Reynolds numbers the turbulence in the outer region of a boundary layer is unaffected by the properties of the wall. For flows over rough walls, this hypothesis is still a controversial issue, see for instance the review of Jiménez [41] (p. 176,181,191). Krõgstad et al. [48] observed an increase in the wall–normal turbulence intensity and the Reynolds–shear stress in the outer region of a boundary layer over a mesh–screen rough wall compared to the boundary layer over a smooth wall. This contradicts the wall similarity hypothesis. A similar behavior was found in experiments by Krõgstad & Antonia [47] for flow over lateral rods glued to the wall. It is interesting to note that Krõgstad et al. [48] suggested that a relation exists between wall permeability and the breakdown of similarity. The increase in the wall–normal turbulence intensity would be caused by a weakening of the wall–blocking effect of the mesh–screen rough wall relative to a solid wall. As a consequence of this, sweep and ejection events become stronger and contribute more to the Reynolds–shear stress.

Recapitulating, the objectives of this study are threefold. The first objective is to develop a formalism for DNS of turbulent channel flow over a permeable wall with a relatively high permeability. The second objective is to gain more insight in the influence of wall permeability on the dynamics and structure of turbulence. A DNS in combination with the VANS equations for the permeable wall is an excellent tool for this, because it provides very detailed information on the flow field. The third objective is to check the wall similarity hypothesis for turbulent flows over permeable walls.

This study is organized as follows. Section 5.2 discusses the continuum approach for flows through porous media. The next section deals with the coupling between the flow in the channel and the flow inside the permeable wall. In section 5.4 a discussion is given of the implications of wall permeability for the scaling of turbulence. Section 5.5 deals with the numerical method. The DNS results are presented in section 5.6. Section 5.7 contains a summary and a discussion.

5.2 Continuum approach for flows in porous media

In this section, the continuum approach for flows in porous media is discussed and the governing equations for the volume–averaged flow are introduced.

The first step in the derivation of the governing equations for the volume–averaged flow is the introduction of the superficial volume average, which is denoted by $\langle ... \rangle^s$ and defined as:

$$\langle \mathbf{u} \rangle^s_{\mathbf{x}} \equiv \int_V \gamma(\mathbf{r})\, m(\mathbf{y})\, \mathbf{u}(\mathbf{r})\, dV \tag{5.3}$$

where the subscript $\mathbf{x}$ means that the volume average is evaluated at the centroid $\mathbf{x}$ of the averaging volume V, $\mathbf{y} = \mathbf{r} - \mathbf{x}$ is the relative position vector, γ is the phase–indicator function that equals unity when $\mathbf{r}$ points in the fluid phase and zero when $\mathbf{r}$ points in the solid phase, and m is a weighting function. The volume–averaging technique is illustrated in figure 5.2. Notice that the volume–averaging operator acts as a filter, which passes only information on the large–scale structure of the flow field. Furthermore, we note that the filtered or volume–averaged flow field is continuous in the sense that it is defined both in the fluid and the solid phase. This is the basis of the continuum approach for flow in porous media. Finally, we remark that the volume–averaging operator can be regarded as a generalization of the filter operator used in LES [56], where in LES γ is always equal to unity due to the absence of a solid phase.

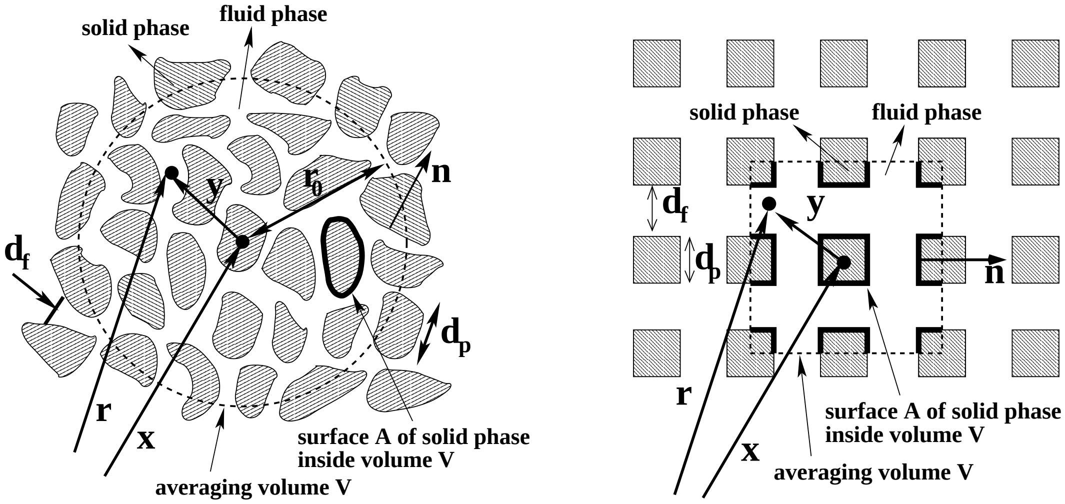

Figure 5.2: Illustration of the volume–averaging technique for a disordered (left) and for an ordered porous medium (right).

For a meaningful definition of a volume average, the weighting function must satisfy the following normalization condition:

$$\int_V m(\mathbf{y})dV = 1 \tag{5.4}$$

In principle the weighting function can be chosen freely, but it is desirable that the filtered flow field contains negligible variations on scales smaller than the dimensions of the averaging volume. We will come back to this point later on in this section.

The velocity at a certain point in a porous medium can be decomposed into a contribution from the volume–averaged velocity at this point and a subfilter–scale velocity $\tilde{\mathbf{u}}$ according to [30]:

$$\mathbf{u} = \langle \mathbf{u} \rangle + \tilde{\mathbf{u}} \tag{5.5}$$

where $\langle \mathbf{u} \rangle \equiv \langle \mathbf{u} \rangle^s / \epsilon$ is the intrinsic volume average and ϵ is the porosity. The latter is defined according to:

$$\epsilon(\mathbf{x}) \equiv \int_V \gamma(\mathbf{r}) m(\mathbf{y}) dV \tag{5.6}$$

Besides the spatial decomposition given by (5.5), later on in this chapter also a temporal decomposition will be used according to [93]:

$$\mathbf{u} = \overline{\mathbf{u}} + \mathbf{u}' \tag{5.7}$$

where the overbar denotes the Reynolds–averaged or time–mean value and the prime denotes the temporal fluctuation from the Reynolds–averaged value. It is easy to show that the time and spatial averaging operators commute [71]: $\overline{\langle \mathbf{u} \rangle} = \langle \overline{\mathbf{u}} \rangle$, $\langle \mathbf{u} \rangle' = \langle \mathbf{u}' \rangle$, $\overline{\tilde{\mathbf{u}}} = \tilde{\overline{\mathbf{u}}}$ and $\tilde{\mathbf{u}}' = \tilde{\mathbf{u}'}$.

In order to derive the volume–averaged form of the Navier–Stokes equations, it is necessary to relate the volume average of a spatial derivative to the spatial derivative of the volume average. Such a relation exists and it is known as the spatial averaging theorem [102]. For instance the volume average of the gradient of the pressure can be expressed as:

$$\langle \nabla p \rangle^s_{\mathbf{x}} = \nabla \langle p \rangle^s_{\mathbf{x}} + \int_A m(\mathbf{y}) \mathbf{n} p(\mathbf{r}) dA \tag{5.8}$$

where A is the contact area between the fluid and the solid phase inside the averaging volume V, and $\mathbf{n}$ is the unit normal at A that points from the fluid into the solid phase (see figure 5.2). The single assumption in the derivation of (5.8) is that the weighting function m is independent of $\mathbf{x}$ and depends only on $\mathbf{y}$.

Application of the spatial filter (5.3) and the spatial averaging theorem (5.8) to the Navier–Stokes equations yields the Volume–Averaged Navier–Stokes (VANS) equations [104]:

$$\begin{aligned}
\frac{\partial \langle \mathbf{u} \rangle}{\partial t} + \frac{1}{\epsilon} \nabla \cdot [\epsilon \langle \mathbf{u} \rangle \langle \mathbf{u} \rangle] + \frac{1}{\epsilon} \nabla \cdot [\epsilon \boldsymbol{\tau}] &= -\frac{1}{\epsilon \rho} \nabla [\epsilon \langle p \rangle] + \frac{\nu}{\epsilon} \nabla^2 [\epsilon \langle \mathbf{u} \rangle] + \mathbf{f} && \text{(5.9a)} \\
\nabla \cdot [\epsilon \langle \mathbf{u} \rangle] &= 0 && \text{(5.9b)}
\end{aligned}$$

where $\boldsymbol{\tau}$ is the subfilter–scale stress, which in the LES literature is known as the subgrid–scale stress, and $\mathbf{f}$ is the drag force per unit mass that the solid phase exerts on the fluid phase. The expressions for $\boldsymbol{\tau}$ and $\mathbf{f}$ are given by:

$$\begin{aligned}
\boldsymbol{\tau} &\equiv \langle \mathbf{u}\mathbf{u} \rangle - \langle \mathbf{u} \rangle \langle \mathbf{u} \rangle = \langle \langle \mathbf{u} \rangle \langle \mathbf{u} \rangle \rangle - \langle \mathbf{u} \rangle \langle \mathbf{u} \rangle + \langle \langle \mathbf{u} \rangle \tilde{\mathbf{u}} \rangle + \langle \tilde{\mathbf{u}} \langle \mathbf{u} \rangle \rangle + \langle \tilde{\mathbf{u}} \tilde{\mathbf{u}} \rangle && \text{(5.10a)} \\
\mathbf{f} &\equiv \frac{1}{\epsilon} \int_A m \mathbf{n} \left[-\frac{p}{\rho} \mathbf{I} + \nu \nabla \mathbf{u} \right] dA = \\
&\frac{1}{\epsilon} \int_A m \mathbf{n} \left[-\frac{\langle p \rangle}{\rho} \mathbf{I} + \nu \nabla \langle \mathbf{u} \rangle \right] dA + \frac{1}{\epsilon} \int_A m \mathbf{n} \left[-\frac{\tilde{p}}{\rho} \mathbf{I} + \nu \nabla \tilde{\mathbf{u}} \right] dA && \text{(5.10b)}
\end{aligned}$$

The inclusion of the drag force is different from the LES equations where in the absence of the solid phase (i.e. $\epsilon = 1$) the drag force is zero. Irrespective of the weighting function used, the VANS equations as given above are exact for Newtonian and incompressible flow in a rigid porous medium with a time–independent porosity. The continuity equation (5.9b) underlines the importance to distinguish between superficial and intrinsic volume averages, because in case of a spatially varying porosity only the superficial velocity is divergence free.

Equation (5.9a) represents a *non–local* transport equation, because volume–averaged quantities appear *inside* volume and surface integrals in the expressions for the subfilter–scale stress and the drag force. This is a complication for the modeling of the drag force as well as the subfilter–scale stress, because they depend on the structure of the volume–averaged flow field over a distance equal to the filter length. An important simplification can be made when the filtered flow field is well–behaved [30], i.e. it contains negligible variations inside the averaging volume: $\langle\langle\mathbf{u}\rangle\rangle \approx \langle\mathbf{u}\rangle$. This then justifies to take volume–averaged quantities out of the volume and surface integrals. The subfilter–scale stress and the drag force can then be approximated by:

$$\boldsymbol{\tau} \approx \langle\tilde{\mathbf{u}}\tilde{\mathbf{u}}\rangle \tag{5.11a}$$

$$\mathbf{f} \approx \frac{1}{\epsilon}\int_A m\mathbf{n}\left[-\frac{\tilde{p}}{\rho}\mathbf{I} + \nu\nabla\tilde{\mathbf{u}}\right] dA + \frac{1}{\epsilon}\left[\nabla\epsilon\right]\frac{\langle p\rangle}{\rho} - \frac{1}{\epsilon}\nu\nabla\epsilon\cdot\nabla\langle\mathbf{u}\rangle \tag{5.11b}$$

Quintard & Whitaker [75] showed that the above approximations for the *local* form of the VANS equations provide criteria for the choice of the filter and the constraints for the filter length. They made distinction between ordered and disordered porous media, as illustrated in figure 5.2. For disordered porous media, they proposed a spherical averaging volume with radius r_0 and a top–hat distribution for the weighting function:

$$m(\mathbf{y}) = \begin{cases} 3/(4\pi r_0^3) & , |\mathbf{y}| \le r_0 \\ 0 & , |\mathbf{y}| > r_0 \end{cases} \tag{5.12a}$$

Ordered porous media are characterized by a unit cell that can be extended periodically in space. For this type of porous medium, Quintard & Whitaker proposed a rectangular averaging volume with a triangular–shaped weighting function:

$$m(\mathbf{y}) = \begin{cases} \prod_{i=1}^{3}\left(l_i - |y_i|\right)/l_i^2 & , |y_i| \le l_i \\ 0 & , |y_i| > l_i \end{cases} \tag{5.12b}$$

where l_i represents the length of the unit–cell basic vector in the direction of y_i.

In order to solve the VANS equations, closures are needed for the subfilter–scale stress and the drag force. In section 2.6, we argued that in porous media subfilter–scale dispersion is normally negligible with respect to the drag force and/or the Reynolds–shear stress of the volume–averaged flow field.

Whitaker [104] gave theoretical support to the following customary parameterization for the drag force:

$$\frac{1}{\epsilon}\int_A m\mathbf{n}\left[-\frac{\tilde{p}}{\rho}\mathbf{I} + \nu\nabla\tilde{\mathbf{u}}\right] dA = -\nu\mathbf{K}^{-1}\epsilon\langle\mathbf{u}\rangle - \nu\mathbf{K}^{-1}\mathbf{F}\epsilon\langle\mathbf{u}\rangle \tag{5.13}$$

where **K** and **F** are respectively the permeability and the Forchheimer tensor. The first term on the right–hand side of (5.13) represents the drag force in the limit of Stokes flow in the pores, whereas the second term is a correction for inertial effects at higher Reynolds numbers. In general, the permeability tensor depends only on the geometry of the porous medium. The Forchheimer tensor depends on the Reynolds number $|\langle \mathbf{u} \rangle| \, d_f/\nu$, with d_f the typical pore diameter, on the geometrical parameters of the porous medium and on the orientation of the solid obstacles relative to the direction of the volume–averaged flow. Generally valid expressions for the permeability and the Forchheimer tensor do not exist, as they are strongly related to the geometry of the porous medium and the Reynolds number. Experiments or numerical calculations of flow through a representative region of the porous medium are required to determine them. Numerical calculations of the permeability and the Forchheimer tensor for several geometries are presented by Zick & Homsy [111], Larson & Higdon [52],[53], Sahraoui & Kaviany [81], Ma & Ruth [60], Lee & Yang [55] and Breugem et al. [13]. A few references to experiments are MacDonald et al. [61], Fand et al. [26], Kececioglu & Jiang [44] and Lage et al. [51]. For flows through packed beds, which are considered in the present study, a widely used relation for the drag force is the modified Ergun equation [7], which is given by (5.13) with the following relations for the permeability and the Forchheimer tensor:

$$\mathbf{K} = \frac{{d_p}^2 \epsilon^3}{180(1-\epsilon)^2} \mathbf{I} \tag{5.14a}$$

$$\mathbf{F} = \tilde{F} \, |\langle \mathbf{u} \rangle| \, \mathbf{I} \quad , \quad \tilde{F} \equiv \frac{\epsilon}{100(1-\epsilon)} \frac{d_p}{\nu} \tag{5.14b}$$

where $d_p \equiv 6V_p/A_p$ is the mean particle diameter with V_p the volume and A_p the surface area of the solid obstacles. The coefficients in (5.14a) and (5.14b) were determined from many experiments with different materials, in which the particle sizes, the porosity and the Reynolds number were varied [61].

5.3 Flow geometry and drag model for the interface region

In our study we consider the flow geometry as sketched in figure 5.3. The upper wall is impermeable. The permeable wall is a homogeneous packed bed. The lower side of the packed bed is bounded by a solid wall. Following Ochoa-Tapia & Whitaker [67], we make distinction between three regions:

1. The homogeneous fluid region or channel region between $z = 0$ and $z = H$ in which the porosity is equal to unity.

2. A small interface region between $z = -\delta_i$ and $z = 0$, characterized by a spatially varying porosity.

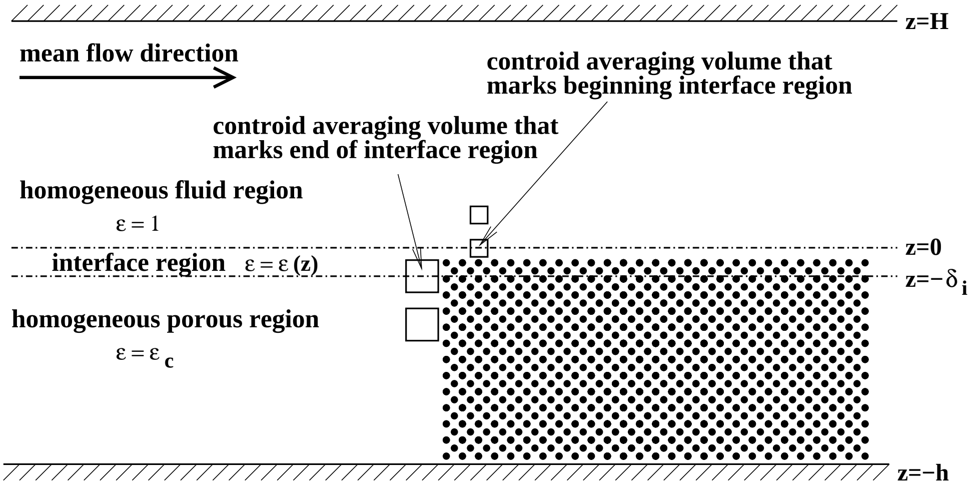
z=H
mean flow direction
controid averaging volume that marks beginning interface region
controid averaging volume that marks end of interface region
homogeneous fluid region
ε = 1
z=0
interface region ε = ε (z)
z=−δ i
homogeneous porous region
ε = ε c
z=−h

Figure 5.3: Sketch of the flow geometry.

3. The homogeneous porous region between $z = -h$ and $z = -\delta_i$, with a constant porosity ($\epsilon = \epsilon_c$).

Below we discuss how the flow is described in each region.

5.3.1 Homogeneous porous region

Based on the arguments given in section 2.6, in the homogeneous porous region subfilter–scale dispersion can be neglected. The drag force is modeled by means of the Ergun equation for packed beds. Combination of equations (5.9a), (5.11b) and (5.13) yields the following transport equation for the flow in the homogeneous porous region:

$$\frac{\partial\langle\mathbf{u}\rangle}{\partial t} + \nabla\cdot\langle\mathbf{u}\rangle\langle\mathbf{u}\rangle = -\frac{1}{\rho}\nabla\langle p\rangle + \nu\nabla^2\langle\mathbf{u}\rangle - \nu\mathbf{K}^{-1}\left(\mathbf{I}+\mathbf{F}\right)\epsilon\langle\mathbf{u}\rangle \tag{5.15}$$

where $\mathbf{K}$ and $\mathbf{F}$ are given by equations (5.14a) and (5.14b) respectively.

5.3.2 Channel region

In the homogeneous fluid region, there are no solid obstacles ($\epsilon = 1$) and hence there is no drag ($1/K = 0$). Thus the VANS equations reduce to the LES equations. The subfilter–scale dispersion term is negligible only when the filter length is sufficiently small. This may not be the case when the *same* filter length is used for the channel region as for the homogeneous porous region. In our DNS we aim to completely resolve the flow field in the channel region. This can be accomplished by assuming that in the channel region the filter length is set by the computational mesh spacing Δ, such that, provided that Δ is sufficiently small, subfilter–scale dispersion is negligible. Consequently, in the channel region $\langle\mathbf{u}\rangle = \mathbf{u}$ holds and the VANS equations reduce to the standard Navier–Stokes equations, i.e. equation (5.15) without the drag term.

5.3.3 Interface region

Like for the homogeneous porous and the homogeneous fluid region, it is assumed that subfilter–scale dispersion can be neglected in the interface region too. The drag force can not be neglected however. It is modeled by means of the Ergun equation in combination with a variable–porosity model, which ensures that the drag force is continuous over the interface region. A similar approach has been used by Ochoa-Tapia & Whitaker [68] to study laminar flow in a plane channel with one permeable wall and one solid wall and by Vafai [95] to analyze the channeling effect in a porous medium near a solid boundary. Below we discuss the variable–porosity model in more detail.

By definition the upper boundary of the interface region ($z = 0$ in figure 5.3) is the position of the centroid of the averaging volume for which the lower part of the averaging volume just touches the solid obstacles in the top region of the permeable wall. The porosity is still equal to unity. When the averaging volume is shifted into the permeable wall, the porosity gradually decreases, until it reaches the value of $\epsilon = \epsilon_c$ at $z = -\delta_i$. In principle, when the topology of the permeable wall is known, the porosity in the interface region can be calculated from equation (5.6), but even for a relatively simple structure of a permeable wall such as sketched in figure 5.3, this is not a straightforward calculation. The porosity is only a function of the vertical position z with a value of one at $z = 0$ and ϵ_c at $z = -\delta_i$. Furthermore, it is demanded that the VANS equations are continuous at the boundaries of the interface region with the homogeneous fluid and the homogeneous porous region. This leads to four additional constraints for the porosity, because it implies that the porosity must have continuous first and second–order derivatives. The simplest profile for the porosity, which satisfies all six constraints, is a fifth–order polynomial in z:

$$-\delta_i \le z \le 0 \ : \ \epsilon(z) = -6(\epsilon_c - 1)\left(\frac{z}{\delta_i}\right)^5 - 15(\epsilon_c - 1)\left(\frac{z}{\delta_i}\right)^4 - 10(\epsilon_c - 1)\left(\frac{z}{\delta_i}\right)^3 + 1 \quad (5.16)$$

The above model for the porosity requires a specification of the thickness δ_i of the interface region. As illustrated in figure 5.3, δ_i is of the order of the filter length.

Combining equations (5.9a), (5.11b) and (5.13), we obtain the following transport equation for the flow in the interface region:

$$\begin{aligned} \frac{\partial \langle \mathbf{u} \rangle}{\partial t} + \frac{1}{\epsilon}\nabla \cdot [\epsilon \langle \mathbf{u} \rangle \langle \mathbf{u} \rangle] &= -\frac{1}{\rho}\nabla \langle p \rangle + \nu \nabla^2 \langle \mathbf{u} \rangle + \frac{\nu}{\epsilon}\nabla \epsilon \cdot \nabla \langle \mathbf{u} \rangle + \\ & \quad \frac{\nu}{\epsilon}\left[\nabla^2 \epsilon\right] \langle \mathbf{u} \rangle - \nu \mathbf{K}^{-1} [\mathbf{I} + \mathbf{F}] \, \epsilon \langle \mathbf{u} \rangle \end{aligned} \quad (5.17)$$

with the porosity described by equation (5.16), and **K** and **F** given by equations (5.14a) and (5.14b) respectively.

To simplify the notation, from now on we will omit the brackets denoting the intrinsic volume average of a quantity.

5.4 Implications of wall permeability for scaling of turbulence

In this section the implications of wall permeability for the scaling of turbulence is discussed. In the DNS the permeable wall is characterized by three different length scales: the thickness h, the mean particle diameter d_p and the square root of the permeability $\sqrt{K_c} \equiv \sqrt{K\,(\epsilon = \epsilon_c)}$. The latter scale can be interpreted as the *effective* pore diameter. The thickness δ_i of the interface region is related to the filter length and hence to d_p, and is thus not an independent length scale. To avoid any influence of the impermeable wall at $z = -h$ (below the porous medium) on the flow in the channel, it is demanded that h is much larger than the penetration depth of turbulence inside the permeable wall. In that case h is no longer a relevant length scale for the flow. This is in contrast to flow over vegetation where the penetration depth of turbulence is usually of the same order as the whole vegetation height [28].
As mentioned in the introduction, a permeable wall is usually also rough. In principle, the additional effect of surface roughness could be quantified by comparing the flow over the *permeable and rough wall* with the flow over an *impermeable wall with the same surface roughness.* The difference between these two walls is illustrated in figure 5.1. In literature it is common practice to characterize a rough wall by the typical height of the roughness elements, which in our case is the mean particle diameter d_p. The effect of roughness depends on the *roughness Reynolds number*, defined according to:

$$Re_d \equiv \frac{d_p u_\tau}{\nu} \tag{5.18}$$

Based on Nikuradse's experiments on flows through circular pipes with a sand–roughened wall, Hinze [35] (p. 635) defines a fully rough wall, i.e. when no viscous sublayer can be distinguished above the top of the roughness elements, by the condition that $Re_d > 55$. According to Hinze's classification, the effect of roughness is negligible when $Re_d < 5$. Although this classification is based on experiments with rough and simultaneously impermeable walls, it can give a clue on the importance of roughness for cases that the wall is not only rough, but also permeable. Similar to (5.18), the effect of wall permeability depends on the *permeability Reynolds number*, defined according to:

$$Re_K \equiv \frac{\sqrt{K_c}\, u_\tau}{\nu} \tag{5.19}$$

As explained in the introduction, wall permeability is expected to have only an influence on the turbulent flow when this ratio is sufficiently large.
In this work we aim to study exclusively the effect of wall permeability. Therefore it is demanded that Re_d is sufficiently small and that Re_K is sufficiently large. This can be accomplished by choosing a small value for d_p and a high value for ϵ_c.
Figure 5.4 shows a sketch of the expected scaling regions for turbulent flow in a plane channel with a solid top wall and a highly permeable bottom wall. In the channel region

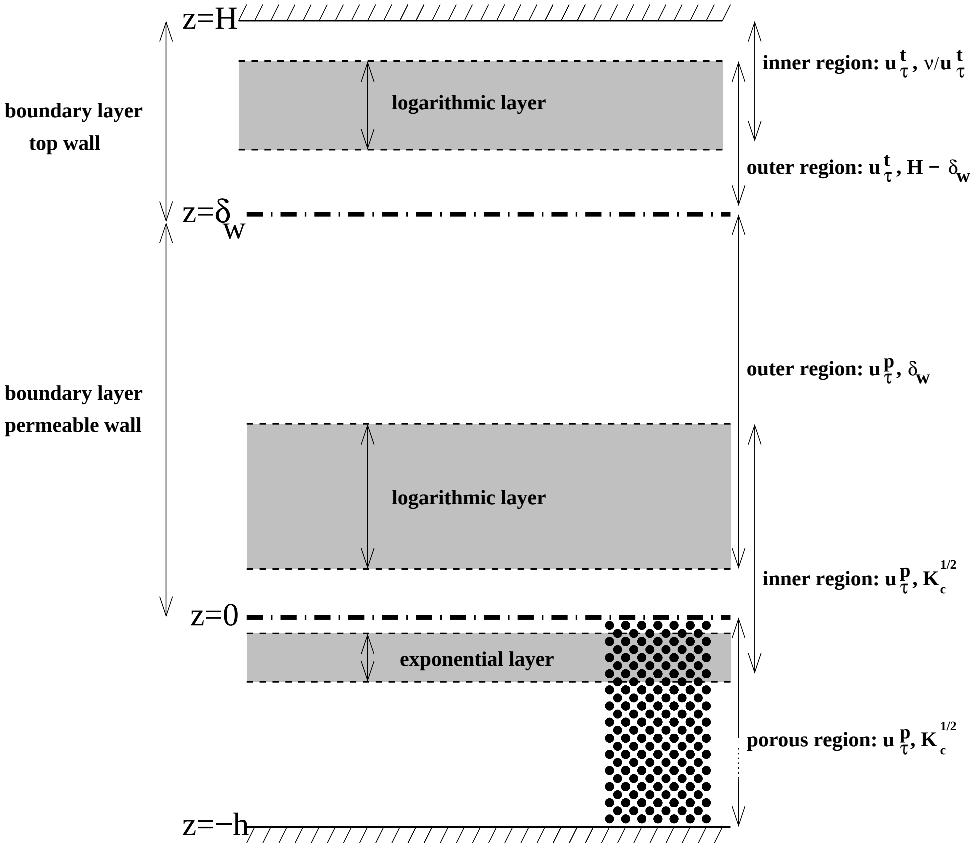
z=H
boundary layer top wall
logarithmic layer
inner region: u_τ^t, ν/u_τ^t
outer region: u_τ^t, H − δ_w
z=δ_w
boundary layer permeable wall
outer region: u_τ^p, δ_w
logarithmic layer
inner region: u_τ^p, $K_c^{1/2}$
z=0
exponential layer
porous region: u_τ^p, $K_c^{1/2}$
z=−h

Figure 5.4: Expected scaling regions for turbulent flow in a plane channel with a solid top wall and a highly permeable bottom wall. It is assumed that the thickness h of the permeable wall is large, that the permeability Reynolds number Re_K is large and that the roughness Reynolds number Re_d is small, such that $\sqrt{K_c}$ is the only relevant length scale of the permeable wall.

two boundary layers can be distinguished: one above the permeable wall and one below the solid top wall. The border between the two boundary layers corresponds to the location of the mean velocity maximum or, equivalent to this, the height $z = \delta_w$ at which the total shear stress τ_{xz} is equal to zero. An expression for the total shear stress is found from the integration of the Reynolds–averaged momentum equation:

$$\frac{\tau_{xz}}{\rho} \equiv -\overline{u'w'} + \nu\frac{\partial\overline{u}}{\partial z} = -\left[(u_\tau^p)^2 + (u_\tau^t)^2\right]\frac{z}{H} + (u_\tau^p)^2 \quad , \quad 0 \le z \le H \qquad (5.20)$$

where $u_\tau^p \equiv \sqrt{\tau_{xz}(0)/\rho}$ is the friction velocity at the permeable wall and $u_\tau^t \equiv \sqrt{-\tau_{xz}(H)/\rho}$ is the friction velocity at the top wall. An expression for δ_w is obtained from substituting $\tau_{xz}(\delta_w) \equiv 0$ into the above equation:

$$\frac{\delta_w}{H} = \frac{(u_\tau^p)^2}{(u_\tau^p)^2 + (u_\tau^t)^2} \qquad (5.21)$$

According to the well–known classic theory [35],[93] for turbulent flow over a solid wall, in the boundary layer at the top wall an inner and an outer region can be distinguished. The characteristic velocity scale for both regions is the same and given by the friction velocity u_τ^t at the top wall. A typical turbulence length scale for the inner region is ν/u_τ^p and a characteristic length scale for the outer region is the thickness $H - \delta_w$ of the boundary layer. The inner and the outer region partly overlap. The familiar 'logarithmic law' for the mean velocity in this overlap region is found from an asymptotic matching of the derivatives of the 'law of the wall' for the inner region and the 'defect law' for the outer region.

Based on a similar analysis we will now show that a logarithmic law is expected also in part of the boundary layer above the *permeable* wall. Like for the boundary layer at the top wall, in the boundary layer at the permeable wall an inner and an outer region can be distinguished. The characteristic velocity scale for both regions is the same and given by the friction velocity u_τ^p at the permeable wall. As explained in the introduction, for $Re_K \gg 1$ it can be expected that the effect of viscosity on the flow is negligible. The single relevant length scales for the turbulence are therefore δ_w and $\sqrt{K_c}$.

The square root of the permeability $\sqrt{K_c}$ is a typical length scale for the inner region. This leads to the following formulation of the law of the wall near a permeable wall for $Re_K \gg 1$:

$$\frac{\overline{u}}{u_\tau^p} = p\left(\frac{z+d}{\sqrt{K_c}}\right) \tag{5.22}$$

where p is a dimensionless function and d is the displacement height, which expresses that the virtual height at which $p = 0$ is located inside the permeable wall ($z < 0$).

The boundary–layer thickness δ_w is a typical length scale for the outer region. This leads to the following formulation of the defect law [38],[77]:

$$\frac{U_m - \overline{u}}{u_\tau^p} = q\left(\frac{z+d}{\delta_w}\right) \tag{5.23}$$

where q is a dimensionless function.

The inner and the outer region partly overlap. Provided that $\delta_w/\sqrt{K_c} \gg 1$, a logarithmic velocity distribution can be derived for the overlap region from an asymptotic matching of the velocity gradients for the inner and the outer region:

$$\lim_{\left(\frac{z+d}{\sqrt{K_c}}\right)\to\infty} \left(\frac{z+d}{\sqrt{K_c}}\right) p'\left(\frac{z+d}{\sqrt{K_c}}\right) = \frac{1}{\lambda} = \lim_{\left(\frac{z+d}{\delta_w}\right)\to 0} -\left(\frac{z+d}{\delta_w}\right) q'\left(\frac{z+d}{\delta_w}\right) \tag{5.24}$$

where λ is equivalent to the Von Kármán constant κ for a solid wall, and where the primes denote differentiation with respect to the argument. Because the arguments of the function p and q are independent of each other, λ is a constant. Integration of the first equality in (5.24) leads to a logarithmic law:

$$\frac{\overline{u}}{u_\tau^p} = \frac{1}{\lambda}\ln\left(\frac{z+d}{z_0}\right) \tag{5.25}$$

where z_0 is proportional to $\sqrt{K_c}$. Based on the right equality in (5.24) and the fact that the defect law (5.23) does not depend on $\sqrt{K_c}$, it is expected that λ is equal to κ. For smooth and rough walls, $\kappa \approx 0.4$ [77]. The displacement height d is expected to depend on the permeability Reynolds number $\sqrt{K_c}u_\tau^p/\nu$. In the limit of $\sqrt{K_c}u_\tau^p/\nu \to 0$, i.e. a smooth and impermeable wall, $d = 0$. In the limit of $\sqrt{K_c}u_\tau^p/\nu \to \infty$, i.e. a completely permeable wall, the turbulence is bounded by the solid wall at $z = -h$ and consequently $d = h$.

Let us now have a closer look at the flow in the porous region. In the homogeneous porous region the Reynolds–averaged VANS equations (5.15) reduce to:

$$0 = -\frac{1}{\rho}\frac{d\overline{p}}{dx} - \frac{\partial\overline{u'w'}}{\partial z} + \nu\frac{\partial^2\overline{u}}{dz^2} - \frac{\nu\epsilon_c}{K_c}\overline{u} - \frac{\nu\epsilon_c\tilde{F}_c}{K_c}\overline{|\mathbf{u}|u} \tag{5.26a}$$

$$0 = -\frac{1}{\rho}\frac{d\overline{p}}{dz} - \frac{\partial\overline{w'w'}}{\partial z} - \frac{\nu\epsilon_c\tilde{F}_c}{K_c}\overline{|\mathbf{u}|w} \tag{5.26b}$$

where the subscript c refers to the constant porosity in this region, and $\tilde{F}_c \equiv \tilde{F}(\epsilon = \epsilon_c)$ with $\tilde{F}$ defined in equation (5.14b). For small Re_K, equations (5.26a) and (5.26b) reduce to the Brinkman equations [14]:

$$0 = -\frac{1}{\rho}\frac{d\overline{p}}{dx} + \nu\frac{\partial^2\overline{u}}{dz^2} - \frac{\nu\epsilon_c}{K_c}\overline{u} \tag{5.27a}$$

$$0 = -\frac{1}{\rho}\frac{d\overline{p}}{dz} \tag{5.27b}$$

The solution is a decaying exponential function, which matches the velocity U_i at $z = -\delta_i$ to the Darcy velocity U_d further down inside the permeable wall:

$$\overline{u} = U_d + (U_i - U_d)\exp\left[z\sqrt{\frac{\epsilon_c}{K_c}}\right] \quad , \quad z \leq -\delta_i \tag{5.28a}$$

$$U_d = -\frac{1}{\mu}\frac{K_c}{\epsilon_c}\frac{d\overline{p}}{dx} \tag{5.28b}$$

where we recall that δ_i is the thickness of the interface region (see figure 5.3). Equation (5.27a) expresses the balance between viscous diffusion of momentum into the permeable wall and the Darcy drag force. For a high value of Re_K, turbulent diffusion and Forchheimer drag become important. However, in that case it is difficult to obtain an analytical expression for the velocity profile from (5.26a). For flows in plant canopies the mean velocity is usually parameterized by an exponential function, and, as will be shown in section 5.6.1, this appears to be a good approximation:

$$\overline{u} \approx U_d + (U_i - U_d)\exp\left[\alpha z\sqrt{\frac{\epsilon_c}{K_c}}\right] \quad , \quad z \leq -\delta_i \tag{5.29a}$$

where α is an empirical coefficient. The velocity U_d is found from the balance between the pressure gradient and two drag terms in equation (5.26a):

$$U_d = \frac{\left(1 - \frac{4}{\mu}\frac{K_c}{\epsilon_c}\frac{d\overline{p}}{dx}\tilde{F}_c\right)^{1/2} - 1}{2\tilde{F}_c} \tag{5.29b}$$

If Re_K is small, then equation (5.29a) reduces to equation (5.28a) with the value of α equal to unity. For very large Re_K, turbulent diffusion is balanced solely by Forchheimer drag. In this case the value for α can be estimated from:

$$\frac{\left[-\frac{\partial\overline{u'w'}}{\partial z}\right]}{\left[-\frac{\nu\epsilon_c\tilde{F}_c}{K_c}\overline{|\mathbf{u}|u}\right]} \sim \frac{\left[\alpha\sqrt{\frac{\epsilon_c}{K_c}}(u_\tau^p)^2\right]}{\left[\nu\frac{\epsilon_c}{K_c}\tilde{F}_c(u_\tau^p)^2\right]} \sim 1 \quad \Rightarrow \quad \alpha \sim \nu\sqrt{\frac{\epsilon_c}{K_c}}\tilde{F}_c \tag{5.30}$$

where it is used that the velocity u scales with u_τ^p. We remark that the scaling factor $(1/\alpha)\sqrt{K_c/\epsilon_c}$ in equation (5.29a) is now equal to $K_c/(\nu\epsilon_c\tilde{F}_c)$, which is the length scale associated with Forchheimer drag instead of Darcy drag, see equation (5.26a). Thus α has the correct limiting behavior for large Re_K.

5.5 Numerical method

In section 5.3 the VANS equations were given for the homogeneous porous region, the interface region and the homogeneous fluid region. In a general and dimensionless form they read:

$$\begin{aligned} \frac{\partial\mathbf{u}}{\partial t} &= -\frac{1}{\epsilon}\nabla\cdot[\epsilon\mathbf{u}\mathbf{u}] - \nabla p + \frac{1}{Re_b}\nabla^2\mathbf{u} + \frac{1}{\epsilon Re_b}\nabla\epsilon\cdot\nabla\mathbf{u} \\ &\quad - \frac{1}{Re_b}\frac{Fo}{Da}\epsilon|\mathbf{u}|\mathbf{u} + \frac{1}{Re_b}\left[\frac{\nabla^2\epsilon}{\epsilon} - \frac{\epsilon}{Da}\right]\mathbf{u} \end{aligned} \tag{5.31a}$$

$$\nabla\cdot[\epsilon\mathbf{u}] = 0 \tag{5.31b}$$

where $Re_b \equiv U_bH/\nu$ is the bulk Reynolds number with U_b the bulk velocity in the channel (between $z = 0$ and $z = H$), $Da \equiv K/H^2$ the Darcy number, and $Fo \equiv \tilde{F}U_b$ the Forchheimer number. The porosity ϵ equals unity in the homogeneous fluid region, it is described by equation (5.16) in the interface region, and it is equal to ϵ_c in the homogeneous porous region. The permeability and the Forchheimer parameter are given by equations (5.14a) and (5.14b) respectively. The boundary conditions are the no–slip and no–penetration conditions for the velocity at $z = -h$ and $z = H$.

To solve equations (5.31a) and (5.31b), we consider a channel with finite dimensions and use periodic boundary conditions in the wall–parallel directions. The equations are discretized in space on a Cartesian mesh, which is non–uniform and staggered in the z-direction. The mesh points are clustered around $z = 0$ (permeable wall) and $z = H$ (top wall). The stretch factor, i.e. the difference in cell width between two neighboring cells, is always less than 3.3%. It is largest at $z = -h$ and $z = H/2$, and it gradually becomes smaller near $z = 0$ and $z = H$. We use a pseudo–spectral method for the spatial derivatives in the wall–parallel directions, and a finite–volume method with the central–differencing scheme for the wall–normal direction. The equations are advanced in time with a pressure–correction method. All terms, except the last one, on the right–hand side of equation (5.31a) are integrated in time with the second–order explicit Adams–Bashforth scheme. For the last term the second–order implicit Crank–Nicholson scheme is used [101]. This avoids a small computational time step for small values of the permeability. Our scheme reads:

$$
\begin{aligned}
\frac{\hat{u}_i - u_i^n}{\Delta t} &= \frac{3}{2}R_i^n - \frac{1}{2}R_i^{n-1} - \frac{dP}{dx}\delta_{i1} + \frac{1}{2}S_i\left(\hat{u}_i + u_i^n\right) && \text{(5.32a)}\\
\frac{\partial}{\partial x_i}\left(\epsilon\frac{\partial \hat{p}}{\partial x_i}\right) &= \frac{1}{\Delta t}\frac{\partial \epsilon \hat{u}_i}{\partial x_i} && \text{(5.32b)}\\
u_i^{n+1} &= \hat{u}_i - \Delta t\frac{\partial \hat{p}}{\partial x_i} && \text{(5.32c)}\\
p^{n+1} &= \hat{p} + 2p^n - p^{n-1} && \text{(5.32d)}
\end{aligned}
$$

where $\hat{u_i}$ and $\hat{p}$ are respectively the prediction velocity and the correction pressure, dP/dx is the mean pressure gradient that drives the flow, and R_i and S_i are defined as:

$$
\begin{aligned}
R_i &\equiv -\frac{1}{\epsilon}\frac{\partial \epsilon u_i u_j}{\partial x_j} - \frac{\partial p}{\partial x_i} + \frac{1}{Re_b}\frac{\partial^2 u_i}{\partial x_j^2} + \frac{1}{\epsilon Re_b}\frac{\partial \epsilon}{\partial x_j}\frac{\partial u_i}{\partial x_j} - \frac{1}{Re_b}\frac{Fo}{Da}\epsilon|\mathbf{u}|u_i && \text{(5.33a)}\\
S_i &\equiv \frac{1}{Re_b}\left(\frac{1}{\epsilon}\frac{\partial^2 \epsilon}{\partial x_j^2} - \frac{\epsilon}{Da}\right) && \text{(5.33b)}
\end{aligned}
$$

The value of dP/dx is adjusted in time to enforce a constant bulk velocity in the channel. In the Crank–Nicolson scheme the velocity at time step $n{+}1$ is estimated by the prediction velocity, but it can be shown that our pressure correction scheme is still second–order accurate. The time step Δt is calculated from the constraints for numerical stability as derived by Wesseling [101] for the second–order Adams–Bashforth scheme.

We will show results from four simulations, for which we only changed the porosity ϵ_c in the homogeneous porous region. We will refer to them as E95, E80, E60 and E0. The corresponding values of the porosity ϵ_c are respectively 0.95, 0.8, 0.6 and 0 (solid wall). In all simulations the mean particle diameter is fixed at $d_p/H = 0.01$. The thickness of the interface region is taken equal to $\delta_i/d_p = 2$, which is reasonable for the spatially periodic porous medium like sketched in figure 5.3. The thickness of the permeable wall is $h/H = 1$. The horizontal dimensions of the computational domain are respectively $L_x/H = 5$ and $L_y/H = 3$. The number of mesh points is equal to 256x192x(128+192) in respectively the streamwise, spanwise and wall–normal direction. The bulk Reynolds number is fixed at $Re_b = 5500$. More characteristics are listed in table 5.1.

The initial conditions for the simulations were either a random velocity field with a prescribed mean velocity profile, or the instantaneous velocity field from a previous simulation. In each simulation the time step was initially adapted to the largest value for which

case	ϵ_c	Da_c	Fo_c	Re^t_τ	Δx^{t+}	Δy^{t+}	Δz_c^{t+}	Δz_p^{t+}	Δt^{t+}	ΔT_b	N
$E95$	0.95	$1.9 \cdot 10^{-4}$	10.5	407	7.9	6.4	$0.5 - 5.3$	$0.5 - 8.5$	0.014	53	60
$E80$	0.8	$7.1 \cdot 10^{-6}$	2.2	354	6.9	5.5	$0.4 - 4.6$	$0.4 - 7.4$	0.015	65	100
$E60$	0.6	$7.5 \cdot 10^{-7}$	0.83	350	6.8	5.5	$0.4 - 4.6$	$0.4 - 7.3$	0.017	66	86
$E0$	0	0	0	350	6.8	5.5	$0.4 - 4.6$	–	0.017	89	58

Table 5.1: Characteristics of the simulations. $Da_c \equiv K_c/H^2$ with $K_c \equiv K(\epsilon = \epsilon_c)$, $Fo_c \equiv \tilde{F}_c U_b$ with $\tilde{F}_c \equiv \tilde{F}(\epsilon = \epsilon_c)$, $Re^t_\tau \equiv u^t_\tau H/\nu$. Δx^{t+} and Δy^{t+} are the mesh spacings in respectively the streamwise and the spanwise direction, normalized by ν/u^t_τ. Δz_c^{t+} and Δz_p^{t+} are the dimensionless mesh spacings in the wall–normal direction in respectively the channel and the permeable wall. Δt^{t+} is the time step, normalized by $\nu/(u^t_\tau)^2$, ΔT_b is the time interval over which the statistics are obtained in units of H/U_b, and N is the number of instantaneous data fields used for the statistics.

the criteria for numerical stability were satisfied. When the value of dP/dx reached a steady state, the time step was fixed in time at the value listed in table 5.1.

5.6 Turbulence statistics

5.6.1 Mean velocity

Figure 5.5 shows the mean velocity profile for different values of the wall porosity ϵ_c. The

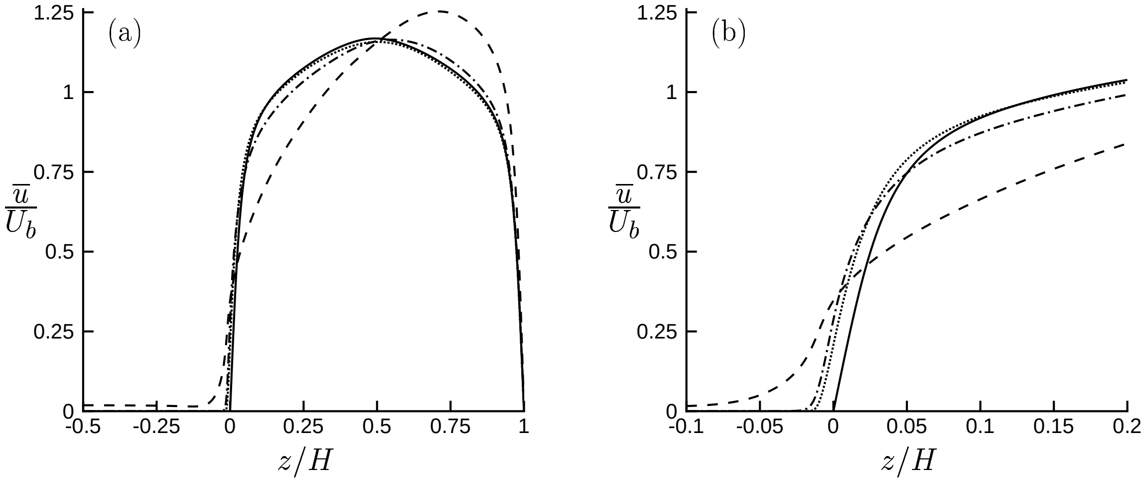

Figure 5.5: (a) Mean–velocity profile for different values of ϵ_c, normalized by the bulk velocity U_b and shown as function of the dimensionless height z/H. For clarity, the region $-1 \leq z/H < -0.5$ is omitted because of a nearly uniform flow. (b) Enlargement of the region around the wall interface. —, case E0; ···, case E60; – · –, case E80; - - -, case E95.

case	ϵ_c	Re^p_τ	Re_K	Re_d	δ_w/H	Re^p_δ	Re^t_δ	$C^t_f(\cdot 10^{-3})$	$C^p_f(\cdot 10^{-3})$
$E95$	0.95	678	9.35	6.78	0.74	498	108	10.9	30.4
$E80$	0.8	398	1.06	3.98	0.56	222	156	8.3	10.5
$E60$	0.6	353	0.31	3.53	0.50	176	175	8.1	8.2
$E0$	0	352	0	0	0.50	176	175	8.1	8.2

Table 5.2: Additional flow characteristics of the simulations. The superscripts t and p refer to respectively the top wall and the permeable wall region. $Re^p_\tau \equiv u^p_\tau H/\nu$, $Re_K \equiv \sqrt{K_c}u^p_\tau/\nu$, $Re_d \equiv d_p u^p_\tau/\nu$, δ_w is defined by (5.21), $Re^p_\delta \equiv \delta_w u^p_\tau/\nu$, $Re^t_\delta \equiv (H-\delta_w)u^t_\tau/\nu$ and $C_f \equiv 2(u_\tau/U_b)^2$.

velocity profile of case E60 is almost identical to the one of case E0. The permeable wall in case E60 behaves apparently similar to a solid wall. For higher wall porosities, the velocity profile is more skewed, with its maximum U_m located closer to the solid top wall. Based on equation (5.21) this implies that the skin friction coefficient $C_f \equiv 2\left(u_\tau/U_b\right)^2$ is larger for the permeable wall than for the solid top wall. In case E95 the difference amounts almost a factor three, see table 5.2. The large skin friction at the permeable wall in case E95 is responsible for a significant increase in the ratio U_m/U_b as compared to case E0, because by definition $\frac{1}{H}\int_0^H \frac{\overline{u}}{U_b}dz = 1$ must hold. It causes even an increase of about 35% in the skin friction coefficient at the top wall.

From figure 5.5.b it is observed that the mean velocity profile exhibits an inflexion point ($d^2\overline{u}/dz^2 = 0$) just below the interface with the permeable wall. An inflexion point was also expected based on the analysis in section 5.4, where it was shown that the mean velocity has a logarithmic behavior in part of the boundary layer above the permeable wall and decays exponentially inside the permeable wall. According to Rayleigh's criterion [23], an inflexion point in the velocity profile is a necessary condition for an inviscid instability, at least for the case of unidirectional laminar flow in a homogeneous fluid region. The inflexional velocity profile could therefore give rise to instabilities of the Kelvin–Helmholtz type, similar to the the instabilities present in a plane mixing layer, as was suggested before by Raupach et al. [77] and Finnigan [28].

Figure 5.6 shows a two–dimensional snapshot along the streamwise direction of the instantaneous flow field in case E95. Near the permeable wall relatively large vortical structures are present, which seem to substantiate the hypothesis of a Kelvin–Helmholtz type of instability. Notice furthermore that the turbulence structure is clearly very different in the boundary layer above the permeable wall compared to the boundery layer below the top wall. Near the top wall elongated streaky structures are observed, which are absent near the permeable wall.

To investigate the properties of the mean flow in the logarithmic layer, the log law (5.28a) is fitted to the mean velocity profile. First the extent of the logarithmic layer is determined from a plot of $(z+d)d\overline{u}^{p+}/dz$, with $\overline{u}^{p+} \equiv \overline{u}/u^p_\tau$, as function of $z^{p+} \equiv zu^p_\tau/\nu$ for several values of d^{p+}. Inside the logarithmic layer this quantity must be a constant equal to $1/\lambda$. Plots of $(z+d)d\overline{u}^{p+}/dz$ are shown in figure 5.7 for cases E0 and E80. In case E0, $d = 0$, because the channel walls are impermeable. A logarithmic layer is present for

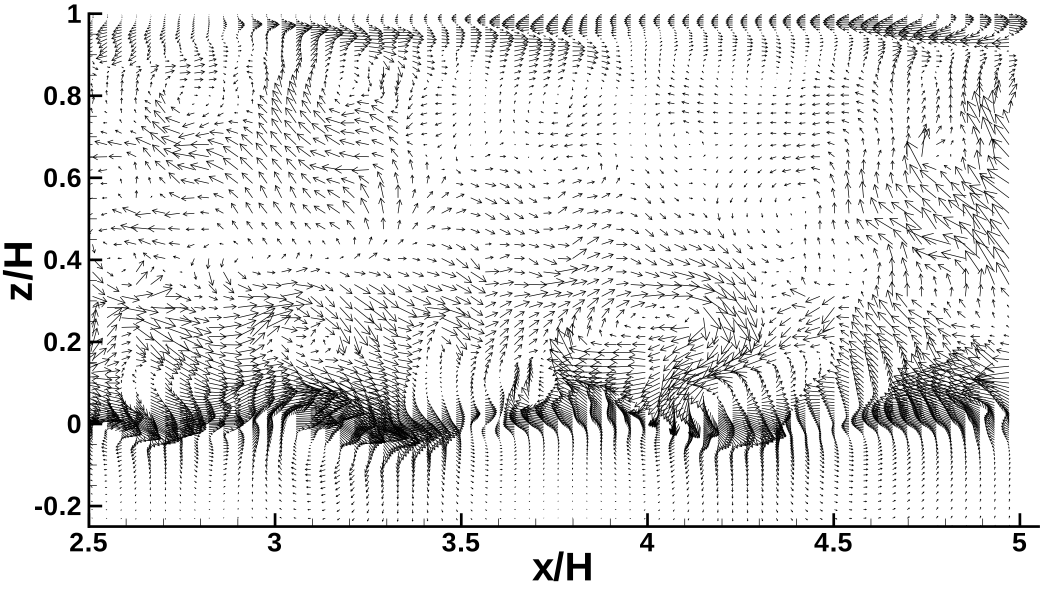

Figure 5.6: Two–dimensional snapshot along the streamwise direction of an instantaneous flow field (u', w') in case E95.

approximately $z^{p+} \in [50 : 120]$. The value of λ is equal to 0.40, which is in agreement with the value of approximately 0.4 for the Von Kármán constant κ for flows over smooth walls. In case E80 a logarithmic layer is found in the range $z^{p+} \in [60 : 140]$ when d^{p+} is taken equal to 21. The corresponding value of λ is 0.31 and this is significantly lower than 0.4. We emphasize that it is not possible to choose d^{p+} such that λ is close to 0.4, which is clear from figure 5.7.b. In case E95 λ is even found to be 0.23. These values are slightly dependent of the choice of the fit interval, but the variation in λ is small. In case E60 the value of d^{p+} was too small to obtain a conclusive value, and therefore it was put to zero. The corresponding value of λ is equal to 0.40, the same as in case E0. The values of d, z_0 and λ obtained from a least–square fit of (5.25) to the velocity profile in the logarithmic layer, are listed in table 5.3.

Figure 5.8.a shows a lin–log plot of the mean velocity in the boundary layer above the permeable wall. The interception of the log law decreases for larger wall porosities, as expected. However, also the slope $(1/\lambda)$ increases for larger wall porosities, which was not expected. We come back to this point later on in this section. In figure 5.8.b a lin–log plot is shown of the mean velocity in the boundary layer below the top wall. The profiles coincide, and this substantiates that the flow near the top wall does not feel the presence of the permeable wall.

According to Jackson [38] and Hinze [35] (p. 637), for many fully rough walls the displacement height in the log law is found to scale with the mean particle diameter d_p according

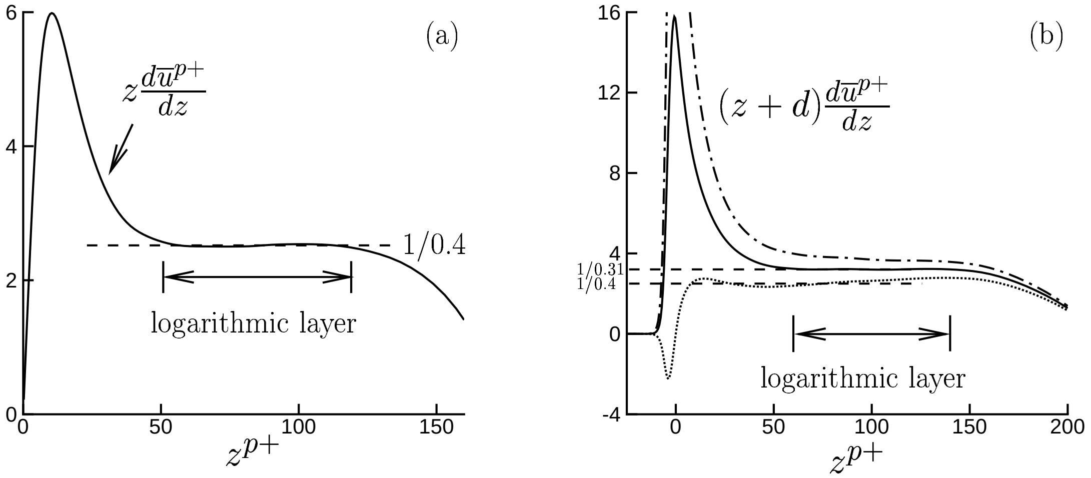

Figure 5.7: (a) $(z+d)\frac{d\overline{u}^{p+}}{dz}$ as function of $z^{p+} \equiv z u_\tau^p/\nu$ for case E0 with $d^{p+} = 0$. (b) Ditto for case E80. The lines correspond to different values of d^{p+}: $\cdots$, $d^{p+} = 0$; —, $d^{p+} = 21$; $-\cdot-$, $d^{p+} = 40$.

case	λ	$z_0/\sqrt{K_c}$	z_0/d_p	z_0/δ_w	z_0^{p+}	$d/\sqrt{K_c}$	d/d_p	d/δ_w	d^{p+}	d^{p+}(JM)	α
*E*95	0.23	5.30	7.32	0.10	49.6	11.3	15.6	0.21	105.6	16.7	0.70
*E*80	0.31	1.33	0.35	0.006	1.41	20.0	5.3	0.10	21.2	4.7	0.99
*E*60	0.40	0.35	0.03	0.0006	0.11	0	0	0	0	3.4	–
I	0.40	∞	∞	0.0006	0.11	0	0	0	0	0	–

Table 5.3: Fit parameters. λ is equivalent to the Von Kármán constant $\kappa \approx 0.4$ for a solid wall. d and z_0 are the length scales in the log law (5.25), normalized by respectively $\sqrt{K_c}$, d_p, δ_w and ν/u_τ^p. The value of d^{p+} in the penultimate column is obtained from Jackson's model (JM), equation (5.39). α is obtained from a least–square fit of (5.29a) to the mean velocity profile in the homogeneous porous region with $z/H \in [-0.85 : -0.02]$.

to $d/d_p \approx 0.3$. For case E95 $d/d_p = 15.6$ and for case E80 $d/d_p = 5.3$, see table 5.3, which is much larger than 0.3. Also the ratio of z_0/d_p is much larger in cases E80 and E95 than the value of approximately 1/30 found from Nikuradse's experiments on flows over fully rough walls covered with homogeneous sand roughness [109] (p. 513). The permeable walls in cases E80 and E95 behave clearly very different from fully rough walls. We note that according to the classification of Hinze [35], the effect of surface roughness is negligible in these cases, because in case E80 the roughness Reynolds number $Re_d \equiv d_p u_\tau^p/\nu = 4$ and in case E95 $Re_d = 6.8$, see table 5.2. The uncommon values for λ, d and z_0 are apparently related to the permeability of the wall. The most striking result is that λ is significantly smaller than 0.4. This is in conflict with an important assumption in the derivation of the log law as discussed in section 5.4, namely that the flow in the outer region does not directly feel the presence of the wall. This is expressed by the defect law (5.23) in which the only relevant length scale is the boundary–layer thickness δ_w, which

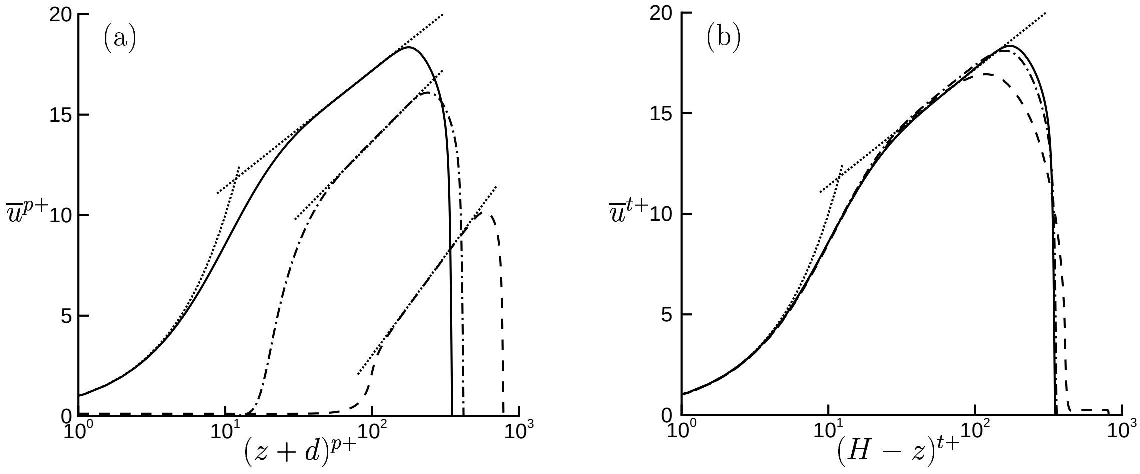

Figure 5.8: (a) Mean velocity $\overline{u}^{p+}$ in the region above the permeable wall, shown as function of the dimensionless shifted height $(z+d)^{p+}$. (b) Ditto, but now in the region below the top wall with $\overline{u}^{t+} \equiv \overline{u}/u_\tau^t$, $d^{t+} \equiv du_\tau^t/\nu = 0$ and $(H-z)^{t+}$ the distance to the top wall. —, case E0; – · –, case E80; - - -, case E95. The dotted straight line are fits of the logarithmic law to the velocity profiles. The fit parameters are listed in table 5.3. The dotted curved lines correspond to $\overline{u}^{p+} = z^{p+}$ and $\overline{u}^{t+} = (H-z)^{t+}$ respectively.

implies that λ should be a universal constant. The other way around, the fact that λ is found to be significantly smaller than 0.4 implies that equation (5.23) does not hold in cases E80 and E95. Figure 5.9.a shows the velocity defect $U_m^{p+} - \overline{u}^{p+}$ as function of $(z+d)/\delta_w$. Indeed it is observed that the velocity defect does not scale with $(z+d)/\delta_w$, but instead figure 5.9.b shows that the velocity defect scales with z/δ_w for $z/\delta_w \gtrsim 0.2$. This observation suggests that the large eddies in the outer region are still blocked by the permeable wall, or sheltered by the mean–shear layer at the interface [36]. We therefore rewrite the defect law according to:

$$\frac{U_m - \overline{u}}{u_\tau^p} = q\left(\frac{z+d-d}{\delta_w}\right) = q\left(\frac{z+d}{\delta_w}, \frac{d}{\delta_w}\right) \tag{5.34}$$

where q is now a dimensionless function of both $(z+d)/\delta_w$ and d/δ_w. Similar to equation (5.24), the asymptotic matching of the velocity gradients for the inner and the outer region yields:

$$\lim_{\left(\frac{z+d}{\delta_w}\right)\to 0} -\left(\frac{z+d}{\delta_w}\right) q'\left(\frac{z+d}{\delta_w}, \frac{d}{\delta_w}\right) = \frac{1}{\lambda} \tag{5.35}$$

where the differentiation is with respect to $(z+d)/\delta_w$. Integration of this equation gives again a log law of the form (5.25), but now λ is a function of d/δ_w. For very small d/δ_w, like in case E60, the value of λ tends to the value of the Von Kármán constant $\kappa \approx 0.4$. For relatively large d/δ_w, like in cases E80 ($d/\delta_w = 0.10$) and E95 ($d/\delta_w = 0.21$), the value

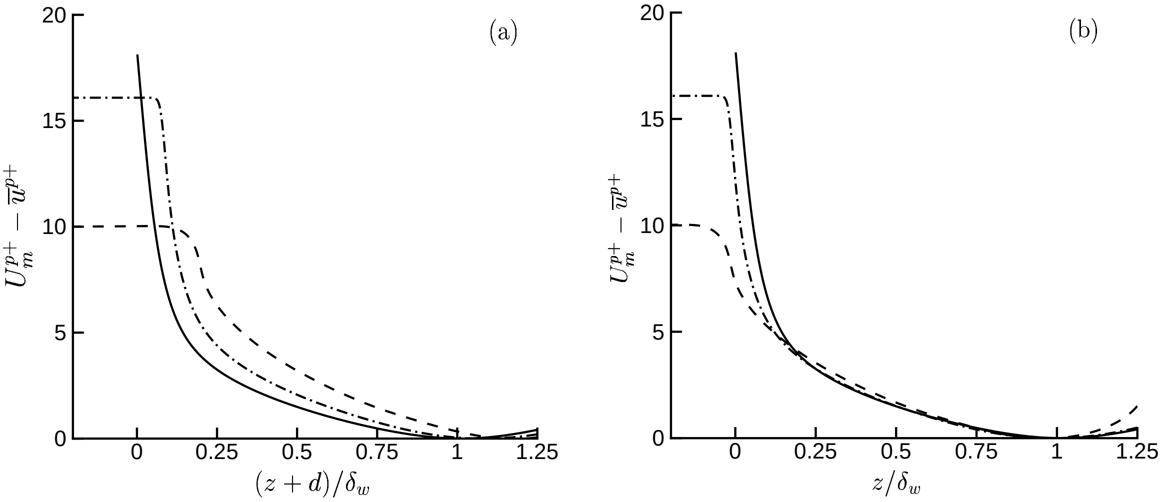

Figure 5.9: Velocity defect $U_m^{p+} - \overline{u}^{p+}$, plotted as function of (a) $(z+d)/\delta_w$; (b) z/δ_w. —, case E0; – · –, case E80; - - -, case E95

of λ becomes significantly smaller than 0.4. We note that for many fully rough walls and vegetation the ratio of $d/\delta_w \sim d_p/\delta_w \ll 1$, which could explain why in these experiments usually $\lambda \approx 0.4$ is found.

Jackson [38] proposed that the displacement height d is related to the point at which the height–averaged drag force acts. For boundary–layer flow over a permeable wall in the absence of a mean pressure gradient this means that d can be calculated from:

$$d = -\frac{\int z f(z) dz}{\int f(z) dz} \tag{5.36}$$

where f is the height–dependent drag force and where the integral extends over the entire height over the permeable wall. Jackson's method is based on the idea that d is related to the penetration depth of the mean flow in the permeable wall. This depth is set by the balance between turbulent and viscous diffusion of momentum into the permeable wall on the one hand and the drag force that absorbs momentum on the other hand. This balance is expressed by the Reynolds–averaged momentum equation for the streamwise direction, which can be obtained from equation (5.31a):

$$-\frac{1}{Re_b}\frac{\epsilon}{Da}\overline{u} - \frac{1}{Re_b}\frac{\epsilon Fo}{Da}\overline{|\mathbf{u}|u} - \frac{1}{Re_b}\frac{1}{\epsilon}\frac{\partial \epsilon}{\partial z}\frac{\partial \overline{u}}{\partial z} - \frac{d\overline{p}}{dx} = \frac{1}{\epsilon}\frac{\partial}{\partial z}\left[\epsilon\overline{u'w'} - \frac{1}{Re_b}\frac{\partial \epsilon \overline{u}}{\partial z}\right] \tag{5.37}$$

Jackson proposed his model for boundary–layer flow in the absence of a mean pressure gradient. In the presence of a mean pressure gradient, the drag force is not only balancing diffusion of momentum, but also the mean pressure gradient. To correct for the effect of the mean pressure gradient, we define the effective drag force f_e as the drag force f (given by equation (5.11b) with equation (5.13) for the surface integral) minus the mean pressure gradient:

$$f_e \equiv f - \frac{d\overline{p}}{dx} = -\frac{1}{Re_b}\frac{\epsilon}{Da}\overline{u} - \frac{1}{Re_b}\frac{\epsilon Fo}{Da}\overline{|\mathbf{u}|u} - \frac{1}{Re_b}\frac{1}{\epsilon}\frac{\partial \epsilon}{\partial z}\frac{\partial \overline{u}}{\partial z} - \frac{d\overline{p}}{dx} \tag{5.38}$$

Furthermore, equation (5.36) is modified according to:

$$d = d_1 + d_2 \quad ; \quad d_2 = -\frac{\int z f_e(z) dz}{\int f_e(z) dz} \quad \text{with} \quad z < -d_1 \tag{5.39}$$

where between $z \in [-d_1 : 0]$ the effective drag force is positive and where the integration is only carried out over the range $z < -d_1$ for which $f_e < 0$. This modification ensures that d approaches the correct limits when $K_c \to 0$ or $K_c \to \infty$ [2]. Figure 5.10 presents profiles of f, $-d\overline{p}/dx$ and f_e in case E95. Also indicated are d_1 and d_2 calculated from equation (5.39). Their sum is equal to $d^{p+} = 16.7$, which is more than six times smaller than the value obtained from a log fit to the velocity profile. For all simulations the value for d obtained from Jackson's model is listed in table 5.3. Although the trend is correct,

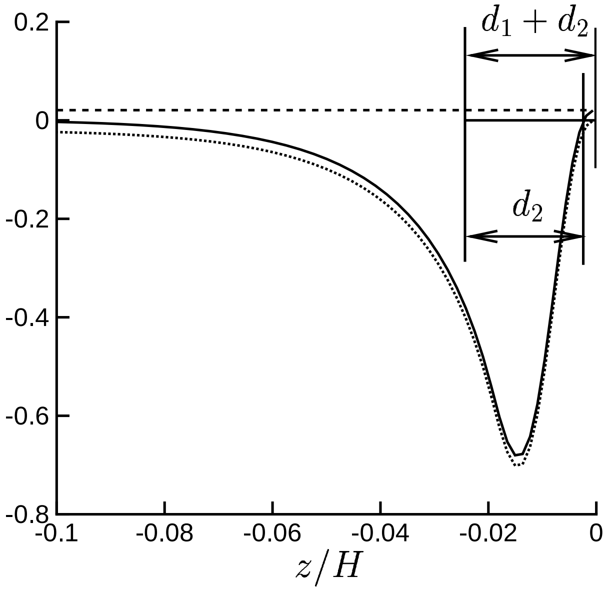

Figure 5.10: Profiles of the pressure gradient, the drag force and the effective drag force in case E95, normalized by $\rho U_b^2/H$ and shown as function of z/H. $\cdots$, f; - - -, $-d\overline{p}/dx$; — f_e. d_1 and d_2 are contributions to the displacement height based on Jackson's model.

---

[2] When $K_c \to \infty$, i.e. no solid obstacles, the effective drag force becomes equal to $-d\overline{p}/dx$. Consequently, $d = d_1 = h$ where h is the whole thickness of the permeable wall, which is the correct value as in this case the impermeable wall at $z = -h$ is the actual wall. When $K_c \to 0$, i.e. when the permeable wall is completely impermeable, there is no flow inside the permeable wall and hence the effective drag force is equal to zero. This leads to the correct limit of $d = 0$.

i.e. d increases with increasing permeability, Jackson's model strongly underpredicts d. The assumption of Jackson that $z = -d$ is the height at which the height–averaged drag force acts, is apparently not correct for the present simulations.
We will now investigate the velocity profile inside the permeable wall. As discussed in section 5.4, the mean flow is expected to decrease exponentially inside the permeable wall. This is confirmed by figure 5.11 which shows the mean velocity in the top region of the permeable wall as function of $\alpha z\sqrt{\epsilon_c/K_c}$. The value of α is obtained from a least–square fit of equation (5.29a) to the velocity profile in the homogeneous porous region. In case E60 α could not be determined, because at $z/H = -0.02$ the mean velocity has already reached the constant Darcy velocity U_d. In case E80 $\alpha \approx 0.99$. This indicates that in the homogeneous porous region the mean flow is governed by the Brinkman equations with the corresponding solution given by (5.28a). In case E95 $\alpha \approx 0.70$, which suggests that turbulent diffusion dominates over viscous diffusion in the top layer of the permeable wall. Notice that the exponential solution (5.29a) gives not only a good fit in the homogeneous porous region, but also in the interface layer up to $z = 0$.

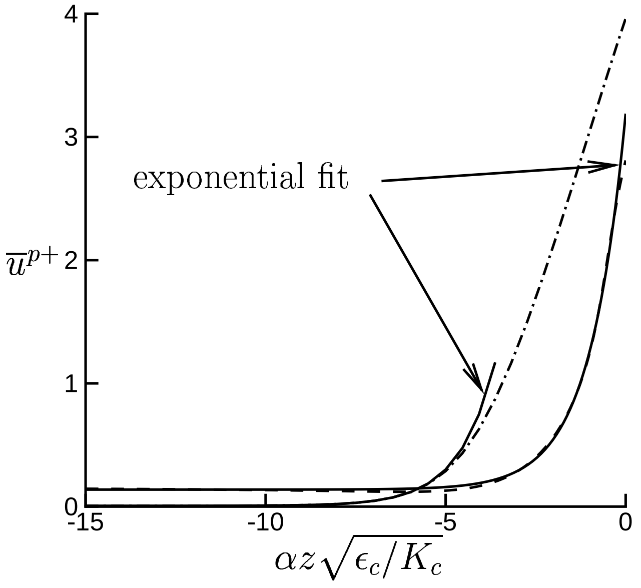

Figure 5.11: Mean velocity $\overline{u}^{p+}$ in the top region of the permeable wall as function of the dimensionless height $\alpha z\sqrt{\epsilon_c/K_c}$. – · –, case E80; - - -, case E95. The solid lines are fits of the exponential function (5.29a) to the velocity profiles. The coefficient α is listed in table 5.3.

5.6.2 Mean kinetic energy

To gain insight in the dynamics of the mean flow, the terms in the transport equation for the mean kinetic energy (MKE) $\frac{1}{2}\overline{u}^2$ have been investigated. This equation is obtained from multiplying equation (5.37) by $\overline{u}$:

$$\begin{aligned} 0 \;=\; & \underbrace{-\overline{u}\frac{d\overline{p}}{dx}}_{P} + \underbrace{\overline{u'w'}\frac{\partial\overline{u}}{\partial z}}_{WS} \underbrace{-\frac{1}{\epsilon}\frac{\partial\epsilon\overline{u}\,\overline{u'w'}}{\partial z}}_{TT} + \underbrace{\frac{1}{Re_b}\frac{\partial^2\frac{1}{2}\overline{u}^2}{\partial z^2}}_{VD} \underbrace{-\frac{1}{Re_b}\left(\frac{\partial\overline{u}}{\partial z}\right)^2}_{D} \\ & + \underbrace{\frac{1}{Re_b}\frac{1}{\epsilon}\frac{\partial\epsilon}{\partial z}\frac{\partial\frac{1}{2}\overline{u}^2}{\partial z} + \frac{1}{Re_b}\frac{1}{\epsilon}\frac{\partial^2\epsilon}{\partial z^2}\overline{u}^2}_{POR} \underbrace{-\frac{1}{Re_b}\frac{\epsilon}{Da}\overline{u}^2}_{DAR} \underbrace{-\frac{1}{Re_b}\frac{\epsilon Fo}{Da}\overline{|\mathbf{u}|u}\,\overline{u}}_{FOR} \end{aligned} \tag{5.40}$$

Term P represents the work by the mean pressure gradient, term WS represents the loss due to deformation work by the Reynolds–shear stress, terms TT and VD represent respectively turbulent transport and viscous diffusion, and term D represents viscous dissipation. The last three terms on the right–hand side are only non–zero inside the permeable wall. The POR–terms originate partly from viscous diffusion and partly from viscous drag, and represent transport and dissipation of energy by local changes in the porosity. The DAR– and the FOR–terms represent the transfer of resolved–scale MKE, i.e. the MKE of the volume–averaged flow, to the subfilter–scale MKE by Darcy drag and Forchheimer drag respectively. The terms in (5.40) are plotted in figure 5.12 for cases E95, E80 and E0. The ultimate source of MKE is the work by the mean pressure gradient $-\overline{u}\,d\overline{p}/dx$, and that is why we have chosen to normalize the budget terms by $U_m\left[(u_\tau^p)^2 + (u_\tau^t)^2\right]/H$. For clarity the terms POR, DAR and FOR are shown separately from the other terms. The sum of all computed terms in (5.40) is very small compared to the dominant terms.

It is observed from graphs (a), (d) and (e) that sufficiently far away from the permeable wall, term P is in local balance with terms WS and TT. Term TT is responsible for transport of MKE from the channel towards the permeable wall. Close to the wall there are considerable differences between the cases. In case E95 terms VD and D are almost negligible. Term TT peaks just below the wall interface, balancing terms WS and FOR. This observation confirms our suggestion in the previous section, based on the value of $\alpha \approx 0.7$, that in case E95 turbulent diffusion dominates over viscous diffusion in the top layer of the permeable wall. In the core of the permeable wall ($z/\delta_w \lesssim -0.15$), term P balances terms DAR and FOR, but, because these terms are very small in this region, this can not be observed.

In case E80 term TT peaks just above the permeable wall and vanishes just below the interface, in a region where viscous diffusion is balanced by viscous dissipation. Further down in the permeable wall, term P balances term DAR. These observations show that in case E80 the mean flow inside the permeable wall is governed by the Brinkman equations, as suggested in the previous section based on the value of $\alpha \approx 1$.

Comparing cases E95, E80 and E0, we observe that in case E95 viscous effects are almost

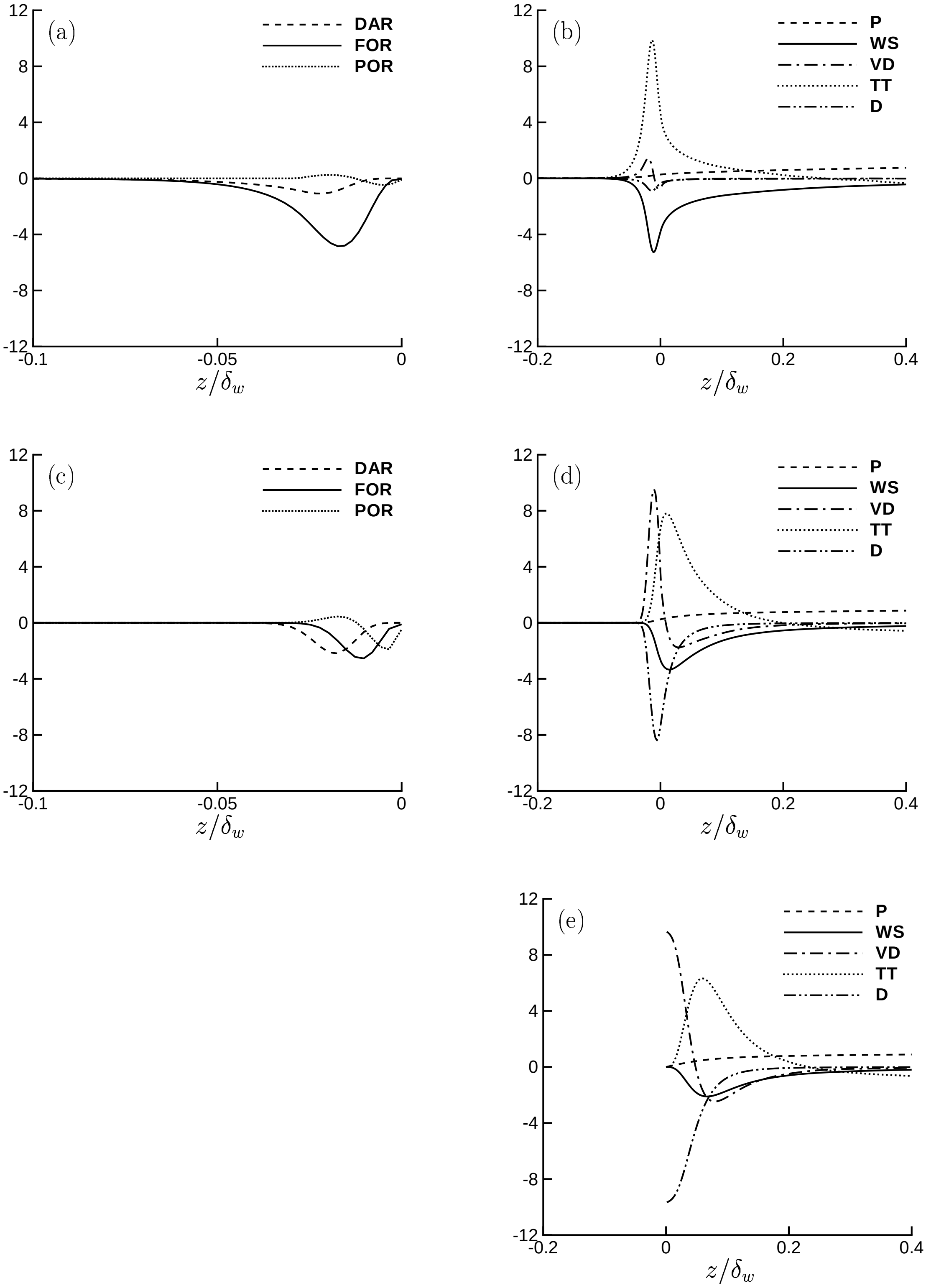

Figure 5.12: Terms in the transport equation for the mean kinetic energy $\overline{u}^2/2$, normalized by $U_m\left[(u_\tau^p)^2 + (u_\tau^t)^2\right]/H$ and shown as function of z/δ_w. (a),(b) case E95; (c),(d) case E80; (e) case E0.

negligible and that in case E80 viscous effects are more confined to the permeable wall relative to case E0. Similar to the classification of rough walls, where a fully rough wall is defined as a wall above which a viscous sublayer is absent, we give the following classification of the permeable walls in cases E95, E80 and E60:

- The permeable wall in case E95 is *highly permeable.*
- The permeable wall in case E80 is *partially permeable.*
- The permeable wall in case E60 is *effectively impermeable.*

As discussed in the introduction, whether or not a wall is permeable for the flow above the wall is basically determined by the permeability Reynolds number $Re_K \equiv \sqrt{K_c} u_\tau^p / \nu$. The values of Re_K for the different simulations are listed in table 5.2. In case E95, $Re_K = 9.35$, which is apparently in the highly permeable regime, whereas a value of 0.31, like in case E60, corresponds to an effectively impermeable wall.

5.6.3 Velocity and pressure fluctuations

Figure 5.13 shows the profiles of the rms velocities for different values of the wall porosity ϵ_c. The rms velocities are normalized by the friction velocity u_τ^t at the top wall and plotted as function of z/H. The symbols represent the profiles from the DNS of Kim et al. [45] of turbulent channel flow between two solid walls, which are in excellent agreement with the profiles of case E0. Close to the top wall the profiles coincide, as expected, which indicates that the influence of the permeable wall on the rms velocities near the top wall is negligible. In the boundary layer above the permeable wall, a strong increase is observed in the rms velocities with respect to the boundary layer below the top wall. This increase is most pronounced for the spanwise and wall–normal fluctuations, which can be attributed to the weakening of the wall–blocking and the wall–induced viscous effect near a permeable wall relative to an impermeable wall.

Figure 5.14 shows again the rms profiles of the velocity components, but now normalized by the friction velocity u_τ^p at the permeable wall and plotted as function of z/δ_w. The profiles of the streamwise rms velocity coincide for $z/\delta_w \gtrsim 0.4$. The profiles of the spanwise and the wall–normal rms velocities exhibit less similarity. As discussed in the introduction, similar observations were made in the experiments of Krőgstad et al. [48] and Krőgstad & Antonia [47] on boundary–layer flows over rough walls. They reported a significant increase in the wall–normal rms velocity, which was attributed to a weakening of the wall–blocking effect, whereas the streamwise rms velocity remained unchanged as compared to a smooth wall.

Close to the permeable wall, the peak in the streamwise rms profile is lower for higher wall porosity, whereas the peaks in the profiles of the two other rms velocities are higher for higher wall porosity. The smaller peak in the streamwise rms profile is consistent with the absence of streaky structures above a highly permeable wall, see figure 5.6. The peak in the turbulent kinetic energy $(u_{\rm rms}^2 + v_{\rm rms}^2 + w_{\rm rms}^2)/2$ therefore decreases for higher wall

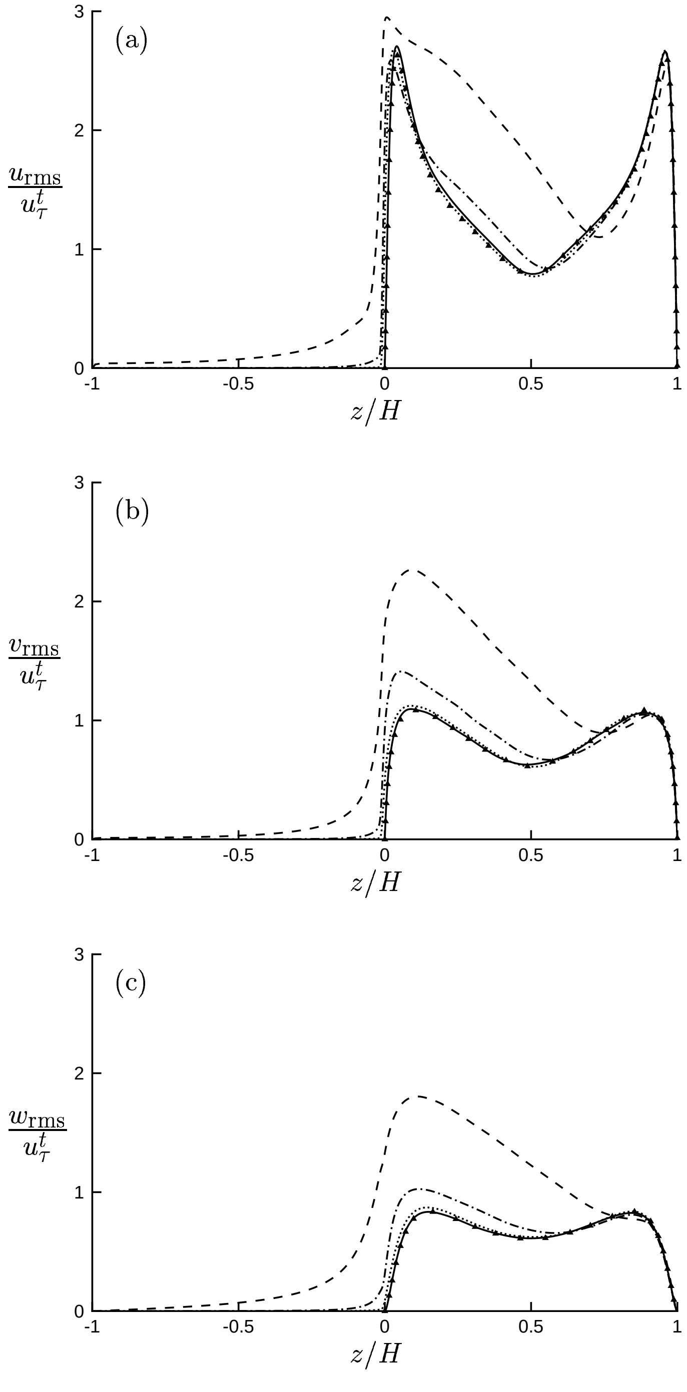

Figure 5.13: Profiles of the rms velocities, normalized by the friction velocity u_τ^t at the top wall, as function of z/H. The symbols refer to the DNS data of Kim et al. [45]. (a) streamwise component; (b) spanwise component; (c) wall–normal component. —, case E0; · · ·, case E60; – · –, case E80; - - -, case E95.

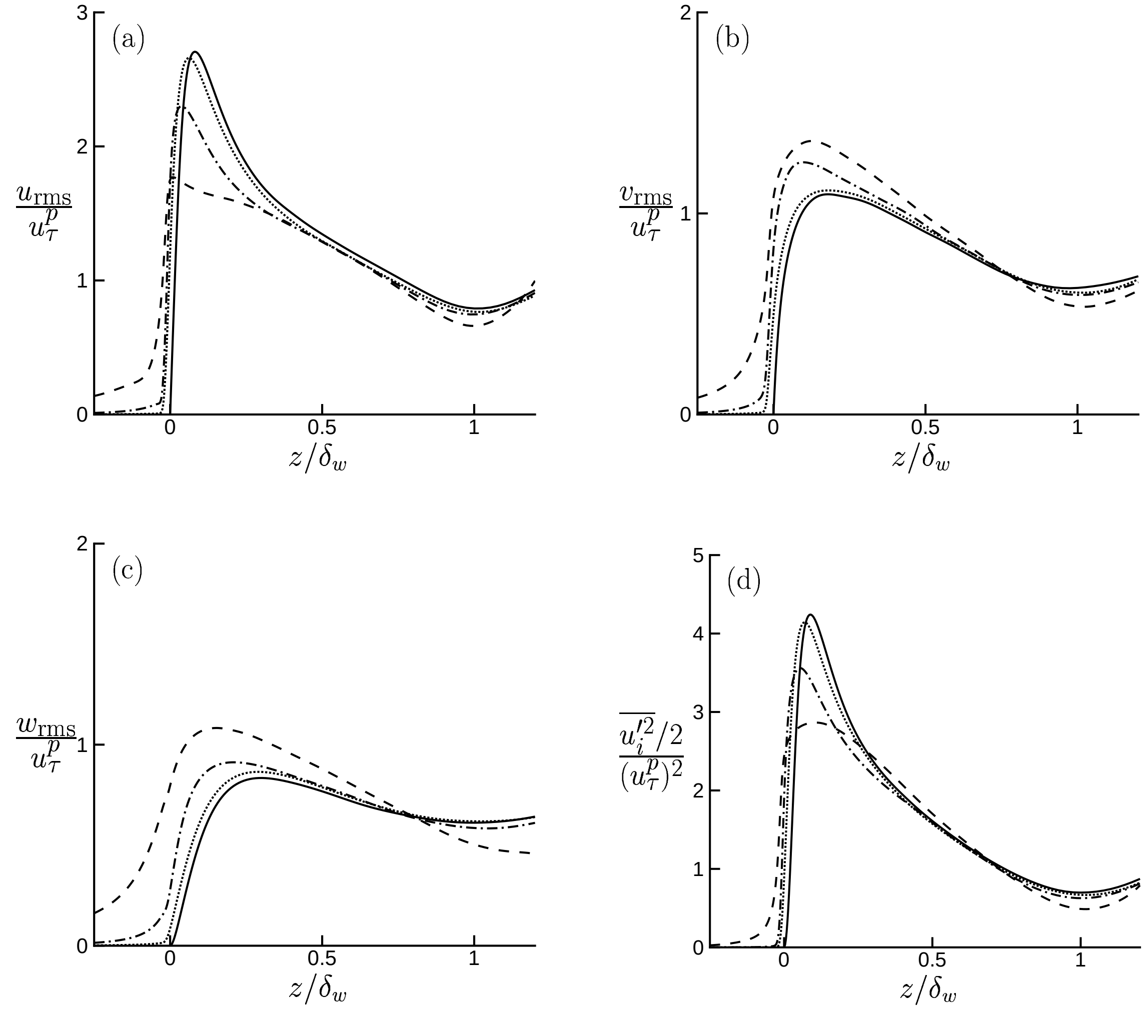

Figure 5.14: Profiles of the rms velocities and the turbulent kinetic energy, normalized by respectively u_τ^p and $(u_\tau^p)^2$ and plotted as function of z/δ_w. (a) rms streamwise velocity; (b) rms spanwise velocity; (c) rms wall–normal velocity; (d) turbulent kinetic energy. —, case E0; $\cdots$, case E60; – · –, case E80; - - -, case E95.

porosity, as can be observed from figure 5.14.d.
The rms velocities decrease rapidly inside the permeable wall, which is a consequence of drag. Far down in the permeable wall, the velocity fluctuations are governed by Darcy's Law with the linearized Forchheimer correction:

$$0 = -\frac{\partial p'}{\partial x_i} - \frac{\epsilon_c}{Re_b Da_c} u'_i - \frac{\epsilon_c}{Re_b Da_c} Fo_c \left[\overline{u} u'_i + u' \overline{u_i} \right] \tag{5.41}$$

The Forchheimer correction is negligible in case E80, but not in case E95, although in that case the Darcy term dominates far down in the permeable wall. Taking the divergence of this equation and assuming that $\partial \overline{u} / \partial z \approx 0$, we obtain a Laplace equation for the pressure fluctuations inside the permeable wall:

$$\frac{\partial^2 p'_i}{\partial x_i^2} \approx 0 \tag{5.42}$$

The solution of this equation reads:

$$p'(x, y, z) \propto \sum_{k_x, k_y} A(k_x, k_y) e^{kz} e^{i(k_x x + k_y y)} \quad , \quad z < 0 \tag{5.43}$$

where $i = \sqrt{-1}$, $k_x = 2\pi n_x / L_x$ and $k_y = 2\pi n_y / L_y$ are the wave numbers in respectively the streamwise and spanwise directions with n_x and n_y integer numbers, $k = (k_x^2 + k_y^2)^{1/2}$, and A is a function of k_x and k_y. The value of A is related to the amplitude of the pressure fluctuations at the interface between the permeable wall and the channel. This solution predicts that the wave components of the fluctuations decrease exponentially, with small–scale fluctuations decreasing more rapidly than large–scale fluctuations. This behavior is also observed from the streamwise pressure spectra shown in figure 5.15.a. Substitution of (5.43) in (5.41) shows that the wave components of the velocity components must also decrease exponentially inside the permeable wall. This is confirmed by the streamwise spectra of the wall–normal velocity in figure 5.15.b and it explains the exponential–like tail of the rms profiles inside the permeable wall, see figure 5.13.
The rms profile of the pressure is presented in figure 5.16. Close to the top wall the profile of case E95 lies above the profiles of the other simulations. We note that the local pressure is related to the entire flow field according to the pressure Poisson equation. This could explain that in case E95 an influence of the permeable wall is observed from the pressure fluctuations close to the top wall, although the velocity fluctuations in this region are not affected.
Inside the permeable wall the rms profiles exhibit an exponential–like tail in agreement with equation (5.43). This result substantiates the findings of Vollmer et al. [97]. They performed experiments of open channel flow over a gravel bed with the objective to investigate the effect of turbulent pressure fluctuations on the exchange of solutes between the flow in the channel and the flow inside the bed. Pressure gauges were used to measure pressure fluctuations at several heights inside the bed. The rms pressure was found to decrease exponentially inside the bed, where high–frequency oscillations were vanishing

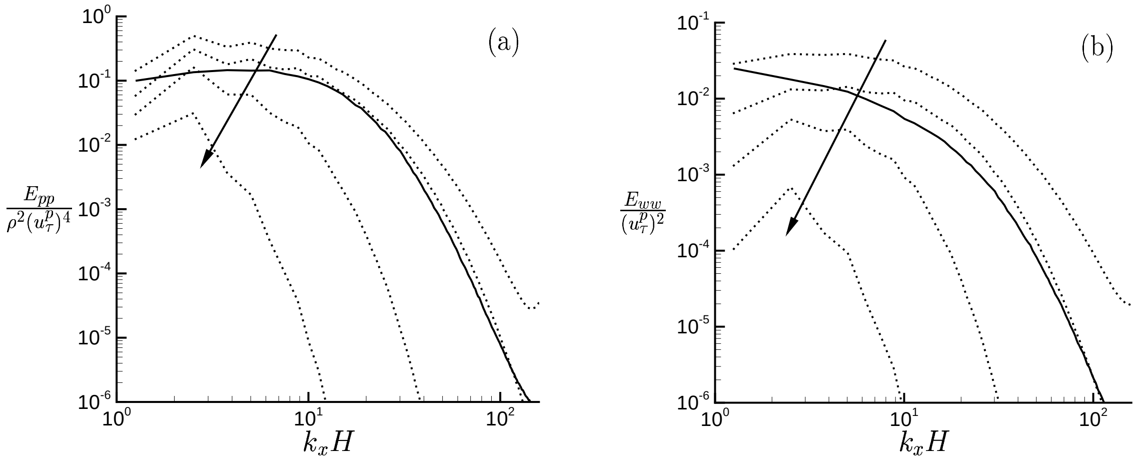

Figure 5.15: One–dimensional streamwise spectra of the pressure and the wall–normal velocity in case E95 (dotted lines) and case E0 (solid line). Each line corresponds to a different height, which is decreasing in the direction of the arrow: $z/H = -0.47, -0.14, -0.035, 0.05$. The solid line of case E0 corresponds to $z/H = 0.05$. (a) E_{pp}; (b) E_{ww}.

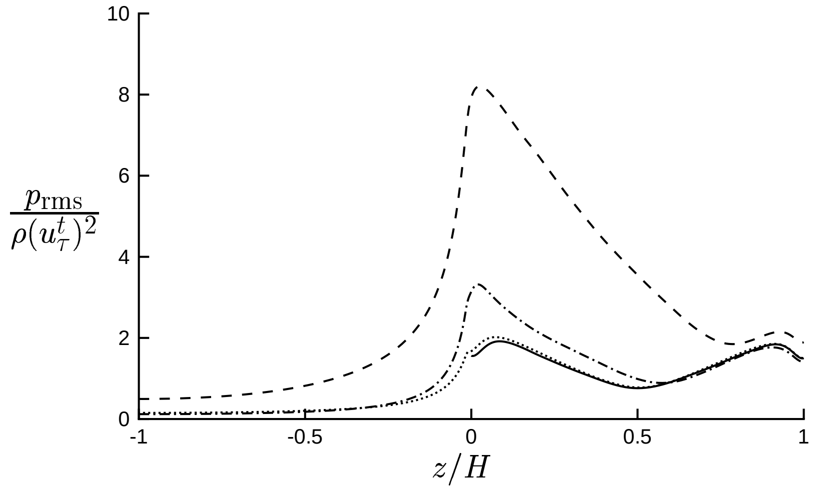

Figure 5.16: Rms profile of the pressure, normalized by $\rho(u_\tau^t)^2$, as function of z/H. —, case E0; $\cdots$, case E60; – · –, case E80; - - -, case E95.

more rapidly than low–frequency oscillations.
According to equation (5.43) the thickness h of the permeable wall must be sufficiently large in order that the flow in the channel does not feel the presence of the impermeable wall at $z = -h$ below the porous medium. Because the wavelength of the largest pressure waves was expected to be of the order of the channel height H, the thickness of the permeable wall in the simulations was taken equal to $h = H$. Figure 5.16 shows that the rms of the pressure at $z = -H$ is small compared to the peak value in the channel, although not negligible. This suggests that there is still an influence of the impermeable wall at $z = -H$ on the pressure fluctuations in the channel. However, preliminary simulations with different heights of the porous medium revealed only slight differences in the turbulence statistics for the channel.
In cases E80 and E95 we observe a large increase in the rms pressure near the permeable wall as compared to case E0. This is investigated in more detail by splitting the pressure fluctuations into contributions from different sources. These sources can be distinguished in the Poisson equation for the pressure fluctuations, which reads:

$$\begin{aligned}\frac{\partial}{\partial x_i}\left[\epsilon\frac{\partial p'}{\partial x_i}\right] &= -2\frac{\partial(\epsilon w')}{\partial x}\frac{\partial\overline{u}}{\partial z} - \frac{\partial^2}{\partial x_i\partial x_j}\left[\epsilon u_i'u_j' - \epsilon\overline{u_i'u_j'}\right] - \frac{1}{Re_b}\frac{\partial}{\partial x_i}\left[\frac{\partial\epsilon}{\partial z}\frac{\partial u_i'}{\partial z}\right] \\ &\quad -\frac{(\epsilon w')}{Re_b}\frac{\partial}{\partial z}\left[\frac{\epsilon}{Da}\right] - \frac{\partial}{\partial x_i}\left[\frac{\epsilon Fo}{Re_b Da}\left(\epsilon|\mathbf{u}|u_i - \epsilon\overline{|\mathbf{u}|u_i}\right)\right] \qquad (5.44)\end{aligned}$$

The left–hand side of the above equation is linear and therefore the pressure fluctuations can be decomposed into distinct contributions from the various terms on the right–hand side. In the numerical study of Mansour et al. [62] of plane channel flow with impermeable walls, distinction is made between three contributions: the rapid, the slow and the Stokes pressure. Similar to this distinction we write $p = p_r + p_s + p_w$, where p_r is the rapid pressure, p_s is the slow pressure, and p_w is the wall–induced pressure. The last contribution incorporates the Stokes pressure of Mansour et al., but it also contains the contribution from the spatially varying drag force inside the permeable wall. The various pressure fluctuations can be calculated from:

$$\frac{\partial}{\partial x_i}\left[\epsilon\frac{\partial p_r'}{\partial x_i}\right] = -2\frac{\partial(\epsilon w')}{\partial x}\frac{\partial\overline{u}}{\partial z} \qquad (5.45a)$$

$$\frac{\partial}{\partial x_i}\left[\epsilon\frac{\partial p_s'}{\partial x_i}\right] = -\frac{\partial^2}{\partial x_i\partial x_j}\left[\epsilon u_i'u_j' - \epsilon\overline{u_i'u_j'}\right] \qquad (5.45b)$$

$$\begin{aligned}\frac{\partial}{\partial x_i}\left[\epsilon\frac{\partial p_w'}{\partial x_i}\right] &= -\frac{1}{Re_b}\frac{\partial}{\partial x_i}\left[\frac{\partial\epsilon}{\partial z}\frac{\partial u_i'}{\partial z}\right] - \frac{(\epsilon w')}{Re_b}\frac{\partial}{\partial z}\left[\frac{\epsilon}{Da}\right] \\ &\quad -\frac{\partial}{\partial x_i}\left[\frac{\epsilon Fo}{Re_b Da}\left(\epsilon|\mathbf{u}|u_i - \epsilon\overline{|\mathbf{u}|u_i}\right)\right] \qquad (5.45c)\end{aligned}$$

The boundary conditions for the above equations are given by:

$$z = -h, H \quad : \quad \frac{\partial p_r'}{\partial z} = 0 \ ; \ \frac{\partial p_s'}{\partial z} = 0 \ ; \ \frac{\partial p_w'}{\partial z} = \frac{1}{Re_b}\frac{\partial^2 w'}{\partial z^2} \qquad (5.46)$$

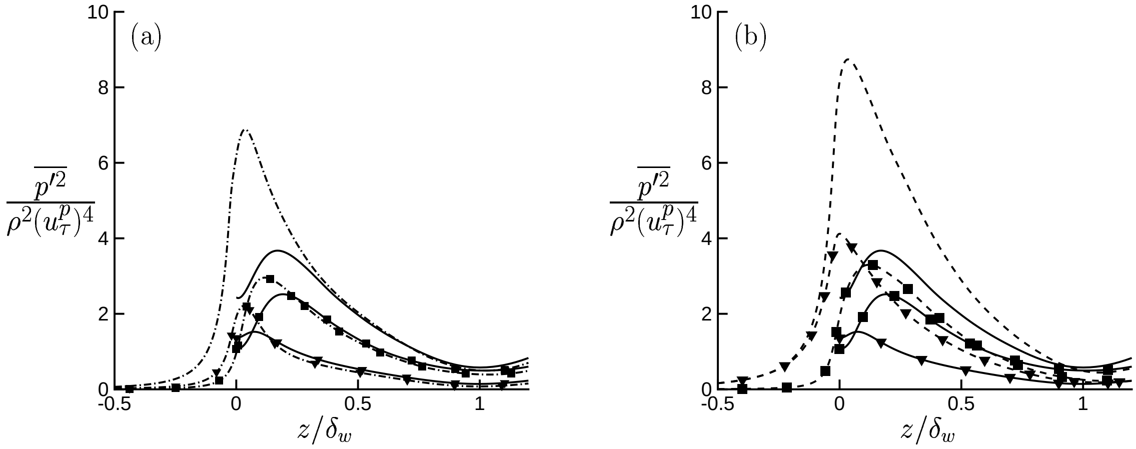

Figure 5.17: Contributions from the rapid and the slow pressure fluctuations, $\overline{p_r'^2}$ and $\overline{p_s'^2}$ respectively, to the total pressure variance $\overline{p'^2}$. The lines without symbols are the profiles of the total pressure variance. Symbols: ▼, variance rapid pressure; ■, variance slow pressure. (a) —, case E0; – · –, case E80; (b) —, case E0; - - -, case E95.

The variance of the total pressure is given by $\overline{p'^2} = \overline{(p_r' + p_s' + p_w')^2}$. The various pressure contributions correlate with each other, but in all simulations the most important contributions to the total pressure variance in the channel are $\overline{p_s'^2}$ and $\overline{p_r'^2}$. In figure 5.17 the variances of the rapid, the slow and the total pressure fluctuations are shown. In figure 5.17.a the profiles of cases E80 and E0 are compared with each other. For $z \gtrsim 0.3$ the profiles of the two cases overlap and in this range the sum of the rapid and slow pressure variances is almost equal to the total pressure variance. Close to the permeable wall the variances of both the rapid and the slow pressure in case E80 are larger than in case E0. In figure 5.17.b the pressure variances of cases E95 and E0 are compared with each other. The sum of the rapid and the slow pressure variances are almost equal to the total pressure variance throughout the channel and the permeable wall, except near the interface with the permeable wall, where also the term $\overline{p_r' p_s'}$ gives an important contribution, although not shown here. Different from case E80, the profiles of case E95 do not overlap with the profiles of case E0. Wall permeability influences apparently also the pressure fluctuations in the outer region. Like in case E80 close to the permeable wall the rapid and the slow pressure variances in case E95 are larger than in case E0. Most remarkable is the very strong increase in the variance of the rapid pressure $\overline{p_r'^2}$. Down in the permeable wall, $\overline{p_r'^2}$ is the only contribution to the total pressure variance. According to equation (5.45a), the rapid pressure fluctuations are related to $(\partial[\epsilon w']/\partial x)(\partial\overline{u}/\partial z)$. Considering the fact that close to the permeable wall the mean velocity gradient in case E95 is much smaller than in case E0, the explanation for the strong increase in the rapid pressure variance in case E95 can therefore be only that in this case the wall–normal velocity strongly varies in the streamwise direction. This can also be observed from the streamwise spectra of the wall–normal velocity shown in figure 5.15.b. At position $z/H = 0.05$ the spectral energy–density of case E95 is much larger compared to case E0.

5.6.4 Vorticity fluctuations

Figure 5.18 presents the rms profiles of the vorticity fluctuations for different values of the wall porosity ϵ_c. In graphs 5.18.(a)–(c) the rms profiles are normalized by $(u_\tau^t)^2/\nu$, so that the profiles coincide near the top wall. To compare the profiles in the wall region above the permeable wall, another scale has to be used. The sum of the variances of the vorticity fluctuations can be written in the following form:

$$\overline{(w'_k)^2} = \frac{\epsilon_d}{\nu} - \overline{\frac{\partial u'_j}{\partial x_i}\frac{\partial u'_i}{\partial x_j}} \tag{5.47}$$

where the Einstein summation convention applies to all indices (i, j and k) and where $\epsilon_d = \nu\overline{(\partial u'_i/\partial x_j)^2}$ is the dissipation rate of turbulent kinetic energy. In the outer region of the boundary layer above the permeable wall, the second term on the right–hand side of (5.47) is very small compared to the first term. In the same region, the dissipation rate of turbulent kinetic energy is approximately in local equilibrium with the deformation work by the Reynolds–shear stress: $\epsilon_d \approx \overline{u'w'}\frac{\partial\overline{u}}{\partial z}$. Because $\overline{u'w'}$ scales with $(u_\tau^p)^2$ and $\partial\overline{u}/\partial z$ scales with u_τ^p/δ_w according to the velocity–defect law (5.34), this then implies that the rms of the vorticity scales with $(u_\tau^p/\delta_w)\sqrt{u_\tau^p\delta_w/\nu}$. This is substantiated by graphs 5.18.(d)–(f), which show that similarity exists for $z/\delta_w \gtrsim 0.35$.

In figure 5.18.d it is observed that the profile of $w_{x,\mathrm{rms}}$ has a different shape in cases E80 and E95 than in case E0. Kim et al. [45] associated the local minimum and maximum in $w_{x,\mathrm{rms}}$ in case E0 with the average position of the edge and the center of quasi–streamwise vortices. The quasi–streamwise vortices originate from the presence of low– and high–speed streaks above the wall. In cases E80 and E95 no local minimum is present near the permeable wall, which indicates a change in the turbulence structure. The latter becomes obvious from figure 5.19, which shows snapshots of the wall–normal vorticity at $z/H = 0.05$. In case E0 elongated streaky structures are present above the wall. These are the result of high– and low–speed streaks and quasi–streamwise vortices, which cause locally large values of $|\partial u'/\partial y|$ and $|\partial v'/\partial x|$. The snapshot of case E80 shows a more irregular structure. Figure 5.19.c shows that in case E95 the streaky structures have completely vanished. For the existence of high– and low–speed streaks a strong mean velocity gradient is required [54] and this condition is not satisfied above the highly permeable wall of case E95. Moreover, because of the weakening of the wall–blocking effect, in case E95 strong wall–normal velocities are present near the permeable wall and this also prevents the development of streaky structures.

In figure 5.18.a–c it is observed that the rms profiles of the vorticity decay faster inside the permeable wall compared to the rms profiles of the velocity shown in figure 5.13.a–c. This is consistent with the earlier observation based on equation (5.41), that small–scale velocity fluctuations decay faster than large–scale velocity fluctuations. These large–scale

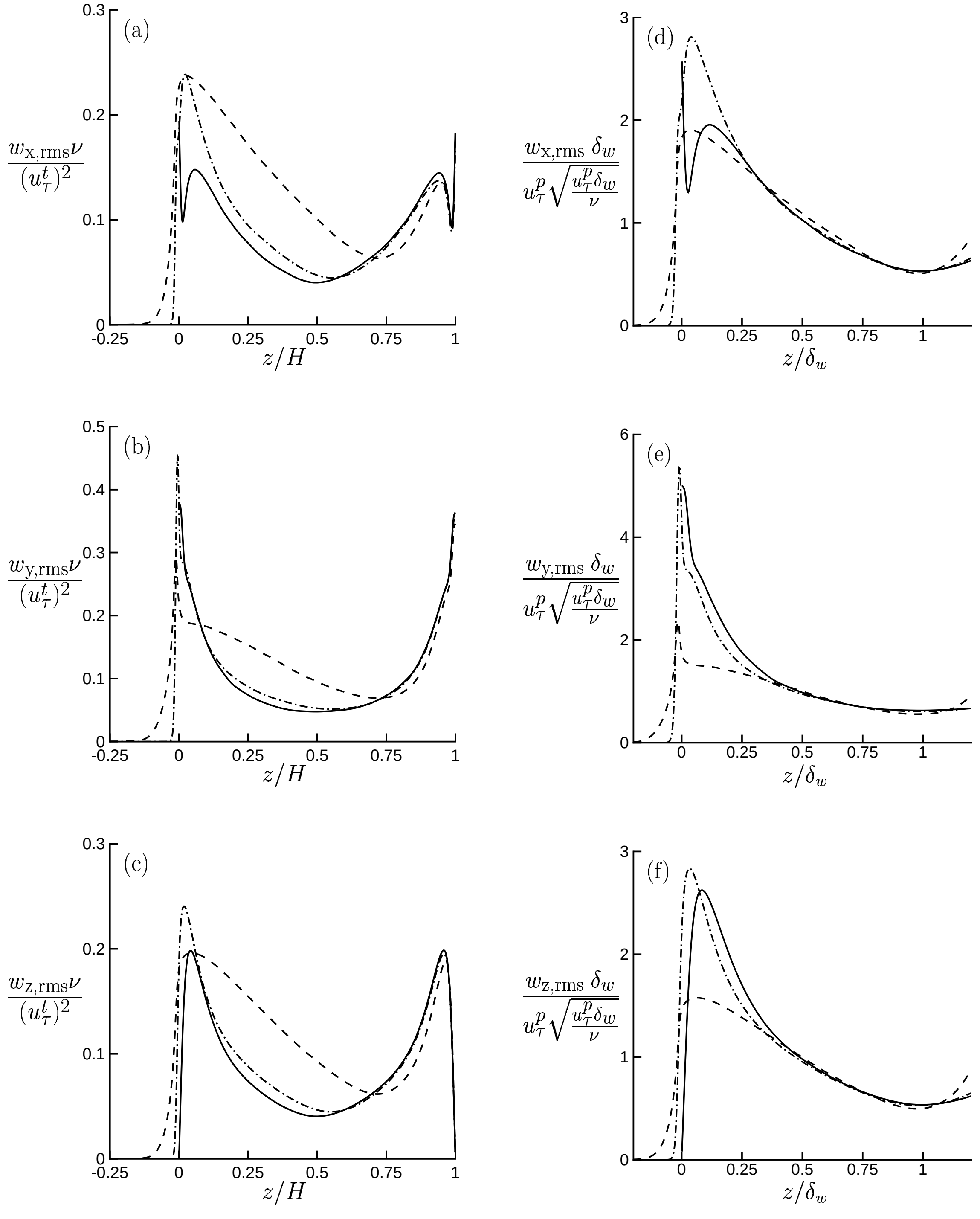

Figure 5.18: (a)-(c) Rms profiles of the vorticity components normalized by $(u_\tau^t)^2/\nu$ as function of z/H. (d)-(f) Rms profiles of the vorticity components normalized by $(u_\tau^p/\delta_w)\sqrt{u_\tau^p\delta_w/\nu}$ as function of z/δ_w. (a)+(d) streamwise component; (b)+(e) spanwise component; (c)+(f) wall-normal component. —, case E0; – · –, case E80; - - -, case E95.

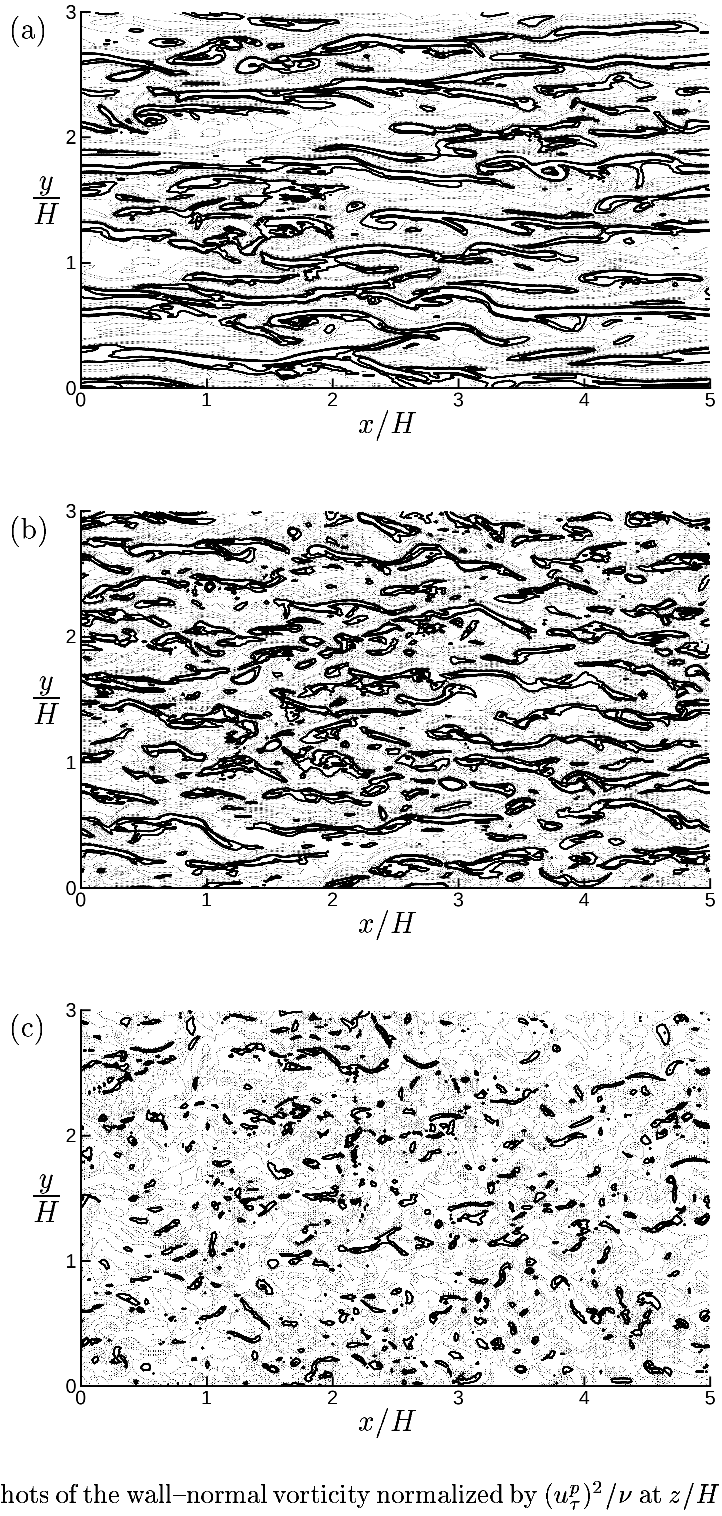

Figure 5.19: Snapshots of the wall–normal vorticity normalized by $(u_\tau^p)^2/\nu$ at $z/H = 0.05$. The dotted and the bold lines are isocontours of respectively negative and positive vorticity at levels: -0.2,-0.1,0,0.1,0.2. (a) case E0; (b) case E80; (c) case E95.

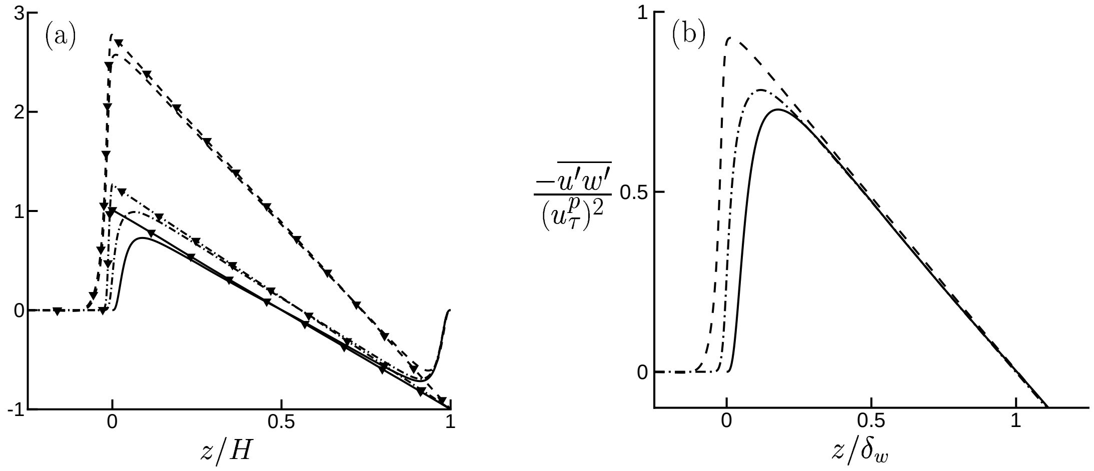

Figure 5.20: (a) Shear stress profiles normalized by $(u_\tau^t)^2$ as function of z/H. The lines with symbols are the profiles of the total shear stress $\tau_{xz} \equiv -\overline{u'w'} + \nu d\overline{u}/dz$, and the lines without symbols are the profiles of the Reynolds–shear stress $-\overline{u'w'}$. (b) Reynolds–shear stress profiles normalized by $(u_\tau^p)^2$ as function of z/δ_w. —, case E0; – · –, case E80; - - -, case E95.

velocity fluctuations contribute to the rms of the velocity, but they do not contribute much to the rms of the vorticity.

5.6.5 Reynolds and total shear stress

Figure 5.20 shows profiles of the Reynolds and the total shear stress for different values of the wall porosity ϵ_c. The total shear stress is the sum of the viscous and the Reynolds–shear stress. Figure 5.20.a shows that the total shear stress is a linear function in z, in agreement with (5.20). The stress profiles are normalized by $(u_\tau^t)^2$. At the top wall the total stress is therefore equal to -1 in all cases. The total shear stress peaks at the interface with the permeable wall. The peak in case E80 and especially in case E95 is much larger than in case E0. It is observed that in case E95 the contribution from the viscous shear stress is almost negligible, which can be explained by the relaxation of the no–slip condition at the permeable wall. The strong increase in the total shear stress is solely caused by a strong increase in the Reynolds–shear stress, which in turn is caused by the weakening of the wall–blocking effect. Turbulent flow may penetrate the permeable wall ($w' < 0$), thereby transporting fluid with relatively high streamwise momentum ($u' > 0$) into the permeable wall. By virtue of mass conservation, fluid with relatively low streamwise momentum ($u' < 0$) is transported from the permeable wall into the channel ($w' > 0$).
Figure 5.20.b presents again the profiles of the Reynolds–shear stress, but now normalized by $(u_\tau^p)^2$ and plotted as function of z/δ_w. As expected, similarity is observed in the outer region for $z/\delta_w \gtrsim 0.25$.

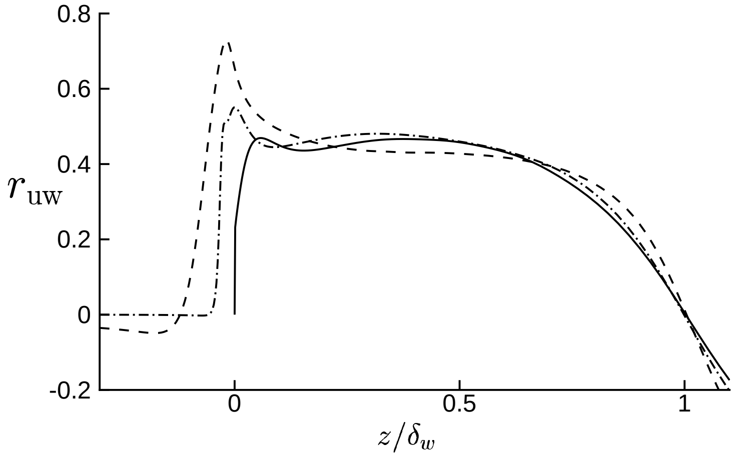

Figure 5.21: Correlation coefficient $r_{uw} = -\overline{u'w'}/(u_{\mathrm{rms}}w_{\mathrm{rms}})$ as function of z/δ_w. —, case E0; – · –, case E80; - - -, case E95.

Figure 5.21 shows the correlation coefficient r_{uw} of the velocity fluctuations u' and w', which is a measure for the efficiency of wall–normal motions to transport streamwise momentum. In a large part of the outer region the correlation coefficient of all three cases scatters around a value of 0.45. The peak close to the permeable wall is larger for higher values of ϵ_c, with a value of approximately 0.7 in case E95 against 0.5 in case E0. It is interesting to note that at the location of this peak, relatively large vortical structures are present in case E95, see figure 5.6, which clearly contribute to the Reynolds–shear stress. The increase in the peak of r_{uw} with increasing ϵ_c indicates that the increase in the Reynolds–shear stress is not just the result of a strong increase in the wall–normal turbulence intensity, but originates also from an increased efficiency of wall–normal velocity fluctuations to transport streamwise momentum. Notice the rapid decay of r_{uw} inside the permeable wall. This observation is consistent with (5.41), which expresses that inside the permeable wall the velocity fluctuations are induced by pressure fluctuations. They are inactive in the sense that they do not contribute to the Reynolds–shear stress.

To investigate the origin of the Reynolds–shear stress in more detail a quadrant analysis [98], [45] has been performed. The fractional contribution from each quadrant to the Reynolds–shear stress is calculated without imposing a threshold value. The fractional contributions are shown in figure 5.22. As expected, in all simulations the most important contributions are from the second and the fourth quadrant. The second quadrant corresponds to $u' < 0$ and $w' > 0$ and this combination is usually called an ejection event. The fourth quadrant corresponds to $u' > 0$ and $w' < 0$ and this combination is usually called a sweep event. It is observed that in case E95 in the range of $0.1 \lesssim z/\delta_w \lesssim 0.7$ sweep events are slightly more important than in case E0, whereas ejection events are slightly less important than in case E0. In the same range however, the contribution from the ejection events is still dominant. Close to the permeable wall it is observed that in

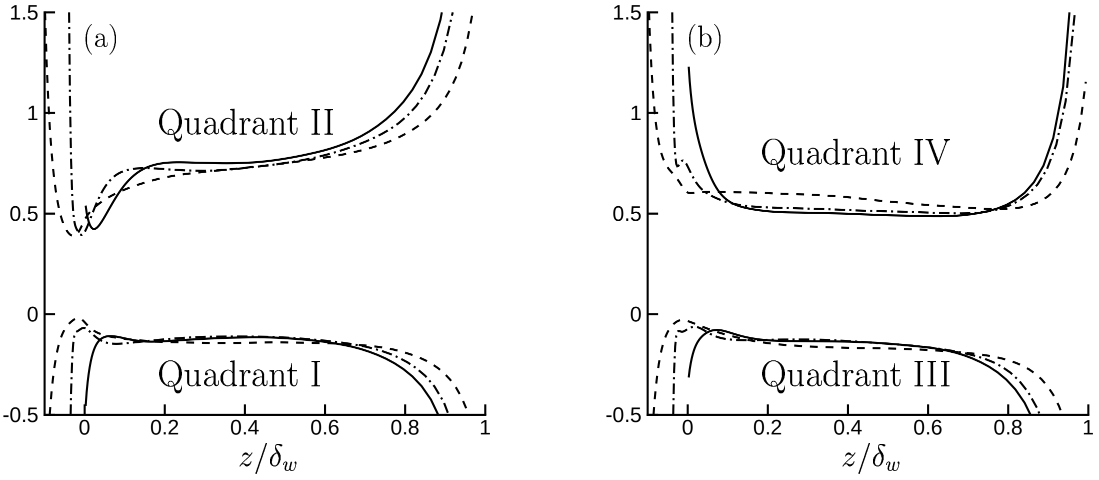

Figure 5.22: Fractional contribution from each quadrant to the Reynolds–shear stress. (a) First and second quadrant; (b) Third and fourth quadrant. —, case E0; – · –, case E80; - - -, case E95.

case E0 sweep events dominate over ejection events. In cases E80 and E95 sweep events still dominate near the permeable wall, but the difference between the two contributions is less strong. The overall conclusion of the quadrant analysis is that the influence of the wall porosity ϵ_c on the fractional contributions is rather small.

5.6.6 Turbulent–kinetic–energy budgets

To gain more insight in the dynamics of turbulence near a highly permeable wall, we have a closer look at the turbulent–kinetic–energy (TKE) budgets of $\overline{(u'^2)}/2$ and $\overline{(w'^2)}/2$. The transport equation for $\overline{(u'_\alpha)^2}/2$ can be obtained from (5.31a), which yields:

$$\begin{aligned} 0 \;=\;& \underbrace{-\overline{u'_\alpha u'_j}\frac{\partial \overline{u}_\alpha}{\partial x_j}}_{WS}\underbrace{-\overline{u'_\alpha\frac{\partial p'}{\partial x_\alpha}}}_{VPG}\underbrace{-\frac{1}{\epsilon}\frac{\partial\left[\epsilon\frac{1}{2}\overline{(u'_\alpha)^2u'_j}\right]}{\partial x_j}}_{TT}+\underbrace{\frac{1}{Re_b}\frac{\partial^2\frac{1}{2}\overline{(u'_\alpha)^2}}{\partial x_j^2}}_{VD}\underbrace{-\frac{1}{Re_b}\overline{\left(\frac{\partial u'_\alpha}{\partial x_j}\right)^2}}_{D}\\ &+\underbrace{\frac{1}{Re_b\epsilon}\frac{\partial\epsilon}{\partial x_j}\frac{\partial\frac{1}{2}\overline{(u'_\alpha)^2}}{\partial x_j}+\frac{1}{Re_b\epsilon}\frac{\partial^2\epsilon}{\partial x_j^2}\overline{(u'_\alpha)^2}}_{POR}\underbrace{-\frac{\epsilon}{Re_bDa}\overline{(u'_\alpha)^2}}_{DAR}\underbrace{-\frac{\epsilon Fo}{Re_bDa}\overline{|\mathbf{u}|u_\alpha u'_\alpha}}_{FOR} \qquad (5.48)\end{aligned}$$

where α is fixed and where the Einstein summation convention applies to the subscript j. Term WS represents production by means of deformation work performed by the Reynolds–shear stress, term VPG is the velocity–pressure–gradient term and is responsible for a redistribution of TKE over the coordinate directions, terms TT and VD represent turbulent transport and viscous diffusion respectively, and term D accounts for viscous

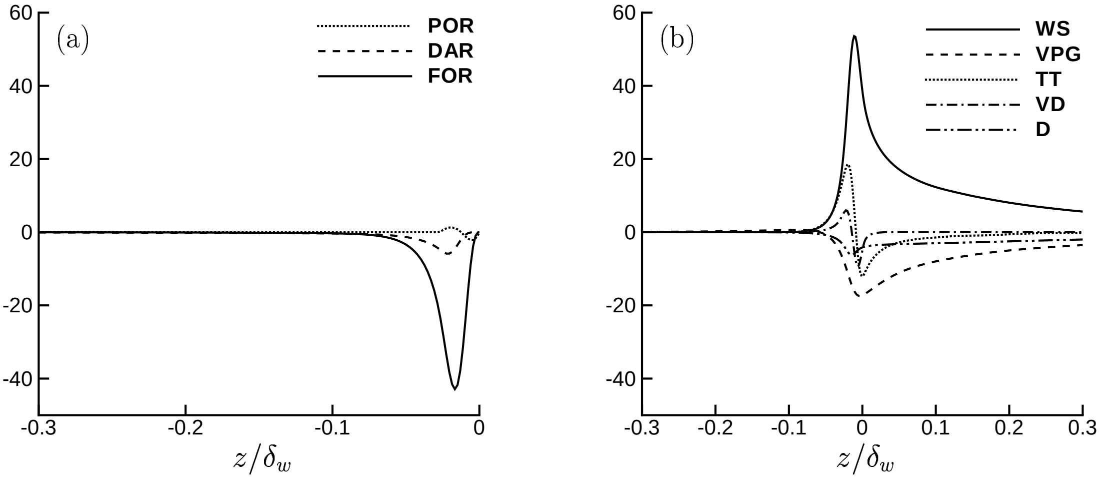

Figure 5.23: Terms in the TKE budget of $\overline{u'^2}/2$ in case E95, normalized by $(u_\tau^p)^3/\delta_w$ as function of z/δ_w. For clarity the terms POR, DAR and FOR, which are non–zero only inside the permeable wall, are shown in graph (a) and the other terms in graph (b).

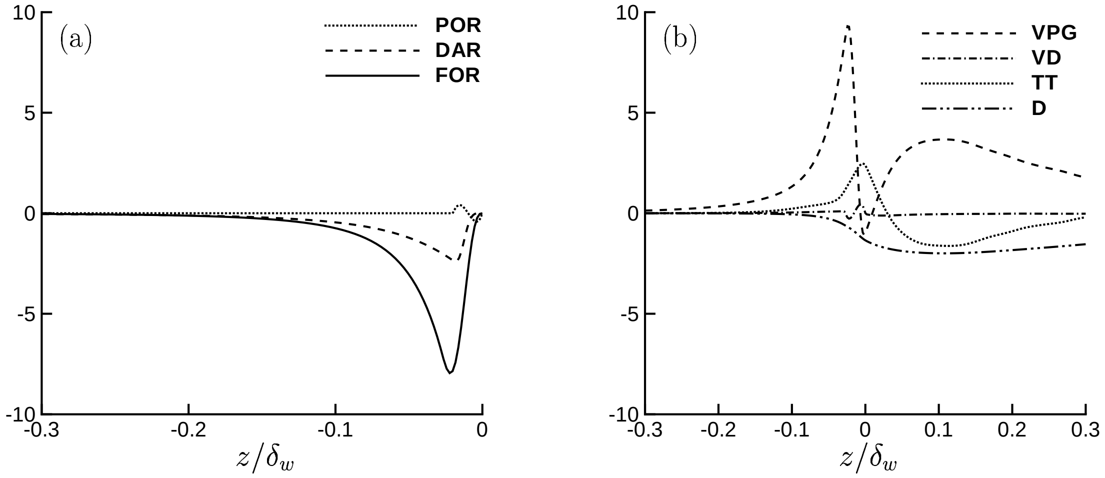

Figure 5.24: Terms in the TKE budget of $\overline{w'^2}/2$ in case E95, normalized by $(u_\tau^p)^3/\delta_w$ as function of z/δ_w. For clarity the terms POR, DAR and FOR, which are non–zero only inside the permeable wall, are shown in graph (a) and the other terms in graph (b).

dissipation of TKE. The last three terms on the right–hand side are non–zero only inside the permeable wall. The POR–terms represent transport and dissipation of TKE by local changes in the porosity. The DAR– and the FOR–term represent the transfer of resolved–scale TKE, i.e. the TKE of the volume–averaged flow, to subfilter–scale TKE by Darcy drag and Forchheimer drag respectively.

Figure 5.23 depicts the terms in the TKE budget of $\overline{(u')^2}/2$ for case E95. For clarity, terms POR, DAR and FOR are shown in the left graph, whereas the other terms are shown in the right graph. The terms are normalized by $(u_\tau^p)^3/\delta_w$, based on the characteristic scales for the outer region. The sum of all computed terms is close to zero.

For $z/\delta_w \gtrsim 0.2$, term WS is in local balance with term VPG and to a minor extent term D. Close to the permeable wall, the terms are very different from the terms in case E0. The latter are not shown here, but they can be found in Mansour et al. [62]. Close to the wall in case E0, term VD is in balance with term D. Close to the highly permeable wall in case E95 however, viscous effects are of minor importance because of the relaxation of the no–slip condition. Instead, term WS is the most important source term, which originates from the weakening of the wall–blocking effect, and terms VPG and TT are the dominant loss terms. In the top region of the permeable wall, term WS reaches its top value. The most important loss term in this region is term FOR. For $z \lesssim -0.1$, term VPG is in local balance with terms DAR and FOR, which is in agreement with (5.41).

In figure 5.24, the TKE budget of $\overline{(w')^2}/2$ is shown for case E95. A major difference with respect to case E0 is the importance of term TT above the permeable wall. In a small layer around the interface it is the most dominant source term, whereas in case E0 it has about the same magnitude as term VPG. This is clearly related to the weakening of the wall–blocking effect near the highly permeable wall in case E95, which allows for an enhanced turbulent transport of TKE from the channel towards the permeable wall. Inside the permeable wall, term VPG is balanced by terms DAR and FOR, in agreement with (5.41).

5.6.7 Turbulence structure

In this section, we have a closer look at autocorrelation functions in order to investigate the turbulence structure in more detail. Figure 5.25 presents the spanwise autocorrelation of the streamwise velocity. The left graph corresponds to case E0, the right graph to case E95. In case E0 the spanwise autocorrelation exhibits a local minimum at $y^{p+} \approx 50$ in the region close to the wall. This local minimum is usually associated with the average spanwise distance between a low–speed and a neighboring high–speed streak. The oscillations in the autocorrelation for larger spanwise spacings indicate a periodicity in the presence of the streaks. We already observed from figure 5.19 that in case E95 these streaky structures have vanished. The larger correlation distance and the absence of oscillations in figure 5.25.b confirm this. We note that the larger correlation distance is consistent with our earlier observation that turbulence near a highly permeable wall is dominated by relatively large vortical structures.

Figure 5.26 presents the spanwise autocorrelation of the wall–normal velocity. In case E0

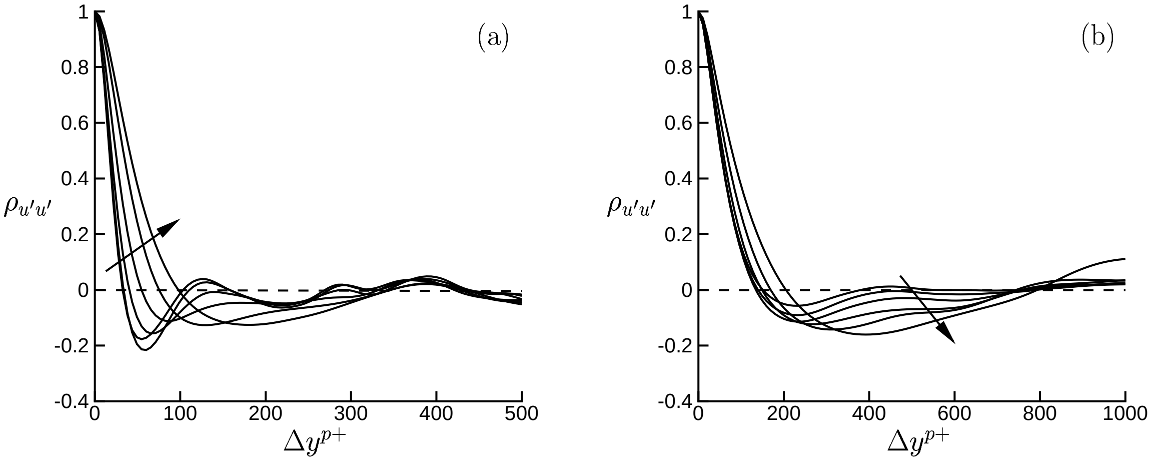

Figure 5.25: Autocorrelation $\rho_{u'u'}$ of the streamwise velocity as function of the spanwise spacing Δy^{p+}. The lines correspond to different wall–normal positions, increasing in the direction of the arrows: $z/H = 0.01, 0.035, 0.075, 0.14, 0.24, 0.49$. (a) Case E0; (b) Case E95.

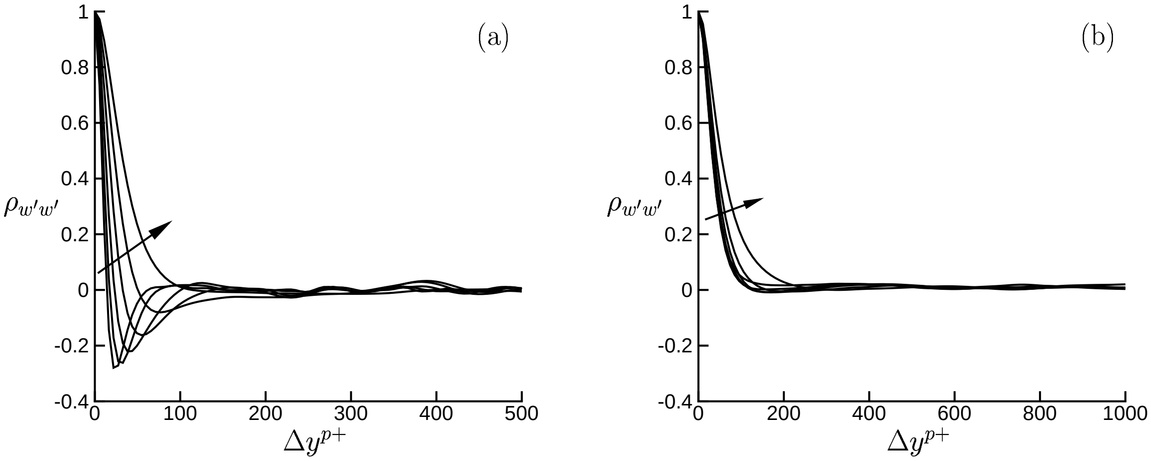

Figure 5.26: Autocorrelation $\rho_{w'w'}$ of the wall–normal velocity as function of the spanwise spacing Δy^{p+}. The lines correspond to different wall–normal positions, increasing with in the direction of the arrows: $z/H = 0.01, 0.035, 0.075, 0.14, 0.24, 0.49$. (a) Case E0; (b) Case E95.

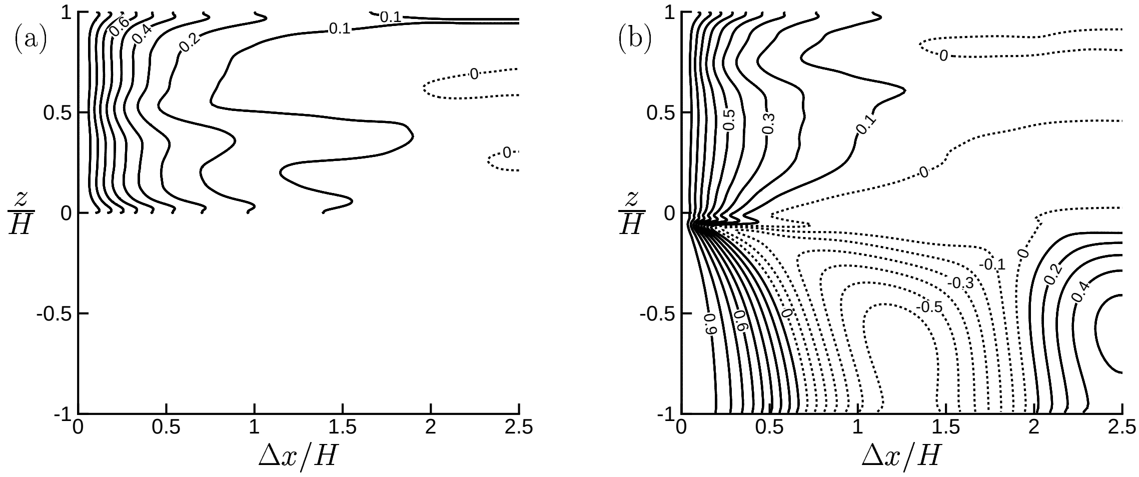

Figure 5.27: Isocontours of the autocorrelation $\rho_{u'u'}$ as function of the streamwise spacing $\Delta x/H$, and shown across the height of the permeable wall and the channel. The solid and dashed lines correspond to respectively positive and negative values of $\rho_{u'u'}$, with a step of 0.1 between two neighboring lines. (a) Case E0; (b) Case E95.

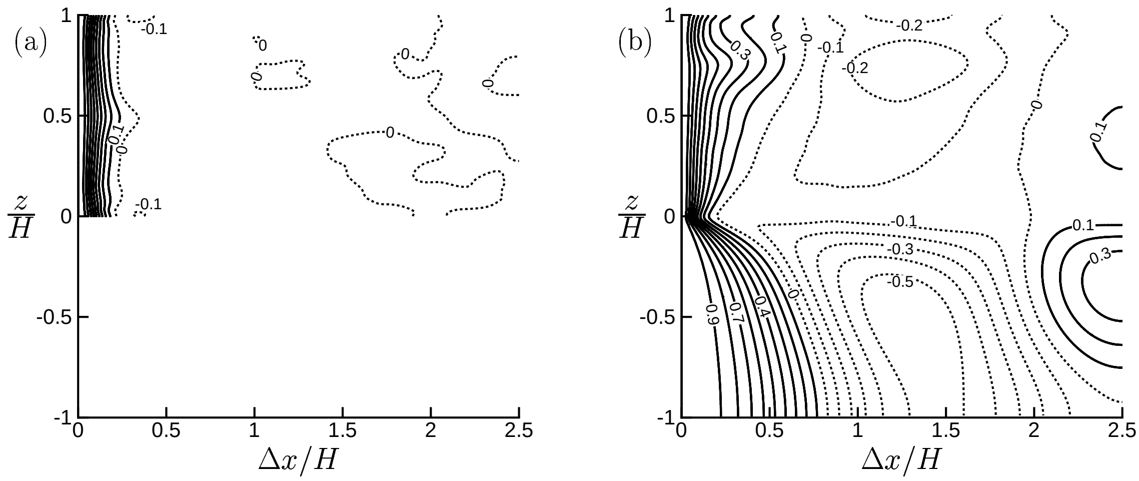

Figure 5.28: Isocontours of the autocorrelation $\rho_{p'p'}$ as function of the streamwise spacing $\Delta x/H$, and shown across the height of the permeable wall and the channel. The solid and dashed lines correspond to respectively positive and negative values of $\rho_{p'p'}$, with a step of 0.1 between two neighboring lines. (a) Case E0; (b) Case E95.

a local minimum at roughly $y^{p+} \approx 30$ is observed close to the wall. This local minimum in case E0 is consistent with the presence of quasi–streamwise vortices with a typical diameter of 30 wall units. This local minimum is absent in case E95. Notice that in this case the autocorrelation function is almost independent of the height.

In figure 5.27 isocontours of the streamwise autocorrelation of the streamwise velocity are shown. Notice that this is a one–dimensional correlation, but plotted across the permeable wall and the channel. The left graph corresponds to case E0 and the right graph to case E95. In case E0 we observe a significant correlation over large distances, especially close to the walls. This behavior is associated with the presence of streaks. The streaks have typically a length of the order of 1000 wall units. In case E0 this would correspond with a correlation distance of roughly $2.5\,H$. In case E95 the correlation distance close to the permeable wall is much smaller than in case E0, which is consistent with the absence of streaks. Inside the permeable wall cell–like patterns are observed. According to (5.41), these originate from large–scale pressure fluctuations just above and inside the permeable wall. As can be seen from the streamwise spectrum of the pressure in figure 5.15.a, the most dominant streamwise wavenumber of the pressure fluctuations is $k_x = 4\pi/L_x$. This is also clearly reflected in figure 5.28.b, which shows a similar cell–like pattern for the streamwise autocorrelation of the pressure as for the streamwise velocity in figure 5.27.b. Notice from figure 5.28.b that in case E95 there is even a significant increase in the streamwise correlation distance for the pressure close to the top wall as compared to case E0. In fact, inspection of the streamwise spectrum of the pressure revealed that $k_x = 4\pi/L_x$ is the dominant wave number throughout the flow domain. Recall that we observed earlier that in case E95 also the rms of the pressure has increased near the top wall, see figure 5.16, whereas the rms velocities were unaffected. This suggests that the increase in the rms of the pressure close to the top wall is related to this large–scale pressure motion, which in turn originates possibly from Kelvin–Helmholtz type of instabilities at the permeable wall interface.

Finally, we have investigated the influence of wall porosity on the wall–normal autocorrelation of the wall–normal velocity. The wall–normal autocorrelation is defined here according to:

$$\rho_{w'w'}\,(z; z_1) \equiv \frac{\overline{w'(z_1)w'(z)}}{\overline{w'(z_1)^2}} \tag{5.49}$$

Rather than the conventional definition, in which the denominator reads $(\,\overline{w'(z_1)^2}\,\overline{w'(z)^2}\,)^{1/2}$, this definition is more suitable for investigating the weakening of the wall–blocking effect for larger wall porosity. Figure 5.29 presents the wall–normal autocorrelation of w' for four different values of z_1/δ_w. For clarity also a dotted line corresponding to $\rho_{w'w'} = z/z_1$ is shown. The profiles of case E80 are close to the profiles of case E0, except for $z_1/\delta_w = 0.25$, where close to the permeable wall $\rho_{w'w'}$ is significantly larger than in case E0. This could also be expected, because for small values of z_1/δ_w the influence of the wall will be felt. In case E95 however, also striking differences are observed for values of z_1/δ_w which are remote from the wall. For values of z/z_1 near unity, the autocorrelation is lower than in

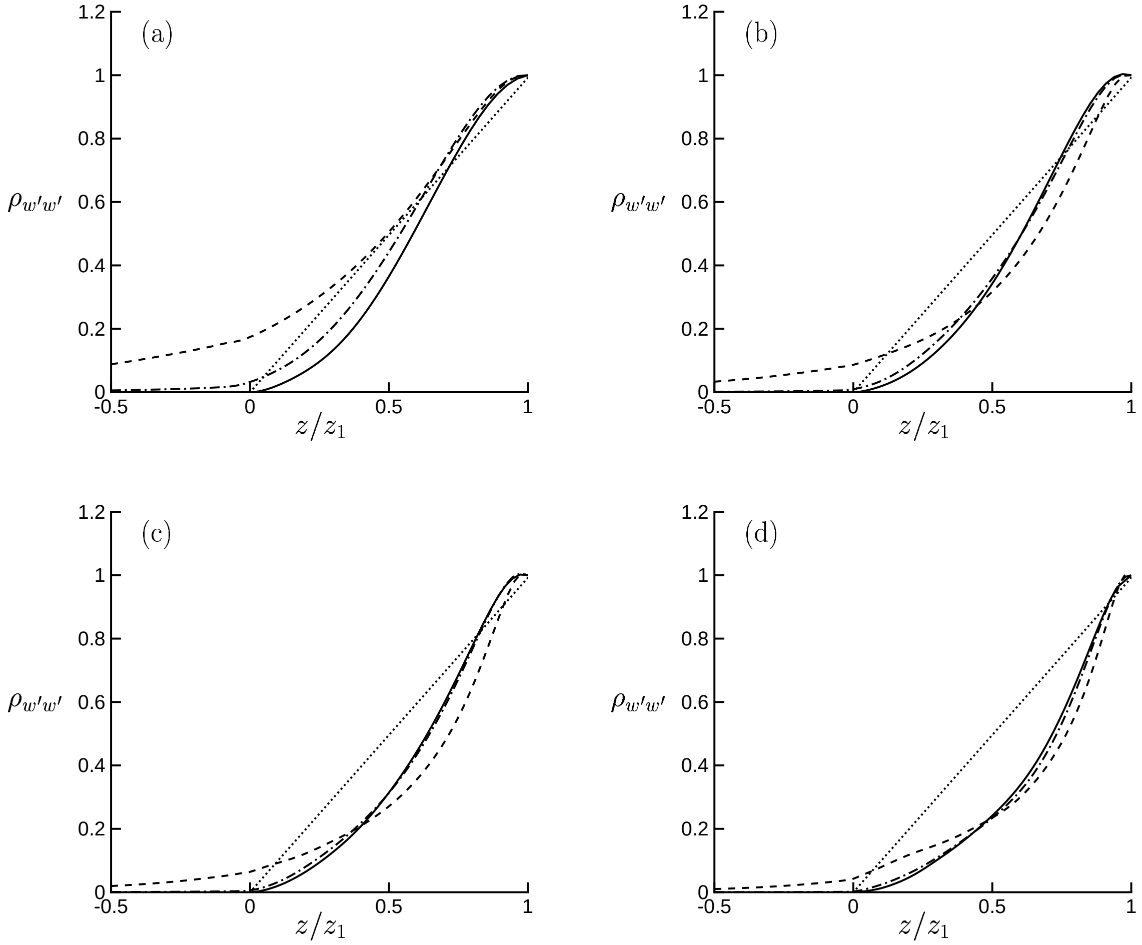

Figure 5.29: Autocorrelation $\rho_{w'w'}$ of the wall–normal velocity as function of the wall–normal distance z/z_1. (a) $z_1/\delta_w = 0.25$; (b) $z_1/\delta_w = 0.5$; (c) $z_1/\delta_w = 0.75$; (d) $z_1/\delta_w = 1.01$. —, case E0; – · –, case E80; - - -, case E95; · · ·, $\rho_{w'w'} = z/z1$.

case E0, but for values of z/z_1 close to the permeable wall the autocorrelation is larger than in case E0. Inside the wall the autocorrelation exhibits an exponential–like tail, because the wave components of w' are decreasing exponentially, recall the discussion of (5.41). Figure 5.29 shows that wall–normal velocities remote from the wall are correlated significantly with wall–normal velocities close to and even inside the permeable wall. This is the result of the weakening of the wall–blocking effect and of the shear–sheltering effect [36]. The combination of these effects enhances the communication between the inner and the outer region. This in turn might explain the departure from similarity in the outer region observed in some turbulence statistics like for instance the wall–normal rms velocity, see figure 5.14.c.

5.7 Summary and discussion

A formalism has been developed for DNS of turbulent flow in a plane channel with a solid top wall and a permeable bottom wall. The permeable wall is a packed bed, which is characterized by the porosity and the mean particle diameter. In order to separate the effect of wall permeability from wall roughness, these parameters have been chosen such that in the simulations the roughness Reynolds number is small and the permeability Reynolds number is relatively large. A continuum approach based on the VANS equations is adopted to describe the volume–averaged flow inside the permeable wall. To solve the VANS equations, closures are required for the drag force and the subfilter–scale stress. The drag force is modeled by means of the Ergun equation for packed beds in combination with a variable–porosity model for the interface region. In the DNS it is assumed that a different filter length is used for the homogeneous porous region than for the channel region. The filter length in the channel region is set by the computational mesh spacing, which is sufficiently small, and consequently subfilter–scale dispersion can be neglected in the channel region. Based on an order–of–magnitude analysis it was shown in section 2.6 that the subfilter–scale stress can be neglected too in the homogeneous porous region.

Numerical results have been shown from four simulations, for which only the wall porosity ϵ_c in the homogeneous porous region is varied. A key parameter is the permeability Reynolds number Re_K. This is the ratio of the length scale associated with the drag force inside the permeable wall, $\propto \sqrt{K}$, to the viscous length scale of turbulence above the permeable wall, ν/u_τ. This number can also be interpreted as the ratio of the effective pore diameter to the characteristic length scale of near–wall eddies. Similar to the classification of rough walls, a *highly permeable wall* is classified as a permeable wall near which viscous effects are of minor importance, which corresponds to $Re_K \gg 1$. Just above such a wall, turbulent transport of MKE is counterbalanced by the work performed by the Reynolds–shear stress, and just below the wall interface the drag force is responsible for an additional dissipation of MKE. For $Re_K \ll 1$, a permeable wall is *effectively impermeable*. Close to such a wall, viscous diffusion of MKE is counterbalanced by viscous dissipation.

In all simulations a logarithmic layer is found in the boundary layer above the permeable wall. Besides the expected downward shift in the interception of the log law for a higher wall porosity, also a significant increase is found for the slope $1/\lambda$. Based on the observation that in the outer region the velocity defect scales with z/δ_w instead of $(z+d)/\delta_w$, it is suggested that the decrease in λ is related to a relatively large value of the ratio d/δ_w. For $d/\delta_w \ll 1$, the value of λ is equal to the Von Kármán constant of approximately 0.4 for flows over solid walls. The large values of d/δ_w in cases E80 and E95 could not be explained by the model of Jackson [38], who postulated that $z = -d$ is the height at which the height–averaged drag force acts.

It is found that the mean velocity profile decreases exponentially inside a permeable wall. For a highly permeable wall, the exponential decay is governed by the balance between turbulence diffusion of momentum into the permeable wall on the one hand and the removal of momentum by drag on the other hand.

It is shown that the structure and dynamics of turbulence near a highly permeable wall are different compared to an effectively impermeable wall. Above a highly permeable wall no low– and high–speed streaks and the associated quasi–streamwise vortices are present, which are typical features of turbulence near a solid wall. The absence of streaks can be explained by a strong reduction in mean shear, which in turn originates from the relaxation of the no–slip condition. Furthermore, turbulent transport across the wall interface, which is due to a weakening of the wall–blocking effect, also prevents the development of elongated streaks. The turbulence near a highly permeable wall is dominated by vortical structures, which are responsible for the exchange of momentum between the top layer of the porous medium and the channel. The vortical structures originate possibly from a Kelvin–Helmholtz type of instability of the inflexional mean velocity profile, as hypothesized by Raupach et al. [77] and Finnigan [28]. The exchange of momentum between the channel region and the top layer of the permeable wall induces a strong increase in the Reynolds–shear stress relative to the case of a solid wall. The main fractional contributions to the Reynolds–shear stress come from sweep and ejection events. Just as for an effectively impermeable wall, for a highly permeable wall sweep events dominate close to the wall interface, whereas ejection events are more important remote from the wall. Near a highly permeable wall, a significant increase is observed in the correlation coefficient r_{uw}. This indicates that the vortical structures near the permeable wall are very efficient in transporting streamwise momentum in the wall–normal direction.

The strong increase in the Reynolds–shear stress explains the strong increase in the skin friction at a highly permeable wall as compared to an impermeable wall. This result is in contrast to the decrease in skin friction found in the simulations of Hahn et al. [32]. They however assumed that the flow near the permeable wall is essentially laminar, and, because wall permeability causes a decrease in the viscous wall shear stress, they therefore found a decrease in the skin friction. As discussed in the introduction, there is experimental evidence that wall permeability causes however an increase in skin friction when the flow is turbulent [110],[112],[46], whereas it causes a decrease in the skin friction when the flow is laminar [5].

The absence of streaks above a highly permeable wall is consistent with a decrease in the peak of the streamwise rms velocity. Despite the increase in the peak of the spanwise and wall–normal rms velocities, due to a relaxation of the no–slip and no–penetration conditions, the peak in the turbulent kinetic energy is therefore smaller. Inside the permeable wall, the rms profiles exhibit an exponential–like tail. It is shown that the turbulence motions inside the wall are inactive in the sense that they are induced by pressure fluctuations and do not contribute to the Reynolds–shear stress. Furthermore, inside the permeable wall, small–scale fluctuations decrease more rapidly than large–scale fluctuations.

A large increase is found in the rms of the pressure above the permeable wall, both in the contributions from the rapid as well as the slow part. The increase in the contribution from the rapid part originates from the strong increase in the spectral content of the wall–normal velocity for large streamwise wavenumbers. This in turn is related to the weakening of the wall–blocking effect, which allows fluid to be transport across the wall interface. Besides an increase in the rms of the pressure, also the velocity–pressure–gradient term in the TKE budget for $\overline{u'^2}/2$ gained in importance near the permeable wall. In the channel region this term is responsible for transfer of streamwise TKE to spanwise and wall–normal TKE. Near a highly permeable wall, the velocity–pressure–gradient term is the most dominant loss term of streamwise TKE, whereas near a solid wall viscous dissipation is the most important loss term. This underlines once more that viscous effects are of minor importance near a highly permeable wall.

In the discussion of the results, special attention has been given to the wall similarity hypothesis. Some statistics exhibit similarity in the outer region, such as the streamwise rms velocity, the rms vorticities and the Reynolds–shear stress. However, other statistics show significant deviations from similarity, such as the spanwise and wall–normal rms velocities and the rms of the pressure. The wall–normal autocorrelation of the wall–normal velocity, $\rho_{w'w'}$, revealed that the wall–normal velocity in the outer region is correlated significantly over large distances up to and inside the permeable wall. This supports the suggestion of Krǒgstad et al. [48] that the departure from similarity in the outer region originates from the weakening of the wall–blocking effect. By means of strong ejection and sweep events, this allows fluid to be transported over a large vertical distance. As a consequence, the outer region is able to communicate with the inner region and this might explain the observed departures from similarity.

Chapter 6

Direct Numerical Simulations of turbulent flow over a permeable wall using a direct and a continuum approach [1]

Abstract *A Direct Numerical Simulation (DNS) has been performed of turbulent channel flow over a 3D Cartesian grid of 30x20x9 cubes in respectively the streamwise, spanwise and wall–normal direction. The grid of cubes mimics a permeable wall with a porosity of 0.875. The flow field is resolved with 600x400x400 mesh points. To enforce the no–slip and no–penetration conditions on the cubes, an Immersed Boundary Method is used. The results of the DNS are compared with a second DNS in which a continuum approach is used to model the flow through the grid of cubes. The continuum approach is based on the Volume–Averaged Navier–Stokes (VANS) equations [104] for the volume–averaged flow field. This method has the advantage that it requires less computational power than the direct simulation of the flow through the grid of cubes. More in general, for complex porous media one is usually forced to use the VANS equations, because a direct simulation would not be possible with present–day computer facilities. A disadvantage of the continuum approach is that in order to solve the VANS equations, closures are needed for the drag force and the subfilter–scale stress. For porous media, the latter can often be neglected. In the present work, a relation for the drag force is adopted based on the Irmay [37] and the Burke–Plummer model [7], with the model coefficients determined from simulations reported by Breugem et al. [13]. The results of the DNS with the grid of cubes and the second DNS in which the continuum approach is used, agree very well.*

---

[1] A slightly different version of this chapter will be published as an article in *Physics of Fluids* [10].

6.1 Introduction

In this research we consider turbulent channel flow over a 3D Cartesian grid of cubes, where the cubes mimic a permeable wall. A permeable wall is defined here as a rigid porous wall with interconnected pores through which fluid may flow, which in our case is coupled to the flow in the channel. The study of flows over permeable walls has various applications. Examples are oil wells, heat exchangers of open–cell metal foam and river beds of for instance sand or stones. To some extent, also forests and densely built–up urban areas can be considered as porous media. In most applications the structure of the porous medium is very complex and often the geometry is not known in full detail. Furthermore, the flow inside a porous medium exhibits usually a wide range of length scales. The smallest scales are typically of the order of the pore size or the diameter of the solid obstacles of which the porous medium is composed, whereas the largest scales might be of the order of the dimensions of the porous medium. The complex structure of porous media and the wide range of length scales of the flow, hampers the direct simulation of turbulent flow over and through porous media. A DNS in which the complete flow field is resolved above the permeable wall as well as within the pores of the wall, would require an enormous computational power. Literature provides however two other methods to simulate the turbulent flow over and through a permeable wall, which are more attractive from a computational point of view.

In the first method, the effect of wall permeability is incorporated in the boundary conditions specified at the wall interface. The main advantage of this approach is that the flow inside the permeable wall need not to be calculated. This approach was adopted by e.g. Hahn et al. [32], who performed DNS of turbulent flow in a plane channel with a solid top wall and a lower permeable wall. The boundary conditions used, were an extension to the boundary conditions proposed by Beavers & Joseph [5] (later on referred to as BJ) to model laminar flow parallel to a permeable wall:

$$\nabla \mathbf{u} \cdot \mathbf{n} = \frac{\alpha}{\sqrt{K}} (\mathbf{u} - \mathbf{U}_d) \tag{6.1a}$$

$$\mathbf{u} \times \mathbf{n} = \mathbf{0} \tag{6.1b}$$

where $\mathbf{n}$ is the unit normal at the wall, α is an empirical coefficient of order unity and K is the permeability. The Darcy velocity $\mathbf{U}_d$ is given by Darcy's Law [4]:

$$\mathbf{U}_d = -\frac{K}{\mu} \nabla p \tag{6.2}$$

where μ is the dynamic viscosity and ∇p the imposed pressure gradient. Theoretical support for the BJ–conditions was given by Saffman [80], who showed that these conditions can be derived from the assumption of Stokes flow inside as well as above the permeable wall. The BJ–conditions can therefore be applied to the case of turbulent channel flow only when close to the permeable wall a viscous sublayer exists, in which the flow is governed by the Stokes equations. As pointed out by Hahn et al. [32], this requirement is satisfied when $\sqrt{K}$ is small compared to the viscous length scale ν/u_τ, where $\nu \equiv \mu/\rho$ is the kinematic viscosity, ρ the mass density, $u_\tau \equiv \sqrt{\tau_w}/\rho$ the friction velocity and τ_w the wall shear stress. The ratio of these two length scales yields the permeability Reynolds number $Re_K \equiv \sqrt{K}u_\tau/\nu$, which expresses basically the ratio of the effective pore diameter ($\sqrt{K}$) to the characteristic length scales of near–wall eddies (ν/u_τ). For small values of Re_K, the eddies are blocked by the wall and consequently a viscous sublayer exists. For large values of Re_K, the eddies may penetrate the permeable wall, and consequently the formation of a viscous sublayer is prohibited. Although it can not be fully excluded, it is not likely that the penetration of turbulence in this case can be modeled in a simple manner by means of boundary conditions, because of the complexity of the dynamics and structure of the turbulent flow near the permeable wall. Therefore, for an accurate simulation of the flow field for large Re_K, we have to describe the flow inside the permeable wall as well.

The second method to simulate flows over porous media, is to model the flow inside the permeable wall as a continuum, which is coupled with the flow outside the wall [8]. The theoretical basis for this continuum approach is provided by the Volume–Averaging Method [105]. In this method the flow is averaged over a small spatial volume such that the volume–averaged flow is defined in the fluid as well as in the solid phase. The volume–averaged flow is governed by the Volume–Averaged Navier–Stokes (VANS) equations. These equations are similar to the equations used in Large–Eddy Simulations (LES) [56], where the difference is due to the fact that the VANS equations have to account also for the drag force that the flow through a porous medium experiences. To solve the VANS equations, closures must be provided for the subfilter–scale stress and the drag force in terms of volume–averaged quantities. In many porous media subfilter–scale dispersion can be neglected with respect to the drag force and/or turbulent diffusion by large–scale motions [8]. Breugem [8] used in his simulations the semi–empirical Ergun equation for packed beds [7] to model the drag force. A polynomial function for the porosity was adopted to model the variation of the porosity in a thin interface region in between the channel and the porous medium.

Whether the continuum approach is successful in accurately modeling the flow, depends on the accuracy of the closures for the subfilter–scale stress and especially the drag force. This motivated the present research, in which we want to evaluate these closures. To this purpose we performed a DNS of turbulent flow in a plane channel over a simple porous medium consisting of a 3D Cartesian grid of cubes, see figure 6.1.a. In this simulation the complete flow field in between the cubes as well as in the channel is resolved. The results of this direct simulation will be compared with a simulation in which the continuum approach is applied to the grid of cubes, see figure 6.1.b.

From now on, the DNS of the channel flow over the 3D Cartesian grid of cubes will be referred to as the *DNS with cubes*, whereas the DNS in which the continuum approach is employed, will be referred to as the *DNS with continuum*. The results from the two simulations will be compared also with a DNS of turbulent flow in a channel with two solid walls, which will be referred to as the *DNS with solid walls*.

This paper is organized as follows. The choice for the grid of cubes as a model porous

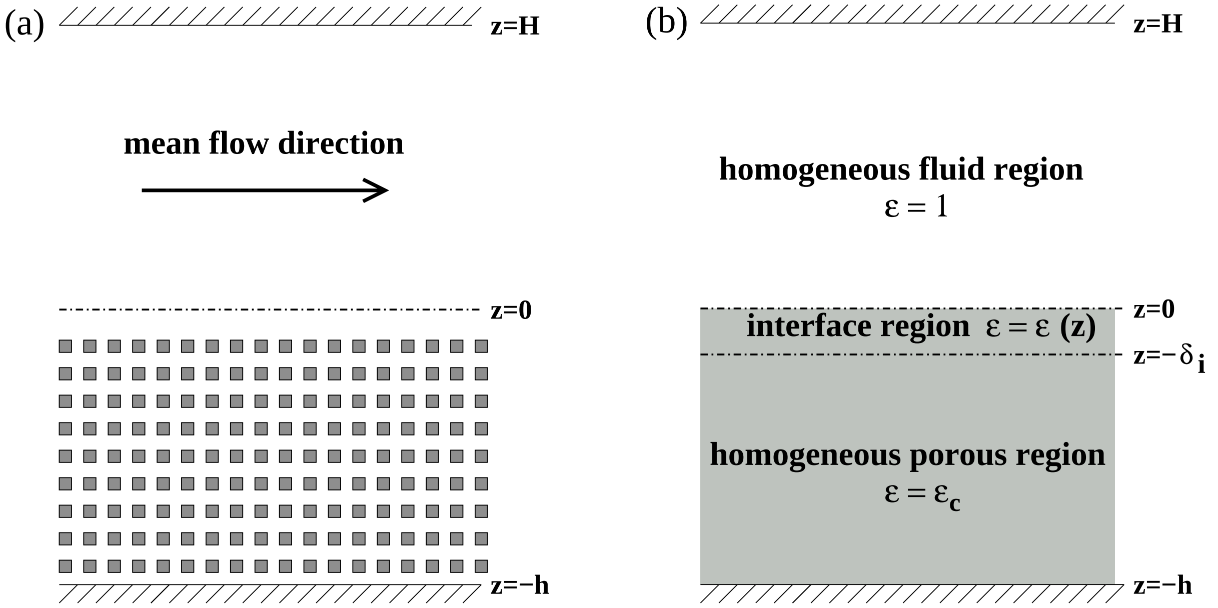

Figure 6.1: Flow geometry. (a) Geometry as considered in the DNS of turbulent channel flow over a 3D Cartesian grid of cubes; (b) Geometry as considered in the DNS in which a continuum approach is employed for the grid of cubes.

medium is motivated in section 6.2. In section 6.3 the VANS equations are introduced. In section 6.4 the DNS with continuum is discussed. Section 6.5 concerns the numerical method used in the DNS with cubes. In section 6.6 the results of both type of simulations are compared with each other and with the results from the DNS with solid walls. Section 6.7 contains a summary and a discussion.

6.2 Cartesian grid of cubes

The choice for a 3D Cartesian grid of cubes as a model geometry for a porous medium is motivated by four considerations:

1. The grid of cubes is spherically isotropic [33], which means that the permeability tensor is isotropic: $\mathbf{K} = K\mathbf{I}$, where $\mathbf{I}$ is the unit tensor. In a volume–averaged sense the grid of cubes can therefore be considered as a simple porous medium.
2. The grid of cubes can be classified as an ordered porous medium, which is characterized by a unit cell that can be extended periodically in space. For this type of porous medium, Quintard & Whitaker [75] have proposed a dedicated filter for the volume averaging of the flow field, which will be used in the present study. The length of this filter is of the same order as the dimension of the pores and solid obstacles. Therefore, the spatial structure of the unfiltered flow field is preserved as much as possible in the volume–averaged flow field. This is a major benefit of

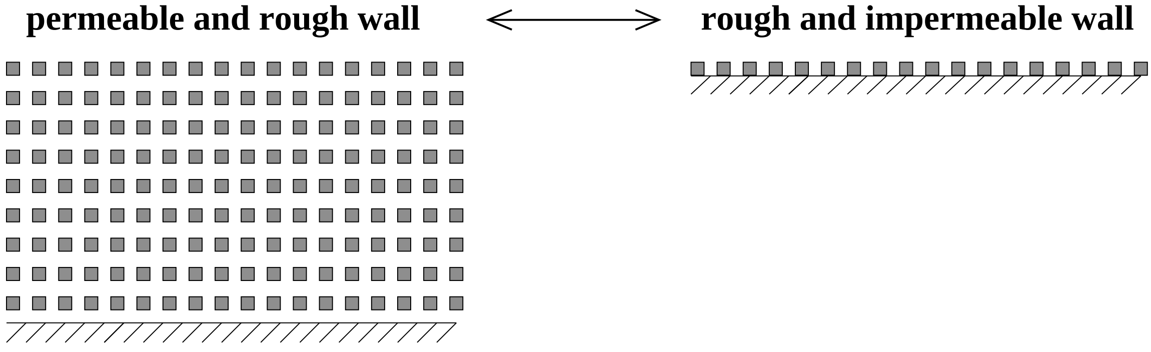

Figure 6.2: Illustration of the difference between a permeable and rough wall, and a rough and impermeable wall with the same surface roughness.

ordered porous media over disordered porous media, because for the latter the filter length should be significantly larger for averaging out local inhomogeneities in the flow field [75].

3. Permeable walls are not only permeable, but exhibit also surface roughness. In principle, the additional effect of surface roughness could be quantified by comparing the flow over a *permeable and rough wall* with the flow over a *rough and impermeable wall with the same surface roughness.* The latter wall is impermeable in the sense that below the geometrical roughness height the flow is forced to zero. The difference between the two walls is illustrated in figure 6.2. In literature it is common practice to characterize a rough wall by the typical height of the roughness elements, which in our case is the cube rib d_p. The effect of roughness depends on the *roughness Reynolds number* $Re_d \equiv d_p u_\tau / \nu$ [35]. Similarly, the effect of permeability depends on the *permeability Reynolds number* Re_K [8], which we have already introduced.
   Our research interest is on the influence of wall permeability rather than the effect of wall roughness on turbulent channel flow. This demands that the roughness Reynolds number is sufficiently small and that the permeability Reynolds number is sufficiently large. The cubes are therefore aligned in a Cartesian grid and the cube rib d_p is chosen small compared to the channel height. Furthermore, the cube rib is chosen equal to the pore dimension ($d_p = d_f$) to ensure a relatively high permeability Reynolds number. Besides, the choice for $d_p = d_f$ seems intuitively also a good choice from a computational point of view, because both the flow along and the flow in between the cubes must be resolved.

4. The cubes can be aligned along a Cartesian computational mesh. This simplifies the volume averaging of the simulation data. An Immersed Boundary Method ([25] and references therein) is employed in which forces are added to the flow field to enforce the no–slip and no–penetration conditions on the cubes. This method allows for the application of fast and accurate numerical algorithms.

6.3 The VANS equations

In this section a brief derivation of the VANS equations is given, based on local volume–averaging of the Navier–Stokes equations.

The formal definition of the volume–averaged velocity at position $\mathbf{x}$ is given by:

$$\langle \mathbf{u} \rangle^s_{\mathbf{x}} \equiv \int_V \gamma(\mathbf{r})\, m(\mathbf{y})\, \mathbf{u}(\mathbf{r}) dV \tag{6.3}$$

where the brackets $\langle .. \rangle^s$ denote the *superficial* volume average, the subscript $\mathbf{x}$ means that the volume average is evaluated at position $\mathbf{x}$, $\mathbf{y} = \mathbf{r} - \mathbf{x}$ is the position vector relative to the centroid $\mathbf{x}$ of the averaging volume V, γ is the phase–indicator function that equals unity when $\mathbf{r}$ points into the fluid phase and that equals zero when $\mathbf{r}$ points into the solid phase, and m is a weighting function. The volume–averaging operator acts as a filter, which passes only information on the large–scale structure of the flow field. Furthermore, we note that the volume–averaged flow field is continuous in the sense that it is defined both in the fluid and the solid phase. This is the basis of the continuum approach for flows in porous media.

For a meaningful definition of volume–averaged quantities, the weighting function must satisfy the following normalization condition:

$$\int_V m(\mathbf{y}) dV = 1 \tag{6.4}$$

In principle the weighting function can be chosen freely, but it is desirable that:

1. the volume–averaged flow field contains negligible variations on scales smaller than the averaging volume;
2. the averaging volume is small in order to preserve as much information of the unfiltered flow field as possible in the volume–averaged flow field.

These two conditions demand that the weighting function matches the topology of the porous medium. With this in mind, Quintard & Whitaker [75] proposed the following weighting function for an ordered porous medium:

$$m(\mathbf{y}) = \begin{cases} \prod_{i=1}^{3} \left(l_i - |y_i|\right)/l_i^2 & , |y_i| \leq l_i \\ 0 & , |y_i| > l_i \end{cases} \tag{6.5}$$

in which l_i is the length of the unit cell in direction i. The above averaging volume and the weighting function are illustrated in figure 6.3 for the Cartesian grid of cubes considered in the present study. Quintard & Whitaker refer to this filter as the *cellular* filter.

According to equation (6.3) the porosity is defined as:

$$\epsilon(\mathbf{x}) \equiv \int_V \gamma(\mathbf{r}) m(\mathbf{y}) dV \tag{6.6}$$

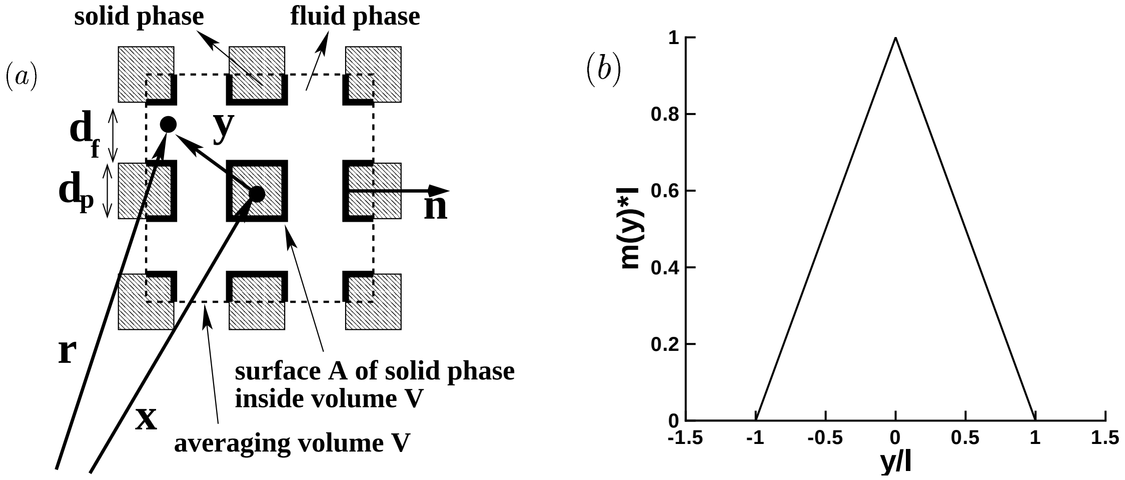

Figure 6.3: The averaging volume (a) and the weighting function (b) corresponding to the cellular filter for flow in an ordered porous medium.

The velocity at a certain point in the fluid phase of the porous medium can be decomposed into a contribution of the volume–averaged velocity at this point and a subfilter–scale velocity $\tilde{\mathbf{u}}$ [30]:

$$\mathbf{u} = \langle \mathbf{u} \rangle + \tilde{\mathbf{u}} \tag{6.7}$$

where $\langle \mathbf{u} \rangle \equiv \langle \mathbf{u} \rangle^s / \epsilon$ is known as the *intrinsic* volume–averaged velocity. Besides the spatial decomposition given by (6.7), in this study also a temporal decomposition will be used:

$$\mathbf{u} = \overline{\mathbf{u}} + \mathbf{u}' \tag{6.8}$$

where the overbar denotes the Reynolds– or ensemble–averaged value and the prime denotes the temporal fluctuation. The spatial and temporal decompositions can be combined together, which yields:

$$\mathbf{u} = \overline{\langle \mathbf{u} \rangle} + \langle \mathbf{u} \rangle' + \tilde{\overline{\mathbf{u}}} + \tilde{\mathbf{u}}' \tag{6.9}$$

It is easy to show that the Reynolds– and spatial–averaging operators commute [71]: $\overline{\langle \mathbf{u} \rangle} = \langle \overline{\mathbf{u}} \rangle$, $\langle \mathbf{u} \rangle' = \langle \mathbf{u}' \rangle$, $\overline{\tilde{\mathbf{u}}} = \tilde{\overline{\mathbf{u}}}$ and $\tilde{\mathbf{u}}' = \tilde{\mathbf{u'}}$.

For deriving the volume–averaged form of the Navier–Stokes equations it is necessary to relate the volume average of a spatial derivative to the spatial derivative of a volume average. This relation is given by the spatial–averaging theorem [102]. For instance, the volume average of the gradient of the pressure is given by:

$$\langle \nabla p \rangle^s_{\mathbf{x}} \;=\; \nabla \langle p \rangle^s_{\mathbf{x}} + \int_A m(\mathbf{y}) \mathbf{n} p(\mathbf{r}) dA \tag{6.10}$$

where A is the contact area between the fluid and the solid phase inside the averaging volume V, see figure 6.3.a, and $\mathbf{n}$ is the unit normal at A that points from the fluid into the solid phase. The single assumption in the derivation of (6.6) is that the weighting function m depends only on $\mathbf{y}$ and not on $\mathbf{x}$.

The application of the volume–averaging operator (6.3) and the spatial–averaging theorem (6.10) to the Navier–Stokes equations yields the VANS equations [104]:

$$\begin{aligned}
\frac{\partial\langle\mathbf{u}\rangle^s}{\partial t}+\nabla\cdot\left[\frac{\langle\mathbf{u}\rangle^s\langle\mathbf{u}\rangle^s}{\epsilon}\right]+\nabla\cdot\left[\langle\mathbf{u}\mathbf{u}\rangle^s-\frac{\langle\mathbf{u}\rangle^s\langle\mathbf{u}\rangle^s}{\epsilon}\right] &= -\frac{1}{\rho}\nabla\langle p\rangle^s+\nu\nabla^2\langle\mathbf{u}\rangle^s+ \\
&\quad \int_A m\mathbf{n}\left[-\mathbf{I}\frac{p}{\rho}+\nu\nabla\mathbf{u}\right]dA \qquad (6.11a) \\
\nabla\cdot\langle\mathbf{u}\rangle^s &= 0 \qquad (6.11b)
\end{aligned}$$

The VANS equations as given above are exact for Newtonian and incompressible flow through a rigid porous medium. The third term on the left–hand side of equation (6.11a) represents subfilter–scale dispersion, i.e. dispersion of volume–averaged momentum by subfilter–scale motions, and the last term on the right–hand side accounts for the drag force that the solid phase exerts on the fluid phase.

Darcy's Law (6.2) follows from the VANS equations for uniform, stationary flow through a homogeneous porous medium (i.e. with a constant porosity):

$$0=-\nabla\langle p\rangle-\mu\mathbf{K}^{-1}\langle\mathbf{u}\rangle^s \qquad (6.12)$$

where the surface integral has been replaced by $-\nu\mathbf{K}^{-1}\epsilon\langle\mathbf{u}\rangle^s$ [104]. The VANS equations can be considered as a generalization of the LES equations as well. The latter follow from the VANS equations for the case that the porosity equals unity, i.e. the absence of a solid phase, and consequently a zero drag force.

6.4 DNS with continuum

As depicted in figure 6.1.b, in the DNS with continuum the flow domain is divided into three regions:

1. The homogeneous fluid region or channel region between $z = 0$ and $z = H$ in which the porosity ϵ equals unity.
2. The interface region between $z = -\delta_i$ and $z = 0$, which is characterized by a spatially varying porosity.
3. The homogeneous porous region between $z = -h$ and $z = -\delta_i$, with a constant porosity ($\epsilon = \epsilon_c$).

Below we discuss how the flow in each region is described.

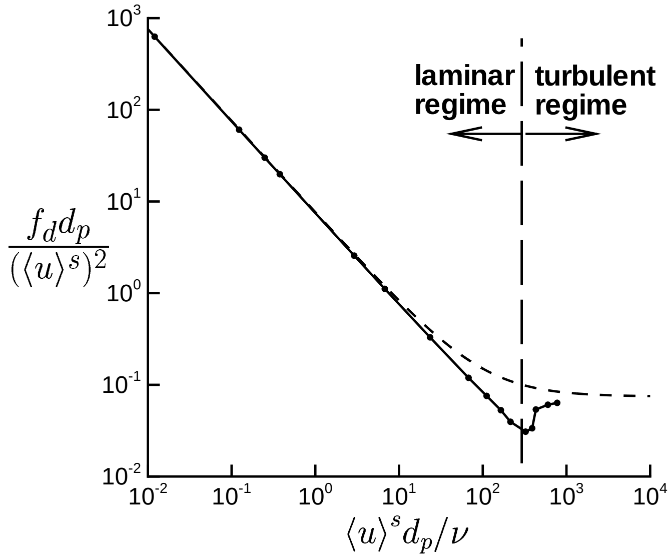

Figure 6.4: Drag force $f_d = (1/\epsilon)\int_A m\mathbf{n}\cdot[-\mathbf{I}\tilde{p}/\rho + \nu\nabla\tilde{\mathbf{u}}]\cdot\mathbf{n}_x dA$ per unit mass of the fluid phase as function of the Reynolds number, where $\mathbf{n}_x$ is the unit vector in the streamwise direction. Each dot corresponds to a separate simulation [13]. The simulation results are compared with a model based on equations (6.14)–(6.16) with $C_K = 11.4$ and $C_F = 0.4$. —, linear interpolation of simulation results; - - -, model.

6.4.1 Homogeneous porous region

The volume–averaged flow in the homogeneous porous region is governed by the VANS equations (6.11a) and (6.11b). These equations can be simplified by assuming that the volume–averaged flow field does not vary significantly inside the averaging volume, i.e. $\langle\langle\mathbf{u}\rangle\rangle \approx \langle\mathbf{u}\rangle$. This is equivalent to the assumption that $\langle\tilde{\mathbf{u}}\rangle \approx \mathbf{0}$. If this assumption holds, then equation (6.11a) can be written as [75]:

$$\begin{aligned}\frac{\partial\langle\mathbf{u}\rangle^s}{\partial t} + \nabla\cdot\left[\frac{\langle\mathbf{u}\rangle^s\langle\mathbf{u}\rangle^s}{\epsilon}\right] + \nabla\cdot\langle\tilde{\mathbf{u}}\tilde{\mathbf{u}}\rangle^s &= -\frac{\epsilon}{\rho}\nabla\frac{\langle p\rangle^s}{\epsilon} + \nu\nabla^2\langle\mathbf{u}\rangle^s - \nu\nabla\epsilon\cdot\nabla\frac{\langle\mathbf{u}\rangle^s}{\epsilon} \\ &\quad + \int_A m\mathbf{n}\left[-\mathbf{I}\frac{\tilde{p}}{\rho} + \nu\nabla\tilde{\mathbf{u}}\right]dA \qquad (6.13)\end{aligned}$$

In order to solve the above equations, closures are required for the subfilter–scale stress and the drag force in terms of the volume–averaged flow field. Whitaker [104] gave support to the following convenient parameterization of the surface integral in equation (6.13)

$$\int_A m\mathbf{n}\left[-\mathbf{I}\frac{\tilde{p}}{\rho} + \nu\nabla\tilde{\mathbf{u}}\right]dA = -\nu\mathbf{K}^{-1}(\mathbf{I}+\mathbf{F})\epsilon\langle\mathbf{u}\rangle^s \qquad (6.14)$$

where $\mathbf{K}$, $\mathbf{I}$ and $\mathbf{F}$ are respectively the permeability, the unit and the Forchheimer tensor. A 3D Cartesian grid of cubes falls in the class of spherically isotropic porous media [33] for which the permeability tensor is isotropic: $\mathbf{K} = K\mathbf{I}$. Irmay [37] derived the following expression for the permeability K of the grid of cubes, valid for $\epsilon \ll 1$:

$$\mathbf{K} = K\mathbf{I} \quad , \quad K = \frac{\left[1-(1-\epsilon)^{1/3}\right]^3 \left[1+(1-\epsilon)^{1/3}\right]}{C_K(1-\epsilon)} d_p^2 \tag{6.15}$$

where $C_K = 12$ on condition that $\epsilon \ll 1$ holds. In general, the Forchheimer tensor $\mathbf{F}$ depends on the Reynolds number, on the geometrical parameters of the porous medium and on the direction of the volume–averaged flow. In the present work, $\mathbf{F}$ is modeled with the Burke–Plummer equation, which is equivalent to the non–linear part of the Ergun equation [7]:

$$\mathbf{F} = F\mathbf{I} \quad , \quad \frac{d_p^2 F}{K} = C_F \left(\frac{1-\epsilon}{\epsilon^3}\right) \left(\frac{|\langle \mathbf{u}\rangle^s| d_p}{\nu}\right) \tag{6.16}$$

where C_F is a constant and for many packed beds approximately equal to 1.8 [61]. In order to determine the values of C_K and C_F more accurately, Breugem et al. [13] performed detailed numerical simulations of flow through a *fully periodic* 3D Cartesian grid of cubes with $\epsilon = 0.875$ (which is equivalent to $d_f = d_p$). Based on these simulations we found that $C_K = 11.4$ and that $C_F \approx 0.4$. The results from these simulations, together with the model prediction based on equations (6.14)–(6.16), are depicted in figure 6.4. The model overestimates the drag force in the transitional regime where both linear and non–linear drag are important, but gives a good fit in the low and the high Reynolds number range. A discussion of the closure problem for the subfilter–scale stress $\boldsymbol{\tau} \approx \langle \tilde{\mathbf{u}}\tilde{\mathbf{u}}\rangle^s$ is given by Breugem [8]. It is argued that in porous media subfilter–scale dispersion is usually negligible with respect to the drag force and/or the Reynolds–shear stress of the volume–averaged flow field. The final form of the momentum equation as used in the continuum approach, therefore reads:

$$\begin{aligned} \frac{\partial \langle \mathbf{u}\rangle^s}{\partial t} + \nabla \cdot \left[\frac{\langle \mathbf{u}\rangle^s \langle \mathbf{u}\rangle^s}{\epsilon}\right] &= -\frac{\epsilon}{\rho}\nabla \frac{\langle p\rangle^s}{\epsilon} + \nu \nabla^2 \langle \mathbf{u}\rangle^s - \nu \nabla\epsilon \cdot \nabla \frac{\langle \mathbf{u}\rangle^s}{\epsilon} \\ &\quad -\frac{\nu}{K}(1+F)\epsilon \langle \mathbf{u}\rangle^s \end{aligned} \tag{6.17}$$

where K and F are given by respectively equations (6.15) and (6.16).

6.4.2 Channel region

The VANS equations (6.11a) and (6.11b) apply to the channel region as well. Because the porosity equals unity in this region, the drag term on the right–hand side of (6.11a) vanishes and hence the VANS equations reduce to the LES equations. The subfilter–scale dispersion term is negligible only when the filter length is sufficiently small. This may not be the case when the *same* filter length is used for the channel region as for the homogeneous porous region. In the DNS with continuum, however, we aim to completely resolve the flow field in the channel region. This can be accomplished by assuming that in the channel region the filter length is set by the computational mesh spacing Δ, such that, provided that Δ is sufficiently small, dispersion by subfilter–scale turbulent motions is negligible. Consequently, the VANS equations (6.11a) and (6.11b) reduce to the standard Navier–Stokes equations with $\langle \mathbf{u} \rangle^s = \mathbf{u}$.

6.4.3 Interface region

As pointed out above, we assume that in the DNS with continuum the cellular–filter length is different for the homogeneous porous region than for the channel region. This implies that the filter length varies across the interface region, with $l_f = d_f + d_p$ (see figure 6.3) in the homogeneous porous region and $l_f = \Delta$ in the channel region. Consequently, in the interface region the volume–averaging theorem (6.10) is not strictly valid, because a spatially varying filter length means that the weighting function m depends not only on $\mathbf{y}$, but also on $\mathbf{x}$. On the other hand, the commutation errors will be small when the filter length is gradually changed over a sufficiently large distance compared to the characteristic length scales of the flow field [17]. The VANS equations (6.11a) and (6.11b) may therefore be applied also to the interface region. As for the homogeneous porous region and the channel region, we assume that subfilter–scale dispersion can be neglected in the interface region too. The drag force can not be neglected, however. It is modeled by means of equation (6.14), with equations (6.15) and (6.16) for K and F respectively. Furthermore, we need a model for the porosity, which must gradually change across the interface region from unity at $z = 0$ to $\epsilon = \epsilon_c$ at $z = -\delta_i$. In a previous study [8] we adopted a fifth–order polynomial for ϵ according to:

$$-\delta_i \leq z \leq 0 \quad : \quad \epsilon(z) = -6(\epsilon_c - 1)\left(\frac{z}{\delta_i}\right)^5 - 15(\epsilon_c - 1)\left(\frac{z}{\delta_i}\right)^4 - 10(\epsilon_c - 1)\left(\frac{z}{\delta_i}\right)^3 + 1 \quad (6.18)$$

This model requires a specification of the thickness δ_i. If the length of the cellular filter would be kept constant at $l_f = d_p + d_f$, then $\delta_i = 3d_p$ for the 3D grid of cubes with $d_f = d_p$. The corresponding porosity profile is plotted in figure 6.5 together with the porosity profile calculated from equation (6.6). The agreement between the model and the exact porosity profile is good. The local value for the porosity in the interface region is used in the expressions for K and F. This assures that the drag force and the VANS equations are continuous across the interface region. The reader may notice that the permeability approaches infinity at $z = 0$. However, in order to solve equation (6.17), we actually compute $1/K$, which remains bounded throughout the flow domain.

Recapitulating, in the DNS with continuum, equations (6.11b) and (6.17) are solved simultaneously for both the channel and the porous medium. The porosity in the interface region is given by equation (6.18). The permeability and the Forchheimer parameter are calculated from respectively equation (6.15) and (6.16). The governing equations are solved by means of a second–order pressure–correction method. A pseudo–spectral

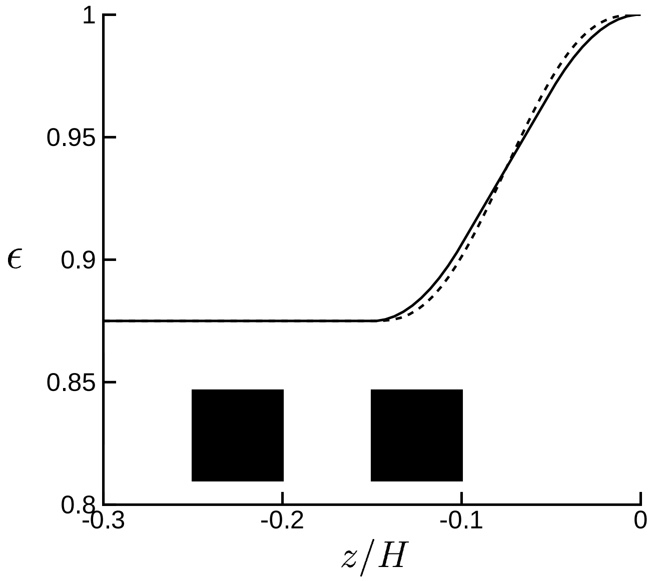

Figure 6.5: Porosity profile corresponding to the flow over a 3D Cartesian grid of cubes with $d_f = d_p$ and $\delta_i = 3d_p$. The black squares mark the positions of the cubes. —, calculated from equation (6.6); - - -, calculated from equation (6.18).

method is used for the spatial derivatives in the wall–parallel directions, whereas the finite–volume method with the central–differencing scheme is used for the wall–normal direction. The reader is referred to Breugem [8] for more details on the numerical scheme. The same code has also been used for the DNS with solid walls. The results from the latter simulation are in excellent agreement with the DNS results of Kim et al. [45].

6.5 DNS with cubes

In this section the numerical method is discussed that is used in the DNS with cubes. The flow geometry has been presented in figure 6.1.a. The computational domain has finite dimensions. It is bounded by two solid walls at $z = H$ and $z = -h$ respectively, at which the no–slip and no–penetration boundary conditions are imposed. Periodic boundary conditions are imposed for the wall–parallel directions. The Navier–Stokes equations are discretized on a fully staggered and uniform Cartesian mesh by means of the finite–volume method based on the second–order central–differencing scheme. The equations are advanced in time with the following pressure–correction scheme:

$$\frac{\hat{u}_i - u_i^n}{\Delta t} = \frac{5}{4}g_i^n - \frac{1}{4}g_i^{n-2} - \frac{1}{\rho}\frac{dP}{dx}\delta_{i1} \tag{6.19a}$$

$$\frac{1}{\rho}\frac{\partial^2 \hat{p}}{\partial x_i^2} = \frac{1}{\Delta t}\frac{\partial \hat{u}_i}{\partial x_i} \tag{6.19b}$$

$$u_i^{n+1} = \hat{u}_i - \frac{\Delta t}{\rho}\frac{\partial \hat{p}}{\partial x_i} \tag{6.19c}$$

$$p^{n+1} = p^n + \hat{p} \tag{6.19d}$$

where $\hat{u}_i$ is the prediction velocity, dP/dx the constant pressure gradient that drives the flow, and $\hat{p}$ is the correction pressure. The function g_i in equation (6.19a) is given by:

$$g_i = -\frac{1}{\rho}\frac{\partial p}{\partial x_i} - \frac{\partial u_i u_j}{\partial x_j} + \nu\frac{\partial^2 u_i}{\partial x_j^2} + f_i \tag{6.20}$$

For the implementation of the cubes an Immersed Boundary Method (IBM) is used, which has been used successfully by Fadlun et al. [25] and references therein. In this method forces are added to the flow field, i.e. $f_i \neq 0$ in equation (6.20), to accomplish a zero velocity on the cubes, as illustrated in figure 6.6. The advantage of an IBM is that no boundary conditions have to be specified on the cubes. As a consequence of this, the Poisson equation (6.19b) can be solved on a continuous domain with very efficient FFT–based solvers.

The IBM that is used here, is similar to the one developed by Fadlun et al. [25]. An advantage of applying the IBM in the present study over the problems discussed by Fadlun et al., which concern rather complicated geometries, is that the cubes can be aligned along the computational mesh. As sketched in figure 6.6, the cubes are aligned along the mesh such that their surfaces coincide with mesh points for the normal (with respect to the surface) velocity. This enables an *exact* implementation of the no–slip boundary condition on the cubes:

$$\mathbf{u} \times \mathbf{n} = \mathbf{0} \tag{6.21}$$

As an example we calculate the force f_t at position (i, k) in figure 6.6 that is equivalent to imposing a no–slip velocity at the location of the cross. The discretized terms in equation (6.20) for the function g that make use of the velocity components $u_{(\mathrm{i,k\text{-}1})}$, $w_{(\mathrm{i,k\text{-}1})}$ and $w_{(\mathrm{i+1,k\text{-}1})}$, are:

$$-\left.\frac{\partial uw}{\partial z}\right|_{(i,k)} = -\left[\frac{uw_{(i,k+1/2)} - uw_{(i,k-1/2)}}{\Delta z}\right]$$

$$\nu\left.\frac{\partial^2 u}{\partial z^2}\right|_{(i,k)} = \nu\left[\frac{u_{(i,k+1)} - 2u_{(i,k)} + u_{(i,k-1)}}{\Delta z^2}\right]$$

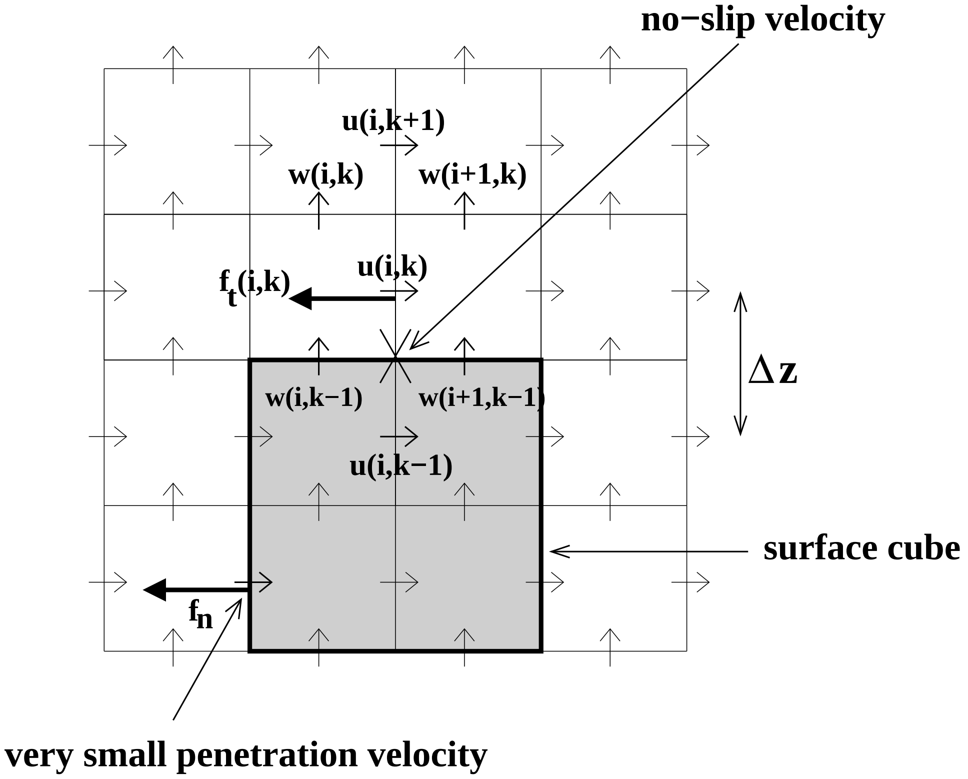

Figure 6.6: Illustration of the IBM in which forces (indicated by f_t and f_n) are applied at mesh points close to and at the surface of the cube to enforce the no–slip and no–penetration conditions. The horizontal and vertical vectors mark the mesh points of the streamwise and wall–normal velocity components respectively.

where $uw_{(i,k-1/2)}$ corresponds to uw at the location of the cross. According to the desired no–slip condition, $uw_{(i,k-1/2)} = 0$ and $u_{(i,k-1)} = -u_{(i,k)}$ must hold. This is equivalent to a force f_t equal to:

$$f_t|_{(i,k)} = -\frac{uw_{(i,k-1/2)}}{\Delta z} - \nu\left[\frac{u_{(i,k)} + u_{(i,k-1)}}{\Delta z^2}\right]$$

The no–penetration condition on the cubes is enforced by putting the prediction velocity $\hat{u}_i$ to zero. According to equation (6.19c) this yields a penetration velocity equal to:

$$\mathbf{u}^{n+1} \cdot \mathbf{n} = -\Delta t \nabla \hat{p} \cdot \mathbf{n} \approx 0 \tag{6.22}$$

Because the pressure is updated every time step, see equation (6.19d), $\nabla\hat{p}$ remains very small. Because Δt is also small, the right–hand side of (6.22) is therefore almost zero. For the case of a stationary flow, the correction pressure will approach zero and the no–penetration condition is then enforced exactly. In the DNS with cubes it has been verified that the largest penetration velocities, which appeared at the corners of the cubes nearest to $z = 0$ in figure 6.1.a, have a magnitude smaller than 10^{-5} times the bulk velocity in the channel.

In the IBM used in the DNS with cubes, forces are not only applied at the outside of the cubes, but also at the inside. Furthermore, the pressure gradient dP/dx on the right–hand side in equation (6.19a) is set to zero in the interior of the cubes. The interior of a cube is therefore very similar to a closed cavity inside which the 'fluid' is at rest.

The use of the IBM has consequences for the stability of the numerical scheme. The forces that are added to the momentum equation, are related to the drag that the flow encounters by the presence of the cubes. From equation (6.14) for the drag force in the VANS equations, it can be deduced that this may cause large negative eigenvalues of the function g_i. It is however difficult to quantify this in a simple manner, because equation (6.14) concerns the drag force experienced by the volume–averaged flow, whereas f_i in the equation for g_i is a point force acting on the unfiltered flow field. The expected difficulties with large negative eigenvalues, motivated our choice to use another time integration scheme (6.19a) than the popular second–order Adams-Bashforth scheme [101].

The stability polynomial for our scheme is found by putting $u_i^{n+1} = e^{i\phi} u_i^n$ with $\phi \in [0, 2\pi)$ and solving the eigenvalue λ from:

$$u_i^{n+1} - u_i^n = \lambda \Delta t \left[\frac{5}{4} u_i^n - \frac{1}{4} u_i^{n-2} \right] \tag{6.23}$$

The solution reads:

$$\lambda \Delta t = 4e^{2i\phi} \left(\frac{e^{i\phi} - 1}{5e^{2i\phi} - 1} \right) \tag{6.24}$$

The above stability polynomial is shown in figure 6.7. Also depicted in this figure is the stability polynomial of the second–order Adams–Bashforth scheme. From the figure it is clear that with respect to the Adams–Bashforth scheme, the time integration scheme used in the present study is much more stable for eigenvalues with a large negative real part. The dotted line in figure 6.7 is the stability polynomial of the Adams–Bashforth scheme multiplied by a factor of 3/4, which falls inside the curve of the stability polynomial given by (6.24). Ignoring the forces added to the momentum equation in the IBM, the computational time step criteria corresponding to the latter stability polynomial are the criteria derived by Wesseling [101] (p. 188) for the second–order Adams–Bashforth scheme multiplied by 3/4:

$$\frac{\nu \Delta t}{\Delta x^2} < \frac{1}{16} \tag{6.25a}$$

$$\frac{\Delta t \sqrt{\sum_i u_i^2}}{\Delta x} < \frac{1}{4} \tag{6.25b}$$

$$\sum_i \left(\frac{\Delta t |u_i|}{\Delta x} \right) \left(\frac{|u_i| \Delta x}{\nu} \right)^{1/3} < \left(\frac{27}{32} \right)^{1/3} \tag{6.25c}$$

These time step criteria are used in the present simulations. As indicated in figure 6.7, a relatively large safety margin exists to account for the destabilizing effect of the IBM forces.

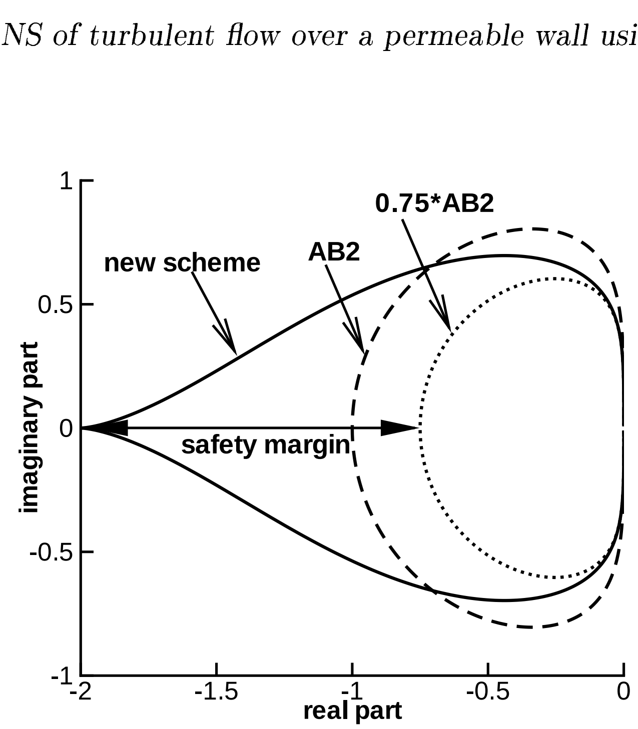

Figure 6.7: Stability polynomials for several time integration schemes. The enclosed areas are the stable regions of the respective schemes. — equation (6.24); - - -, stability polynomial of second–order Adams–Bashforth scheme; · · ·, stability polynomial of second–order Adams–Bashforth scheme multiplied by 0.75.

6.6 Numerical results

In the following sections the results from the DNS with cubes and the DNS with continuum are compared with each other and with the results from the DNS with solid walls. First some characteristics of the DNS with cubes and the DNS with continuum are given.

The dimensions of the computational domain in the DNS with cubes are 3 x 2 x 2 in terms of the channel height H for respectively the streamwise, the spanwise and the wall-normal direction. The porous medium has a height $h = H$ and consists of 30 x 20 x 9=5400 cubes in respectively the streamwise, spanwise and wall-normal direction. The number of cube layers in the wall–normal direction is chosen deliberately large to prevent that the flow in the channel experiences any influence of the solid wall below the grid of cubes. The cube rib equals $d_p = H/20$. The dimension d_f of the pores is equal to d_p, and consequently the porosity ϵ_c in the homogeneous porous region equals 0.875. The Darcy number is given by $Da_c \equiv K_c/H^2 = 3.4 \cdot 10^{-4}$, where K_c is the permeability of the grid of cubes (which was determined in section 6.4.1). The number of mesh points is 600 x 400 x 400=96·10^6. The bulk Reynolds number $Re_b \equiv U_b H/\nu = 5500$, where U_b is the bulk velocity in the channel region. The friction Reynolds number for the top wall $Re^t_\tau \equiv u^t_\tau H/\nu = 394$, where $u^t_\tau \equiv [-\nu\partial\langle\overline{u}\rangle/\partial z]^{1/2}_{z=H}$ is the friction velocity at the top wall. The friction Reynolds number for the permeable wall $Re^p_\tau \equiv u^p_\tau H/\nu = 669$, where $u^p_\tau \equiv [-\langle\overline{u'w'}\rangle + \nu\partial\langle\overline{u}\rangle/\partial z]^{1/2}_{z=0}$ is the friction velocity at the permeable wall. The permeability Reynolds number $Re_K \equiv$

DNS	ϵ_c	d_p/H	$Da_c(\cdot 10^{-4})$	δ_i/H	h/H	Re_b	Re_τ^p	Re_τ^t	Re_K	Re_d
CUB	0.875	0.05	3.4	0.15	1	5500	669	394	12.4	33.4
CON	0.875	0.05	3.4	0.15	1	5500	726	409	13.5	36.3
SOL	0	0	0	0	0	5500	352	350	0	0

Table 6.1: Characteristics of the DNS with cubes (DNS CUB), DNS with continuum (DNS CON) and the DNS with solid walls (DNS SOL). ϵ_c is the porosity in the homogeneous porous region, d_p/H is the rib of the cubes, $Da_c \equiv K_c/H^2$ is the Darcy number in the homogeneous porous region where $K = K_c$, δ_i is the thickness of the interface region, h is the thickness of the permeable wall, $Re_b \equiv U_b H/\nu$ is the bulk Reynolds number where U_b is the bulk velocity in the channel, $Re_\tau^t \equiv u_\tau^t H/\nu$ is the friction Reynolds number based on the friction velocity u_τ^t at the *top* wall, $Re_\tau^p \equiv u_\tau^p H/\nu$ is the friction Reynolds number based on the friction velocity u_τ^p at the *permeable* wall, $Re_K \equiv u_\tau^p \sqrt{K_c}/\nu$ is the permeability Reynolds number based on the friction velocity u_τ^p at the *permeable* wall, and $Re_d \equiv u_\tau^p d_p/\nu$ is the roughness Reynolds number for the *permeable* wall.

$u_\tau^p \sqrt{K_c}/\nu$ is equal to 12.4. Based on the classification of Breugem [8] of permeable walls, the grid of cubes can therefore be considered as a highly permeable wall near which viscous effects are of minor importance. The roughness Reynolds number $Re_d \equiv u_\tau^p d_p/\nu = 33.4$, which according to Hinze [35] is in the transitional roughness regime. The computational time step in the simulation equals $\Delta t = 6.7 \cdot 10^{-4}\ H/U_b$. The number of instantaneous data fields used for the statistics equals 45, spanning a total time interval of 60.5 H/U_b. The values of ϵ_c, d_p, δ_i and Re_b for the DNS with continuum are chosen equal to the corresponding values in the DNS with cubes. Some characteristics of these two simulations are listed in table 6.1. The Reynolds numbers Re_τ^p, Re_τ^t, Re_K and Re_d are about equal, and, because they were determined from the simulation data, this indicates already that also the turbulence statistics of the two simulations are similar. The dimensions of the computational domain in the DNS with continuum are 5x3x2 in terms of the channel height H for respectively the streamwise, the spanwise and the wall-normal direction. The number of mesh points is $256 \text{x} 192 \text{x} 300 = 15.7 \cdot 10^6$. The mesh is stretched in the wall–normal direction with mesh points clustered around the permeable wall interface and the top wall. The computational time step in the DNS with continuum equals $\Delta t = 3.1 \cdot 10^{-4}\ H/U_b$. The number of instantaneous data fields used for the statistics equals 96, spanning a total time interval of 58.7 H/U_b.

We remark that the dimensions of the computational domain in the DNS with cubes are chosen deliberately smaller than in the DNS with continuum, in order to avoid that the number of mesh points in the DNS with cubes would become excessively large. Therefore, a larger computational domain was not feasible. We note that the dimensions of the computational domain in the DNS with cubes, although relatively small, are still much larger than the minimal channel studied by Jiménez & Moin [42]. Furthermore, we verified by means of a simulation of standard channel flow, using the same numerical method as used in the DNS with cubes, that a computational domain of 3x2x1 yields low–order statistics that agree well with the DNS results of Kim et al. [45].

The codes for both the DNS with cubes and the DNS with continuum have been written

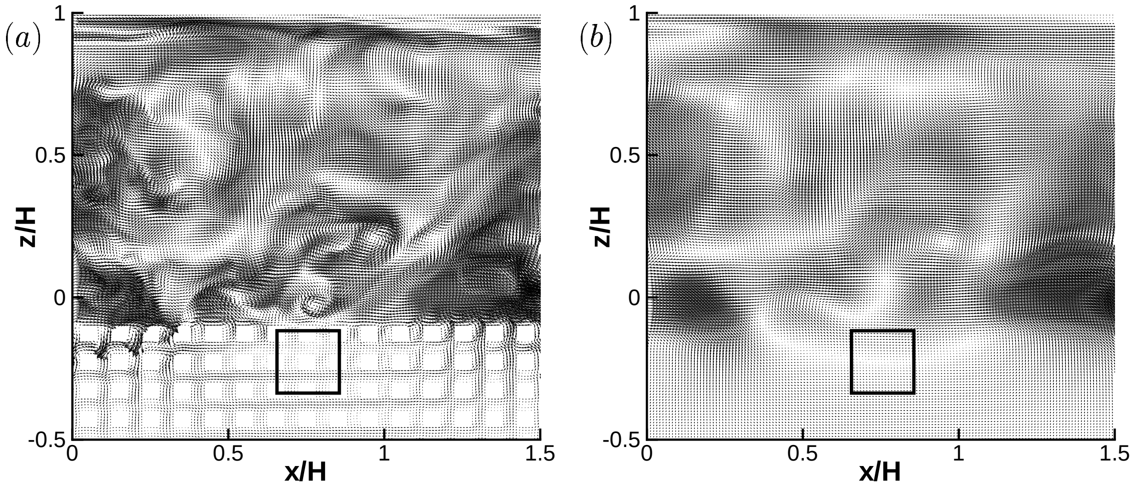

Figure 6.8: Cross–section along the streamwise direction of the fluctuating flow field in the DNS with cubes. For clarity, only part of the cross–section is shown and the number of vectors is reduced by a factor of two in both the x and z direction. The rectangle shows the dimension of the averaging volume of the cellular filter. (a) Unfiltered flow field (u',w'); (b) Corresponding volume–averaged flow field ($\langle u'\rangle^s$,$\langle w'\rangle^s$).

in Fortran 77 and made parallel based on the MPI standard. The DNS with cubes was run on 100 nodes of a SGI Origin 3800 system. The DNS with continuum was run on 32 nodes of a SGI Altix 3700 system.

6.6.1 Volume averaging and mean velocity profiles

Before the results of the DNS with cubes and the DNS with continuum can be compared with each other, the velocity field of the DNS with cubes need to be filtered first according to equation (6.3) with the cellular weighting function (6.5). We remark that the calculation of the volume–averaged velocity at a *single* mesh point involves the evaluation of the discretized form of equation (6.3) over 40^3 neighboring mesh points. Hence, the computation of the volume–averaged velocity at *all* mesh points is fairly time–consuming. Figure 6.8 shows a cross–section of the fluctuating flow field before and after filtering. The white spots in figure 6.8.a mark the location of the cubes. The rectangle indicates the dimension of the averaging volume of the cellular filter. Figure 6.8.b shows clearly that due to filtering the subfilter–scale motions are averaged out and that the volume–averaged flow field is continuous throughout the flow domain. Figure 6.9 shows the effect of filtering applied to the Reynolds–averaged flow field. Furthermore, it illustrates nicely the decomposition (6.7) of the Reynolds–averaged flow field into the volume– and Reynolds–averaged flow field and the subfilter–scale Reynolds–averaged flow field: $\overline{u}_i = \langle\overline{u}_i\rangle + \tilde{\overline{u}}_i$. Notice that the volume– and Reynolds–averaged flow field ($\langle\overline{u}\rangle$,$\langle\overline{w}\rangle$) is one–dimensional and horizontally homogeneous, whereas the unfiltered Reynolds–averaged flow field ($\overline{u}$,$\overline{w}$)

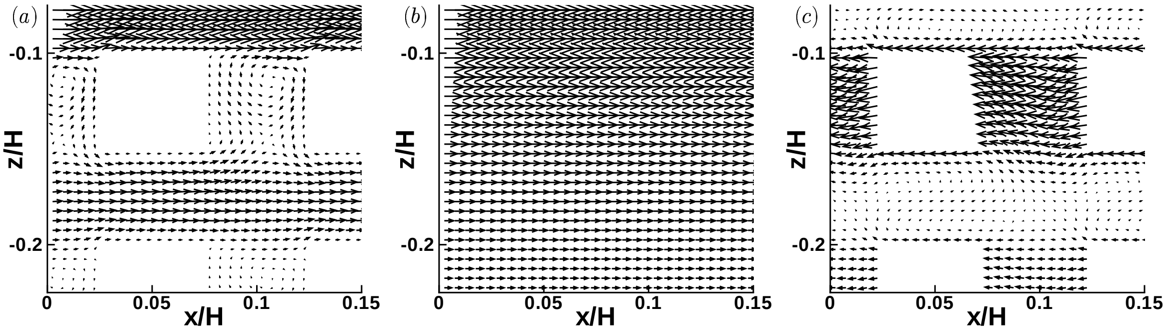

Figure 6.9: Cross–section along the streamwise direction of the Reynolds–averaged flow field in the DNS with cubes. For clarity, only part of the cross–section is shown. The different graphs illustrate the decomposition $\overline{u}_i = \langle\overline{u}_i\rangle + \tilde{\overline{u}}_i$. (a) Reynolds–averaged flow field ($\overline{u}$,$\overline{w}$); (b) volume– and Reynolds–averaged flow field ($\langle\overline{u}\rangle$,$\langle\overline{w}\rangle$); (c) subfilter–scale Reynolds–averaged flow field ($\tilde{\overline{u}}$,$\tilde{\overline{w}}$).

is three–dimensional and horizontally heterogeneous. The horizontal heterogeneity in the unfiltered Reynolds–averaged flow field vanishes rapidly when moving out the grid of cubes into the channel region, with $|\overline{w}|_{\max}/U_b < 10^{-2}$ for $z/H > -0.07$ and $|\overline{w}|_{\max}/U_b < 10^{-3}$ for $z/H > 0$.

It is important to note that in the DNS with cubes the filter length is kept constant at $l_f = d_f + d_p$ in the volume averaging of the flow field, except close to the solid walls at $z = H$ and $z = -h$ where the vertical extent of the averaging volume is gradually decreased to zero, depending on the distance to the wall. We remark that the constant filter length in the DNS with cubes is *different* from the assumption of a variable filter–length in the DNS with continuum. Recall that the variable filter–length in the latter simulation has the advantage that no subfilter–scale stress need to be modeled in the channel region. The disadvantage of a variable filter–length is that it causes a commutation error in the volume–averaging theorem (6.6). Although this error is small, in the DNS with cubes we want to avoid this, and therefore the filter length in the *processing* of this simulation is kept constant. It is important to realize that the difference in the filter length for the channel region between the DNS with cubes and the DNS with continuum, has consequences for comparing the results of the two simulations with each other. We come back to this point in the next section.

Figure 6.10 presents the profiles of the Reynolds– and volume–averaged velocity of the DNS with cubes, the DNS with continuum and the DNS with solid walls. We recall that in the channel region of the DNS with continuum and the DNS with solid walls, the Reynolds– and volume–averaged velocity $\langle\overline{u}\rangle^s$ is equal to the Reynolds–averaged velocity $\overline{u}$, because the mesh spacing is sufficiently small. In the channel region of the DNS with cubes, the profile of $\langle\overline{u}\rangle^s$ is also very similar, although not exactly equal, to $\overline{u}$. Although our main interest is in the behavior of the flow field in the channel region, we still prefer here to plot $\langle\overline{u}\rangle^s$, because this velocity is continuous and horizontally homogeneous in the

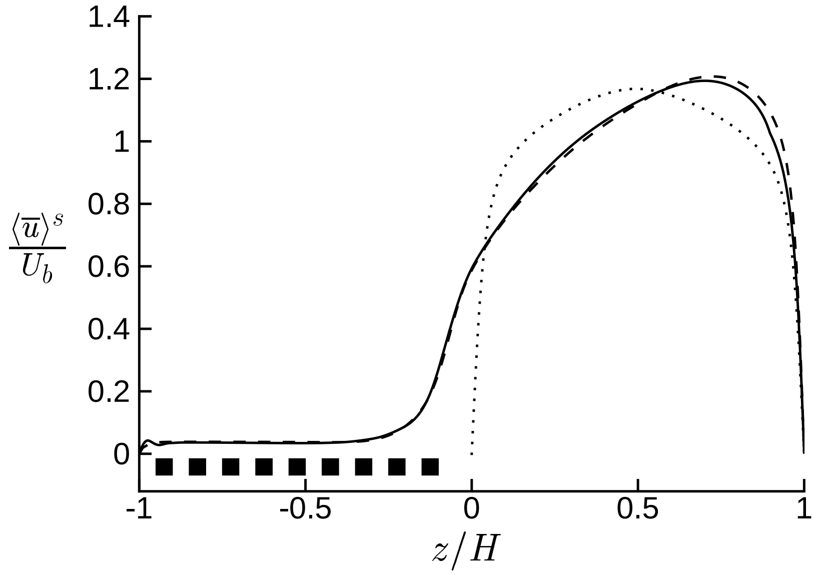

Figure 6.10: Profiles of the Reynolds– and volume–averaged velocity, normalized by the bulk velocity U_b, as function of z/H. The black squares mark the location of the cubes in the DNS with cubes. —, DNS with cubes; - - - DNS with continuum; · · ·, DNS with solid walls.

channel region as well as inside the permeable wall. This is not true for $\overline{u}$.

The profiles of the DNS with cubes and the DNS with continuum overlap each other. Both profiles are strongly skewed with the position $z = \delta_w$ of the maximum velocity well above the centerline of the channel. The position of the maximum velocity corresponds to zero total shear stress. From this condition the following expression can be found for δ_w:

$$\frac{\delta_w}{H} = \frac{(u_\tau^p)^2}{(u_\tau^p)^2 + (u_\tau^t)^2} \tag{6.26}$$

Thus the skewed mean velocity profile is a direct consequence of the larger skin friction at the permeable wall than at the top wall.

The small wiggle near $z/H = -1$ in the profile of the DNS with cubes is caused by the change in the vertical extent of the averaging volume close to the solid wall.

6.6.2 Rms profiles of velocity components and pressure

The volume–averaged root–mean–square (rms) velocity $u_{i,\mathrm{rms}}$ is defined here according to:

$$u_{i,\mathrm{rms}} \equiv \sqrt{\langle \overline{u_i' u_i'} \rangle^s} = \sqrt{\underbrace{\frac{\overline{\langle u_i' \rangle^s \langle u_i' \rangle^s}}{\epsilon}}_{I} + \underbrace{\left[\langle \overline{u_i' u_i'} \rangle^s - \frac{\overline{\langle u_i' \rangle^s \langle u_i' \rangle^s}}{\epsilon} \right]}_{II}} \tag{6.27}$$

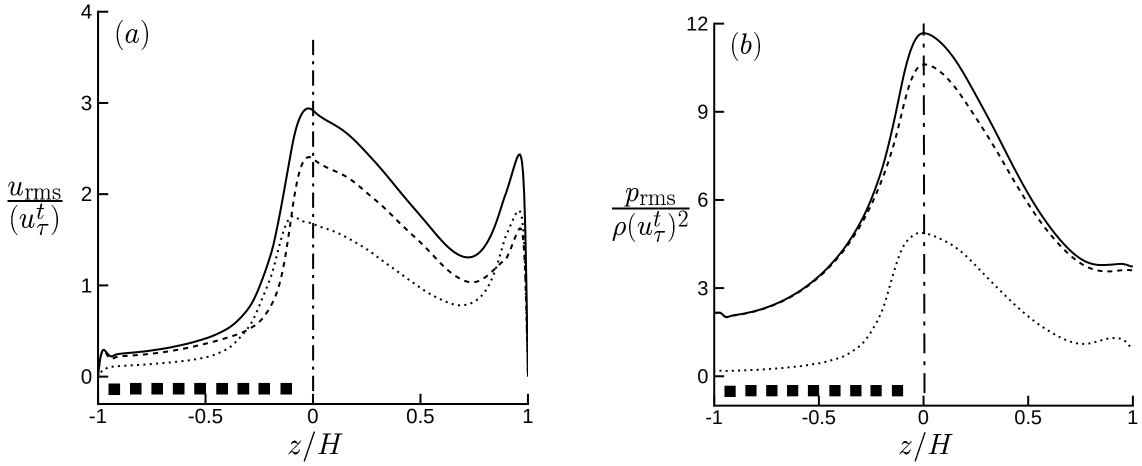

Figure 6.11: Decomposition of the volume–averaged rms velocity and pressure according to equation (6.27) for the DNS with cubes. The black squares mark the position of the cubes. —, total; - - - contribution term I; $\cdots$, contribution term II. (a) Volume–averaged streamwise rms velocity; (b) Volume–averaged rms pressure.

The decomposition of $u_{i,\mathrm{rms}}$ into the above two terms originates from the consideration that, when $\langle\langle u_i'\rangle\rangle^s \approx \langle 1\rangle^s\langle u_i'\rangle = \langle u_i'\rangle^s$ holds, term II is approximately equal to:

$$\begin{aligned}\langle\overline{u_i'u_i'}\rangle^s - \frac{\overline{\langle u_i'\rangle^s\langle u_i'\rangle^s}}{\epsilon} &= \langle\overline{[\langle u_i'\rangle + \tilde{u}_i']\,[\langle u_i'\rangle + \tilde{u}_i']}\rangle^s - \frac{\overline{\langle u_i'\rangle^s\langle u_i'\rangle^s}}{\epsilon} \approx \\ &\overline{\langle u_i'\rangle\langle u_i'\rangle}\langle 1\rangle^s + 2\overline{\langle u_i'\rangle\langle\tilde{u}_i'\rangle^s} + \langle\overline{\tilde{u}_i'\tilde{u}_i'}\rangle^s - \frac{\overline{\langle u_i'\rangle^s\langle u_i'\rangle^s}}{\epsilon} \approx \langle\overline{\tilde{u}_i'\tilde{u}_i'}\rangle^s\end{aligned}$$

Thus, term I and II represent basically the contributions of respectively the volume–averaged velocity $\langle u_i'\rangle$ and the subfilter–scale velocity $\tilde{u}_i'$.

In the DNS with cubes, the contributions of both term I and term II in equation (6.27) can be calculated exactly. Figure 6.11 shows the result for u_{rms} and p_{rms}. The contribution of the subfilter–scale flow field to u_{rms} is significant in the channel region and the top region of the grid of cubes, but appears to be small for $z/H \lesssim -0.5$. The rms pressure is dominated by the contribution of large–scale pressure fluctuations with a small contribution of the subfilter–scale pressure fluctuations throughout the flow domain.

In the DNS with continuum, just the volume–averaged flow field is resolved, and consequently only the contribution of term I can be calculated exactly. At this point we recall the discussion of the variable filter–length in the DNS with continuum (see sections 6.4.2 and 6.4.3). In the channel region it is assumed that the cellular–filter length is set by the mesh spacing, which is sufficiently small, and consequently term II is equal to zero in this region. In the homogeneous porous region, however, the cellular–filter length is equal to $l_f = d_f + d_p$ and consequently in this region term II is not zero. As our main interest is in the behavior of the volume–averaged rms velocity in the channel region, we will not attempt here to model term II in the homogeneous porous region. Instead, in the DNS with continuum term II is simply put to zero.

The profiles of the volume–averaged rms velocities and pressure of the DNS with cubes, the DNS with continuum and the DNS with solid walls are depicted in figure 6.12.a–d. The profiles of the DNS with cubes and the DNS with continuum compare very well. The differences between the profiles of these two simulations are small compared to the differences with the corresponding profiles of the DNS with solid walls. Notice that not only a good agreement exists between the DNS with cubes and the DNS with continuum in the channel region, but also inside the permeable wall, despite neglecting the contribution of term II in the DNS with continuum.

The rms profiles of the DNS with cubes and the DNS with continuum show an increase in all rms velocities and in the rms pressure near the permeable wall as compared to the profiles of the DNS with solid walls, at least when normalized by the friction velocity u_τ^t at the top wall. However, a more appropriate scaling of the rms profiles near the permeable wall is by means of the friction velocity u_τ^p at the permeable wall. Figure 6.13 shows the result for the rms profiles of the streamwise and the wall–normal velocity respectively. The profiles are plotted as function of z/δ_w, where δ_w, given by equation (6.26), is considered as a characteristic length scale for eddies in the outer region of the boundary layer above the permeable wall. The peak in the streamwise rms velocity is smaller for the DNS with cubes and the DNS with continuum as compared to the DNS with solid walls. The large peak for the DNS with solid walls is associated with the presence of low– and high–speed streaks near a solid wall, which originate from the intense mean–shear $(\partial\langle\overline{u}\rangle/\partial z)$ layer near the wall and the wall–blocking effect. The strong reduction in mean shear and the weakening of the wall–blocking effect prevent the formation of the streaks above a highly permeable wall, and this explains the decrease in the peak value of the streamwise rms velocity. The non–existence of streaky structures near the permeable wall in the DNS with cubes and the DNS with continuum can be observed also in figure 6.8. The flow near the solid top wall is characterized by elongated streaky structures, whereas the flow near the permeable wall is dominated by relatively large–scale vortical structures. Similar vortical structures have been detected in experiments of flow over plant canopies, which originate from a Kelvin–Helmholtz type of instability of the inflexional mean velocity profile [28]. The existence of these vortical structures is consistent with the dominant contribution from the volume–averaged flow field to the streamwise rms velocity around $z = 0$ in figure 6.11.a, which is opposite to the behavior close to the solid top wall. Furthermore, as will be discussed in the next section, these vortical structures are also responsible for a strong increase in the Reynolds–shear stress at the permeable wall as compared to a solid wall. A more elaborate analysis of these vortical structures is beyond the scope of the present paper.

Opposite to the effect of wall permeability on the streamwise rms velocity, an increase is observed in the peak of the wall–normal rms velocity. This can be explained by the weakening of the wall–blocking effect, which no longer prohibits wall–normal transport of fluid across the wall interface. Notice that the profiles of the streamwise rms velocity overlap for $z/\delta_w \gtrsim 0.5$, thus exhibiting similarity, whereas in the same region the profiles

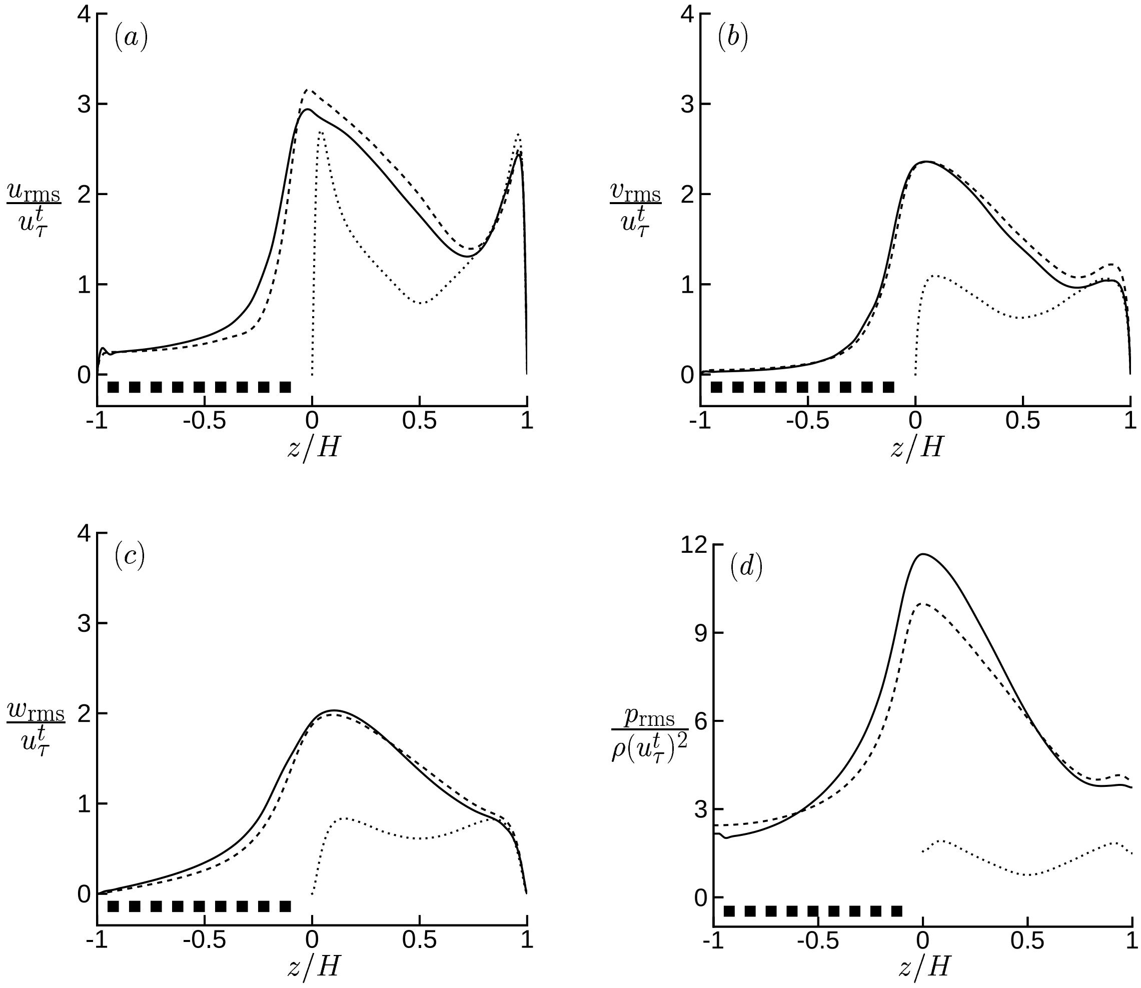

Figure 6.12: Volume–averaged rms profiles of the velocity and pressure fluctuations in the DNS with cubes (—), the DNS with continuum (- - -) and the DNS with solid walls (· · ·). The rms profiles are normalized by u^t_τ and $\rho(u^t_\tau)^2$ respectively, and plotted as function of z/H. The black squares mark the position of the cubes in the DNS with cubes. (a) streamwise rms velocity; (b) spanwise rms velocity; (c) wall–normal rms velocity; (d) rms pressure.

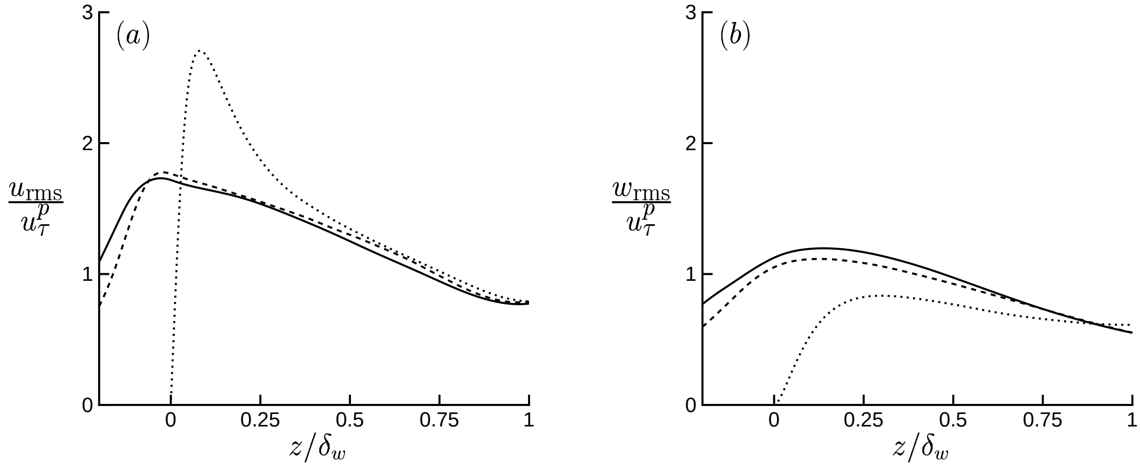

Figure 6.13: Volume–averaged rms profiles of the streamwise and wall–normal velocity fluctuations in the DNS with cubes (—), the DNS with continuum (- - -) and the DNS with solid walls (···). The rms profiles are normalized by the friction velocity u_τ^p at the permeable wall and plotted as function of z/δ_w. The black squares mark the position of the cubes in the DNS with cubes. (a) streamwise rms velocity; (b) wall–normal rms velocity.

of the wall–normal rms velocity of the DNS with cubes and DNS with continuum do not coincide with the profile of the DNS with solid walls.

6.6.3 Shear–stress profiles

The volume–averaged total shear stress $\langle \tau_{xz}\rangle^s$ is defined here as:

$$\langle \tau_{xz}\rangle^s \equiv \underbrace{\nu\frac{\partial\langle\overline{u}\rangle^s}{\partial z}}_{I}\underbrace{-\frac{\overline{\langle u'\rangle^s\langle w'\rangle^s}}{\epsilon}}_{II}+\underbrace{\left[-\langle\overline{u'w'}\rangle^s+\frac{\overline{\langle u'\rangle^s\langle w'\rangle^s}}{\epsilon}\right]}_{III}\underbrace{-\langle\overline{u}\,\overline{w}\rangle^s}_{IV} \tag{6.28}$$

The terms on the right–hand side represent respectively the volume–averaged viscous shear stress (I), the contribution of large–scale motions (II) to the volume–averaged Reynolds–shear stress $\langle\overline{u'w'}\rangle^s$, the contribution of subfilter–scale motions (III) to the volume–averaged Reynolds–shear stress, and the volume–averaged mean shear stress (IV). The terms in equation (6.28) have been calculated separately for the DNS with cubes. The result is shown in figure 6.14. The volume–averaged viscous shear stress (term I) peaks at the top wall due to the no–slip boundary condition, but it is negligible near the permeable wall. This substantiates the classification of the grid of cubes as a highly permeable wall. The kink in the profile of the volume–averaged viscous shear stress at $z/H = 0.9$ is caused by the change in the vertical extent of the averaging volume close to the top wall, which leads to a small commutation error: $\langle\nu\partial\overline{u}/\partial z\rangle^s \neq \nu\partial\langle\overline{u}\rangle^s/\partial z$. The

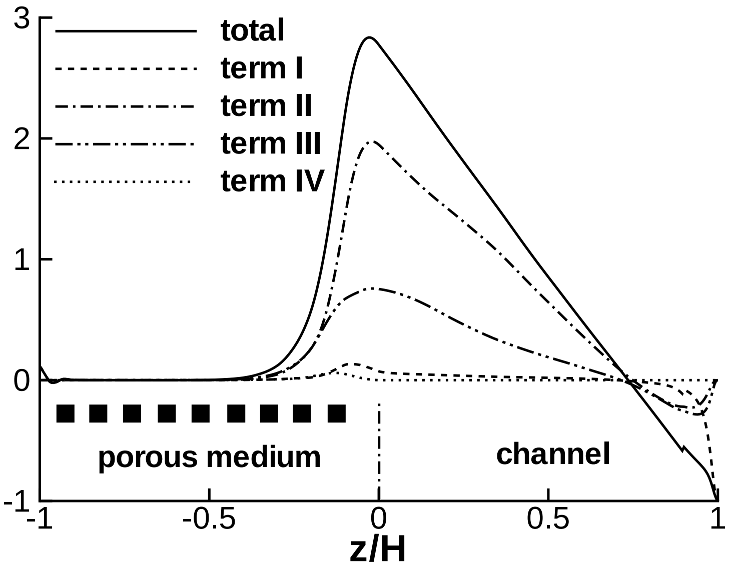

Figure 6.14: Contribution of terms I–IV on the right–hand side of equation (6.28) to the volume–averaged total shear stress $\langle \tau_{xz} \rangle^s$ for the DNS with cubes. The stresses are normalized by $(u_\tau^t)^2$. The black squares mark the position of the cubes.

volume–averaged mean shear stress (term IV) is negligible throughout the flow domain. In most of the channel region the contribution of the large–scale motions (term II) is dominant over the contribution of the subfilter–scale motions (term III), but in the top region of the porous medium both contributions are equal. As mentioned before, at the end of section 6.6.2, the dominant contribution from the large–scale motions around $z = 0$ is consistent with the presence of the relatively large–scale vortical structures observed in figure 6.8. These structures are responsible for an exchange of streamwise momentum between the channel region and the top layer of the permeable wall.

Figure 6.15 presents the profiles of the volume–averaged Reynolds–shear stress $\langle \overline{u'w'} \rangle^s$, viscous shear stress and total shear stress for the DNS with cubes, the DNS with continuum and the DNS with solid walls. In the DNS with continuum, the contribution of the subfilter–scale motions (term III) to $\langle \overline{u'w'} \rangle^s$ and the volume–averaged mean shear stress (term IV) are neglected, based on a similar reasoning as given in the previous section for the contribution of subfilter–scale motions to the volume–averaged rms velocity. The Reynolds–shear stress in the DNS with continuum is slightly overpredicted as compared to the DNS with cubes, although this discrepancy is small compared to the difference with the profile of the DNS with solid walls. With respect to the DNS with solid walls, we find a large increase in the Reynolds–shear stress for the DNS with cubes and the DNS with continuum, especially close to the permeable wall. This can be explained by a weakening of the wall–blocking effect, which no longer prohibits an exchange of streamwise momentum between the channel and the top layer of the porous medium by means

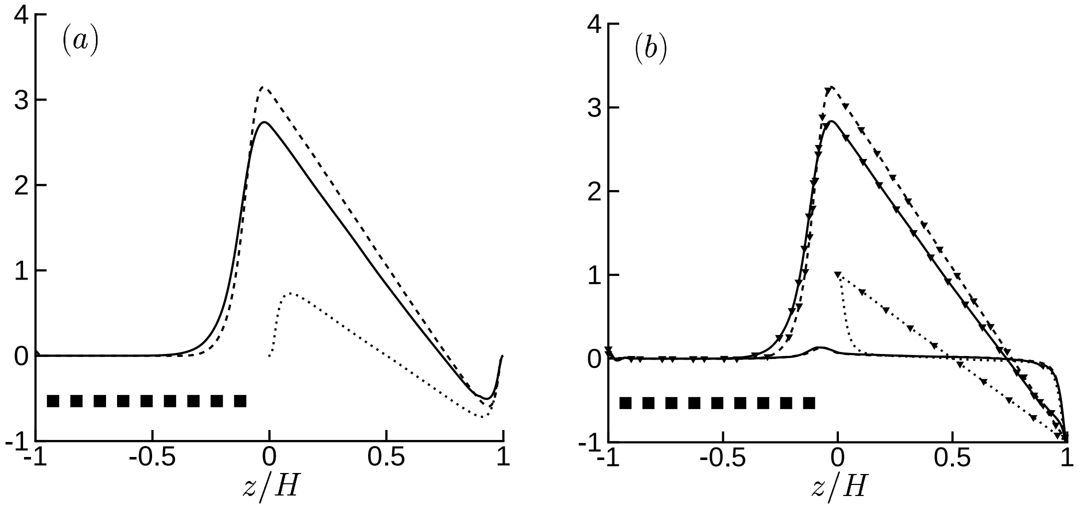

Figure 6.15: Profiles of the volume–averaged Reynolds–shear, viscous shear and total shear stress in the DNS with cubes (—), the DNS with continuum (- - -) and the DNS with solid walls (···). The stresses are normalized by $(u_\tau^t)^2$. The black squares mark the position of the cubes in the DNS with cubes. (a) Reynolds–shear stress; (b) Viscous shear stress (lines without symbols) and total shear stress (lines with symbols).

of the previously observed vortical structures.

Figure 6.15.b shows that also a good agreement exists between the DNS with cubes and the DNS with continuum for the profiles of the volume–averaged viscous and total shear stress. As mentioned before, near the permeable wall the volume–averaged viscous shear stress is negligible. The large peak in the profile for the volume–averaged total stress is thus solely due to the strong increase in the volume–averaged Reynolds–shear stress near the permeable wall.

6.7 Conclusions and discussion

The main conclusion of the present study is that the continuum approach based the VANS equations is capable of an accurate simulation of the turbulent flow over and through a permeable wall, even quantitatively. In order to solve the VANS equations for the volume–averaged flow inside the permeable wall, closures are required for the subfilter–scale stress and the drag force. We have assumed a variable filter–length for the DNS with continuum, with $l_f = d_f + d_p$ in the homogeneous porous region and $l_f = \Delta$ in the channel region. As argued by Breugem [8], subfilter–scale dispersion can usually be neglected in the homogeneous porous region. Because the mesh spacing Δ is sufficiently small, in the DNS with continuum subfilter–scale dispersion can be neglected in the channel region as well. In literature many semi–empirical relations exists for the drag force. In the present study a drag relation was adopted based on the Irmay [37] and the Burke–Plummer model [7], where the model coefficients were determined from simulations reported by Breugem et al. [13]. A variable–porosity model was used for the interface region to ensure that the VANS equations are continuous throughout the flow domain.

We have introduced the concept of a variable filter–length for the DNS with continuum. In the *processing* of the DNS with cubes however, the filter length was kept constant to avoid commutation errors. Figure 6.14 has shown that in this case the volume–averaged mean shear stress $\langle \overline{u}\,\overline{w} \rangle^s$ can still be neglected, but that the contribution of the subfilter–scale motions to the Reynolds–shear stress $\langle \overline{u'w'} \rangle^s$ may be important in the channel as well as in the interface region. In a previous study [8], we proposed a closure for the subfilter–scale stress of the form $-\langle u_i u_j \rangle + \langle u_i \rangle \langle u_j \rangle = (K_p + K_t)(\partial \langle u_i \rangle / \partial x_j + \partial \langle u_j \rangle / \partial x_i)$ with K_p and K_t the mechanical and turbulent viscosity respectively. Although not evaluated in this paper, this model seems to be promising.

The success of the continuum approach depends primarily on the accuracy of the closure for the drag force. In the present work we adopted the Irmay model for the range of low Reynolds numbers. This model is restricted to flow through a Cartesian grid of cubes and might not be suitable for other porous media. For example, for packed beds the Blake–Kozeny model [7] is widely used. The coefficient in the Irmay model was determined from separate simulations through a fully periodic grid of cubes with a porosity of 0.875. The value thus determined was close to the value of 12 proposed by Irmay for small porosities. This indicates that the Irmay model is valid for a large range of porosities, varying from almost zero to values close to unity. To model the drag force in the range of high Reynolds numbers, we adopted the Burke–Plummer model. This model performs well for many porous media, although the coefficient in this model might vary substantially dependent of the structure of the porous medium. MacDonald et al. [61] found that a value of 1.8 is appropriate for many packed beds, while we found a value of about 0.4 for the Cartesian grid of cubes. The difference in these values is due to the fact that packed beds are disordered, whereas the Cartesian grid of cubes is ordered and aligned.

Other requirements for using the continuum approach are that the length scales of the volume–averaged and the subfilter–scale flow field are well–separated, and that the permeability Reynolds number is relatively large. The former condition demands that the dimension of the pores and solid obstacles of the porous medium should be small compared to the channel height, because otherwise the flow in the channel region is more similar to flow around obstacles rather than flow over a permeable wall. Furthermore, the permeability Reynolds number should be relatively large to ensure that the effect of wall permeability on the turbulent flow in the channel dominates over the effect of surface roughness. The difference between wall permeability and wall roughness has been illustrated in figure 6.2. If the effect of surface roughness would be much more important, then it is not likely that the closure for the drag force *in the interface region* will give accurate results. This closure is namely based on the drag relation for uniform volume–averaged flow through a *fully periodic porous medium*, which will be quite different from the drag experienced by flow over the rough and impermeable wall in figure 6.2. Therefore, when surface roughness is important, one has to look for a more appropriate closure model for the drag force in the interface region. Instead of using the continuum approach, a better option in this case is probably a direct simulation, which captures the geometry of the surface roughness. A measure for the effect of surface roughness is the roughness Reynolds number. In the DNS with continuum this number was equal to 36.3, see table 6.1, and according to Hinze [35] this value falls the transitional roughness regime. The permeability Reynolds number was 13.5 and this value corresponds to the highly permeable regime [8]. This suggests that, in addition to the fact that the results of the DNS with cubes and the DNS with continuum agree well, in the present simulations the influence of wall permeability was strongly dominant over the effect of surface roughness. This suggestion is also supported by the relatively large rms velocities inside the permeable wall, and the important contribution of the volume–averaged Reynolds–shear stress to the total shear stress in the top layer of the permeable wall. We are aware that these arguments are only indirect evidence for the dominant effect of wall permeability over wall roughness. For a more conclusive claim concerning the importance of wall roughness with respect to wall permeability, we should actually simulate and compare the two cases shown in figure 6.2. This is however beyond the scope of this paper.

Chapter 7

Main conclusions, discussion and recommendations

7.1 Main conclusions

In section 1.1 we identified four open questions and shortcomings in literature. This motivated the research presented in this thesis. The main research objectives were to gain insight in the influence of wall permeability on laminar and turbulent flows and to develop a DNS methodology for simulating turbulent flows over permeable walls at relatively high permeability Reynolds numbers. In this section we recapitulate the main results and conclusions.

- **Influence wall permeability on laminar boundary layers**

In chapter 3, we presented a theoretical study on the effect of wall permeability on the laminar boundary layer over a wedge. Two boundary layers on top of each other can be distinguished: the classic Prandtl boundary layer above the permeable wall, and the Brinkman boundary layer inside the permeable wall. Using the interface conditions of Ochoa–Tapia & Whitaker [67] (OTW model), a closed set of equations could be derived for the Prandtl boundary layer. A self–similar solution exists for the stream function, in terms of an expansion series in a perturbation parameter. This perturbation parameter can be interpreted as the ratio of the Brinkman to the Prandtl boundary–layer thickness. The self–similar solution is described by a generalized form of the Falkner–Skan equation, which incorporates the effect of wall permeability.
The first–order effect of wall permeability causes a positive non–zero interface velocity, i.e. an apparent slip velocity. A non–zero wall–normal interface velocity is a second–order effect. Furthermore, wall permeability causes a decrease in the wall–shear stress when the freestream flow accelerates, whereas it causes an increase in the wall–shear stress when the freestream flow decelerates.

- **Momentum–transfer models**

In chapter 4, we evaluated two models for the transfer of momentum across the interface of a permeable wall: the OTW model and a variable–permeability model.

The OTW model has been developed for Stokes flow over a permeable wall. This model consists of wall–interface conditions to match the solutions for the volume–averaged flow in respectively the homogeneous porous and the homogeneous fluid region. The OTW interface conditions have been validated by means of a DNS of Stokes flow in a plane channel with a lower permeable wall consisting of a 3D Cartesian grid of cubes. The approximate solution for the velocity profile based on the OTW model, agrees well with the DNS results, except for substantial deviations in the interface region. However, a drawback of the OTW model is that the value of the tangential stress–jump parameter, determined from the DNS results, is sensitive for the definition of the wall interface. Another drawback of the OTW model is that the values of the stress–jump parameters are unknown a priori, and have to be determined from simulations or experiments.

From the aforementioned channel flow simulation, we calculated the profile of the drag force as function of the height. Using the parameterization of the drag force proposed by Whitaker [104], the corresponding permeability profile was computed. This profile was compared to a variable–permeability model, based on the model of Irmay [37], which relates the permeability to the local value of the porosity. The predicted and the exact permeability profiles agree not very well in the interface region. It was found that the computed permeability was varying not only in the interface region, but also in the homogeneous porous region. Because the permeability was only varying in a region where the flow was non–uniform, we speculated that the parameterization of Whitaker should contain an additional diffusion–like term. This was suggested before by Lundgren [59]. In literature, the question whether the effective viscosity is different from the fluid viscosity is still under debate, but our numerical investigation presented in chapter 4 suggests that the effective viscosity is lower than the fluid viscosity. According to the analysis of Lundgren, the effective viscosity might in fact be either higher or lower than the fluid viscosity, dependent of the solidity of the porous medium.

- **Formalism for DNS of turbulent flows over permeable walls**

In chapter 5, a method has been developed for DNS of turbulent flows over permeable walls at relatively high permeability Reynolds numbers. In this formalism distinction is made between the homogeneous porous region, the interface region characterized by a spatially varying porosity, and the homogeneous fluid region. The continuum approach based on the Volume–Averaged Navier–Stokes (VANS) equations has been adopted to describe the flow inside the permeable wall. In order to solve the VANS equations, closures are required for the subfilter–scale stress and the drag force in terms of volume–averaged flow quantities. In porous media subfilter–scale dispersion is usually negligible compared to drag, and it is therefore neglected. The drag force in the interface region is modeled by the same closure model for the drag force as used for the homogeneous porous region, in combination with a variable–porosity model.

The above method has been successfully validated in chapter 6 by means of a DNS of the turbulent flow in a plane channel with a permeable bottom wall composed of a 3D Cartesian grid of cubes. The conclusion is thus that the turbulent flow over a permeable wall can be accurately simulated by means of a DNS combined with the continuum approach based on the VANS equations for the flow inside the permeable wall.

- **Influence wall permeability on structure and dynamics of turbulence**

In chapter 5, results have been presented from DNS of the turbulent flow in a plane channel with a solid top wall and a permeable bottom wall. The continuum approach based on the VANS equations has been used to describe the flow inside the permeable wall. The main objective was to investigate the influence of wall permeability on the structure and dynamics of turbulence. The main conclusions are listed below.

A key parameter to classify a permeable wall is the permeability Reynolds number, which can be interpreted as the ratio of the effective pore diameter to the typical length scale of near–wall eddies. For large values of this number, turbulence penetrates the permeable wall and wall–induced viscous effects are negligible. In this case, the wall is classified as highly permeable. For values of the permeability Reynolds number much smaller than unity, the wall is effectively impermeable and behaves like a solid wall.

The structure of turbulence near a highly permeable wall is different compared to turbulence near a solid (i.e. impermeable, smooth) wall. The latter is characterized by low– and high–speed streaks and the associated quasi–streamwise vortices. These structures are absent near a highly permeable wall. This is a consequence of turbulent transport across the wall and the reduction in mean shear, which are due to the weakening of the wall–blocking effect and wall–induced viscous effects respectively. Turbulence near a highly permeable wall is dominated by relatively large vortical structures, which originate possibly from a Kelvin–Helmholtz instability of the inflexional mean velocity profile. This conclusion supports the hypothesis of Raupach et al. [77] and Finnigan [28] that flow near the top of a plant canopy, which can be considered as a permeable wall layer, resembles more a plane mixing layer than a boundary layer.

The absence of low– and high–speed streaks near a highly permeable wall is consistent with a decrease in the peak of the streamwise rms velocity normalized by the friction velocity at the permeable wall. Despite the higher spanwise and wall–normal rms velocities, the peak in the profile of the turbulent kinetic energy is therefore smaller.

Wall permeability causes a large increase in the rms pressure, both in the contributions from the rapid and the slow part.

The relatively large vortical structures near the highly permeable wall are responsible for exchange of momentum between the channel and the top layer of the permeable wall. This process contributes strongly to the Reynolds–shear stress and consequently to the skin friction. This explains that the skin friction coefficient is higher for a permeable wall than for a solid wall, at least when the flow is turbulent. On the contrary, if the flow is laminar, then the skin friction coefficient is smaller for a permeable wall. In chapters 3 and 4 we found that this a consequence of an apparent slip velocity at the permeable wall.

For highly permeable walls, the slope of the logarithmic fit is substantially larger than the value of $1/\kappa$ commonly found for flows over both smooth and rough walls, where κ is

the Von Kármán constant of approximately 0.4. It is speculated that the increase in the slope of the logarithmic fit is related to the very large displacement height.
We investigated the validity of the wall similarity hypothesis [77] for turbulent flows over permeable walls. A characteristic length scale for the outer region is the boundary–layer thickness, which is defined as the distance between the permeable wall and the position where the total shear stress is zero. The streamwise rms velocity, the rms vorticities and the Reynolds–shear stress are self–similar in the outer region, irrespective the porosity of the wall. On the other hand, the spanwise and the wall–normal rms velocities and the rms pressure show significant departures from similarity. For highly permeable walls, the wall–normal velocity is significantly correlated over a large wall–normal distance. This suggests that the flow in the outer region communicates with the flow in the inner region, and this might explain the observed departures from similarity.

7.2 Discussion

- **Modeling of surface roughness**

In this thesis a formalism has been developed for DNS of turbulent flows over permeable walls. The continuum approach based on the VANS equation is used, to describe the flow inside the permeable wall. The permeable wall is divided into a homogeneous porous region with a constant porosity and an interface region characterized by a spatially varying porosity. With respect to the averaging volume of the filter used, the topology of the interface region is heterogeneous and hence it is different compared to the topology of the homogeneous porous region. For this reason, we consider the interface region as the surface–roughness layer of the permeable wall.
In order to model the effect of surface roughness on the volume–averaged flow correctly, appropriate closures are needed for the subfilter–scale stress and the drag force in the interface region. We argued in sections 2.6 and 5.3 that subfilter–scale dispersion can be neglected. The drag force in the interface region is modeled by means of the *same* closure as used for the drag force in the homogeneous porous region, in combination with a variable–porosity model. This is a rather crude model, because we already mentioned that the interface and the homogeneous porous region have a different topology, which has a strong influence on the drag force. On the other hand, this model ensures that the drag force is continuous over the interface region. Thus, although the permeability and the Forchheimer tensors are not modeled correctly in the interface region, they approach at least the expected limits at the boundaries of the interface region with the homogeneous porous and the homogeneous fluid region. As long as the wall is highly permeable, the error made in this approach is likely to be small, because in this case turbulence penetrates down into the homogeneous porous region. This is substantiated by the results presented in chapter 6, where a good agreement was found between the direct simulation and the simulation in which the continuum approach was used. In these simulations, the roughness Reynolds number was relatively small, whereas the permeability Reynolds number was

relatively high. This may explain the good agreement between the two simulations. However, if a wall is not highly permeable, then our model for the drag force in the interface region probably will yield incorrect results. A more appropriate drag model need to be developed for this case, or one has to perform a direct simulation, which captures the detailed surface roughness of the wall, instead of a simulation using the continuum approach.

- **Logarithmic law**

Jackson [38] interpreted the virtual origin of the logarithmic law as the position where the mean drag force appears to act. This model provides an alternative way of determining the displacement height, instead of using a direct fit of the logarithmic law to the mean velocity profile. The latter leads often to rather inaccurate results when applied to experimental data, due to scatter and the limited amount of measurement locations. DNS data however, is very smooth and the logarithmic layer is well–resolved on many mesh points, which enables a direct fit of the logarithmic law to the velocity profile. It has been found in section 5.6.1, that Jackson's method strongly underpredicts the value for the displacement height found from a direct fit of the logarithmic law to the mean velocity profile, at least for our simulations of flows over highly permeable walls. Because we are not aware of other methods to predict the displacement height, this implies that the displacement height may be obtained only from a direct fit of the logarithmic law to the mean velocity profile. This is a strong complication for the analysis of measurement data, because we just mentioned that a direct fit of the logarithmic law to the measured velocity profile is rather insecure.

In section 5.6.1, we concluded that for highly permeable walls the parameters of the logarithmic law are different than commonly found for fully rough walls. The slope $1/\lambda$, the displacement height d as well as the parameter z_0, are all much larger for a highly permeable wall than expected for an impermeable wall with a similar surface roughness. As will be discussed below, this has important consequences for both experiments on and numerical simulations of turbulent flows over highly permeable walls.

In the analysis of experimental data on turbulent boundary layers, it is usually assumed that the slope of the mean velocity profile in the logarithmic layer is equal to the inverse of the Von Kármán constant. In studies on flow over plant canopies, Jackson's method is frequently used to determine the displacement height. Using this value for the displacement height and assuming the universality of the Von Kármán constant, the friction velocity can then be determined from a fit of the logarithmic layer to the mean velocity profile. It is however clear, based on our findings, that this method to determine the friction velocity can not be applied to turbulent flows over highly permeable walls.

In LES and RANS simulations of turbulent boundary layers it is convenient to use a wall function based on the logarithmic law [107], because the inner wall region can not be resolved. This requires the specification of the parameters λ, d and z_0 in the logarithmic law. However, because no methods are available to accurately predict the values of these parameters at this moment, wall functions can not be used for turbulent flows over highly permeable walls.

7.3 Recommendations for future research

- **LES and RANS simulations combined with continuum approach**

In this thesis, we successfully validated the use of the continuum approach in DNS of turbulent flows over permeable walls. A natural extension of our work is to develop and validate a formalism for using the continuum approach in LES and RANS simulations. The closures needed for respectively the subgrid–scale and Reynolds stresses can be evaluated by means of the DNS data presented in this thesis.

- **Modeling of wall roughness**

In the previous section, we discussed the modeling of wall roughness in the continuum approach based on the VANS equations. We suggested that the interface region of a permeable wall may be considered as the surface–roughness layer. We have explained that if the wall is not highly permeable and the effect of surface roughness is important, then our model for the drag force in the interface region probably will fail. It is recommended to check this, for instance by means of a simulation based on the continuum approach and a direct simulation of flow over a rough wall covered with cubes.

- **Wall roughness versus wall permeability**

As discussed in chapter 1, in the literature experimental evidence exists for the different effects of wall permeability and wall roughness on wall–bounded flows. In this thesis, we aimed to gain insight in the effect of wall permeability. For this reason, the parameters of the permeable walls in chapters 5 and 6, were chosen such that the roughness Reynolds number was relatively small and the permeability Reynolds number relatively high. We have shown that wall permeability is responsible for a change in the structure and dynamics of turbulence. Besides, we showed that the parameters in the logarithmic law have different values for highly permeable walls than expected for impermeable walls with a similar surface roughness. A natural extension of this research would be a more systematic investigation of the different effects of wall permeability and wall roughness, for instance by means of simulations of turbulent flows over a variable amount of cube layers as illustrated in figure 6.2.

- **Logarithmic law**

It is recommended to thoroughly investigate how the parameters of the logarithmic law are related to the properties of the wall. The results presented in chapter 5 suggest that these parameters strongly depend on the permeability Reynolds number. This could be systematically investigated by means of a large number of simulations of turbulent flows over permeable walls with different permeabilities.

- **Parameterization of drag force and effective viscosity**

In chapter 4, we suggested a parameterization for the drag force which includes a diffusion–like term, see equation (4.43). Lundgren [59] suggested that the effective viscosity might be either lower or higher than the fluid viscosity, dependent of the solidity of the porous medium. It is recommended to investigate this in more detail, for instance by means of simulations of Stokes flow through a spatially periodic grid of cubes subject to a spatially varying external force such that the volume–averaged flow is non–uniform.

- **Subfilter–scale stress**
In section 2.6, we proposed closures for the subfilter–scale stress, which still awaits a rigorous validation. The closure problem for mechanical dispersion could be investigated by means of simulations of laminar flow through a staggered arrangement of cubes, subject to a spatially varying external force such that the volume–averaged flow is non–uniform. The closure problem for turbulent dispersion could be investigated by means of a similar simulation, but at a much higher Reynolds number such that the flow is fully turbulent.

Appendix A

Transport equation for the subfilter–scale kinetic energy

In this appendix the transport equation (2.33) is derived for the subfilter–scale kinetic energy $e \equiv \langle u_i u_i \rangle/2 - \langle u_i \rangle \langle u_i \rangle/2$. A similar derivation of this equation was also given by Wang & Takle [99]. They stated (p. 80) that they did not make any assumptions, accept for the parameterization of the drag force. In the derivation below however we show that actually two basic assumptions were made:

1. The porosity is constant.
2. The volume–averaged flow is well–behaved [30], i.e. $\langle\langle u_i \rangle\rangle \approx \langle u_i \rangle$ and $\langle \tilde{u}_i \rangle \approx 0$. A consequence of this assumption is that $e \approx \langle \tilde{u}_i \tilde{u}_i \rangle/2$.

The transport equation for $\tilde{u}_i \equiv u_i - \langle u_i \rangle$ is obtained by subtracting equation (2.19) for $\langle u_i \rangle$ from the Navier–Stokes equation for u_i. Using the assumption of constant porosity, this yields:

$$\frac{\partial \tilde{u}_i}{\partial t} + \frac{\partial}{\partial x_j}\left[\tilde{u}_i \langle u_j \rangle + \langle u_i \rangle \tilde{u}_j + \tilde{u}_i \tilde{u}_j\right] - \frac{\partial \langle \tilde{u}_i \tilde{u}_j \rangle}{\partial x_j} = -\frac{1}{\rho}\frac{\partial \tilde{p}}{\partial x_i} + \nu \frac{\partial^2 \tilde{u}_i}{\partial x_j^2} - f_i \qquad \text{(A.1)}$$

The continuity equation for $\tilde{u}_i$ is given by:

$$\frac{\partial \tilde{u}_i}{\partial x_i} = 0 \qquad \text{(A.2)}$$

The equation for $\tilde{u}_i \tilde{u}_i/2$ may be obtained by multiplying equation (A.1) by $\tilde{u}_i$. The resulting equation is then volume–averaged according to (2.5) in order to obtain the equation for e. The preliminary result reads:

$$\begin{aligned} \frac{\partial \langle \frac{1}{2}\tilde{u}_i^2 \rangle}{\partial t} + \langle u_j \rangle \langle \frac{\partial \frac{1}{2}\tilde{u}_i^2}{\partial x_j} \rangle \quad + \quad & \langle \tilde{u}_i \tilde{u}_j \rangle \frac{\partial \langle u_i \rangle}{\partial x_j} + \langle \frac{\partial \frac{1}{2}\tilde{u}_i \tilde{u}_i \tilde{u}_j}{\partial x_j} \rangle - \langle \tilde{u}_i \frac{\partial \langle \tilde{u}_i \tilde{u}_j \rangle}{\partial x_j} \rangle = \\ - \quad & \langle \frac{1}{\rho}\frac{\partial \tilde{p}\tilde{u}_i}{\partial x_i} \rangle + \langle \nu \frac{\partial^2 \frac{1}{2}\tilde{u}_i^2}{\partial x_j^2} \rangle - \langle \nu \left(\frac{\partial \tilde{u}_i}{\partial x_j}\right)^2 \rangle - \langle \tilde{u}_i f_i \rangle \qquad \text{(A.3)} \end{aligned}$$

With help of the spatial averaging theorem (2.12), the second term on the left–hand side of (A.3) can be rewritten according to:

$$\begin{aligned}
\langle u_j\rangle\langle\frac{\partial\frac{1}{2}\tilde{u}_i^2}{\partial x_j}\rangle &= \langle u_j\rangle\frac{\partial e}{\partial x_j}+\langle u_j\rangle\frac{1}{\epsilon}\int_A m\frac{1}{2}\tilde{u}_i^2 n_j dA\\
&= \langle u_j\rangle\frac{\partial e}{\partial x_j}+\langle u_j\rangle\frac{1}{\epsilon}\left[\int_A m n_j dA\right]\frac{1}{2}\langle u_i\rangle^2
\end{aligned}$$

in which we used the fact that, according to equation (2.10), $\tilde{u}_i = -\langle u_i\rangle$ at the surface A of the solid phase, and that $\langle\langle u_i\rangle\rangle \approx \langle u_i\rangle$; hence $\langle u_i\rangle$ may be taken out of the surface integral. From equation (2.13a) it is found that the last term in the above equation is equal to zero, because the porosity is constant. In a similar manner we can derive for the last two terms on the left–hand side of equation (A.3) that:

$$\begin{aligned}
\langle\frac{\partial\frac{1}{2}\tilde{u}_i\tilde{u}_i\tilde{u}_j}{\partial x_j}\rangle &= \frac{\partial\langle\frac{1}{2}\tilde{u}_i\tilde{u}_i\tilde{u}_j\rangle}{\partial x_j}-\frac{1}{\epsilon}\left[\int_A m n_j dA\right]\frac{1}{2}\langle u_i\rangle^2\langle u_j\rangle = \frac{\partial\langle\frac{1}{2}\tilde{u}_i\tilde{u}_i\tilde{u}_j\rangle}{\partial x_j}\\
\langle\tilde{u}_i\frac{\partial\langle\tilde{u}_i\tilde{u}_j\rangle}{\partial x_j}\rangle &= \langle\tilde{u}_i\rangle\frac{\partial\langle\tilde{u}_i\tilde{u}_j\rangle}{\partial x_j} = 0
\end{aligned}$$

The first two terms on the right–hand side of equation (A.3) can be written as:

$$\begin{aligned}
-\langle\frac{1}{\rho}\frac{\partial\tilde{p}\tilde{u}_i}{\partial x_i}\rangle &= -\frac{1}{\rho}\frac{\partial\langle\tilde{p}\tilde{u}_i\rangle}{\partial x_i}+\frac{1}{\epsilon}\left[\int_A m\frac{\tilde{p}}{\rho}n_i dA\right]\langle u_i\rangle\\
\langle\nu\frac{\partial^2\frac{1}{2}\tilde{u}_i^2}{\partial x_j^2}\rangle &= \nu\frac{\partial^2 e}{\partial x_j^2}-\frac{1}{\epsilon}\left[\int_A m\nu\frac{\partial\tilde{u}_i}{\partial x_j}n_j dA\right]\langle u_i\rangle
\end{aligned}$$

The last term on the right–hand side of (A.3) is equal to zero, because the drag force f_i is a volume–averaged quantity:

$$\langle\tilde{u}_i f_i\rangle = \langle\tilde{u}_i\rangle f_i = 0$$

The final form of the transport equation for e becomes:

$$\begin{aligned}
\frac{\partial e}{\partial t}+\langle u_j\rangle\frac{\partial e}{\partial x_j} &= -\langle\tilde{u}_i\tilde{u}_j\rangle\frac{\partial\langle u_i\rangle}{\partial x_j}+\frac{\partial}{\partial x_j}\left[-\frac{1}{\rho}\langle\tilde{p}\tilde{u}_i\rangle\delta_{ij}-\langle\frac{1}{2}\tilde{u}_i\tilde{u}_i\tilde{u}_j\rangle+\nu\frac{\partial e}{\partial x_j}\right]\\
&\quad -\langle\nu\left(\frac{\partial\tilde{u}_i}{\partial x_j}\right)^2\rangle - f_i\langle u_i\rangle \qquad \text{(A.4)}
\end{aligned}$$

Equation (A.4) is basically the same as equation (20) of Wang & Takle [99], except that we did not include the effect of Coriolis and buoyancy forces in our analysis and that we did not use any parameterization for the drag force.

The first and the last term on the right–hand side of (A.4) appear with an opposite sign in the transport equation for the large–scale kinetic energy $E \equiv \frac{1}{2}\langle u_i\rangle^2$, i.e. the kinetic energy of the volume–averaged flow, which is readily obtained from the multiplication of equation (2.19) for $\langle u_i \rangle$ by $\langle u_i \rangle$. Using the assumption of constant porosity, this yields:

$$\begin{aligned} \frac{\partial E}{\partial t} + \langle u_j \rangle \frac{\partial E}{\partial x_j} &= \langle \tilde{u}_i \tilde{u}_j \rangle \frac{\partial \langle u_i \rangle}{\partial x_j} + \frac{\partial}{\partial x_j} \left[-\frac{1}{\rho} \langle p \rangle \langle u_i \rangle \delta_{ij} - \langle \tilde{u}_i \tilde{u}_j \rangle \langle u_i \rangle + \nu \frac{\partial E}{\partial x_j} \right] \\ & -\nu \left(\frac{\partial \langle u_i \rangle}{\partial x_j} \right)^2 + f_i \langle u_i \rangle \qquad \text{(A.5)} \end{aligned}$$

Thus large–scale kinetic energy is transferred to subfilter–scale kinetic energy due to the work done by the drag force f_i and the subfilter–scale stress $\tau_{ij} \approx \langle \tilde{u}_i \tilde{u}_j \rangle$.

Appendix B

A note on simulations of flows over and through porous media.

Abstract *In section 2.6 we remarked that the nature of subfilter–scale dispersion is fundamentally different from turbulent diffusion by turbulent motions of the volume–averaged flow. In this appendix the implications of this are discussed for LES of flows over and through porous media and for simulations using a Reynolds–averaged form of the VANS equations.*

B.1 Simulations using a Reynolds–averaged form of the VANS equations.

Recently some turbulence models of the $k-\epsilon$ type have been developed for turbulent flows through porous media. Pedras & De Lemos [71] address a controversy in the closures proposed for the drag term in the transport equation for the Turbulent Kinetic Energy (TKE). De Lemos & Pedras [20], Pedras & De Lemos [71] and Silva et al. [88] model this drag term as a *source* of TKE, whereas Antohe & Lage [2] and Getachew et al. [29] model it as a *sink* of TKE. The difference originates from the definition of the TKE. De Lemos & Pedras define the TKE by $\langle\overline{u_i'^2}\rangle/2$, whereas Antohe & Lage define it by $\overline{\langle u_i\rangle'^2}/2$. Assuming that $\langle\langle u_i'\rangle\rangle \approx \langle u_i'\rangle$, the relation between the two TKE definitions is given by:

$$\underbrace{\frac{1}{2}\langle\overline{u_i'^2}\rangle}_{\text{total TKE}} = \underbrace{\frac{1}{2}\overline{\langle u_i\rangle'^2}}_{\text{large–scale TKE}} + \underbrace{\frac{1}{2}\langle\overline{\tilde{u}_i'^2}\rangle}_{\text{subfilter–scale TKE}} \tag{B.1}$$

Thus the definition of De Lemos & Pedras embraces the sum of both the large–scale TKE (i.e. the TKE of the volume–averaged flow) and the subfilter–scale TKE, whereas Antohe & Lage consider only the large–scale TKE. As discussed in section 2.5, the drag force is responsible for a transfer of large–scale kinetic energy to subfilter–scale kinetic energy. This transfer of energy concerns not only TKE, but also Mean Kinetic Energy (MKE).

The transfer of large–scale TKE to subfilter–scale TKE does not directly affect[1] the total TKE, but it causes clearly a decrease of large–scale TKE. For this reason, Antohe & Lage model the influence of the drag force as a sink of large–scale TKE. The transfer of large–scale MKE ($\langle\overline{u}_i\rangle^2/2$) to subfilter–scale TKE[2] causes an increase in the total TKE, and consequently De Lemos & Pedras have to model the influence of the drag force as a source of total TKE.

Similar to the decomposition of the total TKE, the total Reynolds–shear stress $\langle\overline{u_i'u_j'}\rangle$ can be decomposed according to:

$$\underbrace{\langle\overline{u_i'u_j'}\rangle}_{\text{total Reynolds–shear stress}} = \underbrace{\overline{\langle u_i\rangle'\langle u_j\rangle'}}_{\text{large–scale Reynolds–shear stress}} + \underbrace{\langle\overline{\tilde{u}_i'\tilde{u}_j'}\rangle}_{\text{subfilter–scale stress}} \tag{B.2}$$

Consistent with their definition of the TKE, De Lemos & Pedras propose a parameterization for the *total* Reynolds–shear stress $\langle\overline{u_i'u_j'}\rangle$, based on the *total* TKE and the *total* dissipation rate. The drawback of this approach is however that it ignores the different natures of the subfilter–scale stress and the large–scale Reynolds–shear stress. Although subfilter–scale motions may contribute substantially to the total TKE (see section 2.5), these motions are not much contributing to turbulent diffusion of volume–averaged momentum because of the small scales of subfilter–scale turbulence (see section 2.6). We therefore believe that the $k-\epsilon$ model of De Lemos & Pedras [20], Pedras & De Lemos [71] and Silva et al. [88] for the total Reynolds–shear stress, based on the total TKE and the total dissipation rate, overpredicts turbulent diffusion. It is recommended to parameterize the subfilter–scale stress and the large–scale Reynolds–shear stress separately. This approach was followed by Antohe & Lage [2] and Getachew et al. [29], among others. They formulated a $k-\epsilon$ model in which the parameterization for the *large–scale* Reynolds–shear stress is based on the *large–scale* TKE and dissipation rate. The subfilter–scale stress was apparently neglected, which however is usually allowed as discussed in section 2.6.

B.2 LES of flows over and through porous media

Since the first LES of flow over a forest by Shaw & Schumann [87] in 1992, a number of similar LES studies have been reported in literature. It is not surprising that a similar controversy exists about the influence of the drag force on the subgrid–scale (SGS) kinetic energy as also exists for the previously discussed simulations in which a Reynolds–averaged form of the VANS equations is used. Shaw & Schumann [87], Dwyer et al. [24] and Watanabe [100] consider drag as a *sink* of SGS kinetic energy, whereas Su et al. [91] and to some extent Kanda & Hino [43] consider the drag as a *source* of SGS kinetic energy. This problem has been discussed recently by Shaw & Patton [86], who make distinction between resolved–scale kinetic energy, SGS kinetic energy and wake–scale kinetic energy.

---

[1] The transfer of large–scale TKE to subfilter–scale TKE causes actually an enhancement of viscous dissipation, and thus it causes *indirectly* a decrease of the total TKE.

[2] The large–scale MKE is actually transferred to both subfilter–scale TKE *and* subfilter–scale MKE.

In this section we give theoretical support to this distinction. We show that the LES equations for flows through forests are actually filtered twice, which is not explicitly mentioned before in literature. This has important implications for the modeling of the subgrid–scale stress.

As pointed out by Shaw & Patton [86] (p.8) the mesh spacing in LES of canopy flows can be two orders of magnitude larger than the typical length scale of the canopy elements. We estimate the filter length required for the *local* form (see section 2.3) of the VANS equations by roughly ten times the length scale of the canopy elements. Thus the mesh spacing is an order of magnitude larger than the filter length that is required for the local form of the VANS equations. This basically means that in the LES a filtered form of the VANS equations is used, i.e. the original Navier–Stokes equations are filtered twice. We will refer to the first filter to obtain the local form of the VANS equations as the *volume–averaging filter*, and to the second filter as the *grid filter*. In the terminology of Shaw & Patton the subfilter–scale kinetic energy associated with the volume–averaging filter is the wake–scale energy, and the subfilter–scale kinetic energy associated with the grid filter is the SGS kinetic energy. Below we derive the transport equations for the resolved–scale kinetic energy, the SGS kinetic energy and the wake–scale kinetic energy.

The grid average of a volume–averaged quantity may be defined according to:

$$\{\langle \mathbf{u} \rangle\} \equiv \int_{V_g} m_g \langle \mathbf{u} \rangle dV \tag{B.3}$$

where V_g and m_g are respectively the averaging volume and the weighting function of the grid filter. Note that in our definition of the grid average there is no need to use a phase–indicator function like in equation (2.5), because the volume–averaged flow $\langle \mathbf{u} \rangle$ is continuous in space.

Similar to the spatial decomposition given by (2.10), we decompose the volume–averaged velocity $\langle \mathbf{u} \rangle$ into a grid average and a spatial deviation $\hat{\mathbf{u}}$ thereof:

$$\langle \mathbf{u} \rangle = \{\langle \mathbf{u} \rangle\} + \hat{\mathbf{u}} \tag{B.4}$$

To simplify the analysis, we will assume that:

1. The porosity is constant.
2. The volume–averaged flow is well–behaved, i.e. $\langle\langle \mathbf{u} \rangle\rangle \approx \langle \mathbf{u} \rangle$ and $\langle \tilde{\mathbf{u}} \rangle \approx \mathbf{0}$.
3. The grid average of the volume–averaged flow is well–behaved, i.e. $\{\{\langle \mathbf{u} \rangle\}\} \approx \{\langle \mathbf{u} \rangle\}$ and $\{\hat{\mathbf{u}}\} \approx \mathbf{0}$.

Application of the grid filter (B.3) to the VANS equations (2.17a) and (2.17b) yields the Grid–averaged Volume–Averaged Navier–Stokes (GVANS) equations. With the assumption of constant porosity, the GVANS equations read:

$$\frac{\partial \{\langle \mathbf{u} \rangle\}}{\partial t} + \nabla \cdot \{\langle \mathbf{u} \rangle\}\{\langle \mathbf{u} \rangle\} + \nabla \cdot [\{\boldsymbol{\tau}_s\} + \{\boldsymbol{\tau}_w\}] = -\frac{1}{\rho}\nabla\{\langle p \rangle\} + \nu\nabla^2\{\langle \mathbf{u} \rangle\} + \{\mathbf{f}\} \tag{B.5a}$$

$$\nabla \cdot \{\langle \mathbf{u} \rangle\} = 0 \tag{B.5b}$$

where $\{\boldsymbol{\tau}_s\}$ and $\{\boldsymbol{\tau}_w\}$ are respectively the subgrid–scale stress and the grid average of the wake–scale stress. They are defined by:

$$\begin{aligned} \{\boldsymbol{\tau}_s\} &\equiv \{\langle\mathbf{u}\rangle\langle\mathbf{u}\rangle\} - \{\langle\mathbf{u}\rangle\}\{\langle\mathbf{u}\rangle\} \approx \{\hat{\mathbf{u}}\hat{\mathbf{u}}\} && \text{(B.6a)} \\ \{\boldsymbol{\tau}_w\} &\equiv \{\langle\mathbf{u}\mathbf{u}\rangle - \langle\mathbf{u}\rangle\langle\mathbf{u}\rangle\} \approx \{\langle\tilde{\mathbf{u}}\tilde{\mathbf{u}}\rangle\} && \text{(B.6b)} \end{aligned}$$

For clarity we use the subscript w to denote the wake–scale stress, although $\boldsymbol{\tau}_w$ is the same as the subfilter–scale stress $\boldsymbol{\tau}$ in equation (2.17a). Note that the GVANS equations have almost the same form as the VANS equations. The single difference is that in the GVANS equations a subgrid–scale stress is included, which is associated with the subgrid–scale motions of the volume–averaged flow field. If the computational mesh spacing Δ is chosen sufficiently small, smaller than the filter length of the volume–averaging filter, then the grid average is the same as the volume average: $\{\langle\mathbf{u}\rangle\} \approx \langle\mathbf{u}\rangle$. Consequently, the subgrid–scale stress $\{\boldsymbol{\tau}_s\}$ is negligible and the GVANS equations are exactly the same as the VANS equations.

We are now able to derive the transport equations for the resolved–scale kinetic energy $E_r \equiv \frac{1}{2}\{\langle\mathbf{u}\rangle\}\{\langle\mathbf{u}\rangle\}$, the subgrid–scale kinetic energy $e_s \equiv \frac{1}{2}\{\langle\mathbf{u}\rangle\langle\mathbf{u}\rangle\} - \frac{1}{2}\{\langle\mathbf{u}\rangle\}\{\langle\mathbf{u}\rangle\} \approx \frac{1}{2}\{\hat{\mathbf{u}}\hat{\mathbf{u}}\}$ and the wake–scale kinetic energy $e_w \equiv \frac{1}{2}\{\langle\mathbf{u}\mathbf{u}\rangle - \langle\mathbf{u}\rangle\langle\mathbf{u}\rangle\} \approx \frac{1}{2}\{\langle\tilde{\mathbf{u}}\tilde{\mathbf{u}}\rangle\}$. The sum of the three energies is the total grid–averaged volume–averaged kinetic energy:

$$\frac{1}{2}\{\langle\mathbf{u}\mathbf{u}\rangle\} = E_r + e_s + e_w \tag{B.7}$$

The equation for E_r is obtained from the inner product of (B.5a) with $\{\langle\mathbf{u}\rangle\}$. The result reads:

$$\begin{aligned} \frac{\partial E_r}{\partial t} + \{\langle\mathbf{u}\rangle\}\nabla E_r &= \left(\{\boldsymbol{\tau}_s\} + \{\boldsymbol{\tau}_w\}\right)\nabla\{\langle\mathbf{u}\rangle\} + \\ &\quad \nabla\left[-\frac{1}{\rho}\{\langle\mathbf{u}\rangle\}\{\langle p\rangle\}\mathbf{I} - \{\langle\mathbf{u}\rangle\}\left(\{\boldsymbol{\tau}_s\} + \{\boldsymbol{\tau}_w\}\right) + \nu\nabla E_r\right] - \\ &\quad \nu\nabla\{\langle\mathbf{u}\rangle\}\nabla\{\langle\mathbf{u}\rangle\}^T + \{\langle\mathbf{u}\rangle\}\{\mathbf{f}\} \end{aligned} \tag{B.8}$$

The first term on the right–hand side represents the loss of energy due to the work done by wake–scale and SGS stresses. The terms between the square brackets [..] are transport terms. The penultimate term represents viscous dissipation. The last term on the right–hand side represents the loss of resolved–scale kinetic energy by drag.

The derivation of the equation for the subgrid–scale kinetic energy e_s is fairly tedious and is left to the reader. The result reads:

$$\begin{aligned} \frac{\partial e_s}{\partial t} + \{\langle\mathbf{u}\rangle\}\nabla e_s &= -\{\boldsymbol{\tau}_s\}\nabla\{\langle\mathbf{u}\rangle\} + \{\hat{\boldsymbol{\tau}}_w\nabla\hat{\mathbf{u}}\} + \\ &\quad \nabla\left[-\frac{1}{\rho}\{\hat{\mathbf{u}}\hat{p}\}\mathbf{I} - \{\hat{\mathbf{u}}\hat{\boldsymbol{\tau}}_w\} - \{\frac{1}{2}\hat{\mathbf{u}}\hat{\mathbf{u}}\hat{\mathbf{u}}\} + \nu\nabla e_s\right] - \\ &\quad \nu\{\nabla\hat{\mathbf{u}}\nabla\hat{\mathbf{u}}^T\} + \{\hat{\mathbf{u}}\hat{\mathbf{f}}\} \end{aligned} \tag{B.9}$$

The first term on the right–hand side of (B.9) represents the energy extracted from the resolved–scale flow field due to the work done by the subgrid–scale stress. It therefore appears with an opposite sign in the equation for E_r. The second term on the right–hand side is the loss of SGS kinetic energy due to the work done by the wake–scale stress. The terms between the square brackets [..] are transport terms. The penultimate term on the right–hand side represents viscous dissipation. The last term on the right–hand side is the loss of SGS kinetic energy by drag. The above equation is similar to the equation Shaw & Patton [86] propose for the SGS kinetic energy (p.10), although their equation does not contain the second term on the right–hand side of our equation. Furthermore, Shaw & Patton subdivide the drag into form drag and viscous drag and state that by means of viscous drag SGS kinetic energy is directly dissipated and that only the form drag is responsible for a transfer of SGS kinetic energy to wake–scale energy. However, our analysis clearly shows that both form drag *and* viscous drag are responsible for the transfer of resolved–scale and SGS kinetic energy to wake–scale kinetic energy *before* the energy is finally dissipated.

The equation for the wake–scale kinetic energy is the grid average of equation (2.33) for e:

$$\begin{aligned}\frac{\partial e_w}{\partial t} + \{\langle\mathbf{u}\rangle\}\nabla e_w \quad = \quad & -\{\boldsymbol{\tau}_w\}\nabla\{\langle\mathbf{u}\rangle\} - \{\hat{\boldsymbol{\tau}}_w\nabla\hat{\mathbf{u}}\} + \\ & \nabla\left[-\frac{1}{\rho}\{\langle\tilde{p}\tilde{\mathbf{u}}\rangle\}\mathbf{I} - \{\langle\frac{1}{2}\tilde{\mathbf{u}}\tilde{\mathbf{u}}\tilde{\mathbf{u}}\rangle\} - \{\hat{\mathbf{u}}\hat{e}_w\} + \nu\nabla e_w\right] \\ & -\nu\{\langle\nabla\tilde{\mathbf{u}}\nabla\tilde{\mathbf{u}}^T\rangle\} - \{\langle\mathbf{u}\rangle\}\{\mathbf{f}\} - \{\hat{\mathbf{u}}\hat{\mathbf{f}}\} \qquad \text{(B.10)}\end{aligned}$$

where $\hat{e}_w$ is defined according to $\hat{e}_w \equiv \langle\tilde{\mathbf{u}}\tilde{\mathbf{u}}\rangle/2 - \{\langle\tilde{\mathbf{u}}\tilde{\mathbf{u}}\rangle\}/2$. The first and the second term on the right–hand side of (B.10) represent respectively the transfer of resolved–scale and SGS kinetic energy to wake–scale kinetic energy due to the work done by the wake–scale stress. These terms therefore appear with an opposite sign in equations (B.8) and (B.9) respectively. Shaw & Patton do not include these two terms in their equation for the wake–scale kinetic energy. The terms between the square brackets [..] are transport terms. The fourth term on the right–hand side represents viscous dissipation. The last two terms on the right–hand side represent respectively the transfer of resolved–scale kinetic energy and SGS kinetic energy to wake–scale kinetic energy due to the work done by the drag force (both form and viscous drag). These terms therefore appear with an opposite sign in equations (B.8) and (B.9) respectively. As mentioned before, Shaw & Patton do not account for the contribution of the viscous drag to the wake–scale kinetic energy, which might lead to a substantial underestimate of the wake–scale kinetic energy.

Su et al. [91] used a single parameterization for the sum of the wake–scale and the SGS stress, with the associated eddy viscosity based on the mesh spacing and the combined energy of the wake–scale and SGS flow. As discussed in section 2.5, the wake–scale kinetic energy can be of the same order as the large–scale kinetic energy, and consequently the eddy viscosity may become excessively large. This problem was also encountered by Su et al. and they therefore reduced the eddy viscosity inside the forest by a factor four. From our analysis above it is clear that the nature of the wake–scale stress is fundamentally different from the SGS stress, and therefore they should be parameterized separately. In section 2.6 we argued that the wake–scale stress has usually a negligible influence on the volume–averaged flow, and therefore only the SGS stress need to be modeled. This substantiates the approach followed by Shaw & Schumann [87] to model only the SGS viscosity, which was parameterized by the product of the mesh spacing and the square root of the SGS kinetic energy, and to model the influence of the drag force as a loss of SGS kinetic energy.

Bibliography

[1] B. Alazmi and K. Vafai. Analysis of fluid flow and heat transfer interfacial conditions between a porous medium and a fluid layer. *International Journal of Heat and Mass Transfer*, 44:1735–1749, 2001.

[2] B.V. Antohe and J.L. Lage. A general two–equation macroscopic turbulence model for incompressible flow in porous media. *International Journal of Heat and Mass Transfer*, 40:3013–3024, 1997.

[3] G.K. Batchelor. *An introduction to fluid dynamics.* Cambridge University Press, Cambridge, 2000.

[4] J. Bear. *Dynamics of fluids in porous media.* Dover Publications, New York, 1988.

[5] G.S. Beavers and D.D. Joseph. Boundary conditions at a naturally permeable wall. *Journal of Fluid Mechanics*, 30:197–207, 1967.

[6] A.S. Berman. Laminar flow in channels with porous walls. *Journal of Applied Physics*, 24:1232–1235, 1969.

[7] R.B. Bird, W.E. Stewart, and E.N. Lightfoot. *Transport Phenomena.* John Wiley & Sons, New York, 2002.

[8] W.P. Breugem. *The influence of wall permeability on laminar and turbulent flows. Theory and simulations.* PhD thesis, Delft Universtity of Technology, 2004.

[9] W.P. Breugem and B.J. Boersma. The turbulent flow over a permeable wall. In *Center for Turbulence Research – Proceedings of the Summer Program 2002*, pages 215–228, 2002.

[10] W.P. Breugem and B.J. Boersma. Direct Numerical Simulations of turbulent flow over a permeable wall using a direct and a continuum approach. *Accepted for publication in Physics of Fluids*, 17(2), 2005.

[11] W.P. Breugem, B.J. Boersma, and R.E. Uittenbogaard. The influence of wall permeability on turbulent channel flow. *Submitted to Journal of Fluid Mechanics.*

[12] W.P. Breugem, B.J. Boersma, and R.E. Uittenbogaard. The laminar boundary layer over a permeable wall. *Accepted for publication in Transport in Porous Media.*

[13] W.P. Breugem, B.J. Boersma, and R.E. Uittenbogaard. Direct Numerical Simulation of plane channel flow over a 3D Cartesian grid of cubes. In A.H. Reis and A.F. Miguel, editors, *Applications of Porous Media*, pages 27–35. Évora Geophysics Center, 2004.

[14] H.C. Brinkman. A calculation of the viscous force exerted by a flowing fluid on a dense swarm of particles. *Applied Scientific Research*, A1:27–34, 1948.

[15] T. Cebeci and P. Bradshaw. *Momentum transfer in boundary layers.* McGraw-Hill, New York, 1977.

[16] C.Y. Chow. *An introduction to Computational Fluid Dynamics.* John Wiley & Sons, New York, 1979.

[17] J.H. Cushman. Multiphase transport equations: I – General equation for macroscopic statistical, local, space–time homogeneity. *Transport Theory and Statistical Physics*, 12(1):35–71, 1983.

[18] E.R. Damiano, B.R. Duling, K. Ley, and T.C. Skalak. Axisymmetric pressure–driven flow of rigid pellets through a cylindrical tube lined with a deformable porous wall layer. *Journal of Fluid Mechanics*, 314:163–189, 1995.

[19] H.P.G. Darcy. *Les fontaines publiques de la ville de Dijon.* Victor Dalmont, Paris, 1856.

[20] M.J.S. De Lemos and M.H.J. Pedras. Simulation of turbulent flow through hybrid porous medium–clear fluid domains. In *Proceedings of the ASME Heat Transfer Division, HTD-Vol. 366-5*, 2000.

[21] M.J.S. De Lemos and M.H.J. Pedras. Recent mathematical models for turbulent flow in saturated rigid porous media. *Journal of Fluids Engineering*, 123:935–940, 2001.

[22] R.B. Dean. Reynolds number dependence of skin friction and other bulk flow variables in two–dimensional rectangular duct flow. *Journal of Fluids Engineering*, 100:215–223, 1978.

[23] P.G. Drazin and W.H. Reid. *Hydrodynamic Stability.* Cambridge University Press, Cambridge, 1981.

[24] M.J. Dwyer, E.G. Patton, and R.H. Shaw. Turbulent kinetic energy budgets from a Large–Eddy Simulation of airflow above and within a forest canopy. *Boundary–Layer Meteorology*, 84:23–43, 1997.

[25] E.A. Fadlun, R. Verzicco, P. Orlandi, and J. Mohd-Yusof. Combined Immersed–Boundary Finite–Difference Methods for three–dimensional complex flow simulations. *Journal of Computational Physics*, 161:35–60, 2000.

[26] R.M. Fand, B.Y.K. Kim, A.C.C. Lam, and R.T. Phan. Resistance to the flow of fluids through simple and complex porous media whose matrices are composed of randomly packed spheres. *Journal of Fluids Engineering*, 109:268–274, 1987.

[27] J. Feng and S. Weinbaum. Lubrication theory in highly compressible porous media: the mechanics of skiing, from red cells to humans. *Journal of Fluid Mechanics*, 422:281–317, 2000.

[28] J. Finnigan. Turbulence in plant canopies. *Annual Review of Fluid Mechanics*, 32:519–571, 2000.

[29] D. Getachew, W.J. Minkowycz, and J.L. Lage. A modified form of the $\kappa - \epsilon$ model for turbulent flows of an incompressible fluid in porous media. *International Journal of Heat and Mass Transfer*, 43:2909–2915, 2000.

[30] W.G. Gray. A derivation of the equations for multi–phase transport. *Chemical Engineering Science*, 30:229–233, 1975.

[31] S.K. Gupte and S.G. Advani. Flow near the permeable boundary of a porous medium: an experimental investigation using LDA. *Experiments in Fluids*, 22:408–422, 1997.

[32] S. Hahn, J. Je, and H. Choi. Turbulent channel flow with permeable walls. *Journal of Fluid Mechanics*, 450:259–285, 2002.

[33] J. Happel and H. Brenner. *Low Reynolds number hydrodynamics.* Noordhoff International Publishing, Leyden, 1973.

[34] S.M. Hassanizadeh and W.G. Gray. Boundary and interface conditions in porous media. *Water Resources Research*, 25:1705–1715, 1989.

[35] J.O. Hinze. *Turbulence.* McGraw-Hill, New York, 1975.

[36] J.C.R. Hunt and P.A. Durbin. Perturbed vortical layers and shear sheltering. *Fluid Dynamics Research*, 24:375–404, 1999.

[37] S. Irmay. Modèles théoriques d'écoulement dans les corps poreux. *Bulletin Rilem*, 29:37–43, 1965.

[38] P.S. Jackson. On the displacement height in the logarithmic velocity profile. *Journal of Fluid Mechanics*, 111:15–25, 1981.

[39] W. Jäger, A. Mikelić, and N. Neuss. Asymptotic analysis of the laminar viscous flow over a porous bed. *Siam Journal on Scientific Computing*, 22:2006–2028, 2001.

[40] D.F. James and M.J. Davis. Flow at the interface of a model fibrous porous medium. *Journal of Fluid Mechanics*, 426:47–72, 2001.

[41] J. Jiménez. Turbulent flows over rough walls. *Annual Review of Fluid Mechanics*, 36:173–196, 2003.

[42] J. Jiménez and P. Moin. The minimal flow unit in near–wal turbulence. *Journal of Fluid Mechanics*, 225:213–240, 1991.

[43] M. Kanda and M. Hino. Organized structures in developing turbulent flow within and above a plant canopy, using a Large–Eddy Simulation. *Boundary–Layer Meteorology*, 68:237–257, 1994.

[44] I. Kececioglu and Y. Jiang. Flow through porous media of packed spheres saturated with water. *Journal of Fluids Engineering*, 116:164–170, 1994.

[45] J. Kim, P. Moin, and R. Moser. Turbulence statistics in fully developed channel flow at low Reynolds number. *Journal of Fluid Mechanics*, 177:133–166, 1987.

[46] F.Y. Kong and J.A. Schetz. Turbulent boundary layer over porous surfaces with different surface geometries. In *Proceedings of the AIAA 20th Aerospace Sciences Meeting, AIAA-82-0030*, 1982.

[47] P.-A. Krȯgstad and R.A. Antonia. Surface roughness effects in turbulent boundary layers. *Experiments in Fluids*, 27:450–460, 1999.

[48] P.-A. Krȯgstad, R.A. Antonia, and L.W.B. Browne. Comparison between rough– and smooth–wall turbulent boundary layers. *Journal of Fluid Mechanics*, 245:599–617, 1992.

[49] A.V. Kuznetsov. Influence of the stress jump condition at the porous–medium/clear–fluid interface on a flow at a porous wall. *International Community of Heat and Mass Transfer*, 24:401–410, 1997.

[50] J.L. Lage. The fundamental theory of flow through permeable media from Darcy to turbulence. In D.B. Ingham and I. Pop, editors, *Transport Phenomena in Porous Media*, pages 1–30. Pergamon, Oxford, 1998.

[51] J.L. Lage, B.V. Antohe, and D.A. Nield. Two types of nonlinear pressure–drop versus flow–rate relation observed for saturated porous media. *Journal of Fluids Engineering*, 119:700–706, 1997.

[52] R.E. Larson and J.J.L. Higdon. Microscopic flow near the surface of two-dimensional porous media. Part 1. Axial flow. *Journal of Fluid Mechanics*, 166:449–472, 1986.

[53] R.E. Larson and J.J.L. Higdon. Microscopic flow near the surface of two-dimensional porous media. Part 2. Transverse flow. *Journal of Fluid Mechanics*, 178:119–136, 1987.

[54] M.J. Lee, J. Kim, and P. Moin. Structure of turbulence at high shear rate. *Journal of Fluid Mechanics*, 216:561–583, 1990.

[55] S.L. Lee and J.H. Yang. Modeling of Darcy–Forchheimer drag for fluid flow across a bank of circular cylinders. *International Journal of Heat and Mass Transfer*, 40:3149–3155, 1997.

[56] M. Lesieur and O. Métais. New trends in Large–Eddy Simulations of turbulence. *Annual Review of Fluid Mechanics*, 28:45–82, 1996.

[57] F. López and M.H. García. Mean flow and turbulence structure of open–channel flow through non–emergent vegetation. *Journal of Hydraulic Engineering*, 127:392–402, 2001.

[58] T.J. Lu, H.A. Stone, and M.F. Ashby. Heat transfer in open–cell metal foams. *Acta Materialia*, 46(10):3619–3635, 1998.

[59] T.S. Lundgren. Slow flow through stationary random beds and suspensions of spheres. *Journal of Fluid Mechanics*, 51(2):273–299, 1972.

[60] H. Ma and W. Ruth. The microscopic analysis of high Forchheimer number flow in porous media. *Transport in porous media*, 13:139–160, 1993.

[61] I.F. MacDonald, M.S. El-Sayed, K. Mow, and F.A.L. Dullien. Flow through porous media: the Ergun equation revisited. *Industrial and Engineering Chemistry*, 18:199–208, 1979.

[62] N.N. Mansour, J. Kim, and P. Moin. Reynolds–stress and dissipation–rate budgets in a turbulent channel flow. *Journal of Fluid Mechanics*, 194:15–44, 1988.

[63] T. Masuoka and Y. Takatsu. Turbulence model for flow through porous media. *International Journal of Heat and Mass Transfer*, 39:2803–2809, 1996.

[64] P. Moin and K. Mahesh. Direct Numerical Simulation: a tool in turbulence research. *Annual Review of Fluid Mechanics*, 30:539–578, 1998.

[65] H.M. Nepf. Drag, turbulence, and diffusion in flow through emergent vegetation. *Water Resources Research*, 35(2):479–489, 1999.

[66] D.A. Nield. Comments on 'Turbulence model for flow through porous media'. *International Journal of Heat and Mass Transfer*, 40:2499, 1997.

[67] J.A. Ochoa-Tapia and S. Whitaker. Momentum transfer at the boundary between a porous medium and a homogeneous fluid – I. Theoretical development. *International Journal of Heat and Mass Transfer*, 38:2635–2646, 1995.

[68] J.A. Ochoa-Tapia and S. Whitaker. Momentum transfer at the boundary between a porous medium and a homogeneous fluid – II. Comparison with experiment. *International Journal of Heat and Mass Transfer*, 38:2647–2655, 1995.

[69] J.A. Ochoa-Tapia and S. Whitaker. Momentum jump condition at the boundary between a porous medium and a homogeneous fluid: inertial effects. *Journal of Porous Media*, 1:201–217, 1998.

[70] E.G. Patton, R.H. Shaw, M.J. Judd, and M.R. Raupach. Large–Eddy Simulation of windbreak flow. *Boundary–Layer Meteorology*, 87:275–306, 1998.

[71] M.H.J. Pedras and M.J.S. De Lemos. Macroscopic turbulence modeling for incompressible flow through undeformable porous media. *International Journal of Heat and Mass Transfer*, 44:1081–1093, 2001.

[72] B. Perot and P. Moin. Shear–free turbulent boundary layers. Part 1. Physical insights into near–wall turbulence. *Journal of Fluid Mechanics*, 295:199–227, 1995.

[73] D. Poulikakos and M. Kazmierczak. Forced convection in a duct partially filled with a porous material. *Journal of Heat Transfer*, 109:653–662, 1987.

[74] M. Quintard and S. Whitaker. Transport in ordered and disordered porous media I: The cellular average and the use of weighting functions. *Transport in Porous Media*, 14:163–177, 1994.

[75] M. Quintard and S. Whitaker. Transport in ordered and disordered porous media II: Generalized volume averaging. *Transport in Porous Media*, 14:179–206, 1994.

[76] M. Quintard and S. Whitaker. Transport in ordered and disordered porous media IV: computer generated porous media for three–dimensional systems. *Transport in Porous Media*, 15:51–70, 1994.

[77] M.R. Raupach, R.A. Antonia, and S. Rajagopalan. Rough–wall turbulent boundary layers. *Applied Mechenical Review*, 44(1):1–25, 1991.

[78] S. Richardson. A model for the boundary condition of a porous material. Part 2. *Journal of Fluid Mechanics*, 49:327–336, 1971.

[79] J.F. Ruff and L.W. Gelhar. Turbulent shear flow in porous boundary. *Journal of the Engineering Mechanics Division*, 98(EM4):975–991, 1972.

[80] P.G. Saffman. On the boundary condition at the surface of a porous medium. *Studies in Applied Mathematics*, L(2):93–101, 1971.

[81] M. Sahraoui and M. Kaviany. Slip and no–slip velocity boundary conditions at interface of porous, plain media. *International Journal of Heat and Mass Transfer*, 35:927–943, 1992.

[82] A.S. Sangani and S. Behl. The planar singular solutions of Stokes and Laplace equations and their application to transport processes near porous surfaces. *Physics of Fluids*, A1:21–37, 1989.

[83] H. Schlichting. *Boundary-Layer Theory.* McGraw-Hill, New York, 1979.

[84] O. Séro-Guillaume and J. Margerit. Modeling forest fires. Part I: a complete set of equations derived by extended irreversible thermodynamics. *International Journal of Heat and Mass Transfer*, 45:1705–1722, 2002.

[85] R.H. Shaw, G. Den Hartog, and H.H. Neumann. Influence of foliar density and thermal stability on profiles of Reynolds stress and turbulence intensity in a deciduous forest. *Boundary–Layer Meteorology*, 45:391–409, 1988.

[86] R.H. Shaw and E.G. Patton. Canopy elements influences on resolved– and subgrid–scale energy within a Large–Eddy Simulation. *Agricultural and Forest Meteorology*, 115:5–17, 2003.

[87] R.H. Shaw and U. Schumann. Large–Eddy Simulation of turbulent flow above and within a forest. *Boundary–Layer Meteorology*, 61:47–64, 1992.

[88] R.A. Silva and M.J.S. De Lemos. Turbulent flow in a channel occupied by a porous layer considering the stress jump at the interface. *International Journal of Heat and Mass Transfer*, 46:5113–5121, 2003.

[89] J.C. Slattery. *Momentum, energy, and mass transfer in continua.* McGraw–Hill, New York, 1972.

[90] E. Stalio, W.P. Breugem, and B.J. Boersma. Numerical study of heat transfer above a porous wall. In A.H. Reis and A.F. Miguel, editors, *Applications of Porous Media*, pages 191–198. Évora Geophysics Center, 2004.

[91] H.-B. Su, R.H. Shaw, K.T. Paw U, C.-H. Moeng, and P.P. Sullivan. Turbulent statistics of neutrally stratified flow within and above a sparse forest from Large–Eddy Simulation and field observations. *Boundary–Layer Meteorology*, 88:363–397, 1998.

[92] G.I. Taylor. A model for the boundary condition of a porous material. Part 1. *Journal of Fluid Mechanics*, 49:319–326, 1971.

[93] H. Tennekes and J.L. Lumley. *A first coarse in turbulence.* MIT Press, Cambridge, 1999.

[94] R.E. Uittenbogaard. Modeling turbulence in vegetated aquatic flows. In *Riparian Forest Vegetated Channels, Workshop Trento, Italy*, pages 1–17, 2003.

[95] K. Vafai. Convective flow and heat transfer in variable–porosity media. *Journal of Fluid Mechanics*, 147:233–259, 1984.

[96] K. Vafai and S.J. Kim. Fluid mechanics of the interface region between a porous medium and a fluid layer - An exact solution. *International Journal of Heat and Fluid Flow*, 11:254–256, 1990.

[97] S. Vollmer, R. Francisco de los Santos, H. Daebel, and G. Kühn. Micro scale exchange processes between surface and subsurface water. *Journal of Hydrology*, 269:3–10, 2002.

[98] J.M. Wallace, H. Eckelmann, and R.S. Brodkey. The wall region in turbulent shear flow. *Journal of Fluid Mechanics*, 54(1):39–48, 1972.

[99] H. Wang and E.S. Takle. Boundary–layer flow and turbulence near porous obstacles. *Boundary–Layer Meteorology*, 74:73–88, 1995.

[100] T. Watanabe. Large–Eddy Simulation of coherent turbulence structures associated with scalar ramps over plant canopies. *Boundary–Layer Meteorology*, 112:307–341, 2004.

[101] P. Wesseling. *Principles of Computational Fluid Dynamics.* Springer–Verlag, Berlin, 2001.

[102] S. Whitaker. Advances in theory of fluid motion in porous media. *Industrial and Engineering Chemistry*, 61:14–28, 1969.

[103] S. Whitaker. Flow in porous media I: A theoretical derivation of Darcy's Law. *Transport in Porous Media*, 1:3–25, 1986.

[104] S. Whitaker. The Forchheimer equation: a theoretical development. *Transport in Porous Media*, 25:27–61, 1996.

[105] S. Whitaker. *The method of volume averaging.* Kluwer, Dordrecht, 1999.

[106] F.M. White. *Viscous fluid flow.* McGraw-Hill, New York, 1974.

[107] D.C. Wilcox. *Turbulence modeling for CFD.* Griffin Printing, Glendale (United States of America), 1993.

[108] J.D. Wilson. A second–order closure model for flow through vegetation. *Boundary–Layer Meteorology*, 42:371–392, 1988.

[109] A.M. Yaglom. Similarity laws for constant–pressure and pressure–gradient turbulent wall flows. *Annual Review of Fluid Mechanics*, 11:505–540, 1979.

[110] A.F.E. Zagni and K.V.H. Smith. Channel flow over permeable beds of graded spheres. *Journal of the Hydraulics Division*, 102(HY2):207–222, 1976.

[111] A.A. Zick and G.M. Homsy. Stokes flow through periodic arrays of spheres. *Journal of Fluid Mechanics*, 115:13–26, 1982.

[112] H.J. Zippe and W.H. Graf. Turbulent boundary–layer flow over permeable and non–permeable rough surfaces. *Journal of Hydraulic Research*, 21(1):51–65, 1983.

Nawoord

Met het schrijven van dit nawoord leg ik de laatste hand aan dit proefschrift. Ik heb er met veel plezier aan gewerkt. Het is jammer dat er nu een eind aan gekomen is. Aan de andere kant voelt het goed dat het boekje nu eindelijk af is! Op deze plaats wil ik een aantal mensen bedanken die mij hebben bijgestaan in mijn promotieonderzoek over de afgelopen vier jaar.

In de eerste plaats dank ik Bendiks-Jan Boersma, mijn toegevoegd promotor, die in zijn rol als dagelijks begeleider veel heeft bijgedragen aan dit onderzoek. Bedankt voor de prettige samenwerking. Ik waardeer de ruimte die ik kreeg in mijn onderzoek, en de steun die ik van jou ervaren heb. Ik heb veel profijt gehad van jouw kennis en ervaring op het gebied van numerieke simulaties. Bij computerperikelen kon ik ook altijd bij jou terecht. Ik wil je ook danken voor de mogelijkheid die ik kreeg om met jou naar CTR (Stanford) te gaan. Voor mij is dit een hoogtepunt geweest in de afgelopen jaren!

Mijn dank gaat ook uit naar Rob Uittenbogaard, mijn tweede begeleider, die mijn promotieproject geïnitieerd heeft. Ik bewonder je enthousiasme, je scherp inzicht en het gemak waarmee je ingewikkelde materie helder weet te verwoorden. De discussies die wij met elkaar gevoerd hebben, waren altijd inspirerend voor mij en hebben veel bijgedragen tot dit proefschrift.

Professor Frans Nieuwstadt dank ik voor zijn rol als promotor. Via jou kwam ik in contact met professor Jos Spaan van het AMC in Amsterdam, voor wie ik met veel plezier een onderzoek heb uitgevoerd naar de invloed van de zogenaamde endothelial glycocalyx op de stroming van bloed in de microcirculatie. Bedankt voor het lezen en het constructief becommentariëren van de artikelen die ik geschreven heb.

Peter Geelhoed en Rene Delfos hebben, in het kader van Peter's afstuderen, hittedraadsmetingen uitgevoerd aan grenslaagstroming over een poreuze plaat van schuimmetaal. Al had ik geen actieve rol in dit onderzoek, ik vond het leuk om erbij betrokken te zijn geweest. Naar aanleiding van deze experimenten heb ik de invloed van wandpermeabiliteit op een laminaire grenslaag onderzocht, zoals beschreven in hoofdstuk 3.

In ons laboratorium hebben we regelmatig gasten over de vloer. Zo ook Enrico Stalio van de universiteit van Trieste, Italië. Hij heeft op ons lab aan een project gewerkt, dat gerelateerd was aan mijn onderzoek: een numerieke studie van de invloed van wandpermeabiliteit op warmteoverdracht in een turbulente kanaalstroming. Op onderzoeksgebied gingen we ieder onze eigen weg, maar het contact met elkaar was goed.

Met veel plezier heb ik een tweetal studenten begeleid de afgelopen jaren, Francesc Aixela

Palou en Peter Helmendach. Francesc heeft een aantal maanden gewerkt aan een stabiliteitsanalyse van de invloed van wandpermeabiliteit op een laminaire grenslaag. Dit was geen eenvoudig onderzoek, maar kon toch succesvol afgerond worden. Peter is met lof afgestudeerd op de analyse van het sedimentatieproces in de laadbak van een baggerschip. Zowel voor Peter als voor mij was dit een geheel nieuw onderzoeksgebied, en misschien juist daarom extra leuk.

Op regelmatige basis hebben ik, Bendiks-Jan en Rob overleg gehad met Bas Hofland en Rob Booij van de faculteit Civiele Techniek. Bas heeft in het kader van zijn promotieonderzoek experimenten gedaan aan erosie van een rivierbed. Ondanks de raakvlakken in ons beider onderzoek, waren onze projecten te verschillend om de resultaten met elkaar te kunnen vergelijken. Niettemin waardeer ik de bijeenkomsten die we gehad hebben. Bas, veel succes met de laatste loodjes!

Professor Julian Hunt dank ik voor de discussies die we met elkaar gevoerd hebben over mijn onderzoek, met name over hoofdstuk 5.

Bij Mathieu Pourquie kon ik terecht met computervragen. Ik dank jou ook voor de discussies over de Immersed Boundary Method.

Met veel plezier heb ik vier jaar lang ons laboratorium vertegenwoordigd in de AIO–contactgroep van het J.M. Burgerscentrum. Fabio Paravento heeft het stokje onlangs van mij overgenomen. Succes!

Patrizia, Piotr, Ralph, Chiara, Peter V. en Bendiks-Jan waren mijn kamergenoten in de loop der jaren. We hebben ons dagelijks lief en leed met elkaar gedeeld.

Alle collega's en oud–collega's dank ik voor de onvergetelijke tijd die ik gehad heb op ons laboratorium. De dagelijkse koffiebijeenkomsten bij elkaar op de kamer, de schaakpartijtjes, de borrels, de BBQ's, de filmavondjes, het jaarlijks lab–uitje, etc., ze getuigen van de intensieve en goede band met elkaar.

Mijn familie en vrienden dank ik voor hun belangstelling in mijn reilen en zeilen als promovendus en hun ondersteuning.

Tot slot dank ik God voor Zijn zegen over mijn promotieonderzoek en mijn leven de afgelopen jaren. Ik geloof dat Hij deze wereld, inclusief de natuurwetten, geschapen heeft en onderhoudt. Door mijn promotieonderzoek is het ontzag voor Hem en Zijn schepping alleen maar groter geworden!

Wim-Paul Breugem
Delft, november 2004

Curriculum vitae

Wim-Paul Breugem was born in Bleiswijk on March 25th 1976. From 1988 to 1994 he attended the 'Revius College' in Rotterdam for his pre–university education (VWO). In 1994 he started with his studies Applied Physics at the Delft University of Technology. From 1998 to 1999 he worked at Sulzer Innotec AG in Winthherthur, Switzerland, for an internship of twelve months under supervision of Dr.-Ing. W. Jahnen. In this period he developed a numerical model for and performed experiments on the onset and subsequent development of stall phenomena in a single–stage centrifugal compressor. In 2000 he graduated on this project in the Laboratory for Aero and Hydrodynamics of professor Nieuwstadt, and obtained his MSc in Applied Physics. In September 2000 he started his PhD studies in the same laboratory, which finally resulted in this thesis four years later.

Journal publications

W.P. Breugem, B.J. Boersma and R.E. Uittenbogaard. The laminar boundary layer over a permeable wall. *Accepted for publication in Transport in Porous Media.*

W.P. Breugem and B.J. Boersma. Direct Numerical Simulations of turbulent flow over a permeable wall using a direct and a continuum approach. *Accepted for publication in Physics of Fluids*, 17(2), 2005.

W.P. Breugem and D.A.S. Rees. A derivation of the volume–averaged Boussinesq equations for flow in porous media with viscous dissipation. *Submitted to Transport in Porous Media.*

W.P. Breugem, B.J. Boersma and R.E. Uittenbogaard. The influence of wall permeability on turbulent channel flow. *Submitted to Journal of Fluid Mechanics.*

Conference contributions

W.Jahnen, W.P. Breugem and B. Ribi. Instability analysis of a centrifugal compressor stage near peak pressure rise. ASME 2001–GT–318.

W.P. Breugem and B.J. Boersma. The turbulent flow over a permeable wall. In *Center for Turbulence Research – Proceedings of the Summer Program 2002*, pages 215–228, 2002.

W.P. Breugem and B.J. Boersma. Turbulent channel flow over a permeable wall. In R. Friedrich, B.J. Geurts and O. Métais, editors, *Direct and Large–Eddy Simulation V*, 501–508. Kluwer, Dordrecht, 2004.

W.P. Breugem, B.J. Boersma and R.E. Uittenbogaard. Direct Numerical Simulations of plane channel flow over a 3D Cartesian grid of cubes. In A.H. Reis and A.F. Miguel, editors, *Applications of Porous Media*, 27–35. Évora Geophysics Center, Évora, 2004.

E. Stalio, W.P. Breugem and B.J. Boersma. Numerical study of turbulent heat transfer above a porous wall. In A.H. Reis and A.F. Miguel, editors, *Applications of Porous Media*, 191–198. Évora Geophysics Center, Évora, 2004.

W.P. Breugem, B.J. Boersma and R.E. Uittenbogaard. DNS of turbulent channel flow over a 3D Cartesian grid of cubes. In H.I. Andersson and P.-A. Krőgstad, *Advances in Turbulence X*, 285–288. CIMNE, Barcelona, Spain.

Visited conferences

The International Gas Turbine & Aeroengine Congress & Exhibition, New Orleans, 2001.
Center for Turbulence Research — Summer Program, Stanford, 2002.
Ercoftac workshop Direct and Large–Eddy Simulation V, Munich, 2003.
The 2^{nd} International Conference on Applications of Porous Media, Évora, 2004.
The 10^{th} Euromech European Turbulence Conference, Trondheim, 2004.